University of Southampton

Faculty of Engineering and Physical Sciences
School of Chemistry

The Theory and Methodology of Nuclear Spins Diffusing Through Porous Media

by

Topaz Alaska Alice Cartlidge

BSc

ORCiD: 0000-0003-3894-4229

A thesis for the degree of
Doctor of Philosophy

August 2024

University of Southampton

Abstract

Faculty of Engineering and Physical Sciences
School of Chemistry

Doctor of Philosophy

The Theory and Methodology of Nuclear Spins Diffusing Through Porous Media

by Topaz Alaska Alice Cartlidge

The internal architecture of porous media is often a mystery, which poses an issue for diffusional studies aimed at surveying structural parameters. Across many fields, NMR has excelled in determining parameters such as tortuosity and porosity: vital variables that can influence the efficiency of batteries or the proliferation of 3D cell cultures. Yet the technique is hindered by the inhomogeneous magnetic fields introduced when the heterogeneous system is placed within an external field. Any diffusing spins will therefore experience fluctuating fields, contributing to an exceedingly short T_2. Mitigation techniques include the use of long-lived states, magnetically silent states with lifetimes exceeding T_1 and T_2 by orders of magnitude, or transferring to low field at the cost of resolution. Yet there was no defined and proven numerical reasoning behind the effect of diffusion due to internal field gradients (DDIF), which was previously approximated to idealistic linear solutions. This unquantified effect abolishes the possibility of performing diffusion-NMR in some cases unless one can understand and therefore manage it. This thesis details the derivation of a numerical theory that incorporates Brownian dynamics and average Hamiltonian theory to produce a framework capable of calculating DDIF. Through understanding the phenomenon, a field-cycling technique is adopted, utilising a custom-built low-field probe to minimise magnetic susceptibility mismatches but increase sensitivity. The methodology is then applied to 3D cell cultures to provide a means of testing scaffold design for tissue growth.

Table of Contents

Glossary

μ-CT micro-computerised tomography

τ_c correlation time

ACF auto-correlation function

AHT average Hamiltonian theory

BBB blood-brain barrier

BFP bovine fibronectin protein

CED convection enhanced delivery

CFD computational fluid dynamics

CPMG Carr-Purcell-Meiboom-Gill

CSA chemical shift anisotropy

d-NMR diffusion NMR

DD inter-molecular dipole-dipole

DDIF decay due to diffusion in the internal field

DMEM Dulbecco's Modified Eagle Medium

DNP dynamic nuclear polarization

DOSY diffusion-ordered spectroscopy

DTI diffusion tensor imaging

ECM extracellular matrix

ECS extracellular space

EDX energy dispersion X-ray

EPR electron paramagnetic resonance

FA fractional anisotropy

FBS fetal bovine serum

FCS fluorescence correlation spectroscopy

FEM finite element method

FID free induction decay

FWHM full width half maximum

GDL gas diffusion layer

HMSC human mesenchymal stem cell

iDD intra-molecular dipole-dipole

IR infra red spectroscopy

LBM Lattice Boltzmann Method

lf-NMR low-field NMR

LLS long-lived state

M2S magnetisation to singlet

MAS magic angle spinning

MC3T3-E1 murine calvarial pre-osteoblast cell line

MCM Monte Carlo method

MD molecular dynamics

MeOD deuterated methanol

mfnc magnetic fields, no currents

MOC Mouse osteoblastic cells

MRI magnetic resonance imaging

MS mass spectrometry

NMR nuclear magnetic resonance

NSS nuclear singlet spin state

NTA nanoparticle tracking analysis

PBS phosphate buffered saline

PCL polycaprolactone

PEEK polyether ether ketone

PEMFC proton exchange membrane fuel cells

PFA paraformaldehyde fixative solution

PGSTE pulsed gradient stimulated echo

PRE paramagnetic relaxation enhancement

PS penicillin-streptomycin solution

PTFE polytetrafluoroethylene

rf radio frequency

RIE reactive ion etching

S2M singlet to magnetisation

SAD-NMR singlet assisted diffusion NMR

SBF simulated body fluid

SBF$_{10}$ concentrated simulated body fluid

SDF spectral density function

SEM scanning electron microscope

SHG second-harmonic generation imaging microscopy

SR spin-rotation

ss-NMR solid-state NMR

TEM transmission electron microscopy

TMS tetramethylsilane

List of Figures

List of Tables

Declaration of Authorship

I declare that this thesis and the work presented in it is my own and has been generated by me as the result of my own original research.

I confirm that:

1. This work was done wholly or mainly while in candidature for a research degree at this University;
2. Where any part of this thesis has previously been submitted for a degree or any other qualification at this University or any other institution, this has been clearly stated;
3. Where I have consulted the published work of others, this is always clearly attributed;
4. Where I have quoted from the work of others, the source is always given. With the exception of such quotations, this thesis is entirely my own work;
5. I have acknowledged all main sources of help;
6. Where the thesis is based on work done by myself jointly with others, I have made clear exactly what was done by others and what I have contributed myself;
7. Parts of this work have been published as:
   T. A. A. Cartlidge, T. Robertson, M. Utz, and G. Pileio, *J. Phys. Chem. B*, 2022, **126**, 6536-6546
   T. Robertson, R. C. Bannister, T. A. A. Cartlidge, T. Hugger, S. Breham, K. Zick, F. Engelke, S. Thompson, and G. Pileio, *Frontiers Media SA*, 2023, **11**, 1229586
   T. A. A. Cartlidge, Y. Wu, T. Robertson, O. L. Katsamenis, and G. Pileio, 2024, *in press*

Signed:..... Date:.....

Acknowledgements

I would first and foremost like to give a warm and sincere thank you to Associate Professor Giuseppe Pileio for not only his guidance and support but also his patience and kind words. I thoroughly appreciate every moment that was dedicated to my personal development, as well as the inspiring demonstrations of rich theoretical and experimental knowledge. As I move forward with my career, I will continuously say to people that a supervisor can make or break a PhD project. Luckily, I found myself within the group of those motivated and encouraged by theirs, who saw them as a friend and mentor. It goes without saying that this could not have been done without him.

I would also like to extend my thank you to Professor Marcel Utz for his guidance and patience as I ventured into the world of theory and computational studies. I will always look back fondly on the stimulating discussions and be grateful for the skills I learnt.

For her kindness, support and words of wisdom, I would like to thank Giulia Melchiorre. During our shared time in the Pileio group, I thoroughly appreciated her enthusiasm, motivation, and the presence of a friend in a similar situation as myself.

I am also incredibly grateful to Funds for Women Graduates, the Royal Society of Chemistry, and the Institute of Physics for providing me with generous funding. As well as the Desty Scholarship programme, set up through sheer generosity and goodwill by Denis Henry Desty. As well as supporting my general living expenses, these funds have facilitated my attendance at a number of exciting conferences. At which I presented my work and shared my findings with countless NMR enthusiasts.

For all their emotional and proofreading support I cannot exclude my close family members, specifically my Dad and Claire. It was refreshing to be challenged on aspects of my work by brilliant scientific minds not as familiar with this work. I hope you enjoyed your insight into NMR and have not been put off the field by my work!

Lastly, I am forever indebted to my husband, Will, for helping me through every step of the journey. Given all his encouragement, motivation, proofreading, questioning, and sanity checks, I am unsure how anyone could accomplish such a task without him. I maybe didn't say this enough at the time but thank you for keeping me writing.

To my husband. . .

Chapter 1

Aims, hypothesis, and methodology

The term porous media encompasses any solid matrix hosting a series of interconnecting pores and channels. The structure may be ordered with parallel channels of the same width or it may be random and unpredictable such as non-spherical beads packed into a tube. As such, the probing of the internal environment poses many challenges to numerous analytical techniques. Nuclear magnetic resonance (NMR), however, has long since been used to investigate these intricate structures due to its inherent non-invasive nature and penetrating abilities. NMR has previously demonstrated its strengths through the characterization of electrochemical storage abilities, the analysis of rock cores, and the study of tissue cultivations and growth patterns. [1–3]

When diffusion NMR (d-NMR) is applied to porous systems, the principal object of investigation is often a parameter such as the restricted diffusion coefficient, the porosity, or the tortuosity. [2,4] In these studies, the selected pulse sequences rely on the attenuation of transverse magnetization following the application of radio frequency (rf) pulses and gradients. Furthermore, the presence of solid media introduces unwanted localised internal field gradients, bringing about additional field inhomogeneities. As a consequence of this, diffusing spins will encounter a fluctuating external field that varies at a rate dependent on the size and distribution of the pores. This is known to have a detrimental impact on the longevity of transverse magnetisation. [5] Thus, when the system is particularly tortuous, or the pores are sufficiently large, all detectable signal is lost before the nuclear spins have surveyed their surrounding environment.

In limits such as these, conventional NMR techniques are incompatible with the porous media and must be adapted to account for this. However, the theory of NMR is yet to encompass a complete theoretical description of this susceptibility-induced relaxation mechanism. One possible solution to overcome this is the introduction of nuclear singlet spin state (NSS)s, a form of long-lived state (LLS), whose lifetimes have been shown to exceed that of conventional magnetisation by orders of magnitude, in well-studied circumstances. [6,7] Although this is a rapidly developing area of NMR, singlet

assisted diffusion NMR (SAD-NMR) is not yet compatible with all porous systems. To rectify this, the proceeding work aims to question the following hypothesis:

Magnetic susceptibility-induced relaxation is a principal culprit to the inability of NMR to operate within porous media but can be overcome through a combination of techniques such as long-lived states and field cycling methodologies.

To test this, the project aims to develop a quantum mechanical theory of susceptibility-induced relaxation and use a custom-designed methodology for studying previously inaccessible systems. This will be done via a combined computational and experimental approach, and will aim to complete the following objectives:

- $\mathbf{O}_1$ - Produce a numerical simulation framework capable of quantifying the signal loss as a result of magnetic susceptibility mismatches found within porous media,
- $\mathbf{O}_2$ - Enhance the framework by incorporating tortuosity simulations, verified through parallel NMR diffusion experiments run with the aid of nuclear singlet states,
- $\mathbf{O}_3$ - Introduce a custom field cycling methodology to take advantage of increased sensitivity found at high field and reduced low field magnetic susceptibility effects,
- $\mathbf{O}_4$ - Demonstrate the technique by applying both the simulation and the methodology to porous media that are of greater real-world significance and or importance.

This thesis will detail the advances made toward deriving this numerical theory and outline the steps taken toward extending the limits of d-NMR within porous media.

Chapter 2

Introduction

2.1 NMR as a modern tool

The story of NMR has conflicting origins as the very defining principle of the technique began with two parties both discovering the same quantum mechanical breakthrough. In 1926, Uhlenbeck and Goudsmit published their findings on the electron possessing angular momentum, or spin, in addition to mass and charge.[8] This was after R. Kronig originally described this phenomenon but was rejected by W. Pauli over the contradiction this theory would hold against classical dynamics.[9,10] In the era of pioneering quantum mechanics, Uhlenbeck and Goudsmit came to the same conclusion of the electron's spin, unaware of Kronig's discoveries.[10] Again, the theory was dismissed, this time by H. Lorentz, but the two decided to publish despite their lack of support. Following this stemmed a series of quantum mechanical breakthroughs including the emergence of the infamous Pauli spin matrices and Dirac Hamiltonian.[11,12] The two are used, respectively, to define spin along the three Cartesian axes for a particle possessing a spin of $1/2$ and describe the nature of electrons, combining both quantum theory and special relativity.

The idea of nuclei also possessing spin was introduced by D. Dennison who performed his calculations on a hydrogen molecules' specific heat and noted the result was only viable if "the nuclear spin is taken equal to that of the electron".[13] Studies on nuclei, not their overwhelming electron counterparts, were the main focus of I. Rabi, who measured the magnetic moment of a number of nuclei including hydrogen, deuterium, and multiple alkali metals, using weak magnetic fields.[14] His experiments, though revolutionary at the time, used comparatively crude setups whereby atomic beams were passed through a series of magnetic fields in order to observe the splitting due to spin orientations. After this, Rabi *et al.* devised a new setup which subjected the beam of molecules to an oscillating magnetic field, with a maintained frequency but differing strength. All housed within a static field in order to observe the resonance peaks.[15]

This allowed them to measure the magnetic moment of nuclei, within a sample of lithium chlorine. In their ground state, the nuclei within the molecular beam could be directed to the detector following their exposure to the oscillating magnetic field. Should the spins be reorientated, the deflection by means of magnetic fields would no longer be viable and the observed signal would drop, in relation to the field strength.

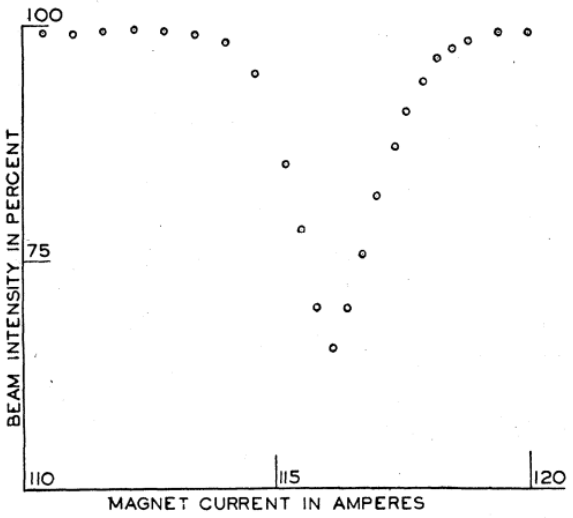

FIGURE 2.1: Original magnetic moment measurement made by Rabi *et al.* showing the particle beam refocused as a result of the field strength, taken from.[14]

Their studies ran in conjunction with Alvarez and Bloch who also brought about resonance in nuclei by subjecting them to oscillating magnetic fields.[16] Their experiments differed in that Alverez and Bloch held their oscillating field at a constant strength, H_0 and varied its frequency, ω. From there, NMR grew exponentially with the development of the theory relaxation and its measurement, made by studying ^{1}H resonance within ferric nitrate.[17] They understood the dissipation of energy from the irradiated nuclei into their surroundings and the role of the lattice in returning the system to thermal equilibrium. Following this came, possibly, the most famous NMR spectrum, demonstrating the ability of the technique to differentiate magnetic environments.[18]

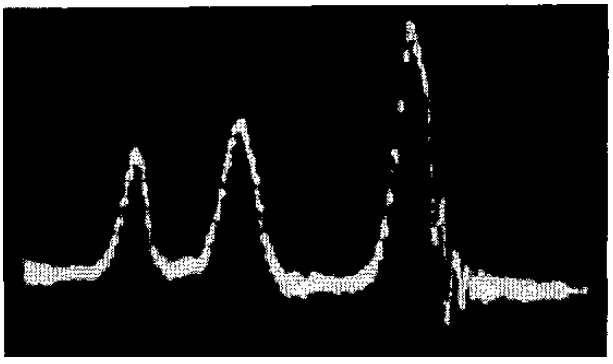

FIGURE 2.2: NMR spectrum of ethanol showing the differentiation of different ^{1}H environments based on their resonance frequency, taken from.[18]

From there, NMR has demonstrated its worth countless times in both liquids and gases, but it is also a useful tool for solid samples. In the liquid state, the molecules are continuously tumbling and re-orientating, their dipoles changing rapidly. Solid-state samples do not have such leniency and so the anisotropic nuclear magnetic interactions that result in signal loss are prevalent in these static samples. To combat this, the sample is spun at the magic angle in order to average out these orientation-dependent effects.[19] Under these conditions, magic angle spinning (MAS)- NMR is a versatile tool for studying a range of materials including soils (for environmental studies), metal-organic frameworks, and lipid membranes.[20–23] Furthermore, MAS-NMR is a principal technique used to study thin films: materials composed of either organic or inorganic materials and can be used in optical devices, biosensors, and solar cells.[20,24–26] Solid-state NMR (ss-NMR) can also be used to resolve the molecular structure, packing, and even the dynamics of thin films.[20] But this is only one example of ss- NMRs importance: it is an imperative tool for countless solid-state chemistry and biological studies.

In addition to structure elucidation, protein studies, and reaction monitoring, NMR can also be used to study dynamic processes such as diffusion. As well as probing the sample as a whole, NMR has the spatial selectivity to irradiate planes individually with each slice being exposed to a differing gradient strength. One can then use this to spatially encode spins and monitor diffusion throughout the system. Techniques such as diffusion-ordered spectroscopy (DOSY) measure diffusion coefficients within pure or complex solutions,[27] indicating the molecular weight of larger structures such as proteins.[28] Not only can one measure the diffusion coefficient, but the individual components of the diffusion tensor can also be determined, using diffusion tensor imaging (DTI). Thus, deciphering both how quickly a species diffuses and the principal direction of diffusion within an anisotropic heterogeneous structure.[29] And where there is information to be gathered on the diffusing molecules, one can also determine geometrical parameters of the system, based on the movement of molecules within it.

One of the main drawbacks to NMR is its inherent low sensitivity, which is discussed in further detail later in this chapter. Where other spectroscopic techniques utilise transitions with large energy changes, such as vibrational and rotational modes, NMR is restricted to nuclear spin transitions. Furthermore, NMR signal is also dependent on each nuclear gyromagnetic ratio (of which a ^{1}H nucleus has one of the largest) and the isotopic abundance. However, analytic techniques have advanced to overcome this issue in a number of situations. Essentially, NMR relies on the population difference between two quantum mechanical states, and the transition between them. Within hyperpolarisation, this natural population difference can be favourably enhanced by many orders of magnitude in order to increase the signal-to-noise ratio. The degree to which the sample is polarised is given by the polarization enhancement factor, ϵ, and can be up to five orders of magnitude greater than thermal equilibrium, at high field.[30]

Without hyperpolarisation, conventional methods for increasing signal lie in using cryogentically cooled probes, increasing the active coil region, and taking multiple scans of the same sample and stacking the results. However, hyperpolarising the sample reduces the need for so many repeated experiments and can reduce the experimental time significantly.[31] Hyperpolarisation can be achieved via many methods, most simply by polarising a sample at high field and then switching quickly to the desired experimental field strength. However, this option only sees use when the target field is either ultra-low or no magnetic field. Additionally, one can use nuclei with an inherently greater polarization and transfer this to a coupled nuclei of low-sensitivity.[31]

A more substantial method is dynamic nuclear polarization (DNP) which is governed by the principle that electrons possess a greater level of polarization compared to nuclei. As we have discovered, electrons are spin-$^1/_2$ particles and therefore have two non-degenerate spin orientations when exposed to an external magnetic field. Additionally, they possess a gyromagnetic ratio ~660 times greater than that of ^{1}H nucleus, and therefore ~2615 times for ^{13}C.[32] If the sample is subject to microwave radiation then the electronic polarization can be transferred to the nuclei, should the radiation be at (or near) the electron paramagnetic resonance (EPR) transition energy.[32] Hyperpolarisation sees its use in a number of NMR studies including drug screening, characterising protein interactions, and studying the kinetics of chemical reactions.[33–35] The technique can be seen to be used hand in hand with nuclear singlet states.[33]

Long-lived states are a relatively new aspect of NMR that exploit particular situations found in some molecules, to store magnetisation for extended periods of time.[36] More detail on their theory and uses will be given in later sections and chapters. To touch on them, these states have been shown to persist for orders of magnitude longer than conventional magnetisation, making them incredibly desirable for applications such as diffusion and *in vivo* studies.[7,37] Eills *et al.* have recently hyperpolarised singlet states in a metabolic molecule for the purpose of magnetic resonance imaging (MRI).[38]

As we have seen, NMR is a valuable tool for studying dynamic processes, such as diffusion, in three dimensions. We have also seen its ability to take a snapshot of the sample and return a quantitative analysis of the nuclei present and their environments. Taking this one step further, NMR can be used to take images, or multidimensional snapshots, of the system to determine spatial macro-environments. The basis of the techniques lies in the ability to selectively spatially encode spins such that only the plane of interest is irradiated. This began with the development of the first gradient echo sequence and paved the way for imaging through magnetic resonance.[39]

Since its introduction as a clinical tool in the 1980's, magnetic resonance imaging (MRI) and its applications have advanced significantly. It has branched into a range of different fields including earth science for studying geological flows, and in material science for the study of polymers and composites,[40,41] whilst maintaining its role

as a principal medicinal technique. Unlike techniques such as micro-computerised tomography (μ-CT), MRI is capable of producing three-dimensional images but does not rely on harmful electromagnetic radiation, making it more applicable to fragile samples. Unfortunately, MRI lacks the resolution of other techniques where μ-CT routinely delivers images with ~1000 times greater resolution than MRI.[42,43]

Aided by the fast-developing modern computational understanding and power, simulations are driving research forward in ways unattainable by physical examination. As such, a fast-expanding approach to performing NMR is within computational chemistry, a powerful and versatile science capable of exploring regimes not currently within the grasp of physical capabilities.[44] One principal area of computational study is within diffusion NMR, where simulated molecules are not subject to the complexities of paramagnetic relaxation or magnetic susceptibility differences, both explored below. Or rather, these effects can be manipulated more easily, in order to target specific regimes or phenomena. In the past, groups have experienced signal-to-noise ratio issues preventing physical DTI calculations.[45] Alternatively, simulations were used to overcome these issues and study the diffusion tensor within randomly and uniformly aligned capillaries where experimental data collection was inaccessible.[46] Where the accuracy of simulated results was verified by checking the bulk diffusion habits of the computational particles against experimental calculated results.

Computational studies also lend themselves to systems that may not be physically studied due to their size, complexity, or suitability for sample preparation.[47,48] Be these delicate biological samples, or intricate porous systems where relaxation parameters cannot be deduced by NMR experiments alone.[49] For example, Fichele *et al.* used simulations to study gas diffusion within 3D-modelled alveolar ducts as a method to study the possible progression of respiratory diseases.[48] Intelligent computational libraries, capable of simulating a whole manner of intricate NMR problems, now exist and are being used for MRI, relaxation, and chemical kinetics.[50,51] These libraries are fed vast arrays of quantum mechanical reasoning in order to predict experimental outcomes.

One area currently lacking a clearly defined theory is the relaxation of nuclear spins diffusing through porous media, encountering random internal field gradients. For molecules diffusing within a porous sample, in a magnetic field, the spins are exposed to the physical confinements of the media and also the internal field gradients produced by the heterogeneous sample. Since different materials are magnetised to differing degrees, field inhomogeneities are introduced at the liquid-solid boundary for a porous system within a magnetic field. This phenomenon is widely recognised, for example within rock samples and infilling water, and countless other porous systems.[52]

Within many studies, relaxation as a result of diffusion has been attributed to an exponential decay that depends on the magnitude of these internal gradients, the diffusion

coefficient, and the echo time.[53–56] However, the evolution of this exponential equation is derived from a system not representative of the porous systems explored within this project. Carr *et al.* derived an analytical expression for decay due to diffusion in the internal field (DDIF); however, their work assumed one-dimensional movement of a given step length through a constant linear gradient applied along the z-axis.[55] Although this expression is used as an approximation to diffusion through a gradient, there is a need for a numerical theory evaluating the extent of the susceptibility-induced relaxation within a porous system of arbitrary complexity.[54,55] After which, one can look to mitigate the effect through experimental techniques.

Pulse sequences have been developed to eliminate the first-order effects of internal field gradients, through manipulation of the spins using gradients and π pulses. In the instance of uncorrected sequences, even small susceptibility differences can lead to large errors in the diffusion coefficient calculation.[52] However, even with the corrected pulse sequence, there are certain limitations regarding the size of the gradient in relation to the sample length. Thus, alternative methods are still required.

Since DDIF is proportional to the external field, as explored in chapter 3, one way to limit its effects would be to shift to a low field; however, this would require a compromise of sensitivity.[57] An alternative method would be the introduction of a nuclear singlet spin state (NSS): a particular nuclear state with a longevity far exceeding T_2 and T_1.[6,7] NSSs would be beneficial at both limits of d-NMR in porous media as they possess immunity to internal gradients.[58] In small pores where T_2 is eradicated almost instantly, NSSs would survive long enough to probe the local environment. On the contrary, where the pores are large enough that T_2 has reduced significantly before the nuclei encounter a restricted region, NSSs would be able to travel further. It has been noted in previous studies that the tortuosity within some sedimentary rocks is not achieved due to limitations in the lifetime of T_1.[52] Furthermore, studies by Tourell *et al.* calculated the tortuosity within micro-bead packings using singlet states but concluded that a more thorough understanding of DDIF would be required before the technique could be applied to other systems.[59]

Be it physical experimentation or computational studies, NMR has proven its value countless times having been utilised in a multitude of scientific fields. As a spectroscopic technique, it is continuously being adapted and developed with the hardware becoming increasingly sophisticated. Yet, despite its progressions, there are still improvements to be made and mysteries present within this technique and its theory. Mysteries surrounding the diffusion of nuclei through complex porous media, and how this contributes to spin relaxation. But before we can delve into this problem, we must first solidify our understanding of NMR and its basic principles.

2.1.1 NMR: exploring the basics

The most central aspect of NMR revolves around spin: an intrinsic form of angular momentum possessed by fundamental particles and symbolised by s. For a generic particle, there are 2s+1 possible spin orientations, each with a magnitude of $1/2$ and given the values $m_s = 1/2$ and $m_s = -1/2$. The spin quantum number, m_s, in the case of the electron, corresponds to either the spin up or spin down configuration for $1/2$ and $-1/2$ respectively. This property is not unique to electrons, as we see nuclei possessing spin in the form of nuclear spin, $\boldsymbol{I}$. This is a vector quantity as it contains both a magnitude and a direction. As with electrons, a ^{1}H nucleus is a spin-$1/2$ system. For nuclei with greater $\boldsymbol{I}$ values, there exist multiple possible nuclear spin values depending on the coupling of the protons and neutrons, which determines the ground state configuration. For a nucleus to be NMR active it must have a non-zero ground state nuclear spin quantum number such that it possesses net angular momentum, $\boldsymbol{I}>0$.

Additionally, since $\boldsymbol{I}>0$ nuclei are charged particles with angular momentum, they also possess a magnetic moment, $\boldsymbol{\mu}$, with a corresponding magnitude, μ. The two are directly proportional through the gyromagnetic ratio, γ, which is unique to each isotope. Within the lab frame, where z is the principle axis, this relationship is most simply viewed in terms of the angular momentum's projection onto the z-axis:

$$\mu_z = \gamma I_z \tag{2.1}$$

For the ground state nuclear spin, I, there exist $2I+1$ degenerate spin states, which are denoted by the magnetic quantum number, m, and may take on the values of $-I \leq m \leq I$ in integral steps. When the system is exposed to an external magnetic field this degeneracy is removed since there will always be a preferred orientation with respect to the static field. For the example of a spin-$1/2$ nucleus, the two states are either $|\alpha\rangle$ or $|\beta\rangle$, which correspond to spin up and spin down respectively, with the lower energy state being $|\alpha\rangle$. The energy separation between the two states is directly proportional to the magnitude of the external field, B_0:

$$\Delta E = 2\mu_z B_0 \tag{2.2}$$

The loss of degeneracy is referred to as the Zeeman interaction and is one of the fundamental reasons for existence of NMR. Due to the relatively small energy difference, the population imbalance between the two levels is only minimal and follows the Boltzmann distribution:[60]

$$\begin{aligned} \frac{N_{Upper}}{N_{Low}} &= e^{\frac{-\Delta E}{K\,T}} \\ &= e^{-\beta \Delta E} \end{aligned} \tag{2.3}$$

Where T is the temperature and K is the Boltzmann constant, with a value of 1.3805×10^{-23} J K^{-1}. For nuclei where $\boldsymbol{I} > {}^{1}/_{2}$, the probability of spins being within a given energy level can be determined by the following equation:

$$P(E_i) = \frac{e^{-\beta E_i}}{\sum_i e^{-\beta E_i}} \tag{2.4}$$

Given that gyromagnetic ratios of commonly used NMR active nuclei lie within the region of 1×10^{7} to 1×10^{8} rad s^{-1} T^{-1}, the population difference between the two states is of the order of 1×10^{-4} to 1×10^{-5}rad s^{-1} T^{-1}.[61] Thus, typically only one in ten thousand nuclei will be aligned with the external field where the other spins are split evenly between the two states. To transition between the two energy levels, one must irradiate the system with radio frequency energy, resulting in a single-quantum transition. This will be touched on in more detail in the following sections.

Where nuclei possess intrinsic spin, related to the nuclear spin quantum number, they also possess physical spin in the form of precession. This is attributed to the slight "wobble" of nuclei about the direction of the external magnetic field, causing them to spin in a similar fashion to a spinning top. The rate of precession, or Larmor frequency, is specific to the system at hand and is given as the number of times, per second, that the nucleus precesses in a circle. The advantage of this natural phenomenon is the precise coding of each nucleus to its corresponding resonating frequency, ν_0.

$$\nu_0 = -\frac{1}{2\pi}\gamma B_0 \tag{2.5}$$

Thus, demonstrating the dependence of precession on the strength of the external field and the nucleus of interest. As mentioned, the resonating frequency of nuclei is specific to their Larmor frequency, which in turn is related to the external field they experience. However, nuclei are not the only charged particle interacting with the field: when electrons are subject to strong magnetic fields, they too produce their own induced magnetic field, albeit a small one. The associated and neighbouring nuclei are then shielded, to a certain degree, from the external field, thus altering the magnetic environment they are subject to. One can then determine the resonating frequency via the effective field strength, B_{eff}, and determine the individual magnetic environments of all active nuclei within a molecule. This deshielding is specific to the nuclear environment and is affected by both the functional groups within the molecules and the other nuclei present. More specifically, the system is susceptible to aromatics and hydrogen bonding, providing a route to study large and complex systems such as proteins and polymers.[62] This elevates our simple system into a powerful spectroscopic tool, providing structural elucidation of molecules, as long as they contain active NMR nuclei. The frequency of nuclei can be predicted based on their near environment and can also be estimated from universal tables of NMR data for a range of nuclei.

Since there exists a range of commercial magnets, each resonating range would therefore differ depending on the external field. As such, the frequency scale is normalised by an external field and reported in ppm to maintain consistency between reported values. Additionally, all ^{1}Hand ^{13}Cchemical shifts are reported against a standard, tetramethylsilane (TMS), as it contains completely equivalent and isolated examples of both ^{1}H and ^{13}C. This is then reported as having a chemical shift of 0 ppm.

$$\delta_{ppm} = 10^{6} \times \frac{\nu - \nu_{TMS}}{\nu_{TMS}} \tag{2.6}$$

Where δ_{ppm} is the chemical shift of a nucleus, ν is the frequency of the resonating nucleus, and ν_{TMS} is the frequency of TMS resonating within the given external field.

Other, complimentary, analytical techniques include the likes of mass spectrometry (MS) which is used for determining the mass-to-charge ratio of molecules. It is often used in conjunction with NMR for structure elucidation. The two techniques can determine the molecular mass, and possibly its fragments, and the relative environments which together form a powerful methodology for determining the molecular configuration. Another technique is infra red spectroscopy (IR) which is used for determining functional groups in molecules. This technique uses infrared radiation to excite molecules and cause movement in the form of bending and stretching etc. This is similar to Raman spectroscopy which is applicable for measuring symmetric movements in molecules whereas IR detects asymmetric movements. Both techniques rely on the absorption of photons and for Raman, this results in the excitation of electrons to higher energy states. In IR, the absorbed energy is converted into vibrational movement where functional groups with dipoles give rise to stronger IR signals. However, these are both structural determination techniques whereas NMR can also be used to measure dynamic processes such as diffusion.

To study molecular dynamics, one can use fluorescence correlation spectroscopy (FCS), a technique used for the measurement of concentration, diffusion coefficients, and molecular interactions.[63] In this technique, a small percentage of molecules are fluorescently tagged and emit light towards the detector. The light beam is intercepted by a pinhole, narrowing the observation window to the sample. Due to diffusion, by Brownian motion, the light seen through the pinhole fluctuates and therefore the measurement of diffusion is possible. This technique sees its drawbacks in its incompatibility with porous media; solid intrusions in the sample would prevent the observation of fluorescence coming from the liquid. This is because only fluorescence present on the focal plane is observed.[64] Diffusion measurements have been made on image slices in a 2D format, or within translucent materials, such as hydrogels or cells.[65,66]

Another two-dimensional technique is nanoparticle tracking analysis (NTA) which is focused on imaging individual particles using an ultramicroscope. This methodology uses laser illumination to visualise particles through their scattered light, over a series

of images compiled into a video. It relies on computational methods to track particle movement and determine parameters such as bulk diffusion coefficients.[64] However, this methodology is only compatible when imaging two-dimensional planes and is affected by the spherical shape of the particles.[64]

In the absence of analytical techniques, there are countless examples of simulations being used to measure diffusion and study porous media.[67–70] These include samples such as gas diffusion layer (GDL)s, polypropylene foam sheets, and model porous media produced via an algorithm. Simulations offer the opportunity to study the small and intricate aspects of a sample that physical experiments lack the accuracy to distinguish. Additionally, they may offer the chance to study systems not previously accessible due to their fragility or inaccessibility. The structure of the porous media can be extracted using techniques such as μ-CT, or extrapolated through statistical means.

In the instance where a material is unsuitable for 3D imaging techniques such as μ-CT, there are examples of internal structural properties being produced through digital reconstruction. These are based on parameters determined through surface analysis such as scanning electron microscope (SEM) imaging and assumptions such as presuming spherical cross-sections of fibres.[71] However, this methodology is only suitable when the porous media is either unchanging, predictable, or random to the point that predictability is unnecessary. Where computational reconstructions and harsh irradiating techniques would either falsely recreate or damage the fragile structure, NMR offers a more gentle option for internal structural elucidation. Used in unison, however, the experimental and computational processes can be very complimentary in a study.

2.2 Theory

2.2.1 Spin dynamics

As mentioned, the project aims to develop the theory of the magnetic susceptibility-induced relaxation mechanism, initially for a system containing a single spin-$1/2$ nucleus. Once complete, this may be incorporated into a simulation framework capable of calculating the spin Hamiltonian propagator responsible for the susceptibility-induced relaxation. To do so, it is best to define the relevant theory leading to this calculation.

At the heart of all spin systems defined by quantum mechanics is the wavefunction, $\psi_{(x_i)}$, the central most important aspect of a problem as it contains all the information needed to describe a particle or ensemble. It is custom to adopt Dirac notation where objects within the complex vector space, such as wavefunctions, are written within kets: $|\psi\rangle = \psi_{(x_i)}$. In addition to this, each ket has a corresponding bra, $\langle\psi| = \psi^*_{(x_i)}$, the complex conjugate of the ket, existing in another space. A wavefunction is constructed by a basis set of functions, these being a collection of functions that form a

mathematical base from which all other wavefunctions in that space can be expanded. The basis set is governed by a few rules such that it must be complete: the number of orthonormal functions must be equal to the dimension of the space they are describing. Orthonormal functions must be both orthogonal and perpendicular to one another:

$$\langle \psi_j | \psi_k \rangle = \delta_{jk} \begin{cases} 0 \text{ if } j \neq k \\ 1 \text{ if } j = k \end{cases} \tag{2.7}$$

and normalised:

$$1 = N^2 \int_{-\infty}^{\infty} \psi^*_{(x_i)} \psi_{(x_i)} dx_i \tag{2.8}$$

Where N is a normalising constant that is specific to each wavefunction. Information is extracted from a wavefunction using operators: mathematical constructs with the ability to transform one function into another, typically distinguished by their hat:

$$\hat{A}|\psi\rangle = |\Phi\rangle \tag{2.9}$$

Where $|\psi\rangle$ and $|\Phi\rangle$ are two different functions. A special class of operators, imperative for quantum mechanics, are eigen-operators: operators that, when acting on a function, return the original function with a scalar component, or eigenvalue:

$$\hat{A}|\psi\rangle = a|\psi\rangle \tag{2.10}$$

If this operator is Hermitian then the eigenvalue, a, is a real number and relates to a physical property of the system that may be measured. The physical value is known as the expectation value and is obtained by performing an experiment many times and averaging the results. This is calculated as:

$$\begin{aligned} \langle \hat{A} \rangle &= \int_{\infty}^{\infty} \psi^*_{(x_i)} \hat{A} \psi_{(x_i)} dx_i \\ &= \langle \psi | \hat{A} | \psi \rangle \end{aligned} \tag{2.11}$$

A key eigen-operator present throughout spin dynamics is the Hamiltonian, the Hermitian operator that returns the energy of a system when acting on the wavefunction. In many physical cases, the Hamiltonian may be time-dependent, as such the system is evaluated using the Schrödinger equation:

$$i\hbar \frac{\partial}{\partial t} |\psi_{(t)}\rangle = \hat{H}_{(t)} |\psi_{(t)}\rangle \tag{2.12}$$

In the simplest case, the Hamiltonian is time-independent and the solution to the above, eq. (2.12), becomes:

$$|\psi_{(t_b)}\rangle = e^{-i\hat{H}\tau} |\psi_{(t_a)}\rangle \tag{2.13}$$

Where τ is the time difference of t_a and t_b and b is always greater than a. In this case, $e^{-i\hat{H}\tau}$ is both a unitary operator:

$$\begin{aligned} \hat{U}^{\dagger} &= \hat{U}^{-1} \\ \hat{\mathbb{1}} &= \hat{U}^{-1}\hat{U} \end{aligned} \tag{2.14}$$

and an exponential operator:

$$\begin{aligned} e^{\hat{A}}|\psi\rangle &= e^{a}|\psi\rangle \\ e^{\hat{A}} &= \hat{\mathbb{1}} + \hat{A} \end{aligned} \tag{2.15}$$

Where a sufficiently small operator can be truncated using the Taylor series to remove the exponential leaving the sum of the operator and the unity operator:

$$\hat{\mathbb{1}} = \begin{pmatrix} 1 & 0 \\ 0 & 1 \end{pmatrix} \tag{2.16}$$

For a nucleus with a nuclear spin quantum number of I, there are $2I + 1$ possible configurations that the spins can exist in. The simplest case we can theorise is that of an isolated spin-$1/2$ nucleus in a static field, where the nuclear spin has a value of $1/2$ and there are two possible configurations:

$$\begin{aligned} |\alpha\rangle &= |1/2, 1/2\rangle \\ |\beta\rangle &= |1/2, -1/2\rangle \end{aligned} \tag{2.17}$$

Where $|\alpha\rangle$ represents the "spin-up" configuration where the spin is aligned with the external field, and $|\beta\rangle$ is the "spin-down" configuration where the spin opposes the field. Therefore, the wavefunction for an isolated spin-$1/2$ nucleus can be written as a linear combination of the basis set components:

$$\begin{aligned} \psi_n &= c_\alpha|\alpha\rangle + c_\beta|\beta\rangle \\ 1 &= |c_\alpha|^2 + |c_\beta|^2 \end{aligned} \tag{2.18}$$

Where each squared coefficient, $|c_n|^2$, is the probability of finding the system in state $|n\rangle$. In conventional NMR, the external field is oriented along the z-axis and the spin angular momentum operator, $\hat{I}_z$, acting on a state, returns the states projection along z:

$$\hat{I}_z = \frac{1}{2}\begin{pmatrix} 1 & 0 \\ 0 & -1 \end{pmatrix} \tag{2.19}$$

For this operator the states $|\alpha\rangle$ and $|\beta\rangle$ form a complete and orthonormal basis set. There also exists analogous operators for defining the projection along both x and y:

$$\hat{I}_x = 1/2\begin{pmatrix} 0 & 1 \\ 1 & 0 \end{pmatrix} \qquad \hat{I}_y = 1/2\begin{pmatrix} 0 & -i \\ i & 0 \end{pmatrix} \tag{2.20}$$

In addition, it may be useful to define a few more operators used extensively within spin dynamics, the raising , $\hat{I}^+$ and lowering, $\hat{I}^-$ operators:

$$\begin{aligned} \hat{I}^+ &= \hat{I}_x + i\hat{I}_y = \begin{pmatrix} 0 & 1 \\ 0 & 0 \end{pmatrix} \\ \hat{I}^- &= \hat{I}_x - i\hat{I}_y = \begin{pmatrix} 0 & 0 \\ 1 & 0 \end{pmatrix} \end{aligned} \tag{2.21}$$

2.2.1.1 Rotation

The majority of NMR is centred around rotations of magnetisation, performed numerically by rotation operators. These exponential operators are capable of calculating the projection of the magnetisation along any combination of x, y, and z following a rotation about a given axis, a, through an angle, θ:

$$\mathbb{R}a\theta = e^{-i\,\theta\,\hat{I}_a} \tag{2.22}$$

For this, there are clear, defined rotation matrices:

$$\begin{aligned} \mathbb{R}x\theta &= \begin{pmatrix} cos(\theta/2) & -i\,sin(\theta/2) \\ -i\,sin(\theta/2) & cos(\theta/2) \end{pmatrix} \\ \mathbb{R}y\theta &= \begin{pmatrix} cos(\theta/2) & sin(\theta/2) \\ sin(\theta/2) & cos(\theta/2) \end{pmatrix} \\ \mathbb{R}z\theta &= \begin{pmatrix} e^{-i(\theta/2)} & 0 \\ 0 & e^{i(\theta/2)} \end{pmatrix} \end{aligned} \tag{2.23}$$

An active rotation is one which rotates the object itself whereas a passive rotation, as found in NMR, is one which rotates the frame around a static object. In the Cartesian frame, a rotation can be done via three successive rotations, the angles of which are named Euler's angles. Conventionally, this is a $z-y-z$ rotation. These rotations are always anticlockwise and are expressed using a rotation operator, $\hat{R}_{\Omega_{12}}$:

$$\hat{R}(\Omega_{12}) = \mathbb{R}z\alpha_{12}\,\mathbb{R}y\beta_{12}\,\mathbb{R}z\gamma_{12} \tag{2.24}$$

With the numbers signifying the initial state, 1, and the final state, 2, following the rotation. Therefore, a rotation by Euler's angle is also written as:

$$\hat{R}(\Omega_{12}) = e^{-i\alpha_{12}\hat{I}_z}\,e^{-i\beta_{12}\hat{I}_y}\,e^{-i\gamma_{12}\hat{I}_z} \tag{2.25}$$

A rotation operator will act in the following fashion:

$$\psi_{(t_b)} = e^{-i\,\theta\,\hat{I}_a}\,\psi_{(t_a)}\,e^{i\,\theta\,\hat{I}_a} \tag{2.26}$$

For the Cartesian angular momentum operators, rotations abide by the following commutation relations:

$$\begin{aligned} e^{-i\,\theta\,\hat{A}}\hat{B}e^{i\,\theta\,\hat{A}} &= \hat{B}cos(\theta) + \hat{C}sin(\theta) \\ [\hat{A},\hat{B}] &= i\hat{C}\circlearrowleft \end{aligned} \tag{2.27}$$

The application of multiple of these matrices in succession will tilt magnetisation from its residing position to lie along another vector in three-dimensional space, as chosen by the operator. For example, magnetisation residing along z at equilibrium may be flipped such that it opposes the external field and lies along -z. Should the opposing state be the higher energy state, as is with most NMR, the magnetisation will steadily return to the equilibrium state, in a process called relaxation.

2.2.1.2 Interaction with a magnetic field

The evolution of a system interacting with the static, external field is defined by the Zeeman Hamiltonian. Unless there is a large quadrupolar moment or the gyromagnetic ratio is small, this tends to be the dominant interaction at high field.

$$\hat{H}_z = -\gamma\hat{\mathbf{I}}\cdot\mathbf{B} \tag{2.28}$$

Where the dot product may be expanded to give:

$$\hat{\mathbf{I}}\cdot\mathbf{B} = \hat{I}_x B_x + \hat{I}_y B_y + \hat{I}_z B_z \tag{2.29}$$

As is conventionally done in NMR, the $\hbar$ constant has been omitted to ease numerical complexity. Since the external field is only applied along the z-axis such that $\mathbf{B} = \begin{bmatrix} 0 \\ 0 \\ B_0 \end{bmatrix}$, the Hamiltonian may be rewritten as:

$$\begin{aligned} \hat{H}_z &= -\gamma B_0\hat{\mathbf{I}} \\ \hat{H}_z &= \omega_0\hat{\mathbf{I}} \end{aligned} \tag{2.30}$$

Incorporating the definition of the Larmor frequency: $\omega_0 = -\gamma B_0$. For an isolated spin-1/2 where the wavefunction is given as $|\psi\rangle = c_\alpha\,|\alpha\rangle + c_\beta|\beta\rangle$, the objects of interest are c_α and c_β. The general form of an operator used to extract these would be:

$$\begin{aligned} \hat{O} &= \begin{pmatrix} \langle\alpha|\hat{O}|\alpha\rangle & \langle\alpha|\hat{O}|\beta\rangle \\ \langle\beta|\hat{O}|\alpha\rangle & \langle\beta|\hat{O}|\beta\rangle \end{pmatrix} \\ &= \begin{pmatrix} O_{\alpha\alpha} & O_{\alpha\beta} \\ O_{\beta\alpha} & O_{\beta\beta} \end{pmatrix} \end{aligned} \tag{2.31}$$

The expected outcome, or expectation value, would be determined via:

$$\begin{aligned}\langle\hat{O}\rangle &= \langle\psi|\hat{O}|\psi\rangle \\ &= (c_\alpha^* \quad c_\beta^*)\begin{pmatrix} O_{\alpha\alpha} & O_{\alpha\beta} \\ O_{\beta\alpha} & O_{\beta\beta} \end{pmatrix}\begin{pmatrix} c_\alpha \\ c_\beta \end{pmatrix} \\ &= c_\alpha^* c_\alpha O_{\alpha\alpha} + c_\alpha^* c_\beta O_{\alpha\beta} \\ &+ c_\beta^* c_\alpha O_{\beta\alpha} + c_\beta^* c_\beta O_{\beta\beta}\end{aligned} \tag{2.32}$$

Another way of writing this is:

$$\langle\hat{O}\rangle = Tr\{\,|\psi\rangle\langle\psi|\hat{O}\,\} \tag{2.33}$$

2.2.1.3 Ensembles

However, the presence of a single isolated spin is next to impossible within nature and a real system would be represented by N_A spins, each with its own wavefunction. In reality, the system therefore contains N_A wavefunctions:

$$|\psi_s\rangle = c_{\alpha,s}|\alpha\rangle + c_{\beta,s}|\beta\rangle \tag{2.34}$$

With s signifies the individual spin. This carries through to the expectation value such that the outcome of the entire system is the sum of all its components:

$$\begin{aligned}\langle\hat{O}\rangle &= \sum_{s=1}^{N_A}\langle\psi_s|\hat{O}|\psi_s\rangle \\ \langle\hat{O}\rangle &= Tr\Big\{\sum_{s=1}^{N_A}|\psi_s\rangle\langle\psi_s|\hat{O}\Big\}\end{aligned} \tag{2.35}$$

Unfortunately, one cannot definitively say all spins of an ensemble will be in the same state, and due to the likelihood of having a factor of $6.022{\times}10^{23}$ spins, the system can only be surveyed through statistical means. For this, we define the average of the ket-bra combination as the density operator, $\hat{\rho}$: the average state perceived within our system given all conditions and influencing factors.

$$\begin{aligned}\hat{\rho} &= \frac{1}{N}\sum_{s=1}^{N_A}|\psi_s\rangle\langle\psi_s| \\ &= \overline{|\psi_s\rangle\langle\psi_s|}\end{aligned} \tag{2.36}$$

In matrix form, this is given as:

$$\hat{\rho} = \begin{pmatrix} \rho_{\alpha\alpha} & \rho_{\alpha\beta} \\ \rho_{\beta\alpha} & \rho_{\beta\beta} \end{pmatrix} \tag{2.37}$$

In the matrix representation, the diagonal elements account for the populations of $|\alpha\rangle$ and $|\beta\rangle$, and the off-diagonal elements are coherences. These coherences account for magnetisation that resides across the transverse plane, as a superposition of $|\alpha\rangle$ and $|\beta\rangle$. In NMR, the -1Q or $\rho_{\beta\alpha}$, single quantum coherence, are those which are observed. The expectation value of the operator may now be expressed as:

$$\langle \hat{O} \rangle = N \; Tr\{ \hat{\rho} \; \hat{O} \} \tag{2.38}$$

This is the prediction of the result of a measurement from an ensemble of spins where each component will contribute $N^{-1}\langle \hat{O} \rangle$. The density operator becomes a statistical representation of an ensemble of spins where outcomes of observation or measurement are probabilistic-driven values. As with the isolated system, working with the density operator requires the defining of at least one instance of a complete and orthonormal basis set, from which the operator can be described. For an ensemble of spin-$1/2$ nuclei, this may be $\hat{\mathbb{1}}$, $\hat{I}_z$, $\hat{I}^+$, and $\hat{I}^-$. To write the density operator out in full would be:

$$\hat{\rho} = \hat{I}^- \, \rho_{\beta\alpha} \; + \; {}^1\!/_2 \, \hat{\mathbb{1}} \, (\rho_{\alpha\alpha} + \rho_{\beta\beta}) \; + \; \hat{I}_z \, (\rho_{\alpha\alpha} - \rho_{\beta\beta}) \; + \; \hat{I}^+ \, \rho_{\alpha\beta} \tag{2.39}$$

This operator is a valuable tool for describing ensemble systems, as will be seen later.

2.2.1.4 Rotating frame

When dealing with the quantum mechanics of NMR, there is always an element of time dependence, since no solution is static and pulses cannot, though we may try, be infinitesimally short. In order to visualise nuclei, we must perturb them from the static field, and thus away from z. We do so using an oscillating field, B_1, placed along x, and operating at the transmitter frequency. Any nuclei within this system will experience this field strength along with its rhythmically fluctuating magnetic field, thus we have a time dependence that we must account for in our calculations. Alternatively, we can deviate from this static laboratory frame, and instead choose a reference frame that compliments our system. We can adopt a rotating frame whereby we are rotating about the z-axis at the same rate as our transmitter frequency, ω_{RF}. Such that the viewpoint from atop our nucleus resonating with the oscillating field, would be a static world. Thus removing this time-dependent aspect from our calculations.

Previously, we had seen our nuclei precess at their Larmor frequency, ω_0, yet in the rotation frame, we must adopt an apparent Larmor frequency to account for us also rotating around z. This is given by the frame frequency, ω_{RF}. We can therefore define the offset, Ω: the difference between the precession frequency and the frame frequency. For nuclei precessing at a rate equal to ω_{RF}, they are said to be on resonance.

$$\Omega = \omega_0 - \omega_{RF} \tag{2.40}$$

2.2.2 Radio frequency pulses

2.2.2.1 On resonance

The manipulation of spins within the system is done via rf pulses: these have the ability. Noting the use of the Cartesian coordinate system, carried forth through these works. By doing so, the net magnetisation can be transferred to the $|\beta\rangle$ state via the use of correct rf pulses. The degree to which a pulse rotates the magnetisation is given by:

$$\beta = \omega_1 \, \tau_p \tag{2.41}$$

Where β is the flip angle, ω_1 is the nutation frequency, and τ_p is the length of the pulse. By fixing either the pulse length or nutation frequency, and altering the other, the desired flip angle can be achieved. When the precession frequency matches that of the rotation frame, or the rf frequency is large compared to the offset, the system behaves as intended and the magnetisation is tilted by the specified angle. NMR as a technique is built upon sequences of these pulses and intermittent delays, through which information and parameters can be determined.

2.2.2.2 Off resonance

In the instance that precession is far from the rotating frame frequency, the spins in our sample will not behave as expected. Instead of an idealistic pulse shifting all spins together, the net magnetisation vector will appear to precess during the pulse, shifting the spins away from the x-y plane. For the example of a 90_x pulse, instead of the magnetisation lying along -y, it will rotate back around, gaining magnetisation in both x and z. We can visualise the effect of an off-resonance pulse based on the probability of achieving a successful transition from $|\alpha\rangle$ to $|\beta\rangle$, via a π pulse.

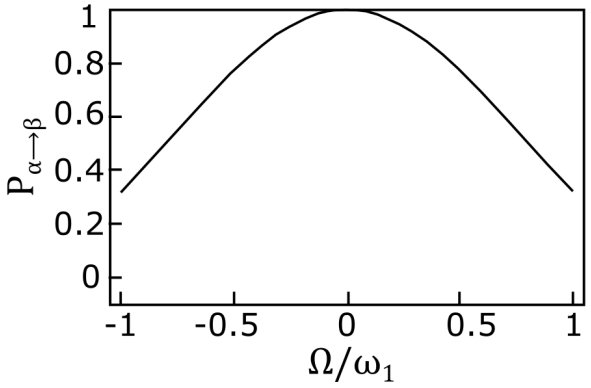

Figure 2.3: The effect of an off-resonance 180° pulse demonstrated as the probability of flipping spins from $|\alpha\rangle$ to $|\beta\rangle$, taken from.[72]

Although these non-ideal pulses exist to some degree in many samples, they can be corrected for and removed efficiently by using techniques such as composite pulses.[73]

2.2.3 Composite pulses

Composite pulses are built such that the sequence of pulses is equivalent to a single pulse; however, they are far more forgiving to imperfections.[73] As with most samples, the internal magnetic field is never flawlessly homogeneous and so, each spin is inherently susceptible to slightly different fields. Thus introducing a range of Larmor frequencies where only one matches the irradiation frequency.[74] For a blank sample containing a simple molecule, this effect is negligible hence standard T_1 and T_2 experiments use single pulses. However, if extra complexity is introduced to the system by way of porous media, the local environment of the spins will be further differentiated by position. Here, a single pulse may result in each spin being tilted by a fraction of the desired amount. Take the example of a 180_y pulse and its composite partner, $90_y180_x90_y$. The desired effect would be a transition from $\hat{I}_z$ to -$\hat{I}_z$, as shown in Figure 2.4 A. However, the complexity of the system may mean that some spins experience a greater offset frequency than others. the composite pulse shown in Figure 2.4 B highlights the potential to compensate for these differences.

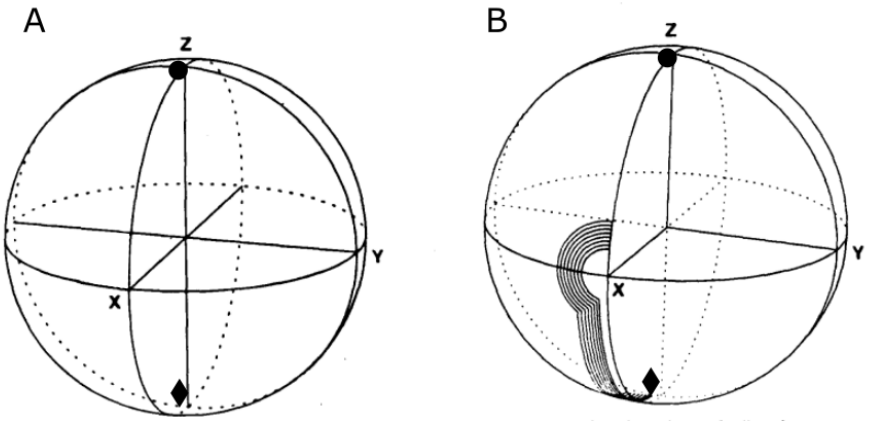

Figure 2.4: Effect of a composite pulse for net magnetisation beginning facing the circle, with the intention to finish facing the diamond, taken and adapted from Levitt.[74]

2.2.4 Phase factors

Another method for suppressing non-negligible interference effects is phase cycling whereby the phase of a pulse is periodically altered to achieve addition or subtraction of successive signals.[73] In our typical NMR experiment, we have selected the principal axis to be z, and have arbitrarily assigned x and y to be perpendicular to z and each other. However, the actual direction of both x and y is defined at the user's discretion, or rather, that of the pulse programmer. Having chosen x to be the axis along which we

measure magnetisation, we can say a pulse along x has a phase angle of zero, and one along y has a phase angle of $\pi/2$. Similarly, the alignment of the receiver will introduce receiver phase into the system. By carefully selecting the phases of both the pulse and the receiver, one can amplify desired signals whilst cancelling unwanted ones, as well as suppress any artefacts arising due to field or timing imperfections.

2.2.4.1 Magnetisation

Within the density matrix, given in eq. (2.37), there are two forms of magnetisation, longitudinal, and transverse. The diagonal terms represent the populations of the $|\alpha\rangle$ and $|\beta\rangle$ states and the difference between these populations results in a net magnetisation called longitudinal magnetisation. Should the system be perturbed such that magnetisation resides in the $|\beta\rangle$ state, the return to equilibrium is deemed relaxation, and is characterized by the longitudinal decay constant, T_1. Since this form of relaxation relies on transitions between the $|\alpha\rangle$ and $|\beta\rangle$ states, it is mediated by frequencies containing a component of the Larmor frequency.

In conjunction, the off-diagonal elements of the density matrix are the coherences. These represent the spin angular momentum in the x-y plane and are responsible for transverse magnetisation. Since all spins are precessing, should the net magnetisation be shifted to the x-y plane, precession continues about the z-axis. However, each spin will experience an ever so slightly different field due to small unavoidable inhomogeneities within the system. As a result, the precession of each spin is different causing an overall dephasing of the spins, quantified by the transverse decay constant, T_2. The value of T_2 can qualitatively be observed on spectra themselves as it is inversely proportional to the width of a peak, known as full width half maximum (FWHM).[75]

2.3 Spin relaxation

2.3.1 Relaxation in solution

These two decay rates are principal aspects of many NMR pulse sequences for example, the attenuation of T_2 of water is the principal driving factor of MRI contrast. However, in liquids, there are many mechanisms that are responsible for the increased decay in longitudinal and or transverse magnetisation. Mentioned above was the Zeeman interaction: usually the dominant Hamiltonian of a system and therefore contributing the most to relaxation. Of the other known mechanisms, those with a significant impact on the samples used within these works are outlined briefly below.

The principal foundation of longitudinal relaxation is the transition of spins from $|\beta\rangle$ to $|\alpha\rangle$ via fluctuations containing a component of the Larmor frequency. However, for

transverse magnetisation, relaxation is quantified by the dephasing of spins in the transverse plane and so relaxation is mediated by fluctuations in magnetic field of any frequency. Often in NMR, the second most prominent form of relaxation is by dipole-dipole relaxation, the coupling interaction between nuclei within close proximity of one another. As molecules tumble, the dipole field created by each nucleus will fluctuate and if experienced by another nucleus, will induce relaxation. There are many forms of dipole-dipole relaxation including the coupling of spins within one molecule, intra-molecular dipole-dipole (iDD), and between nuclei on different molecules, inter-molecular dipole-dipole (DD). Although dipolar coupling is a strong interaction, it is largely dependent on distance and so iDD tends to dominate dipole relaxation. We see the distance dependence in the spin relaxation through the iDD model:[76]

$$R_{iDD} = \frac{3}{2}\left(\frac{\mu_0}{4\pi}\right)^2 \gamma_1^2 \gamma_2^2 \hbar^2 r_{12}^{-6} \tag{2.42}$$

Another relevant mechanism is spin-rotation (SR) relaxation, which is brought about by fluctuations in the experienced magnetic field as a result of rotating atomic groups.[77] In solution, molecules are not only moving randomly as a whole, but each component of the molecule may also be moving randomly both rotationally, and transversely. This is particularly seen within single bonded chains in a molecule, such as free-rotating methyl groups. As the group rotates, the angular momentum brings about a small yet insignificant magnetic field that may be experienced by neighbouring nuclei. As such, this relaxation mechanism has a distinct temperature dependence[78] and can affect each nucleus in the molecule individually. For that reason, the labelling of molecules can be selected such that the nuclear position of interest is as far from the rotating group as possible. Taking all these factors discussed above, the example of pyruvate can be used to demonstrate relaxation as per the labelling site:

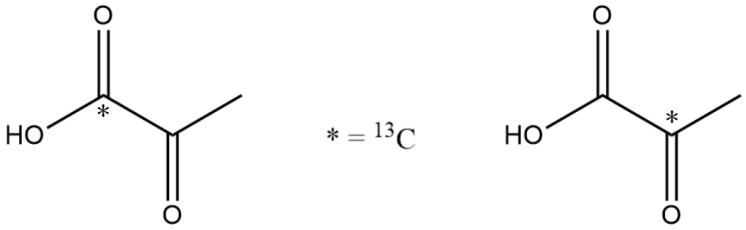

Figure 2.5: Possible positions of ^{13}C labelling within pyruvate.

For the case of pyruvate-1-^{13}C at 3 T, T_1 was found to be 67 s, as opposed to only 39 s for pyruvate-2-^{13}C.[79] Thus meaning the positioning is sufficient to favour one positioning over the other. For example, should a long relaxation time be required, pyruvate-1-^{13}C would be the preferred isomer. In most cases, the mechanism can be described by a Hamiltonian to evaluate the product of a spin system subject to such mechanisms for a given period of time. As with iDD, SR has its own relaxation equation with $\perp$

representing a tensor for the moment of inertia, I, and the spin rotation tensor, C:[76]

$$R_{SR} = \frac{4k_B T}{3\hbar^2 C_\perp^2 I_\perp} \tag{2.43}$$

2.3.2 Paramagnetic relaxation

A particular relaxation mechanism of importance is that of paramagnetic relaxation, or paramagnetic relaxation enhancement (PRE). Paramagnetic materials include metals or those containing unpaired electrons, such as oxygen. As with most relaxation mechanisms, this is facilitated by the random fluctuating magnetic fields experienced as a result of molecular motion. In this case, the magnetic field arises due to the dipoles of paramagnetic materials. Dipoles produced by unpaired electrons are greater than those of nuclei meaning paramagnetic oxygen can significantly reduce magnetisation lifetimes. With studies proving that increased oxygen concentration leads to a significant increase in relaxation rates,[80] both T_1 and T_2 can be enhanced by removing this dissolved gas via the freeze-thaw method or bubbling with a heavier gas.

PRE is also a prevalent, often most important, form of relaxation for geological NMR studies.[81] With the electron spin far exceeding that of nuclear spins, this form of relaxation has strong influences even at small concentrations of paramagnetic materials.[82] Contrary to d-NMR, MRI relies heavily on the shortening of relaxation times, in order to enhance signal intensities.[83] By shortening the lifetimes of resonating signals in inter-tissue areas, greater contrast is achieved for the areas of interest.[84]

2.3.3 Surface relaxation

A prevalent form of relaxation in porous media studies is surface relaxation. This involves the magnetic coupling of nuclear spins with static surface-bound nuclei, typically paramagnetic species.[44] The degree to which the surface enhances spin relaxation is defined by the surface relaxivity parameter, ρ_i, and links T_i to the pore size via:[81]

$$T_i^{-1} = T_{i,B}^{-1} + \rho_i \left(S/V\right) \qquad \text{Where i = 1,2} \tag{2.44}$$

Where T_i is the relaxation constant in the porous system, $T_{i,B}$ is the bulk relaxation constant, and S/V is the surface area to volume ratio of the pore. However, the range of surface relaxivity is typically contained to within a few molecules' width, requiring spins to be very close to the surface for significant relaxation to occur.[82] Through analysis of the temperature dependency of the diffusion coefficient, it was determined in some systems that the main diffusion effect could be attributed to geometrical restrictions as opposed to surface relaxation.[52] However, within all porous systems there exist

diffusion regimes, related to the pore size and diffusion. For larger pores, the majority of spins experience bulk diffusion and the system is within the fast diffusion regime:[85]

$$\rho_i \, l/D << 1 \tag{2.45}$$

Where l is pore size (or diameter) and D is the diffusion coefficient. It is only when there is a sufficiently large surface area to volume ratio that surface relaxation is prevalent, deemed the slow diffusion regime. Should this regime dominate, one can expect significant relaxation effects and multiple relaxation rates within one system.[81] However, this implies that all pores within a system are identical, else one must average over relaxation and pore size to account for differences. Owing to the complexity of some porous systems, the calculation of surface relaxation is no trivial matter. Thus, algorithms are used to determine these structural features of porous media, based on physical properties.[44]

Whether the study of relaxation is computational or experimental, the combination of all applicable relaxation mechanisms sums to total the observed relaxation within the system.[76] Where the state of the system can be calculated through the total spin Hamiltonian containing all time-independent, $\hat{H}_0$, and time-dependent terms, $\hat{H}_1(t)$.[86]

$$\hat{H}(t) = \hat{H}_0 + \hat{H}_1(t) \tag{2.46}$$

2.3.4 Magnetisation measurement

We have already discussed the Zeeman interaction and $\boldsymbol{I}$, and its importance in determining which nuclei are NMR active. We have also seen how magnetisation can be shifted and manipulated within an ensemble of spins. When the system is perturbed in any way, the tendency is for it to return to thermal equilibrium, characterised by a relaxation constant, of which there are two.

Firstly, relaxation of z-magnetisation is characterised by the time constant, T_1. This form of relaxation is centred around the dissipation of energy from the spins to the surrounding lattice. The latter being the collection of surrounding spins, located within the same molecule or neighbouring molecules to the spin in question. In this mode of relaxation, energy is dissipated from each spin with the goal of returning the system to equilibrium. We can see the presence of T_1 in the Bloch equations: a set of mathematical constructs describing the change in magnetisation of a relaxing system. For longitudinal relaxation, we obtain T_1 through the following relation:[87]

$$\frac{dM_z}{dt} = \frac{M_0 - M_z}{T_1} \tag{2.47}$$

Where M_z is the magnetisation in z and M_0 is the initial magnetisation. The solution of this first-order differential equation is:

$$M_z(\tau) = M_0\left(1 - e^{-\tau/T_1}\right) \tag{2.48}$$

Linearizing this solution and plotting signal strength against the delay period, τ, can be done to calculate the longitudinal decay constant of the nucleus. Alternatively, following a 90 ° pulse, our magnetisation now lies within the transverse plane. Precession of the overall magnetisation vector, now lying perpendicular to the z-axis, contributes to the non-zero components, M_x and M_y. Relaxation of this transverse magnetisation is described by T_2 and is an entropically driven process by which the overall energy of the system remains unchanged but the attributed signal loses its coherence. As before, T_2 can be described using a Bloch equation:[87]

$$\frac{dM_{xy}}{dt} = -\frac{M_{xy}}{T_2} \tag{2.49}$$

Where M_{xy} is magnetisation residing in the transverse plane. The solution of this first-order differential equation is:

$$M_{xy}(\tau) = M_0\left(1 - e^{-\tau/T_2}\right) \tag{2.50}$$

Unlike T_1, the measurement of transverse magnetisation is achieved by performing a series of sequential spin-echos with a consistent evolution time. Signal is then plotted against the number of spin-echos in order to determine T_2. The dependence on losing longitudinal magnetisation to witness transverse magnetisation leads to the restriction that T_2 cannot be greater than T_1. In systems with unrestricted diffusion and with regimes of fast molecular motion, we see these values as near equivalent. As all things are, NMR is no stranger to the inevitable imperfections of a system within a chaotic universe. Despite our best efforts, no two spins within a sample are subject to the exact same forces, though they share a nigh-on identical environment. These tiny differences in microenvironments toy with our spins and give rise to T_2*: the decay constant for transverse magnetisation accounting for the subtle difference in field homogeneity. As such, T_2* cannot be bigger than T_2.

Our lattice can be seen as a sea of nuclear magnetic moments, tumbling, rotating, and transforming through space. They are subject to the whims of the molecule which is itself undergoing similar motions. As the molecule tumbles, so do its *internal* magnetic moments, shifting them continuously off of their harmonious alignment with the external field. These motions lead to the production of fluctuating magnetic fields which, when containing a component of the Larmor frequency, can induce relaxation in nearby nuclei. Since the resulting peaks are a measurement of the nuclear resonance frequencies, their widths are a representation of the error associated with that

environment's average magnetic environment. As the system tends towards completely homogeneous, the signal in the resulting spectra tends towards narrow, uniform peaks.

For liquid state NMR, both the solute and solvent are in constant thermal motion. This involves tumbling which occurs via the rotational correlation time (τ_c). This is the average time it takes for a molecule to rotate about an axis by one radian. As well as being specific to each molecule, τ_c is also associated with the rotational diffusion coefficient, D_r.[88] A characteristic value of a particles rotation.

$$\tau_c = \frac{1}{6} D_r^{-1} = \frac{4\pi\rho\eta R^3}{k_B T} \tag{2.51}$$

Where k_B is the Boltzmann constant, T is temperature, ρ is density, η is viscosity, and R is the radius of the assumed spherical molecule. Due to its connection with internal dipolar fluctuations, τ_c can greatly affect the degree of relaxation experienced by nuclei. Isotropic motion occurs when a single value of τ_c corresponds to the tumbling of a molecule. Unfortunately, this is a rarity as it requires a spherically symmetric molecule, not often encountered in nature. As such, each spin within a tumbling molecule may experience slightly differing relaxation rates.

For a single correlation time, the molecule will have a certain "memory" of its previous orientations, encoded within its spectral density function (SDF). This is given by $J_{(\omega)}$ and is proportional to the probability of finding a molecule that has tumbled a component of a radian at a given frequency.[75] We can therefore expect our average molecule to not have tumbled through one radian within τ_c, and few to have rotated further in this time. Of course, this is dependant on the frequency range under which the system is observed. We can plot the SDF as:

$$J_{(\omega)} = \frac{2\tau_c}{1 + \omega^2 \tau_c^2} \tag{2.52}$$

Since T_1 is dependant on fluctuations of a certain frequency, in an idealistic world, it is also related to the spectral density function, $J_{(\omega)}$.[89]

$$\frac{1}{T_1} = \gamma^2 \left\langle B^2 \right\rangle J_{(\omega)} \tag{2.53}$$

With $\left\langle B^2 \right\rangle$ being the mean square of local fluctuating fields. However, there are many relaxation mechanisms that come into play, all contributing to the total relaxation rate. All assumptions so far have assumed a homogeneous field, excluding the possibility of a fluctuating B_0. Furthermore, there are other nuclear interactions that exists within and between molecules, that add complexity to the system.

2.3.5 Couplings

2.3.5.1 Weak coupling

Another form of intranuclear interaction comes in the way of couplings. We have learnt that a spin-$^1/_2$ nucleus may adopt either the $|\alpha\rangle$ or $|\beta\rangle$ orientation, but this is also possible for every nucleus in the molecule. Typically, if a nucleus containing a magnetic moment, and therefore inducing a small magnetic field, is orientated in the spin-up fashion, the electrons in its bonds will be polarised to also align with the external field. As a consequence of this, paired electrons on the adjacent nuclei adopt the spin-down position. This pairing can be seen for a number of bonds, continuing the pattern of polarisation. Nuclei that are non-equivalent and typically within 3 bonds of one another (or 4 in special cases such as aromatic rings) can couple to one another; e.g., the nuclei are in a close enough proximity to be influenced by the small magnetic fields induced by the coupled nuclei, mediated through the bonds.

This phenomenon brings about a splitting pattern in the observed signal due to the possible arrangement of all coupled nuclei. For example, if one spin-$^1/_2$ nucleus is close to another spin-$^1/_2$ nucleus, it may either be slightly deshielded by a neighbouring $|\beta\rangle$ nucleus or shielded by a neighbouring $|\alpha\rangle$, causing the resonating frequency to either shift slightly downfield or up field, respectively. Given an ensemble of spins, there is also an equal chance of the neighbouring spin being up or down and so the resulting signal appears as a doublet of equal height peaks. The coupling constant, J_{12} is equivalent to this frequency difference between the spins resonating in aligned vs opposed orientations. Since this effect is intrinsic, it is not dependent on the external field or the temperature and is always reported in Hz.

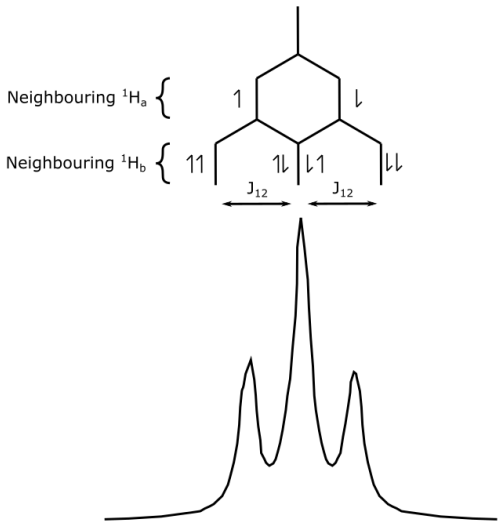

Figure 2.6: Effect of coupled nuclei on the splitting of the NMR signal, forming a triplet with intensities 1:2:1.

Scalar coupling can be used to determine the relative inter-molecular position of nuclei, further increasing the power of NMR. For example, nuclei with fewer bonds between one another tend to have a greater coupling constant. For all nuclei, the multiplicity of the NMR signal abides by the following:

$$\text{Multiplicity} = n + 1 \tag{2.54}$$

Where n is the number of non-equivalent neighbouring nuclei. The relative intensities of the peaks follow Pascal's triangle, which accounts for the stacking of the shielding of multiple neighbouring nuclei.

2.3.5.2 Strong coupling

For two coupled nuclei, there are four Zeeman product states for the system to be under and six total transitions between them. However, only four are physically allowed since NMR only allows $\Delta m \pm 1$, defined in Figure 2.7 as W_1, transitions.

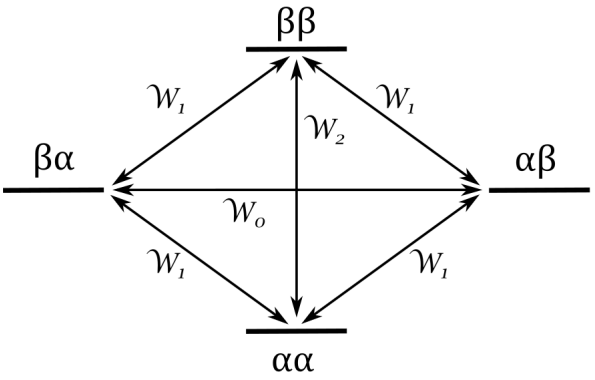

Figure 2.7: Possible transitions for a two spin-1/2 coupled system, adapted from.[90]

When the difference in Larmor frequency between the two spins, $\Delta\nu$, is smaller than their coupling frequency, J_{12}, the two are said to be strongly coupled. The presence of this coupling adds extra complexity to the quantum mechanical problem, as well as the spectra produced. When considering the wavefunction of the system, the second spin means additional states must be incorporated and accounted for:

$$|\psi\rangle = c_{\alpha\alpha}|\alpha\alpha\rangle + c_{\alpha\beta}|\alpha\beta\rangle + c_{\beta\alpha}|\beta\alpha\rangle + c_{\beta\beta}|\beta\beta\rangle \tag{2.55}$$

That is not to say that both spins may only be either 'spin-up' or 'spin-down'. As we have seen, there exist states that are superpositions of $|\alpha\rangle$ and $|\beta\rangle$. As it happens, should the spins be magnetically equivalent, the Zeeman product states shown in Figure 2.7 are not all eigenstates of the system. In this case, one must use an alternative basis

set to obtain the eigenstates in the strong coupling limit.[91] The application of conventional rf pulse sequences may not be sufficient to study such a system and complex methodologies may be required to probe these states.[92]

2.3.6 NMR in porous media

As mentioned, materials classed as porous media typically have an inhomogeneous solid architecture containing voids for liquid or gas flow. The movement of liquids through this medium can be more rigidly assessed in some situations such as packed beds; spherical particles typically packed within a hollow container, often a cylinder. In such a case, the system is porous upon the condition that Darcy's law is satisfied for flow evaluation, at low Reynolds numbers.[93] Initially derived from experimenting with fluid flow through sand beads, Darcy's law describes fluid flow within porous media.[94]

$$q = \frac{-k}{\mu}\Delta P \tag{2.56}$$

Where q is the flux discharge rate over area, measured in m/s, k is the permeability of the material, μ is the liquid viscosity, and ΔP is the pressure gradient. Darcy's law highlights the relationship between flux and the pressure gradient (driving force of flow), with respect to the permeability and the resistance of the liquid to deform. It also contains the following key statements:

- Flow occurs from high to low pressure and requires pressure gradients,
- With increased pressure gradients, comes greater flux,
- And the discharge rate is dependent entirely on the architecture of a material regardless of the pressure gradient.

What is most relevant here is the relationship between flux and other key porous media terms, such as porosity, υ. Where flux relates to the discharge over area, it is dependant on the fraction of porous media that allows for flow and so is related to porosity through the fluid velocity:[94]

$$\upsilon = \frac{q}{\nu} \tag{2.57}$$

Where ν is the velocity and υ is the porosity. The latter can be defined as the ratio between the void space and the total volume of the sample. This is an imperative parameter across a range of fields where the porosity can directly influence the availability of oil within a reservoir, the suitability of cements for bone repair, and the structural integrity of alumina ceramics.[95–97] Most applicable to a later chapter is the influence of porosity on cell viability within *in vitro* samples. Porosity and pore size can be the pinnacle influence in recreating an *in vivo* environment for a 3D cultured cell sample.[98]

Alternatively, motion can be brought about through passive processes such as diffusion. In this case, particles move through the solution via random motion governed by kinetic energy. When the molecules are diffusing within a blank system, diffusion is averaged to the bulk diffusion coefficient, D_0. With the introduction of solid confinements, such as in porous media, the porosity can be determined through the restricted diffusion coefficient, D_{eff}:[99]

$$D_{eff} = \frac{D_0 \upsilon f}{\alpha} \tag{2.58}$$

Where α is the tortuosity, which is explored below, and f is the diffusion-constriction factor: the ratio between the molecular size and pore diameter.[99]

2.4 Diffusion NMR

2.4.1 Measurement

Diffusion NMR (d-NMR) relies heavily on the use of gradients: short rf pulses applied along the transverse plane to induce a spatially dependent phase shift on the spins within the sample. As previously mentioned, all spins within a homogeneous magnetic field will precess at a given frequency, ω_0, provided they share a common gyromagnetic ratio, γ. However, in the presence of a field gradient, $\boldsymbol{g}$ (T m^{-1}), the precession frequency depends on position, $\boldsymbol{r}$, in a linear fashion:

$$\omega_{\boldsymbol{r}} = -\gamma \left(B_0 + \boldsymbol{g} \cdot \boldsymbol{r}\right) \tag{2.59}$$

With g being the gradient intensity, and δ being the gradient length. The ensemble of spins will now precess at different frequencies depending on their position within the sample. Should a gradient be applied following a 90° pulse, the distribution of frequencies will result in a coherence loss as the tilted spins will be out of phase. We can describe phase, ϕ, as the angle between each spin and the x-axis and the phase factor will be determined by the pulsed gradient and its duration, δ.

$$\phi_{\boldsymbol{r}} = -\gamma \ \delta \ \boldsymbol{g} \cdot \boldsymbol{r} \tag{2.60}$$

Where $\boldsymbol{r}$ is the position within the sample. Although dephasing was previously considered to be a hindrance, the advantage of applying the gradient lies in its ability to encode all irradiated spins with spatial information. The effect of applying a pulse is demonstrated below in Figure 2.8:

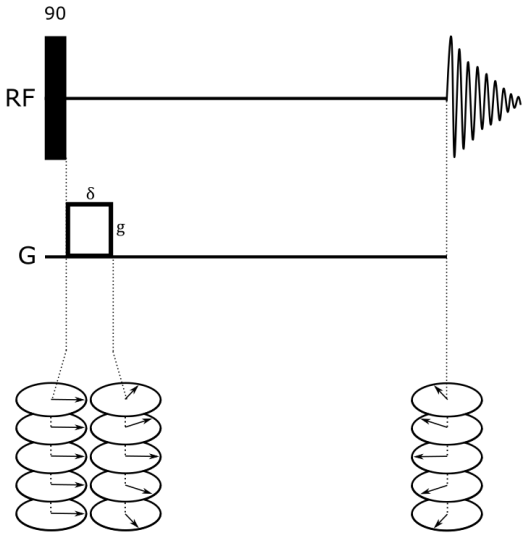

Figure 2.8: Effect of linear gradient on spin order following a 90° pulse.

Should the sample be subjected to a 180° transverse rf pulse, followed by a second gradient of equal magnitude, a completely static sample would show a full retention of signal as the magnetisation is refocused in an echo. However, should any spins diffuse during the evolution time, Δ, between the two gradients, acquisition would result in a less-than-perfect re-phasing of the spins and therefore a decline in signal.

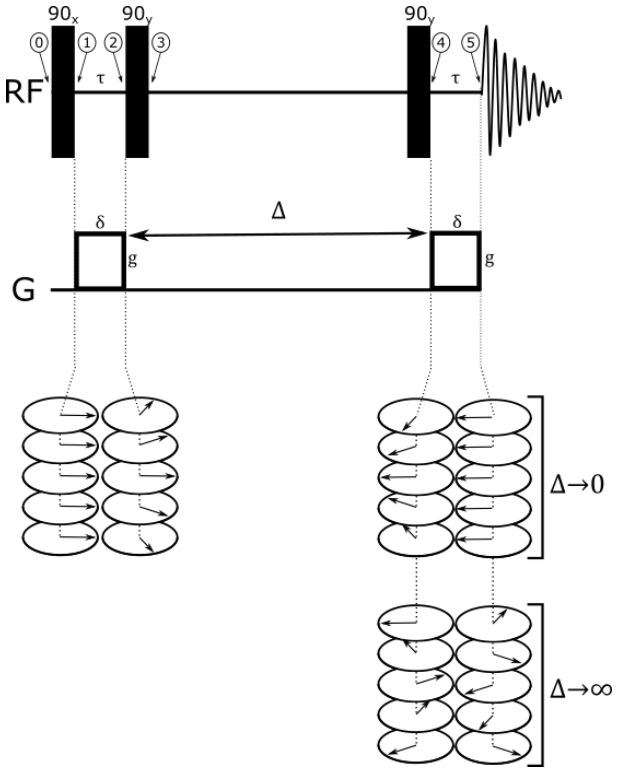

Figure 2.9: The PGSTE pulse sequence and its effects given either a long or short delay.

Within NMR, the most basic pulsed gradient stimulated echo (PGSTE) pulse sequence, developed by Tanner[100] and shown in Figure 2.9, is used to calculate the diffusion coefficient of a molecule. To determine how the signal will evolve during this pulse sequence, requires consideration of how a single spin is manipulated by the PGSTE sequence, assuming a linear gradient. Initially, magnetisation will reside along z:

$$\hat{\rho}(0) = \hat{I}_z \tag{2.61}$$

Following the first pulse 90° pulse (about x), it will be tilted to lie along y:

$$\hat{\rho}(1) = -\hat{I}_y \tag{2.62}$$

The effect of the gradient takes the following form, given the application of commutation relations:

$$\begin{aligned} \hat{\rho}(2) &= e^{-i\gamma g_z \delta z \hat{I}_z}\left(-\hat{I}_y\right)e^{i\gamma g_z \delta z \hat{I}_z} \\ &= -\hat{I}_y cos(\gamma g_z \delta z) + \hat{I}_x sin(\gamma g_z \delta z) \end{aligned} \tag{2.63}$$

And following the second 90° pulse (about y), excluding the effects of chemical shift and scalar coupling:

$$\hat{\rho}(3) = -\hat{I}_y cos(\gamma g_z \delta z) + \hat{I}_z sin(\gamma g_z \delta z) \tag{2.64}$$

If we exclude relaxation and apply the third and final pulse 90° pulse (about y), we achieve the following:

$$\hat{\rho}(4) = -\hat{I}_y cos(\gamma g_z \delta z) - \hat{I}_x sin(\gamma g_z \delta z) \tag{2.65}$$

After the second gradient, assuming the spin has moved due to diffusion:

$$\hat{\rho}(5) = {}^{i}/_{2}\hat{I}^{+}e^{i\gamma g_z \delta (z-z')} - {}^{i}/_{2}\hat{I}^{-}e^{-i\gamma g_z \delta (z-z')} \tag{2.66}$$

A derivation of how the above equation was formed can be found in Appendix 9.5. As mentioned, the observable component of NMR is the -1Q coherences and so the observable would be:

$$\hat{\rho}_{obvs} = -{}^{i}/_{2}\hat{I}^{-}e^{-i\gamma g_z \delta (z-z')} \tag{2.67}$$

We are only concerned with the real part and can therefore make use of Euler's formula once again to determine the effect of the gradients on observable magnetisation:

$$\hat{\rho}_{obvs} = -{}^{i}/_{2}\hat{I}^{-}cos\left(\gamma g_z \delta (z-z')\right) \tag{2.68}$$

However, this only assumes an arbitrary movement of the spin during the diffusion period, with no link to diffusional motion. The overall signal is a combination of both the gradient effects and the distribution function of diffusion through the system. For our spins, the observable signal is a construct of the gradient effect, the probability of

the initial particle being within z and z - dz, and the propagator defining the probability of a particle, at initial position z, to be within z' and z' - dz' after Δ. The second component is given as $p(z)$ and is constant when integrated over all possible positions of z. The last term, the propagator, is given as:[101]

$$P(\Delta, t) = \frac{1}{\sqrt{4\pi D\Delta}} e^{-(z\,-\,z')^2/4D\Delta} \tag{2.69}$$

The observable signal therefore becomes:[101]

$$\begin{aligned} \frac{S(\delta g_z \Delta)}{S_0} &= \int\int cos\left[\gamma g_z \delta (z - z')\right] p(z)\, \bar{P}(z, \Delta)\; dz\; dz' \\ &= e^{-(\gamma g_z \delta)^2 \Delta D} \end{aligned} \tag{2.70}$$

Where S denotes the signal intensity. As γ and S_0 are fixed, a typical experiment will maintain the evolution time and the gradient duration as constant and only change the gradient strength. As such, the only unknown is the diffusion coefficient, which as it is a constant, can be extrapolated from a plot of signal intensity against gradient strength for many acquisitions. The experiment must be performed whilst obeying one specific condition: $T_1 > \Delta$. If this condition is not followed then a significant factor of signal decline can be attributed to standard longitudinal relaxation and not diffusion.

In the instance of encountered restriction, the diffusing particles will travel a shorter distance and therefore relay a smaller diffusion coefficient, termed the restricted diffusion coefficient, D(Δ). Should the PGSTE experiment be repeated for an array of diffusion times, Δ, the particles diffusing will eventually reach a limit at which they have experienced their surroundings fully and have encountered all restrictions. By plotting $D(\Delta)/D_0$ against the diffusion time, Δ, one can start to observe an asymptote as Δ approaches infinity. This asymptotic line is shown below in Figure 2.11 and is referred to as the tortuosity of the system, α. This is otherwise known as the ratio between the molecular path through the system and the most direct route possible. One can imagine a maze and the convoluted path that must be taken to enter one side and exit another, the distance being L_R. Then take, for instance, the possibility of flying straight over the maze, and consider how much shorter this distance would be, L. This is analogous to tortuosity as α may be defined as L_R/L.

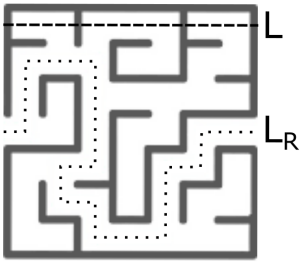

Figure 2.10: Physical representation of tortuosity.

More specifically, tortuosity is defined as:

$$\frac{D(\Delta)}{D_0} = \frac{1}{\alpha} + \frac{(1/\alpha - 1)\theta}{\Delta} + O\left(\frac{1}{\Delta}\right)^{3/2} \tag{2.71}$$

Where θ is a fitting parameter related to pore size.[59] One can link porosity to tortuosity in a structure through the Bruggeman equation:[102]

$$\alpha = \frac{1}{v^{0.5}} \tag{2.72}$$

However, it has been noted that this only holds in exemplar isotropic cases and is not reflective of the inhomogeneous nature of some porous media. As such, the equation can be refined to accommodate for these anisotropies, as detailed by Koponen *et al*:[103]

$$\alpha = 1 + c\frac{1 - v}{\left(v - v_p\right)^m} \tag{2.73}$$

Where c, and m are constants, and v_p is the percolation threshold. This threshold being the point at which long-range connectivity appears in the system: which can in turn be calculated through mathematical means.[104] Within equation 2.71, in the limit of $\Delta \to \infty$, it can be seen that tortuosity is equal to $D_0/D(\Delta)$. On the contrary, in the limit of $\Delta \to 0$, the tortuosity curve can be used to estimate the porous media's surface area to volume ratio when using an alternative expression for tortuosity:[105]

$$\frac{D(\Delta)}{D_0} = 1 - \frac{4}{9}\sqrt{\pi}\frac{S}{V_p}\left(D_0\Delta\right)^{1/2} + c_2\Delta \tag{2.74}$$

Where S and V_p are the surface area and volume of the pores, respectively. The last term, c_2, contains parameters such as the curvature of the pore walls although it is negligible with respect to the first two terms.[106] As such, a plot of $\frac{D(\Delta)}{D_0}$ against $\Delta^{1/2}$ has a gradient proportional to the surface area to volume ratio.

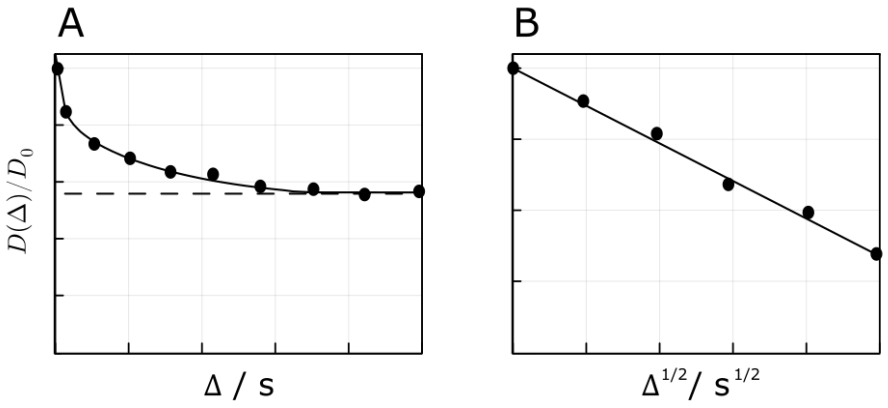

Figure 2.11: Example plots of tortuosity measurements showing A) the asymptote reached as the diffusion time is extended (as in 2.71) and B) how the surface area to volume ratio may be calculated in the limit of short diffusion times (as in 2.74).

There exist other forms of surface area measurements namely the Brunauer-Emmett-Teller (BET) gas-adsorption technique which is known for its sensitivity to surfaces on the molecular scale. One disadvantage to this technique is its requirement for the sample to be dry, which depending on the specific sample, could well have catastrophic effects on the internal architecture or be otherwise completely unachievable.[52]

2.4.2 Diffusion tensor imaging

The measurement of diffusion coefficients is an imperative aspect of exploring porous media; however, it only gives one-dimensional results. As for a more representative approach, one can apply diffusion tensor imaging (DTI): a technique for visualising and studying three-dimensional diffusion within systems. The PGSTE pulse sequence will return the average restricted diffusion coefficient; however, it gives no indication of anisotropy or whether diffusion has prevailed in one direction. Nevertheless, this can be achieved by measuring diffusion along a minimum of six orthogonal directions to produce the independent components of the diffusion tensor in the lab frame. This is a symmetric rank 2 tensor which takes the following form:

$$\boldsymbol{D}(\Delta) = \begin{pmatrix} D_{xx}(\Delta) & D_{xy}(\Delta) & D_{xz}(\Delta) \\ D_{xy}(\Delta) & D_{yy}(\Delta) & D_{yz}(\Delta) \\ D_{xz}(\Delta) & D_{yz}(\Delta) & D_{zz}(\Delta) \end{pmatrix} \tag{2.75}$$

Where all elements reflected through the diagonal are equal to their counterparts. Each element is calculated via a standard PGSTE pulse sequence using a gradient in one of the six chosen directions, in the lab frame. Following the collection of $D(\Delta)$ in all directions, the resulting tensor can be diagonalised revealing its eigenvalues and vectors. The eigenvectors contain information regarding the principal axes of diffusion within the molecular frame. The eigenvalues, or diagonal elements, represent the degree of diffusion within each of the principal axes, in the molecular frame.

$$\boldsymbol{D'}(\Delta) = \begin{pmatrix} D'_{xx}(\Delta) & 0 & 0 \\ 0 & D'_{yy}(\Delta) & 0 \\ 0 & 0 & D'_{zz}(\Delta) \end{pmatrix} \tag{2.76}$$

The eigenvalues and vectors can be used to plot an ellipse which describes diffusion in three dimensions. Where the eigenvalues represent the lengths of the radii in each direction of the ellipse: and the eigenvectors contain information on the orientation with respect to lab frame.

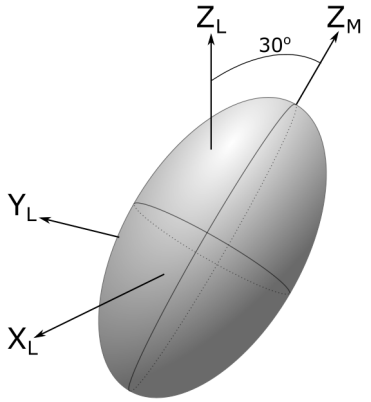

FIGURE 2.12: Example of an ellipse produced by DTI, showing an anisotropic pore tilted 30°.

The degree of anisotropy can be quantified via the fractional anisotropy:

$$FA = \sqrt{1 - \frac{D'_{xx}D'_{yy} + D'_{xx}D'_{zz} + D'_{yy}D'_{zz}}{(D'_{xx})^2 + (D'_{yy})^2 + (D'_{zz})^2}} \tag{2.77}$$

This scalar value ranges from zero to one, indicating unrestricted, isotropic diffusion and completely anisotropic diffusion respectively. The possible diffusion regimes are visualised below using example cases of diffusion:

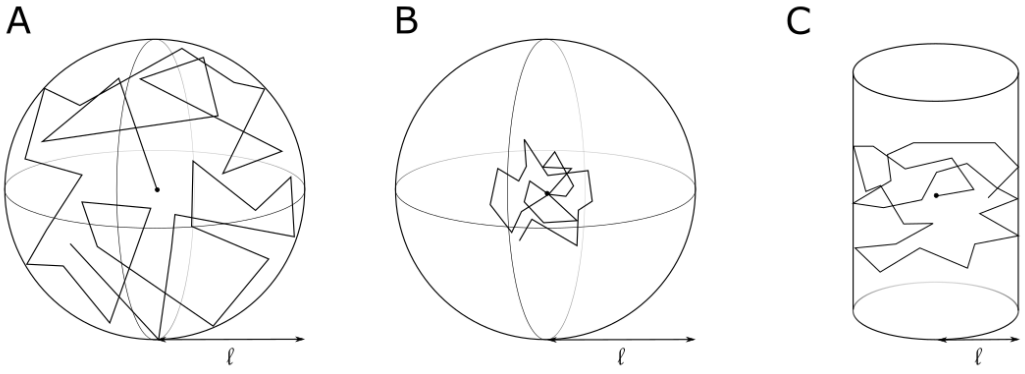

FIGURE 2.13: Demonstration of the different DTI regions that may be found within porous media.

Given an arbitrary diffusion time, one would expect a particle to travel a given distance, r, depending on its diffusion coefficient. Where the average distance travelled by a multiple identical particles would $\langle \Delta r \rangle$. Within each of these regions shown in Figure 2.13, we can expect to observe the following:

Table 2.1: DTI regions expected results

System from Figure 2.13	$\langle \Delta r \rangle$	FA	tortuosity
A	$> \ell$	1	< 1
B	$< \ell$	1	1
C	$> \ell$	< 1	< 1

For the example of Figure 2.13 B, it would be advantageous to extend $\langle \Delta r \rangle$ as much as possible to prevent the possibility of perceived-isotropic diffusion. This can be achieved either by shifting to a lower field where DDIF is less imposing and magnetisation lifetimes increase,[6] or using molecules capable of accessing long-lived states.

Alternatively, a simple workaround would be to perform many scans, at the expense of experimental time. Urbannczyk *et al.* developed a pulse sequence for ultra-fast diffusion measurements that varied the gradient time along the z-axis of the sample such that diffusion could be measured in one scan.[107] Although this significantly reduced the experimental time, it is only sufficient for somewhat consistent samples. A porous media that changes significantly between planes would not benefit from such a pulse sequence. Nor would a system with lacking or low spin concentrations. Such cases would be more suited to traditional diffusion experiments over which the average diffusion could be determined, taking into account the inconsistencies of different compartments, and reduced number of spins.

For inhomogeneously porous samples, such as some rock structures, there may exist unique regions which are larger than the diffusion length scale. In this scenario, there would be subsequent parts to the overall structure, each with its own tortuosity, independent of one another. The overall diffusion coefficient would then be a weighted average of diffusion within the individual parts.[108] It is evident that further studies into diffusion are required to fully utilise NMR as a tool for studying porous media.

Through the use of both computational studies and custom-built methodologies, the following chapters will detail the theory and practicality of measuring diffusion in certain porous systems. They will assess the simulation of DDIF and DTI, and discuss additional improvements to applicable experimental techniques. All in an attempt to enhance diffusion- NMR in porous systems.

Chapter 3

Predicting spin relaxation due to susceptibility inhomogeneities

This chapter is an extended version of T. A. A. Cartlidge, T. Robertson, M. Utz, and G. Pileio, Theory And Simulation Framework for the Relaxation of Nuclear Spin Order in Porous Media, *J. Phys. Chem. B*, 2022, **126**, 6536-6546.[109]

3.1 Synopsis

This chapter is an overview of the work carried out in order to fulfil objective one.

O$_1$ - Produce a numerical simulation framework capable of quantifying the signal loss as a result of magnetic susceptibility mismatches found within porous media.

This chapter discusses the need for the theory of nuclear spins diffusing through inhomogeneous fields. It details the derivation of a quantum mechanical propagator capable of calculating spin relaxation due to factors of the spins' external environment. The derivations draw from the Liouville-von Neumann equation, average Hamiltonian theory (AHT), and the Magnus expansion. The theory is validated through a simulation framework which encompasses modelling the porous media, emulating diffusion, and performing propagator calculations. The calculation of the internal magnetic field within a random and complex porous media is no trivial matter and relies on an accurate digital rendering of the sample in question. As such, the framework requires the aid of high-resolution μ-CT images, and using a series of mathematical tools including Fourier transforms and the convolution theorem.

3.2 Introduction

A complex system is one which contains a multitude of interacting and possibly interconnecting components, arranged in an often unpredictable orientation. As such, these systems may be difficult to model owing to their erratic architecture, or difficult to study due to their fragile nature. In the case of porous media, this can be seen in many structures including rock or cement structures, electrodes, and porous cellular probes.[1,2,110] Such samples require non-invasive and structurally preserving analytical techniques in order to study their interior organisation and formations.

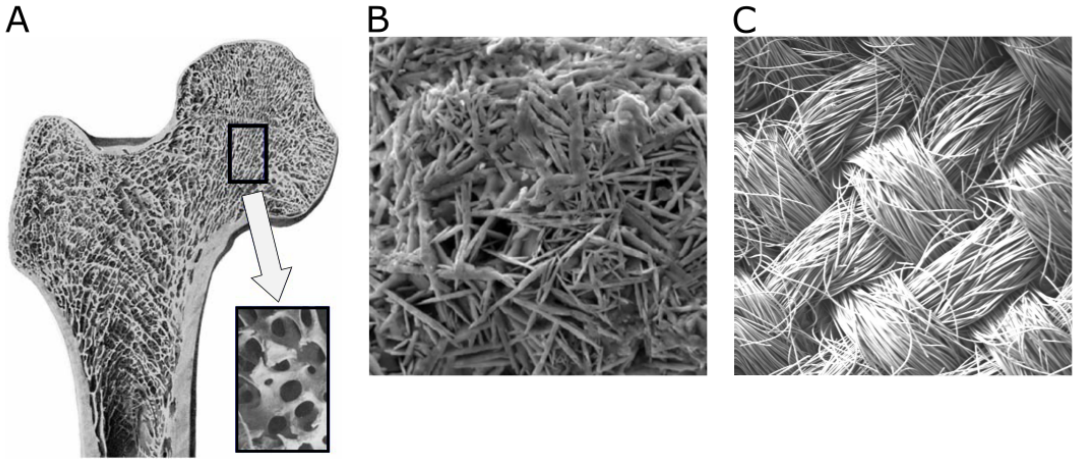

FIGURE 3.1: Examples of complex porous media showing A) a cross-sectional image of a bone (taken from[111]), B) a SEM surface image of sandstone (taken from[112]), and C) a SEM image of a carbon cloth GDL surface.

For many porous media, studies are conducted to determine structural parameters such as pore connectivity and distribution, which can greatly impact diffusion pathways through the pores. In some instances, this directly correlates with the functionality of the sample as poor diffusion can render the structure inadequate for its desired task. For example, the efficiency of transport through porous media is shown to link directly to the performance of Li-ion batteries and the survival of *in vitro* grown tissue cultures.[113,114] One principle method for measuring diffusion is via d-NMR, a class of NMR incorporating rf pulses and gradients to study the nature of porous media from restricted diffusion coefficients to pore size distributions.[57,70] These methods often rely on signal losses due to the diffusion of nuclei from their original, irradiated positions.

Within porous media, this signal attenuation may be increased by the presence of internal field gradients resulting from the difference in magnetic susceptibility between the solid and surrounding liquid. The localised distortion of the external field is known to be greatest at the surface of the intruding solid producing a structurally dependent inhomogeneous field.[115] For spins diffusing through this field, decay due to diffusion in the internal field (DDIF) is known to decrease the lifetime of T_2, therefore, limiting the

experimental time for conventional d-NMR to the lifetime of magnetisation.[47,116–118] The shortened relaxation times may lead to incomplete measurement of diffusion coefficients and tortuosity.[119,120] In geological samples especially, the effect of the porous media is increased by the presence of paramagnetic centres such as iron ions.[53]

Due to the possibly intricate nature of the distortions, or demagnetisation field, many studies assessing the susceptibility-induced relaxation adopt a computational approach. This includes work by Chen *et al.*, who simulated the demagnetisation field within a thin section of sandstone using a commercially available finite element method (FEM) simulation package, FEMLAB.[121] Their work showed the spatial dependence of the internal field resulting from the porous media, concluding a direct relation between the internal field gradients and both the external field and magnetic susceptibility difference.[1] Other studies have explored the phenomena within a single pore involving the computation of the demagnetisation field using COMSOL Multi Physics.[47,121] Their work concluded that poor relaxation times, once the echo time has been minimised, may only be increased through low field experiments. Tranter *et al.*, used a random walk oriented simulation to calculate the tortuosity directly from an image, the disadvantage being the need for accurate digital reconstruction of the porous media.[122]

3.2.1 Magnetic susceptibility

Although the effect of the demagnetisation field is widely known, the underlying theory is yet to exceed the level of a loose approximation stemming from ideal conditions. To solidify an understanding, one must first consider the most crucial parameter, the magnetic susceptibility, χ. This parameter measures the degree to which a material becomes magnetised as a result of an external magnetic field. Magnetic susceptibility is a dimensionless parameter and determines the classification of a material with respect to diamagnetic ($\chi<0$) or paramagnetic ($\chi>0$). It is directly related to the magnetic field strength, $\boldsymbol{H}$, via:

$$\boldsymbol{M} = \chi \boldsymbol{H} \tag{3.1}$$

Where $\boldsymbol{M}$ is the magnetisation: the density of magnetic moments within a given volume. Typically, NMR spectrometers give their magnetic fields in terms of the magnetic flux density, $\boldsymbol{B}$, which is related to field strength through the vacuum permeability, μ_0:

$$\boldsymbol{B} = \mu_0 (1 + \chi) \boldsymbol{H} \tag{3.2}$$

It can be stated that $\boldsymbol{H}$ is a measure of the magnetic field strength and $\boldsymbol{B}$ is a reflection of the total magnetic field given contributions of any materials within the field. That is assuming the material within the field is constant. For a heterogeneous sample, there exists at least two magnetic susceptibilities, that of the liquid and the solid. If the two susceptibilities differ by a significant degree, the external field will be locally distorted

around the phase boundary between the two materials. Furthermore, the effect will become ever more prominent with an increasing difference in susceptibility between the two materials. This can be demonstrated with the example of two micro-beads suspended within a liquid solution of water:

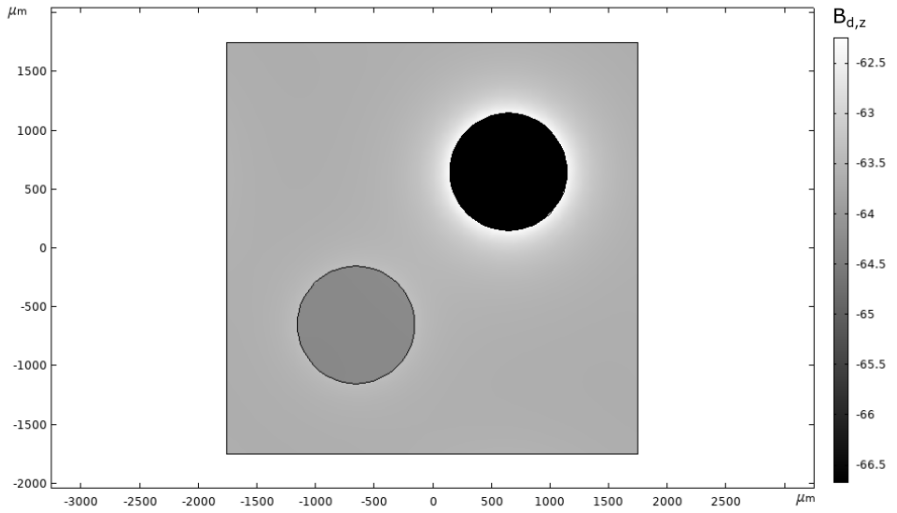

FIGURE 3.2: Demagnetisation field produced by two 750 μm diameter beads of polystyrene (bottom left) and polyethylene (top right) surrounded by water, produced within COMSOL, using the parameters in Table 3.1.

For the examples of polystyrene (PS) and polyethylene (PE) there is minimal change surrounding the closely matched PS but significant distortions around the PE bead. However, within a porous system with thousands of these solid intrusions, packed closely together, the distortions would lead to an inhomogeneous field throughout the whole sample. Diffusion within this would be expected to cause significant signal loss.

TABLE 3.1: Magnetic susceptibility comparison of materials used in Figure 3.2

	H_2O	PE	PS
χ / ppm	9.04 [b]	9.67 [b]	9.06 [b]
$\Delta\chi$ / ppm [a]	-	-0.63	-0.02

[a] $\Delta\chi = (\chi_{H_2O} - \chi)$
[b] Obtained from.[123]

3.2.2 Brownian motion

Within liquid NMR, it can be assumed that the particles are always in motion, diffusing through the sample. Their motion is characterised through the unrestricted diffusion coefficient, D_0, which is dependent on external factors such as the viscosity of the solvent and the radius of the particle under spherical approximations. More specifically,

the motion of liquids can be described as random, independent movements of the individual particles, otherwise known as Brownian motion. This is a time-dependent, random process but can be described by a set of probabilistic laws outlining the stochastic nature of the liquid.[124] One can take an individual particle and associate it to a function, $x_{(t)}$, showing its position at a given time, t. For the movement of the particle to be considered Brownian, the following four conditions must be satisfied:

- $\{x_{(t)},\ t \geqslant 0\}$ is normally distributed
- For any increment where $t > 0$, $x_{(t)}$ is normally distributed
- For all points at $t > 0$, $E[x_{(t)}] = 0$
- $x_{(0)} = 0$

Where t is time and $E[x_{(t)}]$ is the mean of all the variables:[124]

$$E[x_{(t)}] = \int_{-\infty}^{\infty} x f_{(x)}(x) dx \tag{3.3}$$

Where $f_{(x)}(x)$ is the probability density function which contains the likelihood of the particle being at a position, x, after a given time interval. Brownian motion requires random movement where the step taken by the particle is independent of the path previously taken. After any time period, the distribution of displacements from the initial position must be normally distributed. This time period could be from t=0 to the end of the experiment, or from any time period within the limits of 0 and t. Thus, the displacement of the particle during any time increment must be normally distributed. As movement in one direction is equally as probable as movement in the opposite direction, the mean value of displacement must always be zero. Finally, the particle must not have moved at time zero. Thus, movement, be it physical or modelled, must satisfy these four laws in order to be deemed Brownian. Given these conditionals, there exists a correlation between the distance a particle will travel, in one dimension, and a given time period:[125]

$$\langle x^2(t) \rangle = \int_{-\infty}^{\infty} x^2 \frac{e^{-x^2/4Dt}}{\sqrt{4\pi D t}} dz \tag{3.4}$$

Where there exists analogous equations for diffusion in higher dimensions. Using these, the distance travelled can be estimated through the mean square displacement:[126]

$$\langle \Delta r \rangle = \sqrt{2\, n\, D_0\, t} \tag{3.5}$$

Where $\langle \Delta r \rangle$, is the average distance moved, n is the dimension, and t is the time. This is case-specific for unrestricted diffusion and is not representative of bulk movement within a tortuous media.

For the purpose of this study, it was therefore beneficial to devise a system that is statistically reproducible and offers variability with respect to the major contributing

factors such as the susceptibility difference, the pore size, and the field. Such criteria can be found within submerged micro-beads packed into a tube. It can be assumed that if the packing is maximised but completely random, samples may not be physically identical but will statistically contain equivalent structural properties. The beads can be selected in a multitude of materials allowing the comparison of different magnetic susceptibility differences given a common solvent. The sizes of the pore can also be altered by selecting different beads diameters allowing insight into the two extremes.

At one limit, a sufficiently large pore will be too great for any structural information to be determined as T_2 will not persist long enough for the molecule to encounter any restriction. The result of which would be assumed isotropic conditions where in reality, the system is tortuous just on a scale too large to be observed by the molecule. Opposing this is the small pore limit: when localised field distortions exist within close proximity of one another the resulting field is exceedingly inhomogeneous and T_2 may be reduced to such an extent that the molecule is not seen to encounter any restriction. These phenomena can be studied by selecting beads with diameters between 200 μm and 1 mm. NMR spectrometers come in a range of field strengths allowing the option to study the systems across a range of fields.

3.3 Theory

In the case of a relaxation mechanism driven by diffusion through an inhomogeneous field, although the phenomenon is widely known, no previous studies have led to a means of calculating and predicting its effects. To begin the derivation, it can first be noted that the evolution of spin order can be described via a Hamiltonian. The Hamiltonian is time-dependent as a reflection of the dependence of relaxation on the fluctuating magnetic fields experienced by the nuclei. Unfortunately, evaluating the dynamics of an ensemble of spins subject to this Hamiltonian is no trivial matter: conventional techniques for solving time-independent systems are obsolete, and alternate methods must be adopted. Such methods utilise the density operator and describe the dynamics of the ensemble using the Liouville-Von Neumann equation:[127]

$$\frac{\partial}{\partial t}\hat{\rho}(t) = -i\,\hat{\hat{H}}_{(t)}\hat{\rho}(t) \tag{3.6}$$

Where $\hat{\hat{H}}_{(t)}$ is a superoperator. Much like an operator can transform a function, a superoperator can act upon a vector space of linear operators in the following way:

$$\hat{\hat{H}}(t)\hat{\rho}(t) = [\hat{H}(t), \hat{\rho}(t)] \tag{3.7}$$

For a time-independent Hamiltonian, the solution to the Liouville-Von Neumann equation takes the general form of:

$$\hat{\rho}(t) = e^{-i\,\hat{\hat{H}}\,t}\,\hat{\rho}(0) \tag{3.8}$$

Which acts in the following manner:[128]

$$\hat{\rho}(t) = e^{-i\,\hat{H}\,t}\,\hat{\rho}(0)\,e^{i\,\hat{H}\,t} \tag{3.9}$$

In quantum mechanics, the propagator $\hat{\hat{U}}(0,t)$ can be defined as an operator that describes the propagation of the wavefunction from the initial state to the state at time t_k. With respect to the Liouville-Von Neumann equation solution, the propagator is given by $e^{-i\,\hat{\hat{H}}\,t}$. If the Hamiltonian is time-dependent, the propagator becomes an infinite series of exponentials representing the Hamiltonian split into infinitesimally small intervals, τ over which $\hat{H}(\tau_n)$ is constant. This is represented as:

$$\hat{\hat{U}}(0,t) = e^{-i\,\hat{H}_n\,\tau_n} \cdot \ldots \cdot e^{-i\,\hat{H}_2\,\tau_2} \cdot e^{-i\,\hat{H}_1\,\tau_1} \tag{3.10}$$

The derivation of this is given in section 9.1. However, this can only be written as a single exponential under the following condition:

$$e^{Z} = e^{A}\,e^{B} \qquad \text{for } [A,B] = 0 \tag{3.11}$$

In such a case, each component of the Hamiltonian would commute with each other and the solution of the Liouville-von Neumann equation would be:[129,130]

$$\hat{\hat{U}}(0,t) = e^{-i\int_0^\tau \hat{\hat{H}}(t)\,dt} \tag{3.12}$$

Since Hamiltonians at different points in time may not commute, the single exponential is expanded using the Baker-Campbell-Hausdorff relation:[131]

$$e^{\hat{A}}\,e^{\hat{B}} = e^{\hat{A}+\hat{B}+1/2[\hat{A},\hat{B}]+1/12[\hat{A}[\hat{A},\hat{B}]]+\cdots} \tag{3.13}$$

Applying this to eq. (3.10) produces:

$$\begin{aligned}\hat{\hat{U}}(0,t) &\approx e^{-i\,\bar{\hat{\hat{H}}}\,t} \\ &= e^{-i\sum_k \hat{H}_k\tau_k - 1/2\sum_k\sum_{l>k}[\hat{H}_l\tau_l,\hat{H}_k\tau_k]+\cdots}\end{aligned} \tag{3.14}$$

The average Hamiltonian now becomes:

$$\bar{\hat{\hat{H}}} = \frac{1}{t}\left(\sum_k \hat{\hat{H}}_k\tau_k - \frac{i}{2}\sum_k\sum_{l>k}[\hat{\hat{H}}_l\tau_l,\hat{\hat{H}}_k\tau_k] + \cdots\right) \tag{3.15}$$

This can be written out in the form of a Magnus expansion:[132]

$$\bar{\hat{H}} = \bar{\hat{H}}^{(1)} + \bar{\hat{H}}^{(2)} \dots \tag{3.16}$$

The first two terms can be extracted and written in their integral form:[133]

$$\begin{aligned} \bar{\hat{H}}^{(1)} &= \frac{1}{t}\int_0^t \hat{H}(t_1)\, dt_1 \\ \bar{\hat{H}}^{(2)} &= -\frac{i}{2t}\int_0^t dt_2 \int_0^{t_2} [\hat{H}(t_2), \hat{H}(t_1)] dt_1 \\ &\dots \end{aligned} \tag{3.17}$$

In order to truncate the Magnus expansion such that it still represents the total Hamiltonian of the system, the selected terms must converge to give an equivalent result to that of an unaltered Hamiltonian. Such convergence may be found within the limit of:

$$\|H\| t << 1 \tag{3.18}$$

Where the norm of the operator, $\|H\|$ is calculated as the square root of the largest eigen value of $H^T H$. To determine this, the Hamiltonian of the current system must be defined. For a single spin-1/2 diffusing through a spatially-dependent field, it may be assumed that the significant relaxation mechanisms are limited to the Zeeman interaction and DDIF. With an external field applied along the z-axis, the time-dependent Hamiltonian is given as:

$$\hat{H}(t) = -\gamma B_0 \hat{I}_z - \gamma \boldsymbol{B}_d(t) \cdot \hat{\boldsymbol{I}} \tag{3.19}$$

Where $\boldsymbol{B}_d(t)$ is the distortions in the field experienced by the spins, which is proportional to the magnetic susceptibility difference and external field, as will be seen later. It is beneficial here to shift into the Zeeman interaction frame such that the only observable contribution is from that of DDIF. By doing so, the spin dynamics of the system are observed from a frame that is rotating in unison with the Larmor frequency.[134] As such, the Zeeman interaction is eliminated by shifting into the rotating frame via:

$$\tilde{\hat{H}}(t) = R(t)\hat{H}(t)R^{\dagger}(t) - iR(t)^{\partial}/_{\partial t} R^{\dagger}(t) \tag{3.20}$$

Applying this to eq. (3.19):

$$\tilde{\hat{H}}(t) = e^{i\omega_0 \hat{I}_z t}(-\gamma \boldsymbol{B}_d(t) \cdot \hat{\boldsymbol{I}}) e^{-i\omega_0 \hat{I}_z t} \tag{3.21}$$

The Larmor frequency definition has be used for simplicity. The derivation of eq. (3.20) and its application on the Hamiltonian at hand are given in section 9.2. To expand

eq. (3.21), it is first convenient to relay our commutator relations from eq. (2.27):

$$\begin{gathered} e^{-i\hat{I}_x\theta}\,\hat{I}_y\,e^{i\hat{I}_x\theta} = \hat{I}_y cos(\theta) + \hat{I}_z sin(\theta) \\ [\hat{I}_x, \hat{I}_y] = i\hat{I}_z \circlearrowright \end{gathered} \tag{3.22}$$

The Hamiltonian in the Zeeman interaction frame is then given as:

$$\tilde{\hat{H}}(t) = \omega_x(t)[\hat{I}_x cos(\omega_0 t) + \hat{I}_y sin(\omega_0 t)] + \omega_y(t)[\hat{I}_y cos(\omega_0 t) - \hat{I}_x sin(\omega_0 t)] + \omega_z(t)\hat{I}_z \tag{3.23}$$

Where $\omega_a(t)$ is $-\gamma B_a$ respectively for all Cartesian axes. Here we have a time-dependent averaged Hamiltonian which we can truncate to the first term using eq. (3.17). Where the time period is chosen as one over which the Hamiltonian repeats itself meaning the x and y components integrate to zero. Therefore, the only remaining term is the z-component and the integral can be solved using the definition of Riemann integral:[135]

$$\int_0^t f(x)dx \approx \sum_{k=0}^{N-1} f(t_k)\Delta t \tag{3.24}$$

Using which, the Hamiltonian is seen as many different increments, each constant but distinct from the last. This will result in:

$$\tilde{\hat{H}}^{(1)} = \omega_z(t)\hat{I}_z \tag{3.25}$$

Under these pretences, the averaged Hamiltonian satisfies:

$$\left\| \tilde{\hat{H}}^{(1)} \right\| t << 1 \tag{3.26}$$

3.3.1 Propagation

In order to measure the signal attenuation of a spin-1/2 nucleus diffusing through the porous media, a single echo pulse sequence was used, as shown below in Figure 3.3:

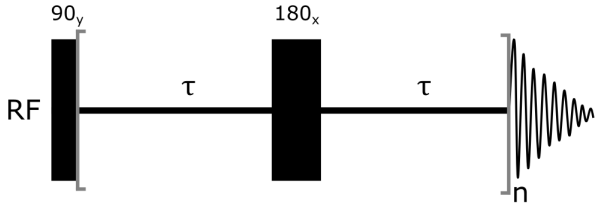

Figure 3.3: Spin echo pulse sequence where n = 1 and τ is variable.

In such a case, the spins will be subject to the demagnetisation Hamiltonian for a time, τ, followed by a 180_x pulse, and finally the demagnetisation Hamiltonian again. As

such, the propagator for such an echo sequence is give by:

$$\hat{\hat{U}}_e(0,2\tau) = \hat{\hat{D}}\; e^{-i\hat{\hat{H}}\tau}\; e^{-i\pi\hat{\hat{I}}_x}\; e^{-i\hat{\hat{H}}\tau} \tag{3.27}$$

Where $\hat{\hat{D}}$, the Dyson time operator, maintains the numerical order of the operations. Using eq. (3.12), the single echo pulse sequence propagator, $\hat{\hat{U}}_e(0,2\tau)$, then becomes:

$$\hat{\hat{U}}_e(0,2\tau) = e^{-i\int_0^\tau \hat{\hat{H}}(t_1)\,dt_1}\; e^{-i\pi\hat{\hat{I}}_x}\; e^{-i\int_\tau^{2\tau} \hat{\hat{H}}(t_1)\,dt_1} \tag{3.28}$$

By utilising laws of rotation operators, this can be simplified in the following steps:

$$\begin{aligned}
\hat{\hat{U}}_e(0,2\tau) &= e^{-i\int_0^\tau \tilde{\hat{H}}^{(1)}(t)\,dt_1}\; e^{-i\pi\hat{\hat{I}}_x}\; e^{-i\int_\tau^{2\tau} \tilde{\hat{H}}^{(1)}(t)\,dt_1}\; e^{i\pi\hat{\hat{I}}_x}\; e^{-i\pi\hat{\hat{I}}_x} \\
&= e^{-i\int_0^\tau \tilde{\hat{H}}^{(1)}(t)\,dt_1}\; e^{i\int_\tau^{2\tau} \tilde{\hat{H}}^{(1)}(t)\,dt_1}\; e^{-i\pi\hat{\hat{I}}_x} \\
&= e^{-i\int_0^\tau \left[\tilde{\hat{H}}^{(1)}(t) - \hat{\hat{H}}(t_1+\tau)\right]dt_1}\; e^{-i\pi\hat{\hat{I}}_x}
\end{aligned} \tag{3.29}$$

Assuming the field fluctuations experience from time 0 to τ are equally as random as those experienced from τ to 2τ. By doing so, the single echo propagator can be divided into two constituents, the propagator superoperator component, $\hat{\hat{U}}(0,2\tau)$, and the rotation component:

$$\hat{\hat{U}}_e(0,2\tau) = \hat{\hat{U}}(0,2\tau)\; e^{-i\pi\hat{\hat{I}}_x} \tag{3.30}$$

Substituting the definition of the first order truncation of the average Hamiltonian from eq. (3.25), and using the definition $\omega_z(t) = -\gamma B_{d,z}(r(t))$, the propagator becomes:

$$\hat{\hat{U}}(0,2\tau) = e^{i\gamma\hat{I}_z\int_0^\tau (B_{d,z}(r(t)) - B_{d,z}(r(t+\tau))\,dt} \tag{3.31}$$

Since the scenario at hand concerns an ensemble of spins, the dynamics of the system are described by the ensemble average of the propagator given in eq. (3.31):

$$\begin{aligned}
\hat{\hat{P}} &= \langle \hat{\hat{U}}(0,2\tau) \rangle \\
&= \langle e^{i\gamma\hat{I}_z\int_0^\tau (B_{d,z}(r(t)) - B_{d,z}(r(t+\tau))\,dt} \rangle
\end{aligned} \tag{3.32}$$

From here, it can be seen that the propagator will converge to unity as the echo time approaches zero. It can therefore be theorised that in the limit of minimised delays between π pulses, the diffusive attenuation effect can be omitted. However, this is not concurrent with current hardware capabilities owing to the limitation of minimising the dead time for rf pulses.

3.3.2 Relaxation

The propagator given above described the dynamics of a spin system as it evolves during the single echo pulse sequence given in Figure 3.3. To determine the effect on both

longitudinal and transverse magnetisation, one must first define the initial condition to apply the propagator to. In this case, this can be taken as the state of the system following the first 90-degree pulse:

$$\begin{aligned}\hat{\rho}(0) &= \hat{I}_x \\ &= \frac{1}{2}(\hat{I}^+ + \hat{I}^-)\end{aligned} \tag{3.33}$$

It is immediately evident that the initial state only contains transverse spin order. If the basis set for the Liouville space is given as $\left\{\hat{I}^-, \hat{I}_z, \hat{\mathbb{1}}, \hat{I}^+\right\}$, then at time t=0 the density operator can be written as:

$$\hat{\rho}(0) = \frac{1}{2}\begin{pmatrix} 1 \\ 0 \\ 0 \\ 1 \end{pmatrix} \tag{3.34}$$

The state of the system following the duration of the single echo pulse sequence can therefore be calculated from:

$$\hat{\rho}(2\tau) = \hat{\hat{P}}\, e^{-i\pi\hat{\hat{I}}_x}\hat{\rho}(0) \tag{3.35}$$

Using this basis set, the matrix representation of the propagator can be written as:

$$\hat{\hat{P}} = \begin{pmatrix} P_{11} & 0 & 0 & 0 \\ 0 & 1 & 0 & 0 \\ 0 & 0 & 1 & 0 \\ 0 & 0 & 0 & P_{11}^* \end{pmatrix} \tag{3.36}$$

Where:

$$P_{11} = \langle e^{i\,\gamma \int_0^\tau (B_{d,z}(r(t)) - B_{d,z}(r(t+\tau))\, dt} \rangle \tag{3.37}$$

Furthermore, the 180° pulse can be written as:

$$\hat{\hat{R}}_x(\pi) = e^{-i\pi\hat{\hat{I}}_x} = \begin{pmatrix} 0 & 0 & 0 & 1 \\ 0 & -1 & 0 & 0 \\ 0 & 0 & 1 & 0 \\ 1 & 0 & 0 & 0 \end{pmatrix} \tag{3.38}$$

As expected, a 180-degree rotation about x on $\hat{I}_x$ has no effect and therefore the product of the single echo pulse sequence acting on the initial state is:

$$\hat{\rho}(2\tau) = \frac{1}{2}\left(P_{11}^*\hat{I}^- + P_{11}\hat{I}^+\right) \tag{3.39}$$

Since NMR observes only the -1Q coherences, the only relevant term is found to be:

$$\hat{\rho}_{obs}(2\tau) = \frac{1}{2} P_{11}^{*} \hat{I}^{-} \tag{3.40}$$

One visible consequence of eq. (3.40) is the lack of application on longitudinal spin order meaning this phenomenon will not contribute to T_1 but only T_2. To further elucidate this, one can represent longitudinal magnetisation in its corresponding vector given the basis set above:

$$\hat{I}_z = \frac{1}{\sqrt{2}} \begin{pmatrix} 0 \\ 1 \\ 0 \\ 0 \end{pmatrix} \tag{3.41}$$

The result of the propagator given in eq. (3.36) acting upon the system leads to no change. Furthermore, the effect of eq. (3.38) will only result in a change of sign and no signal attenuation. In conclusion, DDIF is restricted to a transverse magnetisation relaxation mechanism and bears no mark on the lifetime of T_1. Additionally, the relaxation mechanism is mediated by many experimental factors such as the nucleus in question and principally, the size and frequency of the field distortions experienced by the diffusing spins, $B_{d,z}$.

3.4 Materials and methods

3.4.1 Sample preparation

The porous media used within this study were composed of randomly packed polyethylene (PE) or glass beads submerged in a solution of deuterated methanol (MeOD). The samples were made such that they spanned the probe coil region with a comfortable excess. For PE, this was achieved by weighing ~1.2 g of beads (size dependent) and adding to a standard 5 mm Wilmad LabGlass NMR tube. The glass samples were filled to the same level but required a larger weight due to their density. The bead addition was done in quarterly aliquotes and the tube was shaken for 2 minutes upon each addition of the beads. One study centred around the packing of spheres showed that following 2 minutes, excess shaking did not improve the packing.[136] It was advantageous to obtain stable packing, this being the scenario where downward pressure did not result in movement within the sample, as this would increase the reproducibility. Although the exact configuration in a second sample is statistically almost impossible, if maximum packing density is achieved it can be presumed that repeating the method would produce an equally random structure of a similar packing density.

The polyethylene micro-spheres were sourced from Cospheric's CMPS products in the following sizes: 212-250 μm, 500-600 μm, and 1000-1180 μm. The beads were not purified further in any form. The glass beads were obtain from Sigma-Aldrich and came in sizes: 212-300 μm, 425-600 μm, and 710-1180 μm. They came acid washed and no further purification was done on them. Once the beads were added entirely and checked to ensure they span the active coil region, the methanol solution was added until the beads were submerged. The sample was then shaken again until no air bubbles were visible and the solution was assumed to be evenly distributed throughout the sample. Unfortunately, the samples could not be sonicated due to the possible breakage arising from the vibration of glass beads within the glass tube. As such, manual shaking had to be performed. The methanol solution came from a batch of 0.193 M TMS in deuterated methanol where both the solvent and solute were obtained from Sigma-Aldrich, used without further purification. The samples are summarized below in Table 3.2:

Table 3.2: Sample composition and labelling [(a)]

Sample name	Bead material	Bead size / μm
BLK	-	-
PES	Polyethylene (PE)	212-250
PEM		500-600
PEL		1000-1180
GS	Glass (G)	212-300
GM		425-600
GL		750-1180

[(a)] All samples were immersed in 0.193 TMS in deuterated Methanol

Where S, M, and L symbolise the use of either small, medium, or large beads respectively. The magnetic susceptibilities of the materials are summarised below:

Table 3.3: Magnetic susceptibilities of the materials and their comparison to MeOD

	MeOD	PE	Glass
χ / ppm	−6.96 [(b)]	−9.67 [(c)]	−6.07 [(c)]
$\Delta\chi^{(a)}$ / ppm	-	2.71	-0.89

[a] $\Delta\chi = (\chi_{Me} - \chi)$
[b] Obtained from.[137]
[c] Obtained from.[123]

3.4.2 NMR data acquisition

3.4.2.1 Spectrometers

The NMR data were collected on three separate instruments, each with a different static field: these being 7.05, 9.4, and 16.4 T. Data at 7.05 T were collected on a Bruker Avance III 300 MHz spectrometer running topspin 3.5 and equipped with a 10mm MICWB40 Bruker probe. Data at 9.4 T were collected on a Bruker Avance Neo 400 MHz spectrometer running topspin 4.0.8 and equipped with a 10mm BBO Bruker probe. Data at 16.4 T were collected on a Bruker Avance Neo 700 MHz spectrometer running topspin 4.0.7 and equipped with a Bruker CPP TCI 700S3 probe. Shimming for all samples was performed on a blank sample (BLK) containing only the methanol solution. The blank sample was also used to optimise the 90° and 180° pulses, at all fields.

3.4.2.2 Pulse sequences

Experimental data, obtained by T. Robertson, included the acquisition of 1D spectra, T_1, and T_2 for all seven samples, and the single echo pulse for all six bead-containing samples. The single echo pulse sequence is shown above in Figure 3.3 where n=1 and τ is varied. The measurement of T_2 was acquired using the Carr-Purcell-Meiboom-Gill (CPMG) method.[138] This can be visualised using Figure 3.3 where τ is fixed and the number of echos, n, is varied. The longitudinal magnetisation was measured using a conventional saturation recovery pulse sequence.[139] In this case, the measurement of T_1 begins by first eradicating any previous remaining magnetization using a series of strong 90° pulses. Following this, the sample is left to evolve under a variable delay, τ, where longitudinal magnetisation can recover. For detection, a final 90° pulse brings the magnetisation to the xy-plane where it is detectable and the free induction decay (FID) is read. For T_1 , the variable delay ranged from 0.1 ms to 32 seconds.

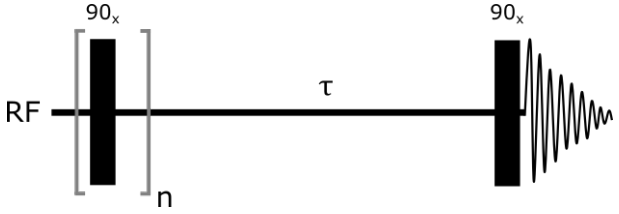

Figure 3.4: Saturation recovery pulse sequence where n = 150 and τ is variable.

Calculations of the relaxation rates, T_1 and T_2, were done in a custom-made palette running within the Wolfram Mathematica software[140] to fit the experimental curves. The fitting was either mono-exponential or bi-exponential depending on the contribution of the beads to the spectra. For all the 7.05 T data, GM 9.4 T, and GL 9.4 T, the

fitting was bi-exponential as the presence of the beads was significant enough to introduce a false baseline. The contribution of the beads to the peak could be distinguished from that of the liquid such that T_2 could be calculated for TMS. In all other systems, mono-exponential fitting was sufficient to acquire the relaxation times.

3.4.2.3 Diffusion experiments

The simulation requires the value of the unrestricted diffusion coefficient of TMS in MeOD, as will be shown in later sections. This was experimentally measured at 7.05 T using BLK, using a standard PGSTE pulse sequence as seen in Figure 2.9.[100] The measurement returned an unrestricted diffusion coefficient of $D_0 = 2.4 \times 10^{-9}$ m^2 s^{-1}.

3.4.3 μ-CT imaging

The structure of the porous media was evaluated using micro-computerised tomography (μ-CT), collected via a modified 225 kVp Nikon/Xtek HMX scanner. The μ-CT images were obtained on samples made using the same methodology as specified above. However, the glass samples were put in a 10 mm Wilmad LabGlass NMR tube to obtain a larger volume. To improve contrast, the PE bead samples were made in 10 mm poly-carbonate tubes made from a section of 10 mm outer diameter, 1.5 mm wall-thickness tubing obtained from clear plastic supplies, with a base adhered. After the shaking procedure, the tubes were sealed and left overnight before being taken to the μ-CT facility. The raw data were composed of whole images of the samples, cropped down to the central 512x512x512 pixels and processed using ImageJ software,[141] by T. Robertson. The data were first filtered via a median filter of three pixels, then binarised, followed by a final median filter of two pixels to reduce noise and ring artefacts. They were then imported into the simulation framework. The central xy-plane for PES, PEM, and PEL are given below in Figure 3.5, and for GS, GM, and GL in Figure 3.6:

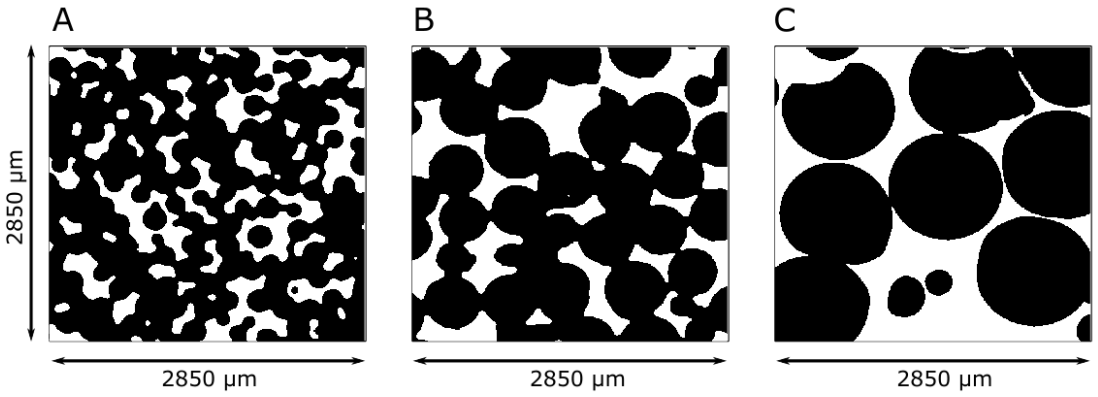

FIGURE 3.5: μ-CT images taken from the central xy-plane slice of the three PE bead packings where A) is PES, resolution of 9.31 μm, B) is PEM, resolution of 5.56 μm, and C) is PEL, resolution of 5.56 μm.

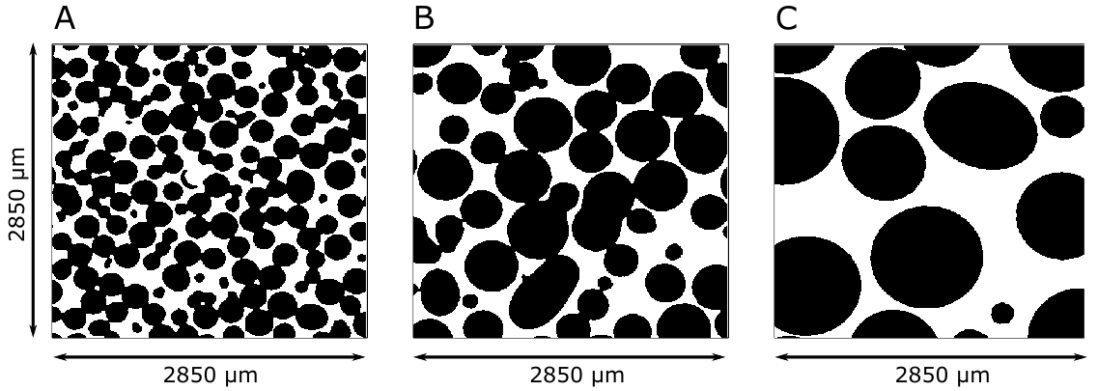

FIGURE 3.6: μ-CT images taken from the central xy-plane slice of the three glass bead packings where A) is GS, B) is GM, and C) is GL. All with a resolution of 5.56 μm.

3.4.4 Computation

All simulations were run in Julia 1.7.1 programming language,[142] with a computer running Windows 10, with a 64-bit operating system, 8 processors, with a speed of 2.8 GHz, 4 cores, and 16 GB of RAM. Each propagation experiment was parallelised across a shared array such that multiple different echo time experiments ran simultaneously. This reduced the run time to three minutes for a total of 1×10^7 successful steps.

3.5 Results and discussion

3.5.1 Simulation framework

As highlighted in the theory, the calculation of transverse magnetisation signal attenuation requires knowledge of the magnetic field experienced by diffusing nuclear spins as a function of time, $B_{d,z}$. However, due to the intricate nature of many porous media, the internal magnetic field within the system may be a complex and inhomogeneous environment that is difficult to measure with any accuracy. As such, a computational approach was adopted to test the validity of the previously derived theory. To do so, the simulation bares a number of requirements including:

1. Access to an accurate digital reconstruction of the physical sample,
2. A means of calculating the internal inhomogeneous magnetic field,
3. A model to simulate restricted diffusion and extract the fluctuating fields experienced by the nucleus as a function of time,
4. Calculation of the quantum mechanical propagator to predict spin relaxation.

The majority of the simulation framework was performed in Julia with the exception of the μ-CT data configuration which was done in ImageJ [141] as described in section 3.4.3. A description of the simulation, broken down into its unpinning steps, is detailed in the following sections, beginning with the preparation of the computerised samples.

3.5.1.1 Digital reconstruction

The digitally reconstructed data, or structure-function $S(\boldsymbol{v})$, provides a framework fit for two purposes; to calculate the demagnetisation field; and to host the simulated nuclei whilst they diffuse. In both cases, there must be a distinct definition between the solid matter, where the nuclei cannot enter, and the pores, where diffusion is situated. For this, the data must be binarised to remove ambiguity between the liquid-solid interface. The result being a structure-function where all pixels corresponding to beads and pores are assigned the value of one or zero, respectively.

In the instance of an erroneous reading, due to detector calibration or poor contrast, a rogue pixel may be misvalued leading to a small pore volume within a bead. During scanning the sample is spun which can cause propagation of the erroneous reading throughout the whole plane, known as ring artefacts. To overcome this, a median filter was applied whereby the values of the surrounding pixels were evaluated to determine the statistically most probable value of the pixel in question. The filter is operated with a specified range to select the surround n layers of pixels to be included within the statistical calculation. The assignment of the target pixel is dependent on the proximity, and therefore weighting, of the values of all surrounding pixels within the range. This is based on their proximity, and therefore weighting, to the central pixel. The data were cropped to the centre-most 512x512x512 pixels as this produced a large enough system to statistically represent the whole sample whilst maintaining computational efficiency. The difference between the unfiltered and filtered data can be seen below.

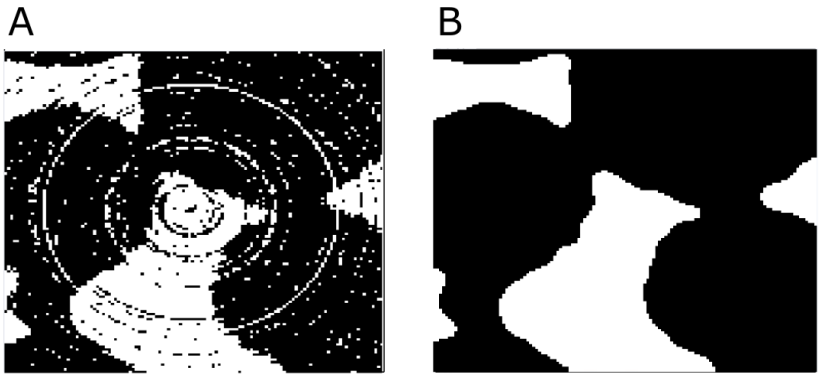

FIGURE 3.7: μ-CT images taken from PEM where A) is the unfiltered raw data and B) is the final data following filters and binarisation.

3.5.1.2 Internal magnetic field

The next step in the framework was to calculate the demagnetisation field within the randomly packed beads. Although applications like COMSOL offer a wealth of computational tools, it was determined that greater efficiency could be achieved by minimising the number of applications that the framework was spread across. And so, the basis of the simulation begins with the structure-function where each voxel exists within a unitless space where the distance dependence is not integrated. As such it was necessary to calculate the magnetic field first in a dimensionless form for units to be inserted at a later time. To do so, the approach taken began with the equation for calculating the magnetic field produced by a single dipole given a distance of $\boldsymbol{r}$ and a dipole magnetic moment, $\boldsymbol{m}$:[143]

$$\boldsymbol{B}_d(\boldsymbol{m},\boldsymbol{r}) \;=\; \frac{\mu_0}{4\pi}\,\frac{3(\boldsymbol{m}\cdot\check{r})\check{r}-\boldsymbol{m}}{r^3} \tag{3.42}$$

Where $\boldsymbol{B}(\boldsymbol{m},\boldsymbol{r})$ is the magnetic field of the dipole and the $\check{r}$ notation represents the normalised vector of $\boldsymbol{r}$. Through manipulation of definitions such as magnetisation, $\boldsymbol{M}$, and introducing a unitless length factor, v to represent distance within the digital array, this equation can be transformed into a completely dimensionless derivative of the dipole magnetic field:

$$\boldsymbol{b}_d(v) \;=\; \frac{1}{4\pi}\,\frac{3(\check{\boldsymbol{B}}_0\cdot\check{v})\check{v}-\check{\boldsymbol{B}}_0}{v^3} = \frac{\boldsymbol{B}_d}{\Delta\chi\; B_0} \tag{3.43}$$

Where v and $\check{\boldsymbol{B}}_0$ are the dimensionless constants for distance and magnetic field strength respectively, and $\Delta\chi$ is the magnetic susceptibility difference between the solid and liquid. Details of this derivative can be found in section 9.3.

The magnetic field across the whole sample can then be calculated using a combination of Fourier techniques and the convolution theorem. Firstly, eq. (3.43) is used to calculate the magnetic field within an empty 512x512x512 array produced by a single dipole positioned at the centre, $\boldsymbol{g}(\boldsymbol{v})$. To maintain the unitless format used within the user-defined function, $\check{\boldsymbol{B}}_0$ is set to $[0,0,1]$ to reflect a dimensionless external field positioned along the z-axis. To calculate the field in $\boldsymbol{S}(\boldsymbol{v})$, every point within the structure-function would need to be cross-multiplied with every point in $\boldsymbol{g}(\boldsymbol{v})$, as follows:[144]

$$\boldsymbol{G}_{(v)}(n) = (\boldsymbol{S}_{(v)} * \boldsymbol{g}_{(v)})(n) = \begin{cases} \displaystyle\sum_{k=-\infty}^{\infty} \boldsymbol{S}_{(v)}(k)\boldsymbol{g}_{(v)}(n-k) \\ \displaystyle\int_{-\infty}^{\infty} \boldsymbol{S}_{(v)}(k)\boldsymbol{g}_{(v)}(n-k)\; dk \end{cases} \tag{3.44}$$

Where k is the dependent variable, and n is the shift in k. Within the simulation, both the structure-function and single dipole field were discretised into grid points meaning the sum function would be more applicable. This is a commutative operation meaning

the response function, $\boldsymbol{G}_{(\boldsymbol{v})}(n)$ is independent of which function possesses the lag.[144] Given that these are both arbitrary functions, they can both be Fourier transformed and the convolution theorem can be used. This theorem states that the cross multiplication of the two functions is equal to the inverse Fourier transform of the product of $\mathscr{F}[\boldsymbol{S}(\boldsymbol{v})]$ and $\mathscr{F}[\boldsymbol{g}(\boldsymbol{v})]$ according to:[145]

$$\mathscr{F}^{-1}\{\mathscr{F}[\boldsymbol{S}(\boldsymbol{v})]\mathscr{F}[\boldsymbol{g}(\boldsymbol{v})]\} = (\boldsymbol{S} * \boldsymbol{g})(\boldsymbol{v}) \tag{3.45}$$

Where $\mathscr{F}^{-1}$ is the inverse Fourier transform. The result of this acting on the dipole field and the μ-CT image produced a 3D field map showing the demagnetisation field, $\boldsymbol{G}(\boldsymbol{v})$, throughout the whole structure. The demagnetisation field was a superposition of all the magnetic fields produced by the dipoles at the vertices of each voxel in the binarised structure. Finally, the field map was interpolated such that the field became a continuous function over the total structure. The interpolation was done following the convolution theorem for improved computational efficiency. The central slice of a μ-CT image and the corresponding demagnetisation field can be seen below in Figure 3.8:

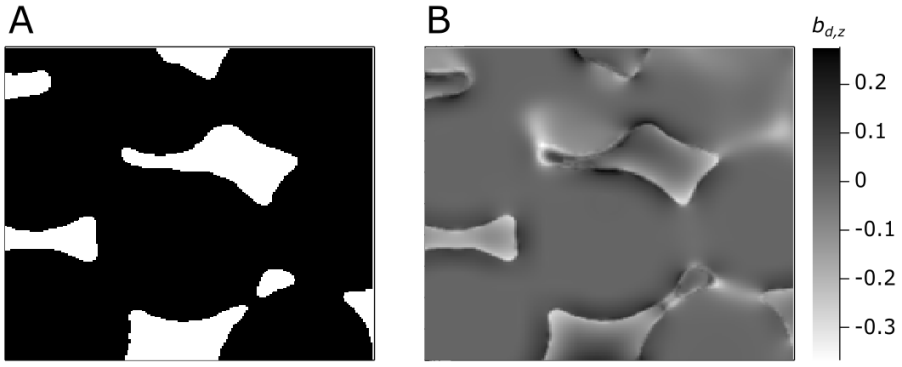

FIGURE 3.8: μ-CT image taken from a section of the central xy-plane slice of PEM showing A) the digital reconstruction and B) the dimensionless demagnetisation field.

3.5.1.3 Fluctuating magnetic fields

The propagator responsible for DDIF relies on $B_{d,z}$ and so, the simulation must be able to capture the fields exposed to the diffusing nuclei as a function of time. Within the framework, this operates via a Monte Carlo approach where a molecule is assumed to be continuously diffusing through the porous network constrained by the solid intrusions. The particle's position can then be extracted following each time step, t_s, which is chosen specifically to ensure that within this interval, diffusion is unrestricted. Should t_s be sufficiently large, the relationship between distance and time breaks down and $\langle \Delta r \rangle = \sqrt{2\, n\, D_0\, t}$ is no longer valid, adding extra complexity to the system. By satisfying this conditional, the distance travelled can be statistically derived to a good approximation. The particle must then diffuse for a sufficient period of time, by taking N_s total steps, such that the total time is far greater than t_s.

The Monte Carlo simulation was executed via the following procedure:

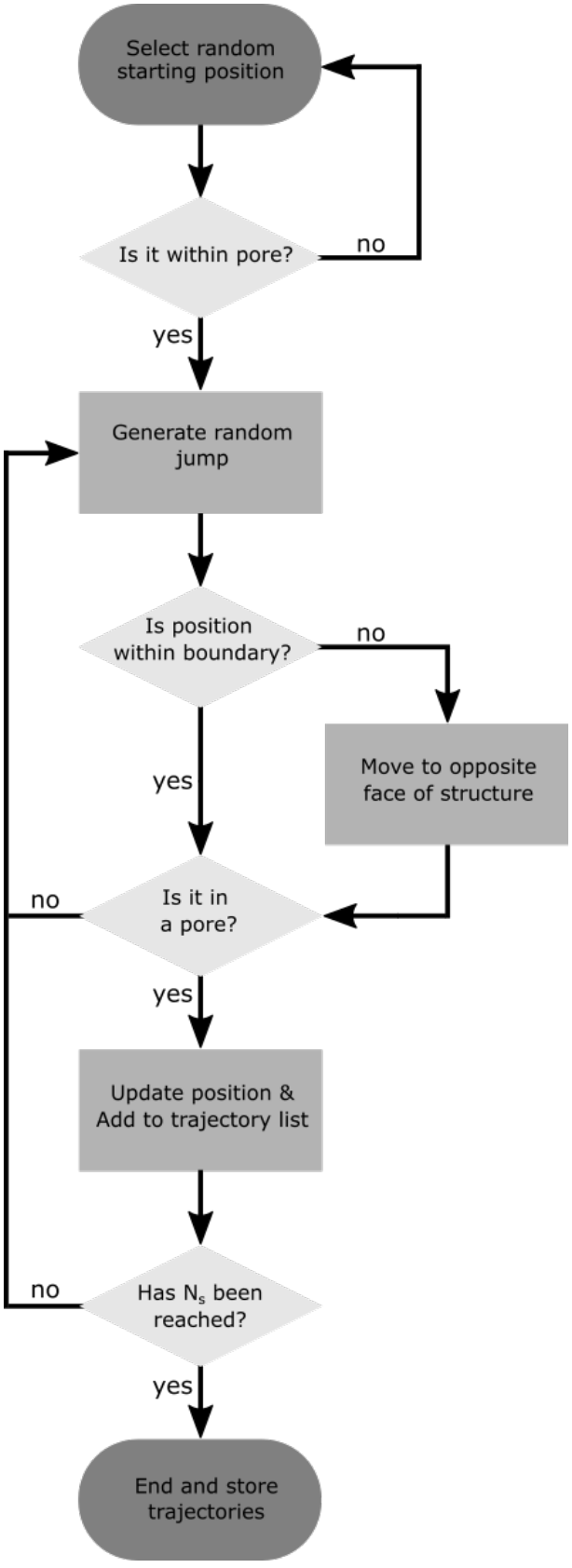

Figure 3.9: Flow diagram of the random walk process within a porous media.

This process is more thoroughly outlined in the following steps:

1. An initial particle position is selected, $\boldsymbol{v_0} = \{x_0, y_0, z_0\}$, from $\boldsymbol{S}(\boldsymbol{v})$ such that $\boldsymbol{S}(\boldsymbol{v_0})$ = 0 and thus the particle is within a pore. If the initial position lies within a bead a new point is randomly generated until the above clause is satisfied. After which, the step counter, x, is set to one and the position is stored within a trajectory array,

2. A vector of three random numbers is produced, $\{\delta x_j, \delta y_j, \delta z_j\}$, each generated from a Gaussian distribution with a mean of zero and a standard deviation relating to the mean square displacement. This is added to the previous particle's position to determine its new position, $\boldsymbol{v}_n = \{x_{j-1} + \delta x_j \ , \ y_{j-1} + \delta y_j \ , \ z_{j-1} + \delta z_j\}$,

3. The position of $\boldsymbol{v}_n$ is verified to ensure it resides within pore volume. If this is satisfied, the point is added to the trajectory array, $\boldsymbol{p} = \{p_0, p_1, ..., p_j\}$ and the counter increments by one. If the particle now resides within a bead, the counter remains unchanged and a new vector is generated,

4. The function iterates over steps two and three until the counter reaches N_s when the loop is broken and the trajectory array is saved.

The simulation operates with periodic boundary conditions assuming the structure-function represents a unit cell within the whole bead sample. As such, should the particle's step take it beyond the boundary of $\boldsymbol{S}(\boldsymbol{v})$, it is positioned on the opposite face of the unit cell having moved inwards the remaining distance of the step. The loop then continues from step three. The disadvantage is the large field difference that may exist between the two steps, not indicative of the particle's actual movement. To limit this, the initial position is selected from the centre most 150x150x150 pixels within the array to prevent the particle from experiencing the unit cell boundary.

To accurately represent the dynamics of a vast number of spins, the function could be performed from many initial positions, simulating the walks of a large number of spins. Each walk must then be sufficiently long that it spans a typical experimental time: for liquid-state NMR, that being up to the order of hundreds of milliseconds. In such a case, the total walking time for each molecule would be determined as $N_s * t_s$. An alternative and perhaps more convenient approach adopted in this simulation consists of simulating a very long trajectory (hundreds of seconds, for example) but for a single molecule starting in a sole and randomly chosen position. This walk can then be subdivided into many sub-walks over which the propagator can be averaged. The two approaches produce statistically equivalent data sets if a large number of trajectories are calculated in the first case, and a single trajectory, long enough that the molecule explores a significant portion of the available space, is calculated in the second case. Most notably, the one walk method produces far more individual works due to the

number of times the trajectory list can be subdivided. Thus increasing the number of walks to average over, therfore improving the accuracy.

Thus far, the simulation has been performed in the absence of units or length scales meaning a random walk within this domain would produce an unquantified, distance-independent walk irrespective of the laws of Brownian motion. To quantify this movement, each step must be related to the μ-CT resolution, l, and mean square displacement such that an arbitrary step on the grid carries a physical length scale. To do so, the Gaussian distribution from which the step vector is selected must be scaled to the system at hand. By dividing the mean square displacement by the resolution, each movement within the dimensionless binarised structure can be scaled up to represent a physical movement within three-dimensional space:

$$v = \frac{\sqrt{2\,D\,t_s}}{l} \tag{3.46}$$

Using the demagnetisation field, $\boldsymbol{G}(\boldsymbol{v})$, the elements of the trajectory array can be superimposed onto the field map. The result is an array containing the value of the demagnetising field experienced by the diffusing spins as a function of time, $\boldsymbol{b}_{d,z}(t)$:

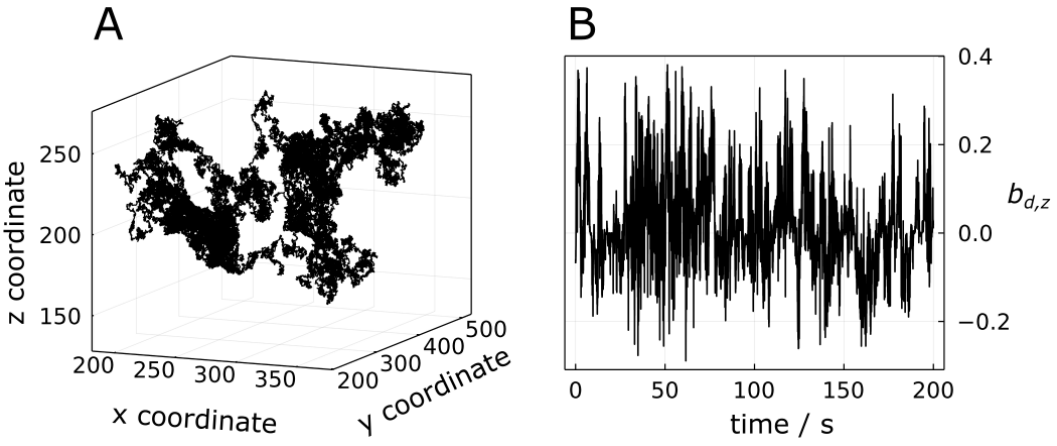

FIGURE 3.10: Typical result of A) the random walk experienced by the particle diffusing within PEM and B) the demagnetisation field it experiences as a function of time. Simulation parameters are given below in Table 3.4.

Note that in Figure 3.10 A, the beads have been removed from the graphic for visual ease but one can see, from the plot, precisely where the pores are.

3.5.1.4 Predicting relaxation

Before the fluctuating field function can be integrated into the propagator equation given in eq. (3.37), it must be adapted to its dimensionless form as written as:

$$P_{11} = \langle e^{-i\,\gamma\,\Delta\chi\,B_0 \int_0^\tau (b_{d,z}(v(t)) - b_{d,z}(v(t+\tau))\,dt} \rangle \tag{3.47}$$

The equation above requires the averaging of many fluctuating field functions, each of a specific length, τ, in order to calculate the ensemble average. To obtain this, $\boldsymbol{b}_{d,z}(t)$ can be subdivided into smaller overlapping trajectories whose lengths correspond to that of the echo time. The simulation takes the first one through x points of $\boldsymbol{b}_{d,z}(t)$ where the product of x and t_s equates to the echo time, τ. It then computes one element of the propagator in eq. (3.47) and stores it, p_{11}. Following this, the simulation repeats the process for elements 2:x+1 and continues until the last instance of a complete echo time remains within the array. It then averages over all of the calculated propagator results. The whole process is nested within an outer loop which iterates over the list of given echo times to capture the extent of signal attenuation as diffusion time increases.

3.5.1.5 Calibration of the simulation

Within the simulation, the diffusing molecule is viewed at discrete time points such that the fields it experiences can be written as a function of time. Therefore, the simulation must be considerate of the selected step length to survey the structure of the porous media whilst maintaining computational efficiency. In order to capture the convoluted nature of the demagnetisation field a step time length of 20 μs was used. Therefore, given the system of interest and a resolution in the order of micro-meters, one step will be the equivalent of ~0.05 pixels. Within such limits, each step can be determined to be unrestricted, maintaining the relation between the Gaussian distribution and the diffusion coefficient. Additionally, the step is not too short that the overall length required is unobtainable. Thus, the diffusing molecule may experience the true breadth of the intricate demagnetisation field within a manageable number of steps.

The μ-CT data used is a 512x512x512 pixel grid as this gives the largest representation of the data taken from the μ-CT scans. However, a TMS molecule positioned at the centre of an empty tube containing only MeOD would take ~10 minutes to reach the walls of the container. As such, the simulation must be calibrated to ensure sufficient steps and step lengths are performed. The walk must be sufficiently long that the molecular path represents a statistically replicable region of the field map where it must experience all instances of the possible field values. Alternatively, the walk must not be long enough that it infringes on incompatible running times. To determine a correct length, a random walk was performed where the number of steps was 50 million and the step length was set to 20μs. The walk was then subdivided into five walks of 10 million steps, each starting with either one or a 10 millionth point. From each of these walks, the first one million and five million steps were also taken producing 16 walks in total including the original 50 million step walk. The propagator for all the walks and the average and standard deviation within each set were calculated:

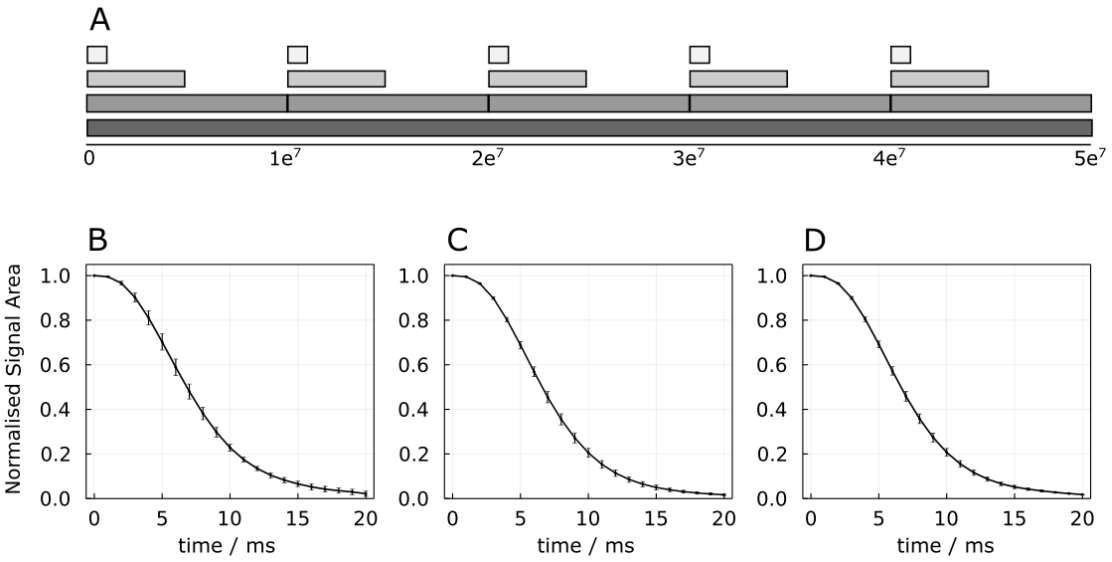

FIGURE 3.11: The averaged propagator calculation and resulting standard deviations for five walks of equal length performed within PES at 9.4 T using a step size of 20 μs showing A) a schematic of how the walks were selected for B) walks of 1×10^6 steps, C) walks of 5×10^6 steps, and D) walks of 1×10^7 steps.

As such, it was determined that a walk of 10 million steps was sufficient to sample a statistically large enough area of the structure in the case of a 20 μs step length. For a simulation run using the below parameters, the computation time was ~three minutes:

TABLE 3.4: Simulation parameters

Parameter	Symbol	Value
CT image resolution	l	9.31 μm [a] 5.56 μm [b]
Diffusion coefficient TMS in MeOD	D_0	2.4×10^{-9} m^2 s^{-1}
Susceptibility difference	$\Delta\chi$	2.71 ppm [c] -0.89 ppm [d]
Number of steps in the walk	N_s	1×10^7
Step duration	t_s	20 μs
Total walk duration	$T_{tot} = N_s * t_s$	200 s
Average step distance	$d_s = \sqrt{2Dt_s}$	0.253 μm
Average total distance	$D_s = \sqrt{2DT_s}$	800 μm

[a] Sample PES [b] All other samples
[c] PE samples [d] Glass samples

An examination of the simulation format was carried out to determine if the "one walk" method was quicker than the "many walks" method. To do so, the simulation was run in three samples, PES, PEM, and PEL, at 7.05 T. The data is summarised below

in Table 3.5. It is worth noting that the one walk method results in a minimum of 9.998×10^6 paths being used and averaged where as the results below were for only 1×10^5 paths within the many walks method.

TABLE 3.5: Ratio of computation times for the many walk or single walk methodology

Sample	PES		PEM		PEL	
Method	one	many	one	many	one	many
Normalised Computation time	1	5.31	1	5.13	1	5.18

As a result, it was determined that the one-walk method was both computationally and statistically more viable as it offered an increase in both computational speed and walks to average over. The simulation can therefore be summarised as follows:

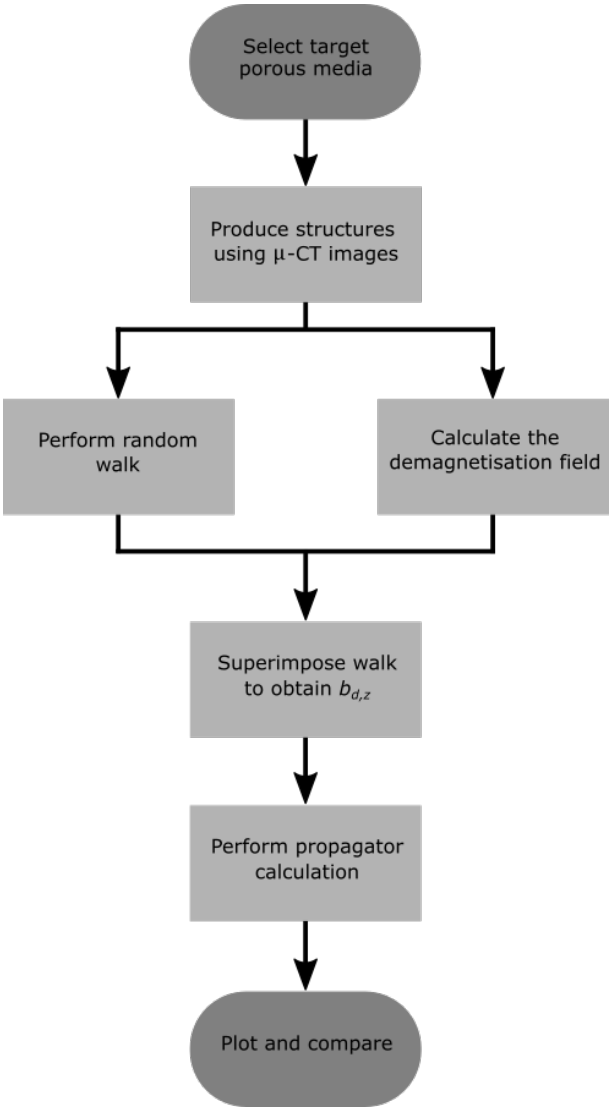

FIGURE 3.12: Flow diagram of the simulation framework.

As such, the "one walk" simulation method was performed for all six bead containing samples given in Table 3.2, using the parameters given above in Table 3.4. The simulated propagator calculation and its corresponding experimental data set were plotted for each packing system, across the three fields, and are given in full in section 9.4.

3.5.2 Experimental data

For each bead size and the empty tube, a 1D spectrum was collected to show the effect of the demagnetisation field on T_2, and therefore line width. The spectra for each bead system, at 16.4 T, is given in section 9.4. The drastic changes can be seen in Figure 3.13:

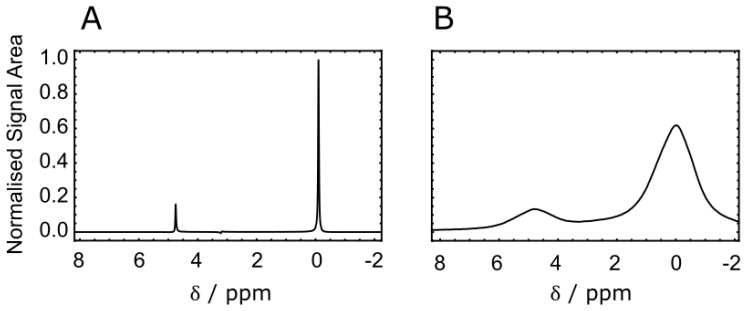

FIGURE 3.13: 1D NMR spectra of A) BLK B) PES taken at 16.4 T. The TMS peak is centred at 0 ppm, the peak at 4.5 ppm corresponds to residual protons in the solution due to incomplete deuterisation of the solvent.

3.5.2.1 Longitudinal magnetisation

The T_1 relaxation decay constant was measured for all samples, at the three magnetic fields using a saturation recovery pulse sequence. The relaxation variable delay time ranged from 0.1 ms to 32 s. The results are given below in Table 3.6:

TABLE 3.6: T_1 relaxation decay constants for all samples

sample name	T_1 / s		
	7.05 T	9.4 T	16.4 T
BLK	5.0 ± 0.2	5.4 ± 0.1	5.7 ± 0.1
PES	4.7 ± 0.1	5.2 ± 0.1	5.6 ± 0.1
PEM	4.8 ± 0.1	5.4 ± 0.1	5.7 ± 0.1
PEL	4.7 ± 0.1	5.3 ± 0.1	5.6 ± 0.1
GS	4.8 ± 0.1	5.3 ± 0.1	5.5 ± 0.1
GM	5.0 ± 0.2	5.3 ± 0.1	5.8 ± 0.1
GL	5.0 ± 0.1	5.3 ± 0.1	5.8 ± 0.1

All errors in the calculations arise from the fitting process performed within the Mathematica notebook. It can be noted that the demagnetisation effect is purely a contribution to transverse magnetisation decay where the longitudinal magnetisation is unaffected by DDIF.

3.5.2.2 Transverse magnetisation

The T_2 relaxation decay constant was measured at the three magnetic fields in the PEM sample. This was done using a Carr-Purcell-Meiboom-Gill pulse sequence for variable echo times. The results are given below in Table 3.7:

Table 3.7: T_2 relaxation decay constants for sample PEM using different echo times

τ / ms	T_2 / s		
	7.05 T	9.4 T	16.45 T
0.5	1.93 ± 0.02	1.84 ± 0.02	1.18 ± 0.02
1	1.30 ± 0.03	1.29 ± 0.03	0.61 ± 0.02
2	0.64 ± 0.03	0.60 ± 0.01	0.25 ± 0.01
4	0.29 ± 0.02	0.23 ± 0.01	0.09 ± 0.01
8	0.13 ± 0.01	0.09 ± 0.01	0.05 ± 0.01
16	0.10 ± 0.01	0.06 ± 0.01	0.04 ± 0.01

It can be seen that as the delay time gets larger, the relaxation decay time gets smaller as the spins have more time to diffuse from their original positions and there is a loss of coherence not refocused by the echo. The single echo pulse sequence was therefore utilised within the region of 0 to 20 ms to capture the signal attenuation as a result of diffusion through the demagnetisation field. It can also be noted that there is a clear dependence on the external field, as predicted by the propagator in eq. (3.32).

3.5.3 Discussion

At present, the simulation relies on several assumptions, the validity of which will be addressed here. Firstly, it is assumed that the μ-CT scans taken within the 10mm tubes represent the structures found within the 5mm tubes, used to collect the NMR data. Provided that both systems contain randomly packed beads, and the shaking procedure maximised the packing density, the samples can be considered equivalent. The systems where discrepancies may intrude are PEL and GL, due to wall effects. For beads packed into a container, the beads in contact with the walls see a higher ordering and produce a structure with greater porosity.[146,147] Within such a case, the simulation

would overestimate the contribution of DDIF to signal attenuation as a more inhomogeneous demagnetisation field would be calculated. Due to the field dependence, it is expected that this effect will be most significant at larger fields. With all other samples, it may be assumed that the μ-CT images are taken in a region irrespective of wall effects. However, since the walk is initiated within the centremost region of $\boldsymbol{S}(\boldsymbol{v})$, the discrepancy between the simulation and experiments is expected to be minimal.

Secondly, the propagator only calculates the contribution to relaxation from DDIF. As such, it is assumed that there is no surface relaxation, or iDD, present which does not hold true for systems where the susceptibility-induced mechanism is not the only prevalent form of relaxation. In cases where there are paramagnetic centres within the solid matrix, such as magnetic metal atoms, paramagnetic relaxation enhancement (PRE) may be contributing significantly and the simulation will not reflect the value of T_2 experimentally calculated within the sample. For samples containing little to no paramagnetic centres, surface relaxation will account for some discrepancy between the simulated and experimental data but to a much lesser degree.

3.5.3.1 Bead size

The effect of the pore size was evaluated by calculating the propagator within three systems, each containing different bead sizes. For this case, the bead material and the field remained constant. An example of this is shown below in Figure 3.14:

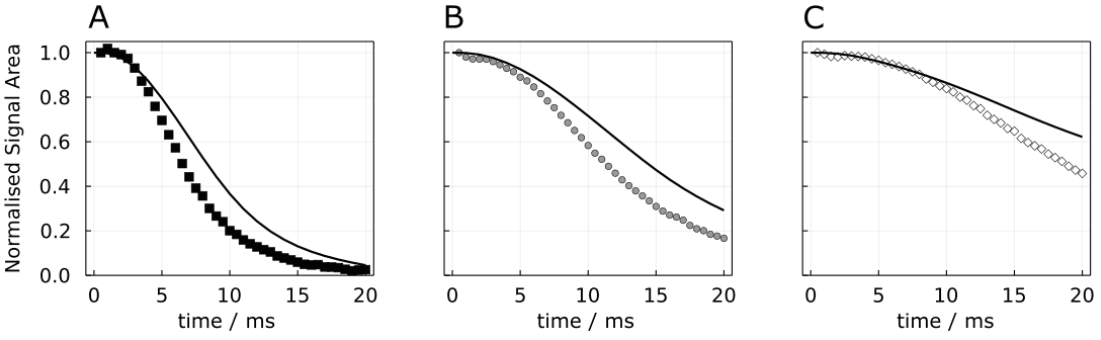

Figure 3.14: Simulated propagator calculation (solid line) and corresponding experimental data (symbols) at 7.05 T for A) PES, B) PEM, and C) PEL. Simulation parameters are collected in Table 3.4.

Within Figure 3.14, the calculation of the propagator and the experimental data show good consistency with a small difference existing most likely due to other relaxation mechanisms, such as surface relaxation, not included in the simulation. A comparison of the bead sizes shows a negative trend between the average suspected pore size and the rate of relaxation, evident in both the propagator curves and the experimental data. In systems with larger beads, such as PEL, the pores will be comparatively larger, on average, than those found in PES. Since the magnetic field is locally distorted around

the solid-liquid boundaries, it can be expected that structures with a larger surface area to volume ratio will show more inhomogeneity within their demagnetisation field. Owing to the distance dependence of the field produced by a single dipole, the distortions at the solid-liquid interface will also dissipate upon approaching the centre of a pore. As such, the larger pores within PEL will introduce regions at the centre of the pore volume where the demagnetisation field is somewhat homogeneous. As a result, a molecule diffusing through this region will experience less fluctuating magnetic fields and therefore DDIF will not contribute as much to relaxation. Additionally, as the pore sizes increase, the probability of inter-pore exchange is decreased and molecules tend to stay within the pore they originated in. As such, the range of fluctuating fields they experience is restricted, further reducing their rate of relaxation.

At the limit of small pores, the field at the centre of the void volume will still be distorted and there will exist no region of relative homogeneity. This can be seen in Figure 3.14 A where molecules diffusing within the small beads experience far greater relaxation as a result of DDIF. Furthermore, the reduced pore size means the molecular path is more likely to experience intra-pore and inter-pore movement, the latter occurring through the interconnecting channels. Channels which display regions of very low homogeneity due to their close proximity to the solid intrusions from almost all directions. Both forms of movement account for the molecule experiencing a far greater frequency of fluctuating fields when compared to molecules diffusing within PEL. The same trend is evident within both the glass and plastic samples, for all fields.

3.5.3.2 Field

The effect of the field strength was evaluated by maintaining both the bead size and composition and changing only the field strength across the three external fields evaluated. The comparison within PES can be seen below in Figure 3.15:

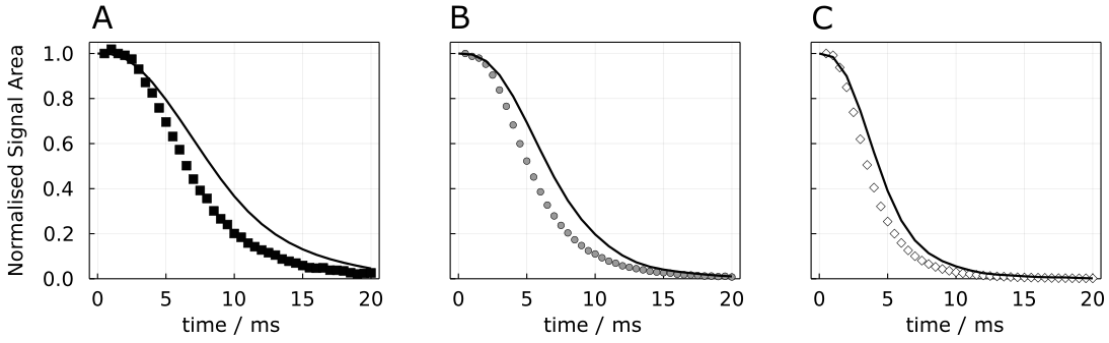

Figure 3.15: Simulated propagator calculation (solid line) and corresponding experimental data (symbols) in PES at A) 7.05 T, B) 9.4 T, and C) 16.4 T. Simulation parameters are collected in Table 3.4.

Again, there is good consistency between the simulated curves and experimental results, both showing a negative trend between the field strength and the longevity of transverse magnetisation. This can be accounted for by the direct relationship between the external field strength and the propagator given in eq. (3.32). This field dependence is traced back, in turn, to the calculation of the demagnetisation field. As such, the local distortions in the magnetic field are increased when a larger external field is present. Therefore, spins diffusing at bead surfaces will be relaxed quicker at higher field strengths where the fields experienced fluctuate more rapidly. This is further enhanced should the spins diffuse from the surface to the pore centre, and visa versa.

The simulated and experimental plots show the greatest consistency at the shortest echo times. At this limit, it can be assumed that many of the spins experience unrestricted diffusion but are still subject to fluctuations in the local field. Thus, DDIF is the principle form of relaxation causing drastic decreases in transverse magnetisation. However, at larger echo times, other relaxation mechanisms may contribute to relaxation causing the simulated curve to underestimate the signal attenuation at longer diffusion times. For PES, it can be seen that the simulated and experimental data show the greatest consistency at larger fields. This may be attributed to DDIFs contribution to relaxation being far greater at 16.4 T than at 7.05 T. As a result, any other relaxation mechanisms present will be less notable, even at longer echo times.

3.5.3.3 Composition

In addition to the propagator being proportional to the external field, it is also related to the magnetic susceptibility difference. To explore this, the propagator was calculated for two systems, each with different susceptibilities, and compared across the three possible bead sizes. This is shown below in Figure 3.16:

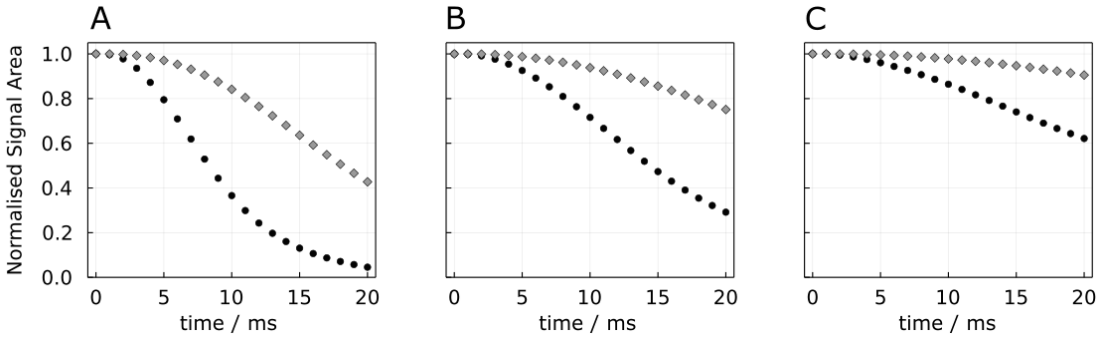

Figure 3.16: Simulated propagator calculation for PE (black circles) and glass (grey diamonds) at 7.05 T for A) small bead sizes (PES and GS), B) medium bead sizes (PEM and GM), and C) large bead sizes (PEL and GL). Simulation parameters are collected in Table 3.4.

As seen in Table 3.3, the susceptibility difference between glass and MeOD is far less than that of polyethylene and MeOD. As a consequence of this, the propagator for glass decays far slower than that of PE. It is worth noting that the propagator is proportional only to the susceptibility difference within the system. Thus, the more diamagnetic glass beads do not heighten the internal field gradients when compared to polyethylene, as glass has a magnetic susceptibility more similar to that of MeOD.

The magnetic susceptibility of the glass is only an estimate taken from calculations performed by Wapler *et al* on another soda-lima-silica glass.[123] To more accurately determine the susceptibility, samples of the glass beads, of all sizes, were taken to the SQUID-VSM Magnetometer (Quantum design) at the Diamond light source facility. Unfortunately, no quantitative results were obtained as the samples could not be mounted correctly. The facility was set up to mount samples either by glueing them to a glass rod or filling a plastic capsule. Since the SQUID is predominately used to measure the magnetic susceptibility of paramagnetic materials, the presence of the glass rod and the glue would not hinder experimental readings. However, when the target substance was itself weakly diamagnetic, the presence of the mounting equipment contributed significantly to the measurements. As such, the value given by Walper *et al.* was used as the most suitable substitute to physically obtaining these data.

3.5.3.4 Surface relaxation

Where the PE systems show a good agreement between the simulated and experimental data, the glass simulations do not correlate to the experimental data. For example, taking the case of GS across the three fields, shown below in Figure 3.17:

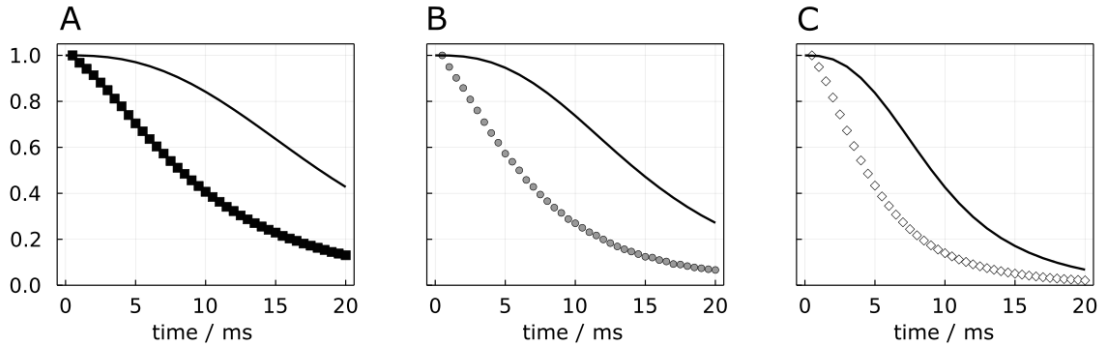

FIGURE 3.17: Simulated propagator calculation (solid line) and corresponding experimental data (symbols) for GS at A) 7.05 T, B) 9.4 T, and C) 16.4 T. Simulation parameters given in Table 3.4.

It is clear from Figure 3.17 that the experimental decay does not match the simulated curves. The reason being attributed to the presence of paramagnetic centres within the glass beads. The chemical composition of which contains, by weight, 0.08% Fe_2O_3

with iron being an extremely paramagnetic ion.[123] It is expected that the paramagnetic centres will be visible to the diffusing spins within a given affected volume, introducing "total signal loss" zones. Should the spins encounter this volume, they will be relaxed at a much greater rate as seen in all three plots of Figure 3.17.

It can also be seen in each experimental case that signal intensity drops off significantly at very low echo times, not indicative of the expected exponential decay. On the contrary, the experimental data plateaus at longer echo times, which is expected from the exponential decay. This may be attributed to the rapid loss of signal for all spins within close proximity to the bead surfaces. Any surviving magnetisation is likely persisting within nuclei at the centremost volume of the pores, or in nuclei travelling away from the surface, where the spins can continue to diffuse as in the PE samples.

3.5.3.5 Low field prediction

In addition to rationalising experimental results, the simulation can be used to predict the contribution to relaxation from DDIF within given conditions, such as other field strengths. The propagator calculation was performed within PES at a series of low fields under 1 T, shown below in Figure 3.18. When compared to the plots in Figure 3.15, it should be highlighted that the low field speculated curves are plotted up to 60 ms; however, none of the three curves decay fully. As can be seen, T_2 longevity is predicted to be far greater when the field is ≤ 1 T.

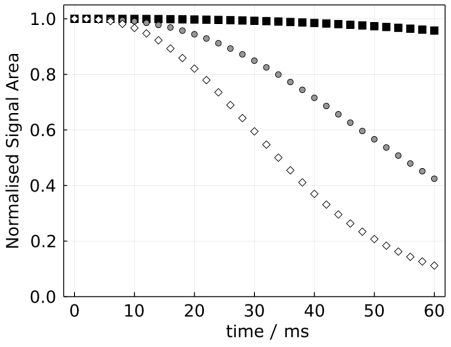

Figure 3.18: Simulated propagator calculation for PES at 1 T (white diamonds), 0.5 T (grey circles), and 0.1 T (black squares). Simulation parameters are collected in Table 3.4.

3.6 Conclusion

The theory of nuclear spins diffusing through an inhomogeneous field, during a single echo pulse, has been derived. The theory predicts a dependency on external field strength and magnetic susceptibility difference for the magnetisation decay. This is reflected in the experimental data collected within systems of packed micro-beads of varying sizes and compositions.

In addition, the contribution of signal attenuation caused by DDIF was evaluated via a simulation framework capable of calculating the propagator for the single echo pulse sequence. The simulation utilised an accurate digital reconstruction of the bead packings to perform Monte Carlo simulations and magnetic field calculations. The simulated data matched the PE experimental data with a good fit owing to DDIF being the dominant form of relaxation in the plastic systems. For glass, the simulation failed to capture the extent of relaxation within the system as there is enhanced surface relaxation due to paramagnetic species within the glass. However, the simulation has highlighted a clear dependence of T_2 longevity on the pore size, magnetic susceptibility difference, and external field. As such, it is now a useful tool for determining the conditions within which d-NMR may be accessible in given porous media.

With the foundations of the simulation framework now complete, the calculation can now be altered to encompass any experimental variable or system of arbitrary complexity. As previously shown, the external field can be changed but the magnetic susceptibility difference could also be altered to compare relaxation within different materials or solvents. Moreover, the framework is capable of performing propagator calculations should another porous media of any complexity be imported in.

Chapter 4

Expanding the simulation to the realm of tortuosity

4.1 Synopsis

This chapter is an overview of the work carried out in order to fulfil objective two.

O_2 - Enhance the framework by incorporating tortuosity simulations, verified through parallel NMR diffusion experiments run with the aid of nuclear singlet states.

The purpose of this chapter is to introduce progressions made within the simulation framework, mainly the extension of the simulation to include tortuosity predictions. Using the previously developed random walk method, the simulation extends to measuring diffusion within porous structures, allowing the measurement of tortuosity and other related structure-dependent properties. The simulation applies similar principles to the experimental detection methods within d-NMR including diagonalisation of the diffusion matrix and analysis of both eigenvalues and eigenvectors. The methodology is tested within a range of exemplar structures. Finally, the results are compared to previously collected experimental data within similar systems, to verify the findings.

4.2 Introduction

Tortuosity is an imperative parameter for a number of material science applications including drug delivery and oil recovery.[148,149] In both instances, the ideal path is hindered by a matrix of interconnected solid media, obscuring a direct and quicker route of travel. Although a diffusion pathway may be possible, the convoluted nature of the host material directly influences the ease and efficiency of the task at hand, be it delivering a drug or extracting oil from a reservoir rock. In the second instance, the characteristics of the specific reservoir rock must be determined in order to apply the most suitable extraction technique.[149] Such characteristics include tortuosity and porosity and adequate evaluation of both parameters can alter the efficiency and success of oil extraction.[95] In recent studies, it was determined that tortuosity cannot simply be measured in a purely geometric fashion and that gas adsorption and other external factors may play a vital role in determining the movement of gases and liquids within a porous media.[150] He *et al.* opted to study diffusion through kerogen shales using computational means as it allowed the accurate calculation of gas adsorption effects which would otherwise skew experimental tortuosity calculations.

Although d-NMR has been used extensively to calculate tortuosity within porous media, it comes with its own tribulations including signal loss, distortions, and blurring. The causes of these artefacts can be attributed to currents, inhomogeneities, and magnetic susceptibility mismatches.[151] The rectification of these imperfections due to susceptibility clashes requires the systematic use of extensive correction methods.[151] One drawback to this mitigation method is the possibility of introducing currents caused by sample heating when exposing the sample to continuous or powerful pulses.[58] However, the computational equivalent of d-NMR is not subject to the same physical constraints or imperfections as the experimental version since the magnetic susceptibility factor can be omitted. The simulation cares only for the boundary between pore and solid, thus the space in which diffusion is possible and the space where it is not. Additionally, there is no possibility of currents within the simulation as the process of particle movement is completely random and not affected by temperature gradients or eddys. Both of which can have detrimental impacts on physical experiments by introducing biased movement into the system. As a result of this, many studies into the tortuosity of porous media are conducted through computational means.

One vital application of tortuosity is testing the efficiency of convection enhanced delivery (CED), a method of drug delivery that relies on the production of a pressure gradient at the catheter tip to enhance delivery straight to tumours.[152] This methodology prevails over alternative methods as it bypasses previous restrictions such as the blood-brain barrier (BBB), which is impervious to pharmaceutical molecules with a molecular weight > 400 Da.[153] Where this poses a complication is in the definition of a small drug, which is defined as a molecule of < 1500 Da, meaning the majority of

"small" drugs are still unable to cross the BBB.[154] Where CED can bypass the BBB, the effectiveness of the delivery method is then entirely dependent on the tortuosity of the receiving material.[155] The major contributor to tortuosity is within the extracellular space (ECS) which, although its width is sub-micrometre, the matrix of inter-connected channels can account for 1/5 of total brain matter volume.[155] Simulating tortuosity has become of principal interest in order to determine the structural properties of the ECS, centred around digital models of brain matter and random walk methods.

In the case of conductivity, σ, where a liquid of conductivity σ_w is saturating non-conducting grains, the tortuosity plays a principle role:[52]

$$\sigma = \sigma_w \frac{v}{\alpha} \tag{4.1}$$

Conductivity is an imperative parameter for many materials from both angles be it high conductivity for electrodes or low conductivity for insulating foams.[156] The efficiency of porous electrodes relies heavily on internal conductivity pathways, making tortuosity a principal parameter in battery studies.[157] Due to the need to study electrode micro-structures, Nguyen *et al.* opted for a computational approach, building upon open-source frameworks to measure flux within porous electrodes.

These are only two instances where tortuosity is the principal area of investigation but highlight the necessity of studying this parameter within porous media. They also demonstrate the requirement for computational studies within modern science. Where physical techniques lack the delicacy to deal with fragile samples, computational methods offer a "hands-free" method for investigating complex and sensitive samples. They offer the potential to study systems either entirely through computation or to determine key influences to a system such that they may be mitigated and improve the overall efficiency of the practical experiment.

4.2.1 Simulation methods

The diffusion of molecules through a volume is often modelled using the Monte Carlo method (MCM): a class of algorithms centred around performing sequential random calculations to either optimize, integrate, or determine probabilities.[158] Monte Carlo simulations are used extensively within computational chemistry, in a range of different fields from devising polymer structures and predicting the backscattering of electrons, to simulating crystal growth.[159–161] As we have seen, they can also be used to model diffusion in porous media for the purpose of calculating relaxation due to DDIF.

Its main application is within diffusion modelling as the movement of molecules in liquids and gases is often attributed to being a random process, such as Brownian motion

discussed above in section 3.2.2. Within MCMs are random walks: a form of MCM that rely on repeated random steps to transform through a mathematical space. In their simplest form, in one dimension, a random walk is a sequential selection of one of two possible outcomes, chosen via a random selection process. That is to say, from a given position, r_0, with the possibility of moving to either r_1 or r_{-1} for each step, what will the destination be after the nth steps? In this case, the final position can be calculated from a Gaussian distribution that depends on the number of steps taken. If we know where it began and how it moves then through probabilistic modelling, we can determine where a particle will be after a given period of time. As with many cases, the larger the sampling pool, the smoother and less erroneous the normal distribution.

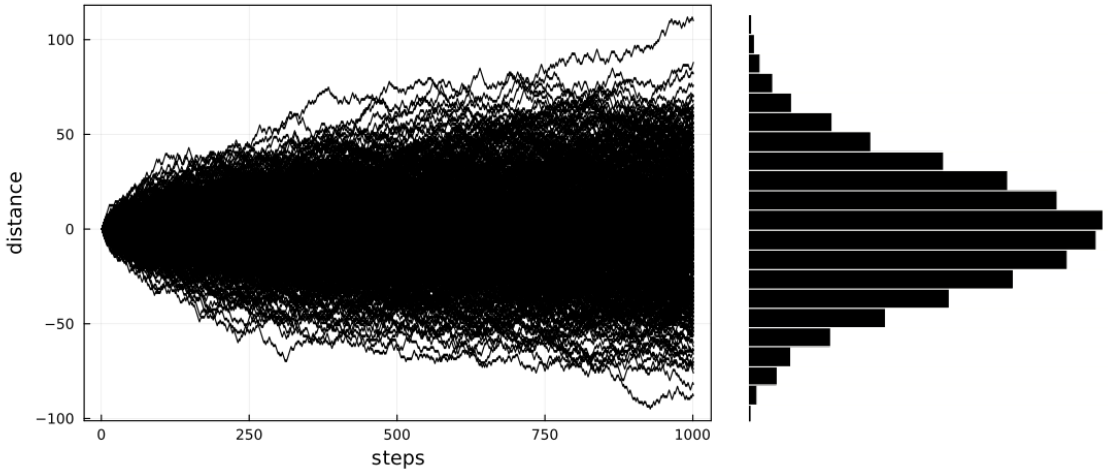

FIGURE 4.1: The routes of particles taken within a simple 1D random walk algorithm where all particles start at 0 and can move either r_1 or r_{-1} each step, including the resulting histogram of final distance travelled away from the origin.

It is because of these probabilistic tendencies that studies frequently incorporate these algorithms into time-dependent studies. As is done in this work, the random walk function relies on observing the position of a diffusing particle at incremental time steps, t, given the probability of where the molecule will have travelled to in t.

These calculations can either be performed in custom-written algorithms in a range of programming languages, or within readily available programs designed specifically for MCMs and random walks.[162] Hrabe *et al.* used MCell[163] to measure diffusion within the ECS via the counting box method. This method involves placing a series of permeable, invisible boxes within the computational model, which change in volume over the experiment. For each iteration, a box volume is selected and all molecules begin at the centre of the box. At various time points, the total number of molecules within the box is recorded and this is averaged over multiple time boxes to determine the restricted diffusion coefficient.[162] However, there are restrictions imposed on the counting box sizes as too large a volume will skew the result since too many molecules

will be reflected back into the counting space. Thus, returning an exceptionally low D_0.

The sophistication of these computational methods has increased, particularly within the biological sciences, to introduce transition probabilities for molecules diffusing through semi-permeable membranes.[164] These computations have the capability to model diffusion between membranes where the diffusion coefficient on each side is different, which is more representative of biological systems such as the ECS and the cell's internal volume.[165] In both cases, the random walk function works off of a time-dependent rather than distance-dependent process as is used above. That is to say, each random step is attributed to a given time interval and the distance travelled is taken from a normal distribution, as demonstrated in Figure 4.1. The specifics of the calculation can be tuned to the experimental parameters by correcting the distribution curve to relate to the diffusion coefficient of the molecule. As such, the average distance travelled within each time increment is related to D_0.

An alternative computational method is molecular dynamics (MD) whereby all external forces imposed on individual atoms are integrated into the simulation to determine how the particle behaves in a given period of time. This method works off of first principles by solving Newton's equations of motion to understand the system's dynamic behaviour. These forces include but are not limited to the particles' position and velocity.[62] The sequential steps in MD involve calculating the forces imposed on each particle, moving each atom according to these forces, advancing the simulation by an incremental period of time, and then repeating the previous steps.[166] MD exhibits many advantages over other computational methods due to the accuracy of how the individual particles behave in time with respect to their surrounding and bonded atoms. It is often used for the computation and refinement of protein structures to determine protein folding and other molecular processes such as ligand bonding.[62]

Although imperative for protein structure simulating, MD can also be used to measure diffusion and other time-dependent processes.[69] However, when comparing the two, it has been noted that the overall complexity of MD limits the extent of molecules that can be modelled in this manner.[167] Where MCMs are probability-driven and readily produce results for large ensembles, the sheer scale of calculations required for billions of MD particles is outside of the scope of average computational power. The computational effort can be reduced by grouping atoms into units to lower the total number of independent items; however, this has been known to overestimate the diffusion coefficient.[168] As such, a random walk is more applicable to the studies within these works.

4.2.2 Long lived states

Systems of only a single spin-1/2 nucleus are not the only object of interest in d-NMR, another well-studied system is that of two coupled spin-1/2 nuclei. In such a case, each spin may either be in the $|\alpha\rangle$ or $|\beta\rangle$ state. The combination of which is four states:[169]

$$\begin{aligned} |\alpha\rangle \otimes |\alpha\rangle &\Longrightarrow |\alpha\alpha\rangle \\ |\alpha\rangle \otimes |\beta\rangle &\Longrightarrow |\alpha\beta\rangle \\ |\beta\rangle \otimes |\alpha\rangle &\Longrightarrow |\beta\alpha\rangle \\ |\beta\rangle \otimes |\beta\rangle &\Longrightarrow |\beta\beta\rangle \end{aligned} \tag{4.2}$$

However, these are only eigenstates of the total Hamiltonian operator within the weak coupling limit. This occurs when the difference between the chemical shift frequency of the two spins is larger than that of the scalar coupling frequency. In contrast, if the two spins, j and k, are strongly coupled, their individual chemical shifts will be near equivalent. Within such a situation, the scalar coupling frequency is greater than the chemical shift difference and the eigenstates become:[169]

$$\begin{aligned} |T_{+1}\rangle &= |\alpha\alpha\rangle \\ |T_0\rangle &= 1/\sqrt{2}(|\alpha\beta\rangle + |\beta\alpha\rangle) \\ |S_0\rangle &= 1/\sqrt{2}(|\alpha\beta\rangle - |\beta\alpha\rangle) \\ |T_{-1}\rangle &= |\beta\beta\rangle \end{aligned} \tag{4.3}$$

When the external field approaches zero, $|S_0\rangle$ becomes an exact eigenstate of the total Hamiltonian. $|S_0\rangle$, named the nuclear singlet spin state (NSS), is an intriguing state that possesses no net angular momentum and is asymmetric with respect to spin-exchange.[170] That is to say, $\hat{P}|S_0\rangle = -|S_0\rangle$ with $\hat{P}$ being the exchange operator. The remaining three states can be grouped into the term "triplet state": these have net angular momentum and are symmetric under spin exchange. The mean population difference between the singlet state and the triplet state is called singlet order and its decay is characterized by the time constant T_s.[171] Containing only two spin-1/2 nuclei, the NSS is the simplest form of long-lived state (LLS), though states of higher orders are obtainable. In order to access the NSS, the molecule must have the following properties:

- Contain an isolated spin-$\frac{1}{2}$ pair of nuclei,
- The nuclei in the spin pair must be magnetically inequivalent,
- The chemical shift difference of the pair must be minimised.

The advantage of singlet order over conventional magnetisation is its immunity to some relaxation mechanisms which dominate longitudinal and transverse relaxation. Most

importantly, the NSS is unaffected by iDD relaxation within the spin pair as the process by which this mechanism induces relaxation is symmetric with respect to spin exchange.[172] As such, it is incapable of inducing transitions from the NSS to the triplet states, preventing the rapid magnetisation decay that occurs within the triple states. Moreover, the symmetry of the NSS also prevents it from relaxation due to components of the chemical shift Hamiltonian, further increasing its longevity. As such, the lifetime of singlet order may persist for upwards of two hours, in specific circumstances[6]

Although singlet order is immune to multiple mechanisms, it is still susceptible to other forms of relaxation such as paramagnetic relaxation enhancement (PRE) and other lesser mechanisms not mentioned here. In addition, it bears its own form of relaxation called singlet-triplet leakage. This is a weak contribution mediated by the slight difference in chemical shifts required to populate the singlet order.[173] The shift difference breaks the symmetry between the states and allows slight mixing between them.[174] Since the triplet states are being rapidly relaxed via iDD, any population transfer to the triplet states will be lost at a rate equal to that of T_1.

Due to the longevity of NSSs, they have been used extensively in the study of large and complex systems where previous experimentation was capped by the comparatively fast relaxation of conventional magnetisation.[59] Since the singlet state has no net magnetisation, long and complex pulse sequences are required to probe the state.

4.2.3 Singlet assisted diffusion

Unlike conventional d-NMR experiments, there are additional steps that must be adhered to in order to perform diffusion measurements on singlet state-bearing molecules. The basis of this lies in the measurement of T_s, the relaxation constant attributed to the decay of singlet order. The probing of singlet states was first developed by Carravetta and Levitt (2004) who discovered the singlet states' invariance to the main relaxation mechanism present for longitudinal magnetisation.[172] Advancements in accessing singlet order were explored by Pileio *et al.* who using a range of techniques and devised the magnetisation to singlet (M2S) sequence which allows access into the world of NSSs in either high or low field.[92] The group recognised the singlet states' potential in a range of NMR applications such as enhancing hyperpolarization and investigating the relations between distant molecules.[172]

The first major display of the power of singlet states came when Pileio *et al.* found a singlet hosting molecule with a T_s of 26 minutes, demonstrating the possibility of preserving information for orders of magnitude longer than in T_1.[175] This enhancement

has steadily increased such that 2020 saw a nuclear singlet state, present in a ^{13}C spin-$^1/_2$ pair, persist for upwards of 1.5 hours.[6] For these high field experiments, T_s is typically measured using the magnetisation to singlet (M2S) pulse sequence which is applicable for near equivalent spins in high field. The sequence uses synchronised echo trains to convert between the singlet and triplet states mentioned above and can be adapted for singlet assisted diffusion NMR (SAD-NMR), as outlined below:

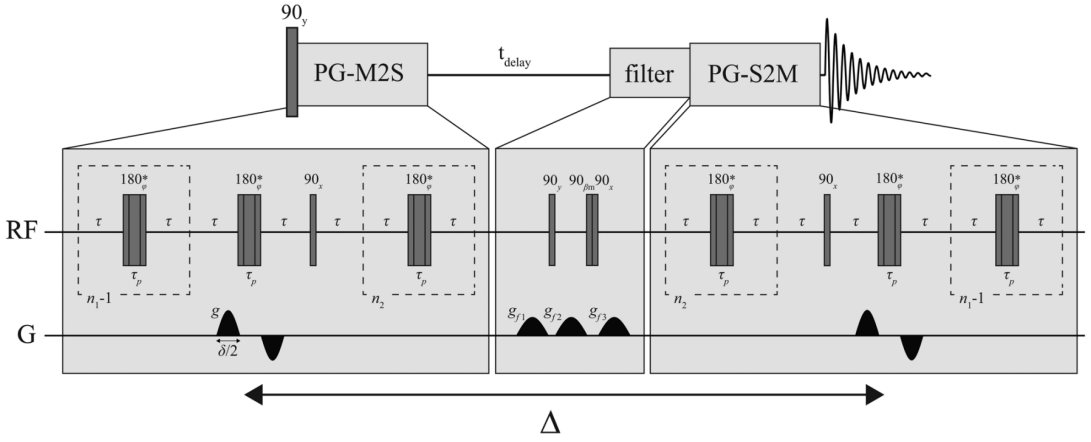

FIGURE 4.2: SAD-NMR pulse sequence for performing d-NMR in singlet states, where asterisks represent a composite pulse.[58] Where "RF" indicates the normal channel and "G" indicates the gradient channel.

Where n_1 and τ are determined by the scalar coupling, J, and chemical shift difference, $\Delta\nu$, between the two nuclei, $n_2 = {}^{n_1}/_2$, $n_1 = {}^{\pi J}/_{2\Delta\nu}$, and $\tau_e = \tau_p + 2\tau = {}^1/_2\sqrt{J^2 + \Delta\nu^2}$.[59] The sequence begins by first converting longitudinal magnetisation into transverse magnetisation with an initial 90° pulse. The pulsed-gradient magnetisation to singlet (M2S) portion of the sequence contains chains of synchronised echoes that introduce the long-lived state by creating coherences between the singlet state and the remaining triplet states.[176] It contains a gradient to spatially encode the nuclear spins and generates a population difference between $|S_0\rangle$ and $|T_0\rangle$, thus equating to singlet order.[176]

During the evolution period, the singlet order will steadily decay after which it is converted to magnetisation via the singlet to magnetisation (S2M) portion of the sequence. Just prior, there is a filter to ensure only singlet order remains and contributes to the signal readout.[58] The S2M component is identical to M2S but in reverse chronological order. This allows the previously "invisible" state to be converted to preserved magnetisation making it detectable via conventional NMR techniques. The filter, which had previously removed all residual longitudinal magnetisation before that which is stored in singlet is converted to observable signal, ensures the observable signal comes only from the singlet state. One disadvantage of the pulse sequence is the theoretical conversion rate from magnetisation to singlet being limited to $^2/_3$.[177] The removal of the gradients produces the standard M2S sequence: used to measure the lifetime of the singlet state, in the absence of diffusion measurements.

However, there are other methods for studying NSSs such as spin locking, and field cycling methods. Upon initial investigation, it was revealed that the spin-locking method requires the constant irradiation of spins, via a radio frequency pulse, to prevent mixing between the singlet and triplet states. The disadvantage being the necessity for the spins to maintain at high field for the duration of the spin-locking.[178] The constant irradiation could also lead to sample heating which poses issues with the accurate measurement of diffusion coefficients. Additionally, the field cycling technique involves the movement of the sample from high to low field, and back again. Although this can be achieved by altering the field around a static sample, is it more easily achieved by moving the sample within the stray field of the magnetic.[169] However, it has been noted that movement of the samples must be achieved on an order that is fast with respect to T_1.[169] As porous media may contain mobile components and diffusion is a major contributor to relaxation, it could be disadvantageous to move the sample with quick motions. As a result, the preferred technique for accessing nuclear singlet states is via the M2S- S2M pulse sequence method.

When considering the study of porous media, there are two limitations to experimental studies. In systems where the pores are sufficiently large, all forms of conventional magnetisation will have depleted before the bulk spins have encountered any form of restriction in the form of porous structures. In such a case, the use of NSSs would be advantageous due to their increased longevity, as has been shown in previous studies involving SAD-NMR.[59] Similarly, sufficiently small pores produce extremely inhomogeneous fields within which transverse magnetisation will decay before encountering any form of restriction. Although singlet states would be more advantageous, the magnetisation may deplete before the M2S pulse sequence has been completed.

Extensive studies have delved into the sustaining of the singlet state,[6,7,179] showing greater increases in longevity at low fields and higher temperatures. However, the use of NSSs in the field of diffusion is currently in progress. Within the M2S pulse sequence, the echo trains contain delays, τ, of up to 30 *ms* meaning the singlet state can only be accessed when magnetisation persists for greater than this time.[59] As such, the introduction of heightened field inhomogeneities, such as in porous media, reduces the transverse magnetisation decay rate such that all magnetisation is lost before the M2S sequence has been completed. As a result, the engineering of the experimental process must be altered in order to encompass the heightened T_2 relaxation restricting the conversion of magnetisation to singlet order.

4.3 Materials and methods

For the experimentally collected data, the samples were produced by packing polyethylene micro-beads into a 10 mm NMR tube and imbibing the beads in a 0.14-0.18 M solution of sodium-2,20 -((1,2,3,4,6-pentakis-(methoxy-d_3)-7-(propan-2-yl-d_7)naphthalene-5,8-diyl)bis(oxy))diacetate-4a,8a-13C_2 in D_2O. Synthesis details of the naphthalene derivative shown below can be found in Tourell *et al.*[59]

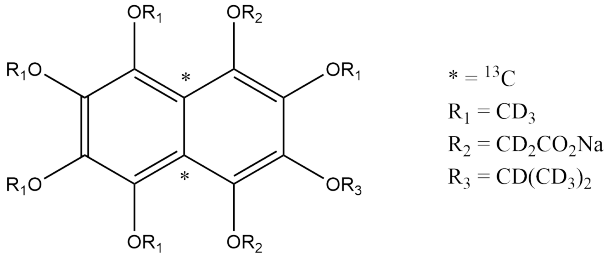

FIGURE 4.3: Molecular structure of sodium-2,20 -((1,2,3,4,6-pentakis-(methoxy-d_3)-7-(propan-2-yl-d_7)naphthalene-5,8-diyl)bis(oxy))diacetate-4a,8a-13C_2.

This molecule was selected due to its large T_s value and ability to prepare the singlet state at high magnetic fields (~7 T). Two systems were made, one with 500-600 μm diameter polyethylene (PE) beads (PS) and another with 1000-1180 μm PE diameter beads (PL), purchased from Cospheric's CMPS products. The samples were produced by Tourell et.al[59] but are no longer available for further investigation. As such, the simulations were run within the analogous samples produced as described in chapter 3. Within these, the samples consisted of identical bead sizes but were packed into 10 mm poly (carbonate) tubes to improve the contrast of the μCT images taken. Collection of the μCT images is described above in section 3.4.3. Although the solution and spy molecule differed within the physical samples, the simulation only requires the diffusion coefficient so the components of the physical sample are irrelevant.

4.3.1 Pulse sequence

The data collected by Tourell *et. al*,[59] whilst conducting experiments to measure diffusion in samples PS and PL, were collected on a 7.05 T Bruker Avance III 300 MHz spectrometer equipped with a 10mm $^1H/^{13}C$ micro-imaging probe. Prior to tortuosity measurements, the unrestricted diffusion coefficient was calculated within the blank samples (prior to the addition of beads), using a standard PGSTE pulse sequence as seen in Figure 2.9. When referring to the PGSTE sequence the delay period (Δ) was 200 ms, the gradient duration (δ) was 2 ms, and the gradient strength (g) was varied. The measurement returned an unrestricted diffusion coefficient of $D_0 = 2.2 \times 10^{-10}$ m^2 s^{-1}.

For the bead-containing samples, the diffusion was measured using the singlet incorporating pulse sequence given above in Figure 4.2. The parameters used in the SAD-NMR were experimentally derived through optimisation techniques and were as follows:

Table 4.1: Tortuosity measurements within bead packings, at 7.05 T

Parameter	τ / ms	τ_p / μs	n_1	n_2
Value	4.5	82	20	10

Theoretically, the echo time must be set to $\tau = 1/(4(J_{12}^2+(J_{13}-J_{23})^2)^{1/2})$ and the number of echoes to $n_1 = \pi/(2\ ArcTan(J_{13}-J_{23}/J_{12}))$ with $n_2 = n_1/2$.[180] However, these were further calibrated by varying the parameters within the M2S pulse sequence through manipulation of the synchronised spin echo. The optimised values were then recorded and used in further experiments of the same singlet molecule.

4.3.2 Initial data

For both the blank and bead-containing samples Tourell *et al.* measured both T_1 and T_s and averaged the results across the different samples. T_1 was measured using the standard saturation recovery pulse sequence outlined in the previous chapter, and T_s was measured using the standard M2S sequence described above.

Table 4.2: T1 and Ts measurements within bead packings, at 7.05 T

Composition	T_1 / s	T_s / s
No beads	3.5 ± 0.2	128 ± 11
Beads	3.9 ± 0.3	123 ± 25

Following this they measured diffusion within the two bead-containing samples where the variable diffusion time, Δ, ranged from 0.2 to 240 seconds with at least 6 independent gradient strengths measured at each time point. The results were linearised as in conventional d-NMR to obtain the diffusion coefficient. Their tortuosity measurements are given below in Table 4.3:

Table 4.3: Tortuosity measurements within bead packings, at 7.05 T

PE 500-600 / μm		PE 1000-1180 / μm	
Δ / s	$D(\Delta)/D_0$	Δ / s	$D(\Delta)/D_0$
0.2	1.0	0.2	1.0
1	0.899	1	0.948
15	0.750	10	0.857
30	0.648	50	0.775
45	0.664	90	0.770
60	0.609	150	0.781
90	0.589	240	0.695
120	0.641		

4.3.3 Computation

All simulations were run on Julia 1.7.1, with a computer running Windows 2012 R2, with a 64-bit operating system, and 3 processors, each with a speed of 2.4 GHz, resulting in a total of 17 cores, 32 base processors, and 512 GB of RAM. Each propagation experiment was run in parallel across 15 processors via a shared array. This reduced the computation time to 18 minutes for a total of 1.1×10^9 successful steps. For each of the diffusion times, the simulation calculated diffusion along the six independent directions (Dxx, Dxy, Dyy, Dxz, Dyz, and Dzz), averaged each, produced the diffusion tensor, and calculated the average diffusion coefficient as $1/3\ \mathrm{Tr}(\boldsymbol{D'})$.

4.4 Results and discussion

4.4.1 Initial data

For the initial data, the immunity of both T_1 and T_s to magnetic susceptibility effects is quite prominent. In previous cases, T_2 was reduced drastically when the system was subject to DDIF. However, for both longitudinal relaxation and singlet states, there is little impact on the overall signal decay. With respect to the tortuosity measurements, the results reflect those of diffusion being limited by solid intrusions. That is to say, where there are bigger beads, and therefore bigger pores, the tortuosity is lessened. As would be expected, the average diffusing molecule has a statistically larger distance to cover before encountering a boundary when in PL (with >1 mm diameter beads) than in the more closely knit PS sample.

4.4.2 Simulation

The simulation of molecular movement within the tortuosity framework follows a very similar process to that of the propagator calculation with two main differences, as highlighted below. With the random walk function remaining almost constant, the simulation can be divided into two further parts producing the following workflow:

- Simulation of the random walk to emulate diffusion,
- Calculation of the diffusion tensor,
- Calculation of the tortuosity within the system.

For the initial step, the simulated diffusion works in a similar way to that which is described in Figure 3.9 except the boundaries are solid, not periodic. A periodic boundary would incorporate large jumps in the distance travelled and produce non-representative results. Where the propagator calculation was riddled with drastic changes in the experienced field, the tortuosity simulation is not so forgiving to these fluctuations. It is no longer an option to mask the sudden changes arising from periodic boundary conditions within the data. This is because the tortuosity simulation is centred around the distance travelled not the field experienced across a repeating unit cell. Additionally, there is no interest in each specific step taken so the random walk process only stores the starting position and the final position. The path taken is not of concern, only the distance travelled. One advantage is the reduced computation time as there was no need to store the list of coordinates for the duration of the experiment.

The second difference comes from the number of molecules simulated. The propagator calculation subdivides one long molecular walk into smaller components, accepting movement between the periodic faces of the unit cell. However, the tortuosity simulation, with its solid boundaries, aims to prevent the molecules from encountering the walls of the digitised structure. Both reflections on solid boundaries and period boundary conditions would result in unrepresentative reductions in the distance travelled, skewing the tortuosity to be lower. As such, it was decided to simulate many molecules within the time frame of the experiment, not subdividing the walks, to limit contact between the molecules and the boundaries.

To calculate the diffusion tensor for diffusion tensor imaging (DTI), the simulation requires both a number of molecules over which to average the results and a diffusion time. For each Cartesian axis, the distance travelled is calculated and given as $r_{\alpha\beta}$ where α and $\beta \in$ x, y, z. The corresponding diffusion coefficient is calculated as:

$$D_{\alpha\beta} = \begin{cases} \frac{\left(r^{\alpha}_{1,n}\ \mathrm{a}\right)^2}{2\Delta} & (\text{for } \alpha = \beta) \\ \frac{\left(r^{\alpha}_{1,n} r^{\beta}_{1,n}\right)\mathrm{a}^2}{2\Delta} & (\text{for } \alpha \neq \beta) \end{cases} \tag{4.4}$$

Where a is the resolution, 1 and n represent the molecular position at the first and last positions of the diffusion period, and $r^{\alpha}_{1,n}$ is the distance between the first and nth positions along the Cartesian axis, α.

The tortuosity was then calculated by repeating the calculation above for various diffusion times to build up an array of restricted diffusion coefficients as a function of time. This is done for diffusion along all three independent Cartesian axes as well as the average diffusion coefficient found as the trace of the diffusion tensor. As the previous μ-CT images of PS and PL were unobtainable, the simulation described within section section 4.4.2 was run within images taken of the samples produced in 3, PEM and PEL. This is because our PEM and PEL samples were most similar in size to the previously collected PS and PL samples, making them suitable substitutes. As with the simulation outlined in 3, the digitised μ-CT images wee biarized and used as structure functions through which the simulated particles could diffuse.

The simulation also required the following parameters; number of simulated molecules, N$_m$; the bulk diffusion coefficient D_0; and the number of steps each molecule takes, N_s. As mentioned, the each diffusing particle is allowed to diffuse for a given time period t_s which is determined by the total duration of the diffusion period, Δ and the number of steps. As such, this value changes for with Δ. We can also calculate the average distance travelled in one step, $|< r_{j,k} - r_{j-1,k} >|$, e.g., the average distance to step j from step j-1. Furthermore, the total average distance travelled is $|< r_{N_s,k} - r_{1,k} >|$. The simulation parameters are summarised in Table 4.4:

Table 4.4: Parameters for tortuosity simulations in bead-containing samples

Parameter	Value
N$_m$	20,000
D_0	2.2×10^{-10} m^{2}s^{-1}
N_s	5,000
τ_s (for $\Delta = 60$ s)	12 ms
$\lvert< r_{j,k} - r_{j-1,k} >\rvert$ (for $\Delta = 60$ s)	4.0 μm
$\lvert< r_{N_s,k} - r_{1,k} >\rvert$ (for $\Delta = 60$ s)	281.4 μm

4.4.3 Simulation calibration

In order to maximise the computational efficiency, the simulation was run with various individual step numbers for each walk. Individual molecules in each of the experiments walked for the same total time, but that walk was split into either two, five, ten, or twenty-thousand individual steps. The simulation was run with the PEM μ-CT example described above. An in-depth discussion on the tortuosity results obtained here is expanded on later in this chapter. As can be seen below, there was a negligible difference between the results of the four experiments with the finer walk producing

marginally more accurate results than the more coarse method. However, the finer walk resulted in a significant time cost with an almost linear relationship between the number of steps taken and the computation time for the later three examples.

Table 4.5: Normalised computational time for different step numbers

N_s	2×10^3	5×10^3	1×10^4	2×10^4
Time	0.7	1	2.21	4.17
t_s max / s	0.12	0.048	0.024	0.012
$\langle r \rangle$ max / pixels	2.27	1.43	1.01	0.72

Run time for 5,000 steps being 24 minutes.

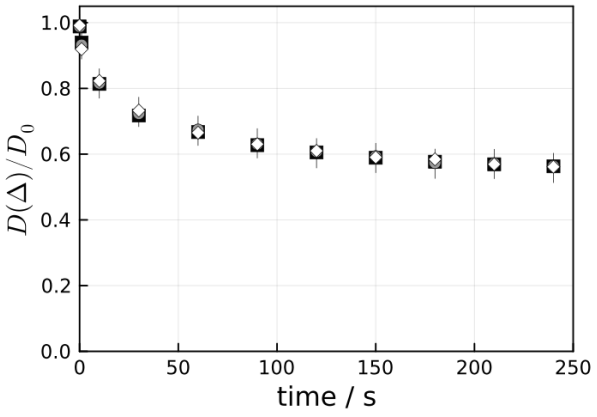

Figure 4.4: Tortuosity calculation within PEM using 20,000 (white diamonds), 10,000 (grey circles), 5,000 (black squares), and 2,000 (vertical lines) steps. The simulation was run with 20,000 molecules where $D_0 = 2.2\times10^{-10}$ m^{2}s^{-1}.

As a result, it was determined that taking 5,000 steps was adequate for the purposes of the simulation. Although it could be theorised that reducing the number of steps further would be more advantageous, there could be significant complications arising from the large average step distance. For the 2,000-step walk, the previously linear relationship between the computation time and number of steps is broken with the computation taking longer than projected. Furthermore, as discussed in chapter 3, the individual components of the total walk must be sufficiently small that diffusion can be considered unrestricted within that time frame. In the case of the 2,000-step walk, this cannot be validated as the average step would take the molecule multiple pixels from its previous position. Although the results for both the two and five-thousand-step walks are equivalent in this case, there may be complications in a porous media with smaller pore sizes. As such, 5,000 steps was deemed an appropriate number to subdivide the total walk into.

Furthermore, the number of molecules to average was also examined for the purposes of improving the efficiency. To do so, the tortuosity was measured within a blank spherical array where it was expected that the ratio between the bulk and restricted diffusion

coefficient should remain one. As before, a further examination of the results is given in the later sections of this chapter. For the calibration, the simulation was run with the parameters shown in Table 4.4 where N_m was varied between 100 and 20,000. The results of which are given below:

TABLE 4.6: Tortuosity measured using different total molecule numbers and their respective normalised time taken

N_m	1×10^2	5×10^2	1×10^3	5×10^3	1×10^4	2×10^4	5×10^4
$D(\Delta)/D_0$	0.9844	0.9841	0.9925	0.9955	1.001	1.000	1.000
Time	0.42	0.42	0.44	0.46	0.64	1.00	2.39

Run time for 2×10^4 molecules being ~18 minutes.

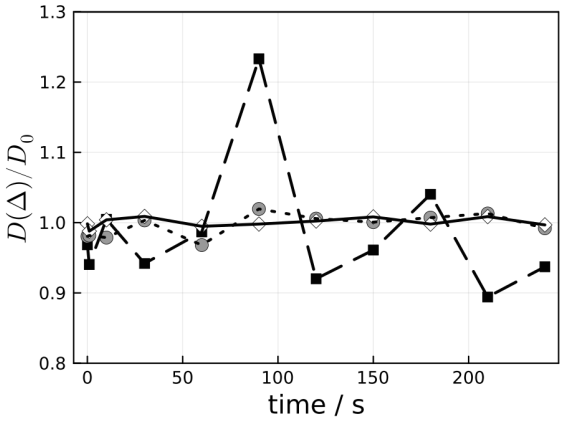

FIGURE 4.5: Tortuosity calculation within a sphere using 100 (black squares-dash line), 5,000 (grey circles-dot line), and 20,000 (white diamonds-solid line) molecules.

It was determined that 2×10^4 was sufficient molecules over which to average the tortuosity measurements. It can be noted that although using 1×10^4 molecules produces a respectable result, a sphere is the simplest case and the added complexity of a tortuous system will require a more absolute answer. Therefore, it was decided to use 2×10^4 and not increase the number of molecules further as this results in a significant computational time increase ruling 5×10^4 too inefficient for the purposes of the experiment.

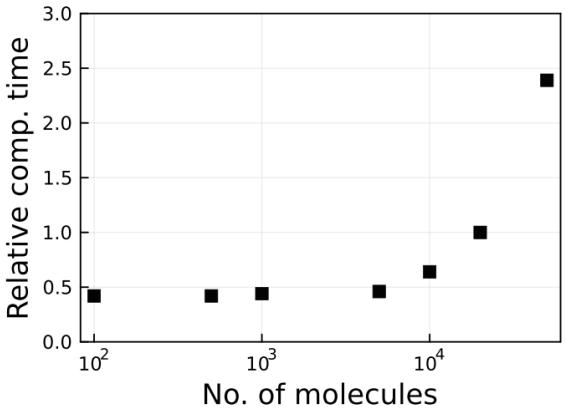

FIGURE 4.6: Relative computational time, normalised to $2{\times}10^4$ experiment, for varying the total numbers of molecules.

4.4.4 Simulation validation

4.4.4.1 Spherical example

The simulation was run within an empty sphere to test the capability of the model to capture isotropic, unrestricted diffusion where no boundaries are present. Within such a scenario, it can be anticipated that diffusion will be identical along every direction originating from the centre of the sphere. Additionally, within the volume of the sphere, excluding the surface layer in contact with the walls, diffusion should not be hindered. The spherical model was produced via a 512x512x512 binary array containing a centre sphere of radius 2.5 mm where each pixel within this corresponded to a value of $s(r) = 0$ thus indicating pore space. The remaining pixels corresponded to a value of $s(r) = 1$ and acted as a boundary to diffusing molecules. The structure was interpolated to increase the mesh resolution within which the molecules could walk.

To prevent influences from the boundary, the starting positions of the molecules were taken from a cubic region with a width of ~2 mm residing within the centre of the sphere. Due to the diffusion coefficient of the molecules and the distance to the wall, it was not anticipated that any molecules would encounter a boundary. The simulation was run with the parameters given in Table 4.4 and Table 4.7, which also show the average distance travelled in the structure during the longest walk. For a range of diffusion times from 0 to 240 s diffusion was measured along 6 directions including along the three Cartesian axes. The resulting diffusion tensor was diagonalized to find the principal directions of diffusion and the related diffusion coefficient, as shown below. For each of the diffusion times in the calculation each component of the principal diffusion coefficient, $D_{\alpha\alpha}(\Delta)$ ($\alpha \in$ x, y, z) was plotted against the other diffusion components to determine the principle direction of diffusion, as seen in Figure 4.7.

Firstly, when comparing diffusion along the three components, it can be noted that diffusion is equivalent along each axis. Thus displaying the isotropic nature of diffusion experienced by all the molecules within this particular case. Secondly, it can be noted that the apparent diffusion coefficient, which can be determined as the average of the three principal directions of diffusion, is approximately equal to the unrestricted diffusion coefficient. Thus implying that diffusion within the system is in fact unrestricted. That is to say, all molecules diffused in accordance with the laws of Brownian motion, assuming an isotropic environment larger than the maximum possible distance that could be travelled. Any deviations between D_0 and $D_{\alpha\alpha}(\Delta)$ can be attributed to a molecule potentially interacting with the sphere wall, or systematic errors arising due to the sample size. However, the selected sample size, N_s, is deemed appropriate within the compromise of error-reducing and computational workload.

$$\boldsymbol{D'}(240\ s) = \begin{pmatrix} 2.21 & 0 & 0 \\ 0 & 2.22 & 0 \\ 0 & 0 & 2.24 \end{pmatrix} \times 10^{-10}\ \mathrm{m^2\ s^{-1}}$$

Table 4.7: Simulation parameters for the tortuosity simulation ran in an empty sphere (Δ = 240 s where relevant)

Parameter	Pixels	Size / mm
resolution	1	9.77×10^{-3}
container size	512	5
starting area	150 : 362	1.47 : 3.54
starting volume	212^3	2.07^3
radius	256	2.5
Av. distance per direction	33.3	0.325
Av. distance travelled	57.6	0.56
Actual distance travelled	53.1	0.52

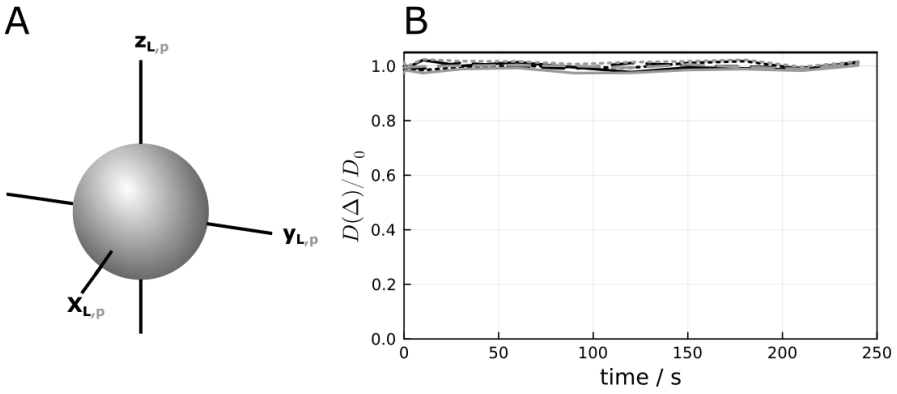

Figure 4.7: DTI in a sphere showing A) the ellipse, and B) the tortuosity for Lab-X (solid black), Lab-Y (dash black), Lab-Z (dot black), Principal-X (solid grey), Principal-Y (dash grey), and Principal-Z (dot grey).

4.4.4.2 Cylindrical example

Following this, the simulation was run within a cylinder with a length of 10 mm and a radius of 0.5 mm, tilted 30 degrees through the x-axis. As before, the volume within the cylinder corresponds to pixels with an assigned value of $s(r) = 0$, indicating a pore. Analogous to the spherical model, interpolation of the structure allowed a more accurate diffusion model to be adopted. The cylindrical structure was chosen to test the capability of the simulation to determine the orientation of diffusion in a structure, with respect to rotations away from z. Additionally, it introduces an aspect of anisotropy which the computation must comply with. The simulation was run with the parameters given in Table 4.4 and Table 4.8.

Again, the molecules were started within a centre cube such that they were not expected to reach the maximum and minimum confines of the model along z and any restrictions in z came from the cylinder walls. However, significant restriction in both x and y was highly anticipated with the average molecule covering sufficient distance to interact with the walls within the time frame of the experiment. Therefore, within this case, it was expected that diffusion along z would be minimally hindered whilst diffusion along x and y would be significantly reduced, as seen in the diagonal tensor below. This is reflected in Figure 4.8, where the resulting ellipsoid shows almost unrestricted diffusion along the z-axis and significant restriction in both x and y.

As before, diffusion was measured in the laboratory frame and the resulting matrix was diagonalised to find the principal direction of diffusion. For the molecular frame results, there is little difference between $D_{zz}(\Delta)$ and the unrestricted diffusion coefficient. This is not the case for the Lab-Z diffusion which shows a more restrictive environment attributed to the angle of rotation of the cylinder. Had a more harsh rotation been adopted, this would have been decreased in accordance, and visa versa for a more shallow tilt. As for the x and y directions, diffusion is restricted by a similar degree within these two axes. Unfortunately, the simulation was not capable of distinguishing x and y between the two frames. It was expected that Principal-X and Principal-Y would be identical due to the symmetry of the cylinders' cross section in that plane. However, there is as large a difference between these two as there is for Lab-X and Lab-Y meaning this aspect may need further investigation.

Furthermore, it can be seen that the diffusion tensor calculated by the algorithm can accurately deduce orientation with respect to z in the lab frame, Z_L. It was determined that the angle between the principal diffusion axis and Z_L was 30.75° meaning the model can catch orientation features within the system. The deviation between the calculated and the physical angle can be interpreted as a slight numerical error present due to a finite number of molecules being averaged. It is expected that increasing N_m would reduce this error but at significant computational and time costs.

TABLE 4.8: Simulation parameters for the tortuosity simulation ran in a 30° tilted cylinder (Δ = 240 s where relevant)

Parameter	Pixels	Size / mm
resolution	1	16.9×10^{-3}
container size	512	8.7
starting area	150 : 362	2.55 : 6.15
starting volume	212^3	3.6^3
radius	29	0.5
length	588	10
Av. distance per direction	19.2	0.325
Av. distance travelled	33.3	0.56
Actual distance travelled	25.7	0.436

$$\boldsymbol{D'}(240\ s) = \begin{pmatrix} 1.22 & 0 & 0 \\ 0 & 1.36 & 0 \\ 0 & 0 & 2.20 \end{pmatrix} \times 10^{-10}\ \mathrm{m^2\ s^{-1}}$$

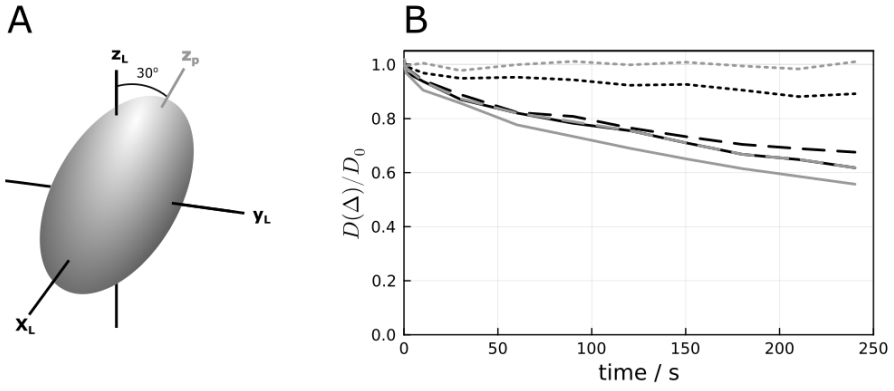

FIGURE 4.8: DTI in a 30° tilted cylinder with a radius of 0.5 mm and length of 10 mm showing A) the ellipse, and B) the tortuosity for Lab-X (solid black), Lab-Y (dash black), Lab-Z (dot black), Principal-X (solid grey), Principal-Y (dash grey), and Principal-Z (dot grey).

One can also assess the speed at which the simulation converges on the cylinder's orientation. For this, the angle between Principal-Z and Lab-Z, β, was plotted for each of the diffusion times within the tortuosity experiment. One can assume that the first few data points are almost randomly assigned as these cases exhibit isotropic diffusion where the diffusion tensors' orientation is arbitrary. However, as the diffusion time increases, the angle β stays more consistently around 30°.

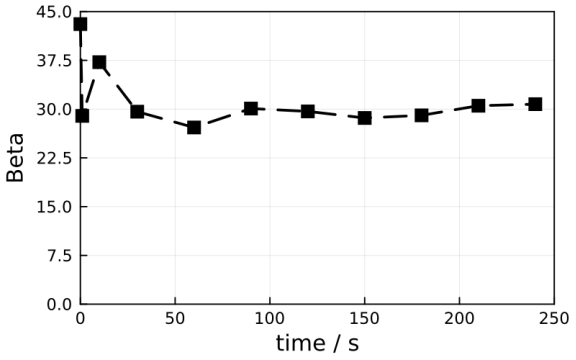

FIGURE 4.9: Angle between Z_p and Z_L (Beta) calculated for each diffusion time within a 30-degree tilted 0.5 mm radius cylinder.

4.4.4.3 Comparison

It was noted that, in the 30° titled cylinder example, there was an unexpected result within the X_p and Y_p data. To explore this further, the same experiment was run within the following samples:

TABLE 4.9: Samples used for the simulation calibration

Sample	Length / mm	Radius / mm	Tilt / °
Sph	N/A	2.5	0
Cyl_0_5	10	0.5	0
Cyl_30_5	10	0.5	30
Cyl_60_5	10	0.5	60
Cyl_90_5	10	0.5	90
Cyl_30_25	10	0.25	30

Where the labelling refers to the shape (cyl for cylinder, sph for sphere), the second number corresponds to the tilt angle, β, and the last number is the radius of the cylinder (either "5" for 5 mm or "25" for 0.25 mm). Although barely noticeable in the Cyl_30_5 sample, when the tilt angle is further increased, the difference between the lab and the principal frame becomes quite distinct. One can see at 60° a significant difference in the lab frame where diffusion along y is less restricted than along z. Tortuosity data for all samples in Table 4.9 are given below in appendix 9.7. The difference in the frame is most notable when looking at the percentage difference between the two for the three Cartesian components by plotting $\frac{(A_p - A_L)}{A_L}$ where A is X, Y, or Z. Here we see very little deviation for the x components and significant differences in both y and z as the cylinder rotates through until Y_L and Z_p are identical.

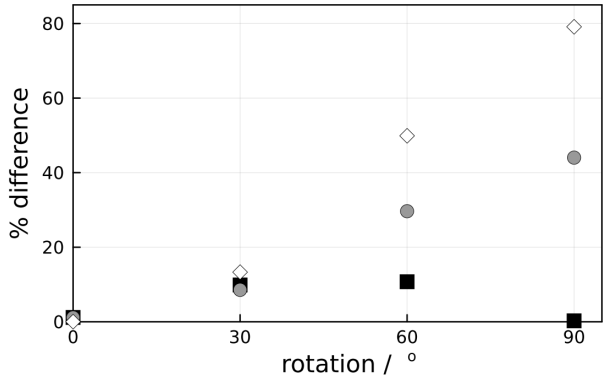

FIGURE 4.10: The difference between the lab frame and principal frame against the tilt of the cylinder showing the x components (black squares), y components (grey circles), and z components (white diamonds).

For all calibration cases, the fractional anisotropy (FA) was plotted for the duration of the experiment. For the sphere, the fractional anisotropy remained at zero for the duration of the experiment indicating completely isotropic diffusion throughout. The fractional anisotropy was consistent for all cylinders with a radius of 0.5 mm as FA is calculated within the principal frame, but increases significantly when the radius is reduced. This indicates that the simulation is capable of capturing both isotropic, unrestricted diffusion and the nature of diffusion within a tilted or centred channel.

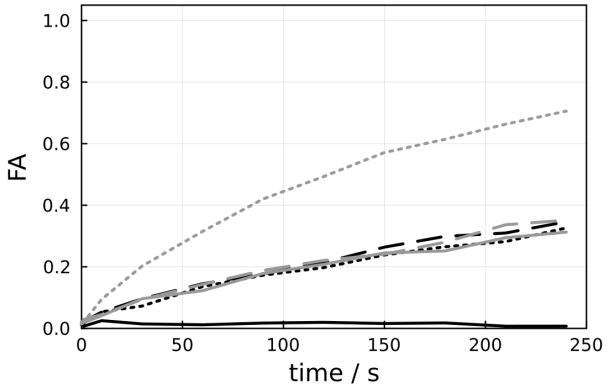

FIGURE 4.11: FA calculated for the duration of the diffusion experiment within the sphere (solid black), Cyl_0_5 (dash black), Cyl_30_5 (dot black), Cyl_60_5 (solid grey), Cyl_90_5 (dash grey), and Cyl_30_25 (dot grey).

4.4.5 Within porous media

The simulation then progressed to measuring tortuosity within two model systems of randomly packed beads, PS and PL. μCT images of the PEM and PEL samples produced digitized 3D models of the samples which could be used within the simulation as the structure functions, $s(r)$. The images also elucidated the non-spherical nature of the beads thus offering a complex and unpredictable internal environment to measure diffusion. The simulation used the parameters given in Table 4.4 and Table 4.10.

Table 4.10: Simulation parameters for bead systems (Δ = 240 s where relevant)

Parameter	Pixels	Size / mm
resolution	1	5.556×10^{-3}
container size	512	2.85
starting area	150 : 362	0.83 : 2.01
starting volume	212^3	1.18^3
Av. bead width (PS)	98.8	0.55
Av. bead width (PL)	189.4	1.054
Av. distance per direction	58.5	0.325
Av. distance travelled	101.3	0.56
Actual distance travelled (PS)	68.3	0.379
Actual distance travelled (PL)	76.7	0.426

For each of the diffusion times in the tortuosity calculation, the apparent diffusion coefficient was calculated and plotted against the experimental data collected within the corresponding sample. Additionally, each component of the apparent diffusion coefficient, $D_{\alpha\alpha}(\Delta)$, was calculated by measuring diffusion along the relevant axis ($\alpha \in$ x, y, z), and was plotted against the other components to determine the principle direction of diffusion. Experimental results were previously collected by former members of the group. The simulations run within these works match closely with the previously obtained experimental data displaying the simulation's ability to catch diffusive nature within an unknown environment.

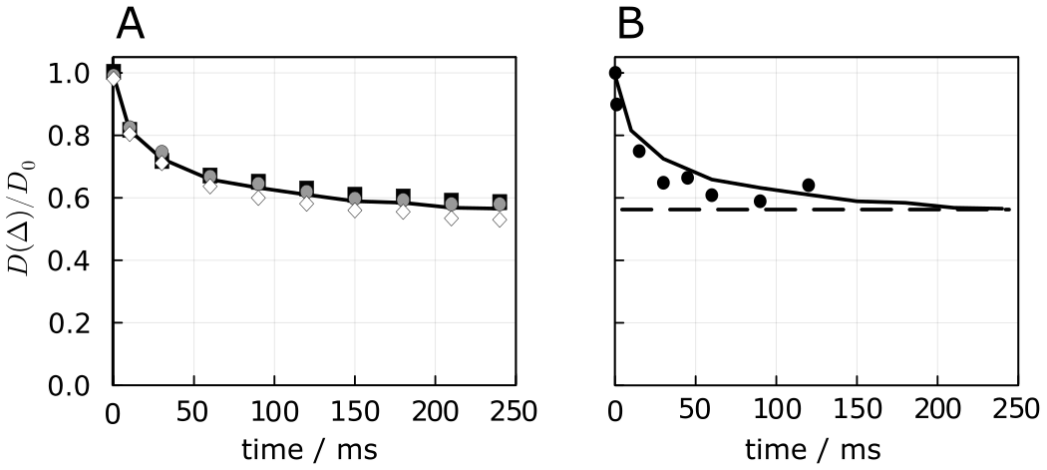

Figure 4.12: Tortuosity measured within PS showing A) the simulation for D_{xx} (black square), D_{yy} (grey circle), D_{zz} (white diamond), and the tortuosity (solid line) and B) the experimental (black circles), the simulated tortuosity (solid line), and the extrapolated tortuosity (dash line).

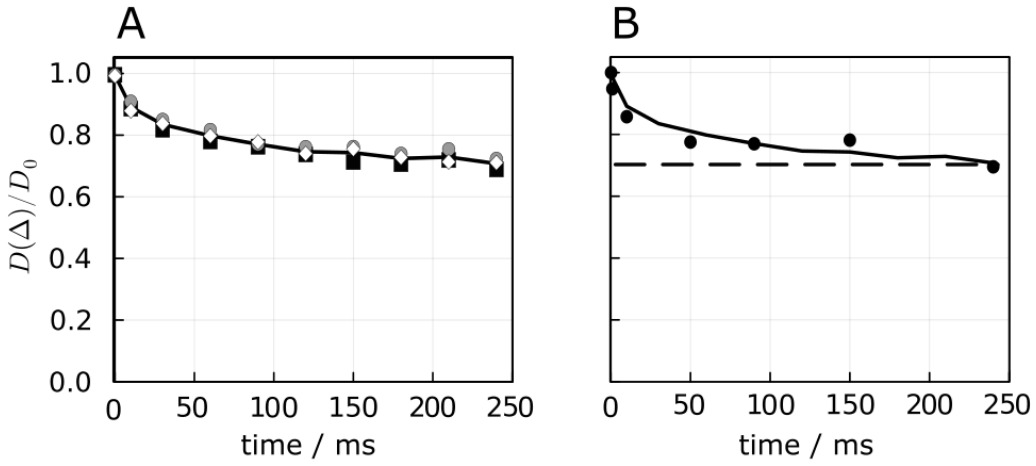

FIGURE 4.13: Tortuosity measured within PL showing A) the simulation for D_{xx} (black square), D_{yy} (grey circle), D_{zz} (white diamond), and the tortuosity (solid line) and B) the experimental (black circles), the simulated tortuosity (solid line), and the extrapolated tortuosity (dash line).

In both examples, the tortuosity can be displayed by comparing the experimental data with the simulated apparent diffusion coefficient, $D_a(\Delta)$. The components of $D_a(\Delta)$ are plotted adjacent to demonstrate the changes in diffusion along the principal axes. In both cases, the simulation is capable of capturing the tortuosity of the porous media in good agreement with the experimental data.

TABLE 4.11: Structural properties of both PS and PL as determined from both experimental and simulated data

Sample	Tortuosity		FA
	Exp	Sim	
PS	0.61 [a]	0.56	0.058
PL	0.695	0.70	0.025

[a] Value taken as a projection of the data up to 240 s.

For both PS and PL, it can be noted that there is little difference in diffusion along the three constituent axes, further solidified by the fractional anisotropies being close to zero in both instances. It can be inferred that although the systems offer a non-spherical array of varying-sized beads, the packings are sufficiently random with no preferred diffusion direction. Furthermore, the system with the smaller beads shows a more tortuous system owing to the smaller pore sizes created by the smaller beads. Within the time frame of the experiment, the molecules were capable of inter-pore movement through channels exhibiting increased restriction. After which, the diffusion in the small "spherical" pores resulted in an isotropically reduced value of tortuosity. As for the larger beads, the rate of inter-pore travelling is predicted to be smaller, and the pores themselves are of greater volume, explaining the larger tortuosity found in PL as

opposed to PS. As with the propagation calculations, the experimental and simulated results match with sufficient accuracy that external effects such as surface relaxation are expected to be minimised. In a case where surface relaxation may significantly affect experimental results, the two may not overlay so accurately.

4.5 Conclusion

Within this chapter, the necessity and uses of tortuosity were outlined and explained. The need for computational versus physical experiments was explored in a range of scenarios. In order to evaluate the tortuosity in complex porous media the simulation at hand was expanded to incorporate tortuosity and fractional anisotropy measurements. The simulation was calibrated in terms of both the number of molecules averaged over, and the number of steps taken by each molecule. This was done with careful consideration of the computational time so as to produce an efficient simulation framework.

Furthermore, the simulation was verified in a few exemplar cases, such as a sphere and a tilted cylinder. Within the two, the simulation was capable of capturing the nature of both isotropic and anisotropic diffusion. Additionally, in the case of the cylinder, the framework could successfully determine the orientation of the rotated shape with respect to the lab frame z-axis.

Following the calibration and verification, the simulation was tested against experimentally derived results using randomly packed beads. The simulation accurately determined the tortuosity within the packings and was in good agreement with the physical data. It was determined that the simulation is capable of calculating tortuosity within porous media of interest, using a digital reconstruction of sufficient resolution.

Although the simulation is capable of capturing the nature of diffusion within a range of systems, there is room for improvement within the framework. One further expansion could see the introduction of surface effects into the random walk function. Where the particles are currently able to diffuse freely, a more realistic approach would be the introduction of a reduced random step away from a surface, in a particular direction according to reflection, following a collision. Such an adaption would reflect surface attraction and adsorption that occurs at solid-liquid boundaries. However, this would entail the determination of surface attraction between individual molecules and the porous materials, which is outside of the scope of this project.

Chapter 5

Exploring DTI at Low field

This chapter is an extended version of T. Robertson, R. C. Bannister, T. A. A. Cartlidge, T. Hugger, S. Breham, K. Zick, F. Engelke, S. Thompson, and G. Pileio, A dual-core NMR system for field-cycling singlet assisted diffusion NMR, *Frontiers Media SA*, 2023, **11**, 1229586.[181]

5.1 Synopsis

This chapter is an overview of the work carried out in order to fulfil objective three.

O$_3$ - Introduce a custom field cycling methodology to take advantage of increased sensitivity found at high field and reduced low field magnetic susceptibility effects.

The purpose of this chapter is to introduce progressions made within the experimental aspect of the project. This includes the incorporation of field-cycling techniques into diffusion NMR to increase the signal-to-noise ratio and extend the limiting factor of current d-NMR experiments. The experiments shift to using a custom-built low-field probe to enable d-NMR studies in magnetically inhomogeneous samples via field-cycling techniques, taking advantage of the reduced susceptibility mismatch effects at low field. The possibility of applying the technique to gas diffusion layer (GDL) disks of various compositions is outlined and discussed. Furthermore, the methodology for producing degassed porous samples is described, including its calibration and testing.

5.2 Introduction

Advancements of NMR have progressed further and further whilst using increasingly strong magnets: with commercially available magnets now exceeding fields of 1 GHz.[182] The advantage of this being the increased signal-to-noise ratio obtained with the greater external field strength. As we have seen, the introduction of stronger magnetic fields further increases the effect of susceptibility-induced relaxation. It would therefore be advantageous to have a methodology that utilises both the signal enhancements of high field and the lessened effect of DDIF found at low field. On the opposite end of the spectrum are bench-top NMRs; compact, readily accessible magnets ranging from hundreds of mT to ~ 2 T. They also boast the advantage of compact sizes and relatively low cost and maintenance when compared to their high field cousins.[183] The difference in their strength comes from the production of the magnetic field. Where high field spectrometers require superconducting magnets, cooled to liquid helium temperatures, bench-top NMR requires low maintenance permanent magnets.

Nevertheless, low-field NMR(lf-NMR) is a useful tool for many applications including borehole logging, measuring pore structure in cement, phytochemical analysis, and conducting analysis within a fume hood, for samples that may be too hazardous to be on a normal bench.[184–186] The first of which is deemed "inside out" NMR as the magnet and associated electronics are formed within a rod that is inserted into a rock structure, where conventional NMR sees the placing of the sample inside the spectrometer.[185] Low-field NMR has repeatedly proven its worth in a range of applications including the study of textural features and moisture content of food, the ageing and longevity of polymers, and the analysis of bio-fluids for diabetes marker identification.[183,187,188]

Low-field NMR is also a useful tool for measuring diffusion, with pulsed-field gradient pulses capable of measuring diffusion at 43 MHz for ^{1}H.[189] Given the issues associated with T_2 at high field, highlighted in chapter 3, one could assume bench-top NMR to be a suitable alternative to conventional high field NMR for the application of diffusion studies. Unfortunately, low-field NMR does not come without its own disadvantages, mainly the reduced resolution and sensitivity when compared to high-field. This has led to some people developing alternative methods to increase signal, such as estimating diffusion coefficients from bench-top signals using computational means.[189] The intention of this is to rectify peak overlapping resulting from poor signal-to-noise ratio. Given that porous media already poses the issue of limited solution volume and the imposed conversion limit of magnetisation to singlet order, the complication of reduced signal is an unnecessary disadvantage.

An alternative method is field-cycling NMR which centres around spectroscopy in the frequency domain, as opposed to the time domain, and produces dispersion curves. It is also a low-field technique that rapidly switches the external field strength by either varying the current supplied to the superconducting magnet or manually shuttling the

sample. This branch of NMR is used extensively within the food industry for a range of applications such as the characterisation of ageing balsamic vinegar, the ripening of Parmigiano Reggiano cheese, and to study the supra-molecular formation of triglyceride structures in extra-virgin olive oils.[190–192] Additionally, it is used readily for the study of water molecule dynamics within close proximity of proteins, soil science, and probing the structure of nanosponges: a novel class of materials with extensive applications in drug delivery and nanoparticle catalyst supports.[193–195]

Field-cycling NMR utilises the frequency domain to isolate spectroscopic features that indicate molecular dynamics processes. This is because the relaxation (T_1) tends to change when there is a change in the molecular dynamics of the system. This could, for example, be the binding of a protein to a paramagnetic nucleus or adsorption of the molecule of interest onto a surface.[196,197] Since spin relaxation is centred around fluctuations in the surrounding field, if a particular event occurs which corresponds to this frequency, the dispersion curve will reflect the increased relaxation. This technique can also be utilised to measure the diffusion coefficient by plotting the relaxation rate against the square root of the resistance frequency and extrapolating D_0 from the resulting curve.[198] The relaxation slope of the curve, A, is extrapolated as follows:[198]

$$R_1(\nu) \cong -A\sqrt{\nu} \tag{5.1}$$

Where the diffusion coefficient is retrieved from:[199]

$$A = N_{spin}\left(\frac{\mu_0}{4\pi}\gamma^2\hbar^2\right)^2\left(\frac{\sqrt{2}+8}{30}\right)\left(\frac{\pi}{D_0}\right)^{3/2} \tag{5.2}$$

Where N_{spin} is the density of spins, $\hbar$ is Planck's constant, and γ is the gyromagnetic ratio of the nucleus of interest. As with many experimental techniques, groups such as Ates *et al.* have developed simulations to complement the practical applications.[200] They produced dispersion curves showing the effect on relaxation rate for the varying frequency, for a set of differing correlation times. Field-cycling can also be adopted as a method for accessing LLS, as pioneered by Carravetta and Levitt, and developed further by additional groups.[172,201]

Of the two cycling methods mentioned above, both come with distinct advantages and disadvantages. When altering the field using an electrical current, the sample is typically polarized at "high field" with evolution occurring at low field. However, this "high" field is still only ~1 T which is arguably still low in the grand scheme of NMR.[185] The advantage of the reduced DDIF is therefore counteracted by the loss of sensitivity achieved at the relatively low fields. On the contrary, manually shuttling the sample allows for a large polarization to be built and detected at high field, followed by use at low field. Although, one must be careful with the transport process so as not to disrupt the sample. Zhukov et el. carried out fast field-cycling using a rack-and-pinion system which performed sample motion from 5 nT to 9.4 T in 0.5 seconds.[202] Although this

provided access to measurements in fields over 9 orders of magnitude, it would pose many challenges when measuring diffusion, mainly in the introduction of irregular fluid motion. Furthermore, it has been noted that field-cycling NMR as a tool for diffusion measurements is limited to slow diffusion regimes, restricting the applicability of the technique.[194] This technique does offer access into the realm of diffusion measurements, but there is still a need for increased sensitivity in order to probe intricate systems, potentially using nuclear singlet states.

5.2.1 Low field probe

The work carried out in the preceding subsection is contained within the overall research project but was not within the scope of this PhD and was performed by T. Robertson (unless otherwise specified). Further details can be found in Robertson et al.[181]

It is intuitive that a particle diffusing at a slower rate will experience the localised distortions in the field to a far lesser degree than its more agile partner. This may lead to the assumption that a particle with a lower diffusion coefficient would be more beneficial for the purposes of d-NMR. However, the experiment is still limited by the lifetime of spin order and if the particle cannot experience a large enough volume to statistically represent the sample, the results will not be representative of the system. Other ways of limiting the effects of DDIF include reducing $\Delta\chi$ or using a lower field.

Firstly, for some systems, the components of the porous media cannot be altered and so the susceptibilities cannot be matched. As for the second impacting factor, although a lower field provides a less harsh environment for susceptibility-induced relaxation it also provides lower sensitivity and therefore less signal than at high field (HF). As a result, a custom-built low-field (LF) probe was developed, for the purpose of signal-enhancing, field-cycling d-NMR measurements. The foundation of the venture being the increased signal achieved by polarising, and later detecting, at high field, combined with the dampening of the susceptibility mismatch effects at low field.

The probe was designed as an extension to a 7.05 T Oxford Instruments unshielded magnet. Its design and manufacturing were performed in collaboration with Bruker BioSpin GmbH. It sat within the stray field of the magnet, ~62.4 cm above the sweet spot of the high field probe, such that the LF coil resides within a sweet spot with a field of 46.4 mT. For ^{13}C nuclei, this corresponds to the frequency of 500 kHz. This was found using a hall device to measure the stray magnetic field in 1 cm intervals above the magnet, then refined by taking smaller measurements around the target area. The probe was equipped with a Bruker Micro 2.5 WB 3-axis gradient system powered by a Bruker GREAT 60 A amplifier rack and could generate up to 1.5 T m^{-1} strength gradients, facilitating the measurement of diffusion. Shimming was achieved through a z-shim coil limited to 5 A and installed within the low-field probe. The probe was

positioned on an aluminium mounting made in-house. A full schematic of the set-up is shown below in Figure 5.1.

Movement of the sample was achieved via a sample shuttle, powered by a Trinamic TMCL-1160 stepper motor and was controlled through custom software developed by Hall *et al.*[6] The stepper motor controlled a rotating spindle wheel able to wind the connected sample up through the magnetic bore via attachment through a Dyneema cord. The cord had a low stretch ratio and was connected to a rectangular guidance rod, cut with millimetre precision to the guiding hole within the LF probe to prevent rotation during movement. The rod was in turn connected to the sample such that the whole system moved as one when the motor was active. Shuttling required approximately three seconds for the sample to travel the whole 62.4 cm where a 0.5 settling time was applied following sample movement either up or down. A more in-depth description of the system and associated hardware is within the aforementioned publication.[181]

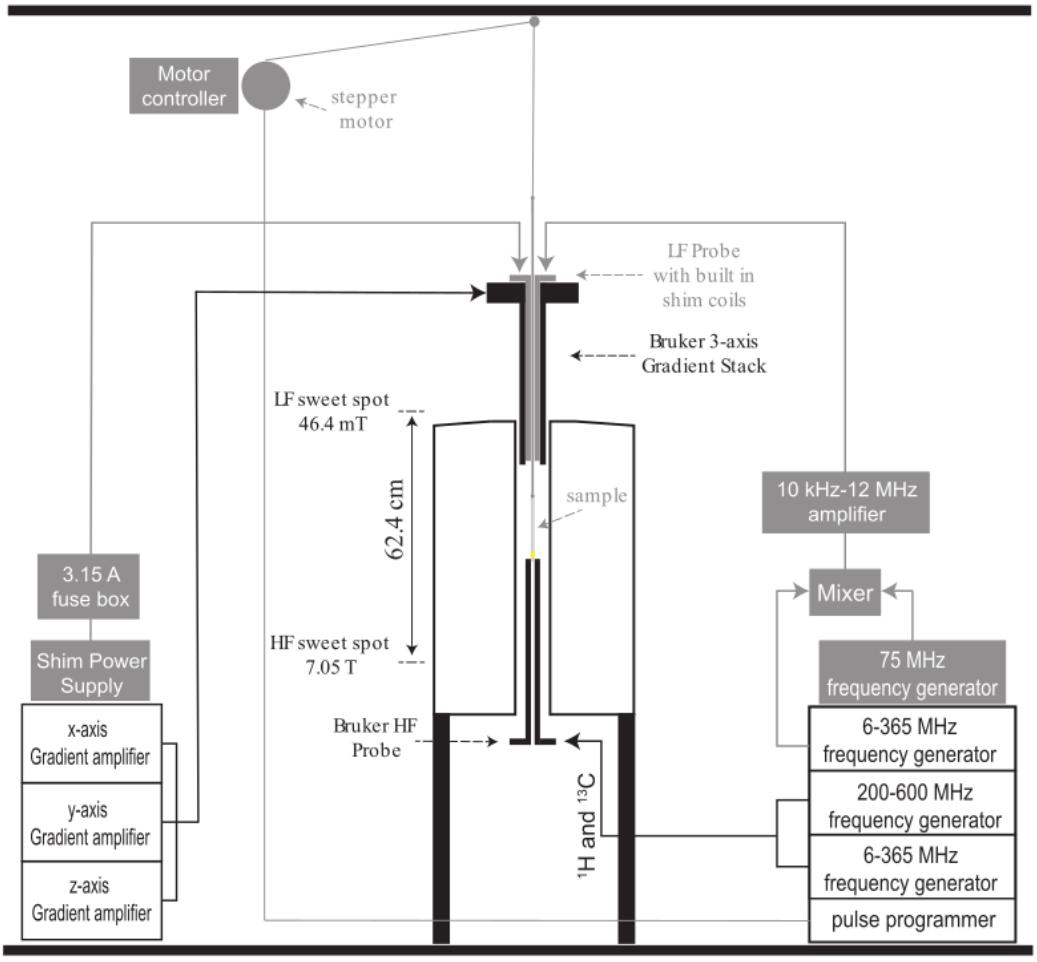

FIGURE 5.1: A schematic of the dual-core system showing the additional features in grey, supplementary to the original magnet. Taken from.[181]

With the coil residing in the stray field and encompassing a length of 20 mm, it was found to possess an almost linear gradient across the coil of ~4.8 mT. Considering

the localised gradients that are introduced by the porous media, it was imperative to maintain as homogeneous a background field as possible. As such, a correction to the field could be made by supplying the Z-shim coil with an optimised current. In order to determine this value, the field across the coil region was measured with varying values of supplied current. This was performed within the LF probe where negative values of distance refer to regions below the LF sweet spot.

Table 5.1: Magnetic field in mT measured within LF probe coil region when varying Z-shim coil currents are applied

Distance	Current in shim coil / A						
/ mm	0	0.5	1.0	1.5	2.0	2.5	3
10	44.1	44.5	44.9	45.3	45.7	46.1	46.5
5	45.3	45.5	45.7	45.9	46.1	46.3	46.5
0	46.4	46.5	46.5	46.5	46.5	46.5	46.5
-5	47.7	47.5	47.3	47.1	46.9	46.7	46.5
-10	48.9	48.5	48.1	47.8	47.4	47.1	46.2

To more accurately determine the correction current needed, signal was measured following a single echo pulse sequence, as seen in Figure 5.2 A, to minimise the loss due to inherent field gradients. Unfortunately, the results bear imperfections as a result of manual positioning; however, a correction current of 3.2 A was found to best homogenise the field. The impact of a continuous correction current was then assessed against the internal temperature of the probe. For a 3 A correction current the temperature rose by 18 °C in 80 minutes, given a 23 °C room temperature. This time scale far exceeds the time scale of any expected diffusion measurements.

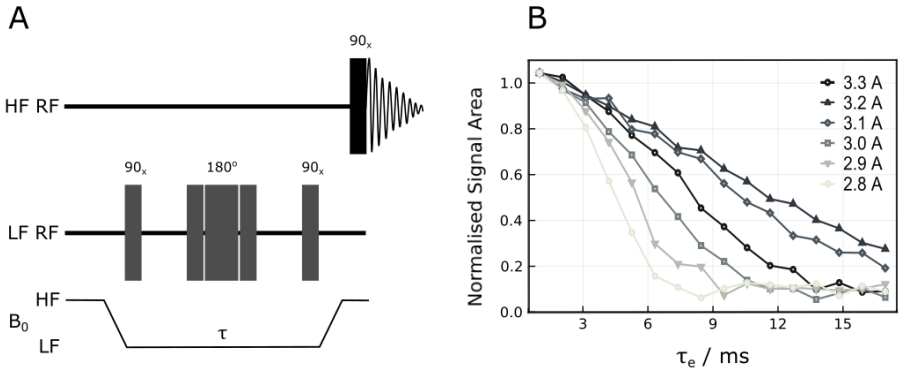

Figure 5.2: Calibration of the single echo using A) a LF single echo pulse sequence where 180° represents a composite pulse formed of $90_x180_y90_x$ and the duration of the 90° pulse was 21.5 μs. And producing B) a plot of signal against echo time τ_e for varying correction currents in the z-shim. Adapted from.[181]

5.2.2 Gas diffusion layers

Gas diffusion layers (GDL)s are porous materials found within fuel cells with the primary function of facilitating molecular movement throughout the cell. Contradictory to their name, they possess multiple roles including but not limited to the delivery of reactant gases. Their role involves delivering reactants evenly to the catalyst surface, removing heat and water produced, and facilitating current passage to the collector plates.[203] Not only this but they provide structural support to the fuel cell. They play a critical role in the efficiency of fuel cells; they are of particular interest to proton exchange membrane fuel cells (PEMFC)s, with permeability being the major factor in cell efficiency.[68] Efficiency of the cell often fails when water builds up in the GDL, which prevents gas diffusion. In some instances the fibres of the GDL are coated in a low wettability material, such as polytetrafluoroethylene (PTFE), to prevent build-up.[204]

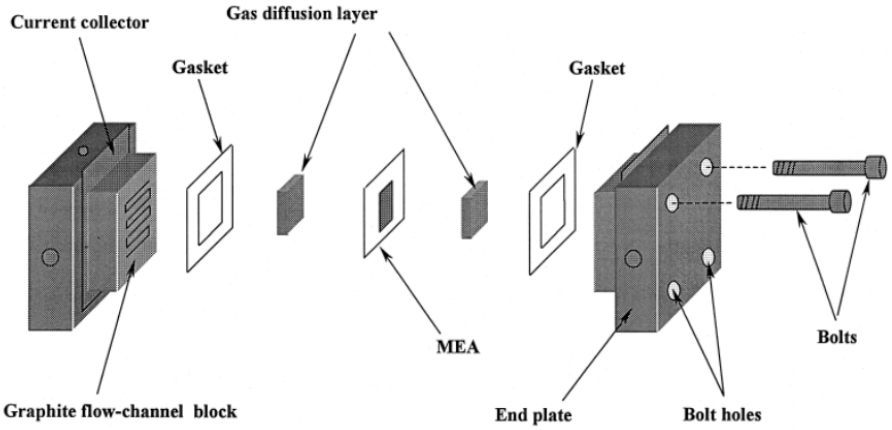

Figure 5.3: Schematic of a PEMFC including the location of the GDLs. Adapted from Lee *et al.*[205]

Where MEA is the membrane electrode assembly consisting of a proton-exchange membrane, catalyst, and electrode.[205] Fuel cells have been studied extensively in an attempt to increase fuel cell efficiency, either by altering the structure of the fuel cell or compressing it.[205] For the latter, one group, Lee *et al.*, studied the compression of a GDL to determine how the change in both the porosity and the layer thickness altered the efficiency of the cell. This is in reference to the in-plane porosity as opposed to the through-plane porosity. This was done by measuring the performance against the torque applied to the bolts shown in Figure 5.3. They stated that a decrease in porosity leads to an increase in electrical conductivity for one particular GDL, yet for a more rigid layer, more torque led to a decrease in performance, possibly due to damage to the structure.[205] However one can not help but consider whether a measure of tortuosity would be more suitable for the study at hand. As has been discussed, a high porosity can be found within a species with larger voids but considerably low connectivity, meaning tortuosity could be a better basis for measuring liquid and gas movement.

In the theme of the previous two chapters, there are also extensive studies into the use of simulations to study GDLs. Initial simulations took a primitive approach in assuming a homogeneous porous media boding a constant permeability using computational fluid dynamics (CFD).[206] The simulations quickly rose in sophistication to simulations of micro-scale flow through carbon paper GDLs in a 3D structure.[68] Hussain *et al.* used a range of modelling techniques including pore visualisation, fluid flow visualisation, and 3D distributed modelling to test the optimisation of porous GDLs, showing the versatility of computational methods with respect to complex media.[207]

5.2.3 SEM imaging

For the purposes of the GDLs, it was advantageous to analyse the surface of the samples to understand the fine nature of the porous structure and assess the possible pore sizes. To do so, scanning electron microscope (SEM) imaging was adopted as it provides high-resolution images of surface structures. The operation of SEM involves bombarding the sample with high-energy primary electrons such that the surface atoms release a valence electron or secondary electron. This secondary electron is then detected and used to produce a topographic-sensitive map of the sample surface. Brighter pixels in the resulting image are a result of a greater intensity of detected electrons, such as an area closer to the electron source. The process is carried out at high vacuum to limit the incidence of secondary electrons being intercepted by stray gaseous molecules in the chamber. The sample is often coated in a conductive material such that absorbed electrons can flow through and out of the sample. This is done to prevent charge accumulation, which can result in extreme bright spots within the image. To collect an image with the greatest resolution, the number of electrons entering the sample must match those leaving it, producing a particular energy, kV, specific to each sample.

5.2.3.1 Low vacuum SEM

For some samples, coating the surface is not a viable option as it may damage the sample or render it unusable. Additionally, some more fragile samples may not be suited for the low pressures within the sample chamber, such as biological samples.[208] Therefore, low vacuum, meaning higher pressure, can be utilised to produce high-resolution images when the sample is neither conductive nor suited to low pressures.[209] Low vacuum SEM operates by separating the gun chamber from the sample chamber such that two different pressures can be present within the system. The gun chamber remains at a high vacuum to maintain a well-directed electron beam, whilst the sample chamber contains a relatively low vacuum. This form of SEM utilises a 100 μm aperture that ensures the pressure difference between the two chambers by inhibiting the flow of gaseous molecules into the gaseous chamber.[210]

The gaseous molecules within the sample chamber serve to limit the charge build-up in the sample by redirecting the electron flow. The electron beam produces cations from the gaseous stray molecules, which in turn are attracted to the negative charge building on the surface of the sample. The gaseous molecules can strip away the excess electrons and ground the charge via the walls of the sample chamber, and continue to prevent the sample charge from accumulating.[210] Unfortunately, the presence of stray gaseous molecules can reduce the signal-to-noise ratio as secondary electrons from the sample are absorbed by the stray molecules. However, the advantage of imaging fragile samples, and reusing them following the process, outweighs the slight resolution reduction caused by low vacuum SEM imaging. This form of SEM imaging was adopted for all studies mentioned within these works as it allowed the sample to be reused, thus preventing the waste of materials.

5.2.4 EDX analysis

Another non-destructive analytical technique is energy dispersion X-ray (EDX), an application of X-ray spectroscopy that allows both qualitative and quantitative analysis of surface composition. With this technique, the sample is irradiated with a high-energy beam of electrons with the intent to eject an electron in the targets' K or L shell. These being the lower energy, centre most shells containing either two or eight electrons, respectively. With vacancies in inner shells, a high-energy valence electron will then fill this space, releasing X-rays of a certain energy. The energy released is specific to the element being radiated and the shell that loses the electron. The released energy is then detected and algorithms are used to predict the elements present based on their pattern of K and L energy releases compared to universal detection tables. This is used to compose a spectrum showing the energy of the detected photons (in KeV) and the relative intensities. Due to hydrogen and helium having insufficient valence electrons, they are invisible to EDX, and some lighter elements that eject low-energy X-rays are difficult to detect: their irradiation may be absorbed before detection.

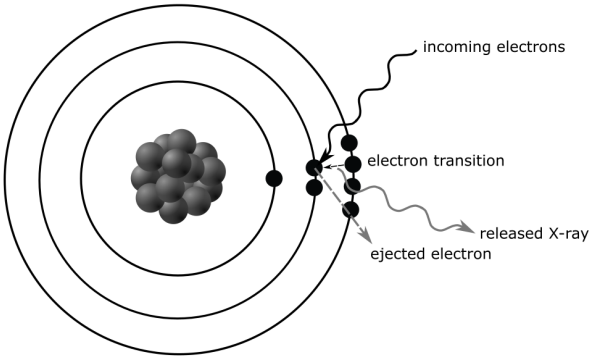

Figure 5.4: Schematic of the process of EDX involving X-ray absorption and emission.

5.2.5 Pyruvate

Pyruvate is a principal molecule with respect to biochemical studies as it sits at the centre of the metabolic production of energy and is also a known antioxidant.[211] More specifically, pyruvate is the end product of glycolysis, and facilitates the production of ATP in mitochondria. The hydrolysis of ATP then, in turn, produces energy for the organism.[212] Should the metabolism of pyruvate be hindered, tissues which are accustomed to high levels of ATP turnover are susceptible to the contraction of severe disease.[213] As such, the metabolism of pyruvate, and the associated enzymes, have been in the spotlight of medicinal studies for many years. Due to its significant role in many metabolic processes, relative pyruvate concentrations can be an indicator of disease such as Coronavirus-19 (COVID-19) severity levels.[214] Elia *et al.* took this one step further and studied the metabolic pathways of pyruvate to determine links between tumorous environments and the ability of cells to suppress anti-tumour immunity.[215]

Within NMR circles, pyruvate can be hyperpolarised before being used as a tool to study metabolic pathways and tumour characterisation. In previous examples it has aided in the elucidation of pyruvate dehydrogenase's role in the glucose-lipid cycle.[216] Furthermore, another group hyperpolarised ^{13}C labelled pyruvate and used it to develop an *in vivo* imaging technique for phenotyping tumours.[217] Although prevalent as a tool in both the chemistry and medicinal research circles, pyruvate poses a number of complications as a material of interest. One disadvantage is its instability in solution: within both acidic and basic solutions it is prone to forming a range of isomers and dimers.[218–220] This dilutes the actual amount of pyruvate available for analysis.

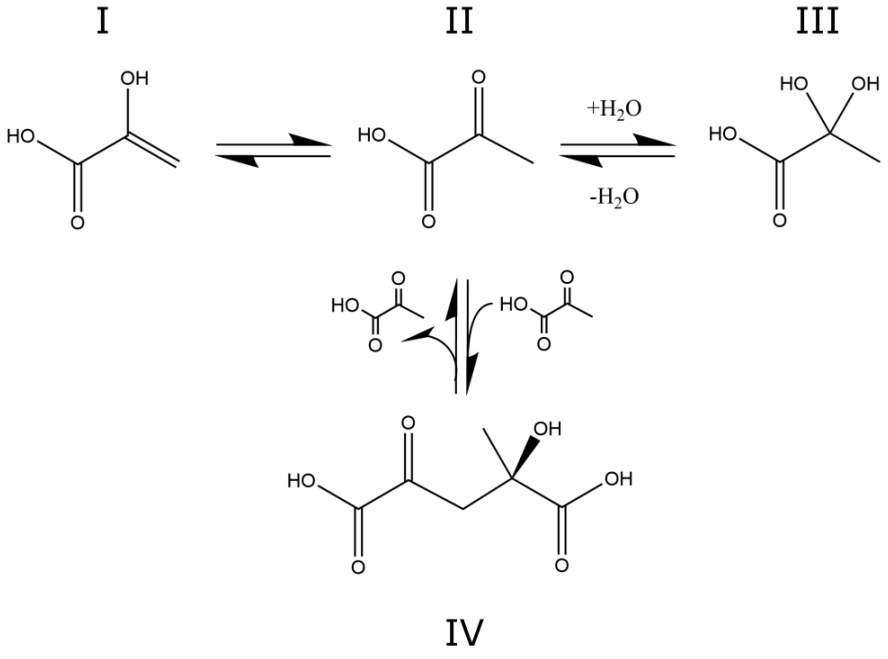

Figure 5.5: Products of pyruvate in basic solutions forming a dimer (iv), and in acidic solutions forming pyruvate enolate (i), pyruvate (ii), and pyruvate hydrate (iii).

Within a basic solution, the ratio of pyruvic acid to its hydrated counterpart (the diol) is significantly lowered from as much as ~60 % diol at pH 1 to ~6 % from pH 5 upwards.[221] Some contradicting studies exist; some state having <8 % pyruvate hydrate in their solution between pH 7.5-8.2.[222] Opposing this is the conclusion reported by NBS: Center for Analysis Chemistry, National Bureau of Standards, USA who determined that pyruvate is unstable at 22 °C with a pH greater than 6.0. Their studies reported dimer levels up to 9.1 % following 24 hours, and up to 18.4 % after 48 hours.[223]

On the contrary, basic conditions are known to induce the dimerisation of pyruvate into parapyruvic acid, which is known as being cytotoxic to cells in *in vitro* experiments.[211,218,220] Not only this, but pyruvate can oligomerise and form a host of linear and cyclic parapyruvic acid derivatives when in an aqueous solution, noting that the substitution of H_2O for D_2O had no apparent effect on the reactions.[218] Although these reactions can be photo-catalysed, the products of both dimerisation and oligomerisation are prevalent in dark solutions.[224] One can therefore deduce that a pyruvate solution with a pH between 5.0-6.0 has the greatest concentration of pure pyruvate, accounting for both the diol and dimer forms. For ^{13}C centred experiments, it is the likes of the dimerisation that must be prevented. However, pyruvates' plentiful biological abundance, importance in a multitude of metabolic pathways, and relatively low relaxation rates (leading to a T_1 of ~45 seconds at 9.4 T and ~65 seconds at 7 T) make it a suitable spy molecule for NMR centred experiments.[225] Although the current studies are confined to pure pore space diffusional studies, the applicability of pyruvate opens up opportunities to study different diffusion regimes. One can look towards studying live or *in vivo* samples, incorporating inter-cell diffusion as well as bulk and surface diffusion, potentially whilst hyperpolarising the sample too.

5.3 Materials and methods

5.3.1 Solution preparation

The selected samples consisted of gas diffusion layer (GDL) disks, composed of carbon cloth or carbon paper, packed into a flat bottom NMR tube and submerged in solution. The disks were compressed using an insert to reduce excess space between layers. The solution was D_2O containing a 0.4 M solution of sodium-pyruvate-1-^{13}C. This molecule was selected due to its large T_1 times and the particular isotope was selected due to its reduced relaxation rates when compared to its alternatively labelled isotopes.

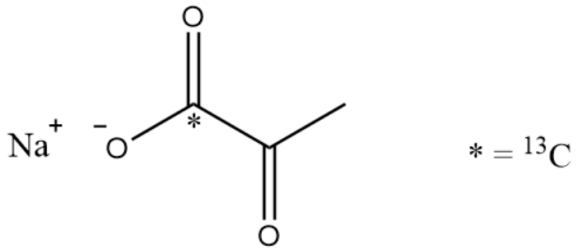

Figure 5.6: Molecular structure and labelling of sodium-pyruvate-1-^{13}C.

As mentioned, pyruvate forms a varied range of molecules within an aqueous solution. In order to combat this, the solution can be acidified below pH 6, whereby dimer formation is limited, but not too low such that the diol form dominates.[221,223] In order to do so, a solution of 0.05 M HCl in D_2O was made and added sequentially to the 0.2 M solution of pyruvate in D_2O until the pH settled at 5.9. To monitor this, a small solution of the original pyruvate solution, with a pH of 8.4, was added to a 5 mm NMR tube. Additionally, an equivalent tube containing the pH 5.9 solution was produced and a spectrum of each was collected in the weeks following the sample solution preparation. As can be seen, the uncorrected solution began to form subsequent peaks associated with the additional pyruvate derivatives present in the solution.

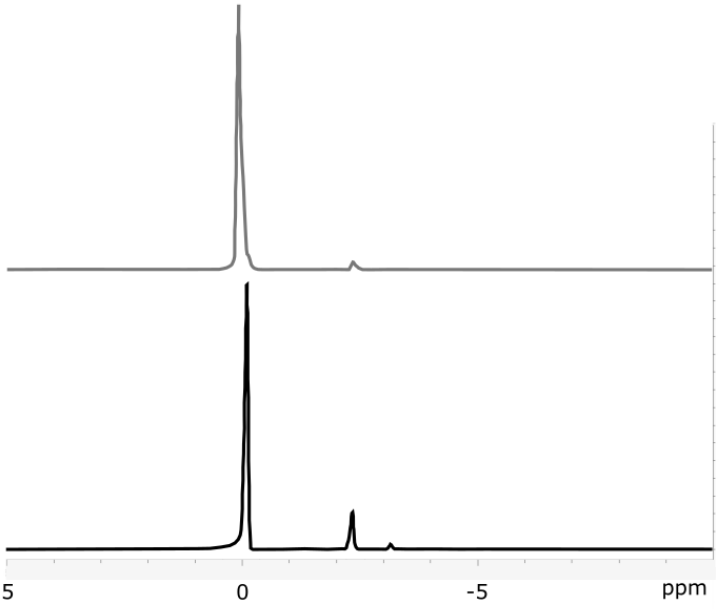

Figure 5.7: 1D spectra of pH-corrected pyruvate solution (grey line) and uncorrected pyruvate solution (black line) taken 7 days after sample preparation.

A blank sample of pyruvate-1-^{13}C was also produced to test the low-field apparatus. This was made by dissolving 40 mg of sodium-pyruvate-1-^{13}C in 500 μL of D_2O within a 5 mm OD Wilmad-Labglass pressure/vacuum valve NMR tube.

5.3.2 Sample preparation

Both the carbon cloth and paper came in large sheets and had a thickness of 0.31 mm and 0.17 mm respectively. In order to cover the active coil region, the solid samples were stacked to 22 mm requiring 70 disks of cloth and 120 disks of paper. When packing the tubes with the GDL disks, it was noted that there was excess space between each disk and packing was not optimised. Since diffusion along z was of principal importance, the packing density was increased by pressing the solid sample down with an insert and holding the disks in place. This was achieved via a cylindrical polyether ether ketone (PEEK) insert with an O-ring nestled in a groove to fix its position, and holes drilled to facilitate solution movement. There were three holes in total to improve fluid movement. Each hole went through the width of the insert and returned to the opposite face. The insert was designed such that there was sufficient space to capture any excess liquid and prevent it from forming a pool above the O-ring. Therefore, diffusion between the porous media region and excess bulk fluid was limited. Not visible in the diagram is the thread above the O-ring used for removing the insert. A PTFE rod with a threaded appendage was used to screw into the insert and pull it up.

Tube A was used for each sample preparation and simply washed prior to each degassing process. The tube B cap also had a threaded top meaning the whole sealed tube could be screwed onto the sample shuttling system and shuttled during the dual-core field-cycling methodology. All tubes were medium walled and internal pressures were kept above 1 atm such that any minor leakage would lead to gas escaping as opposed to oxygen-containing air leaking in. PEEK was used for the degassing apparatus tubes and insert due to its inert nature, so it would not interfere with the sample solution.

In order to increase relaxation times, paramagnetic relaxation was limited by removing any potential sources of paramagnetism. These include dissolved oxygen and metal ions resulting from equipment or contamination. As such, sample preparation was performed within a fume hood with plastic tools. The sample was degassed by bubbling with argon to displace all the oxygen in the solution. Argon was chosen owing to it being inert and more dense than oxygen. However, the solution could not be bubbled within the sample tube due to the presence of the GDL disks. Therefore, degassing was done via a custom-built in-house degassing set-up developed in the group by Giulia Melchiorre and depicted in Figure 5.9. The degassed solution was then transferred through a decontaminated system into the sample chamber, as explored further below.

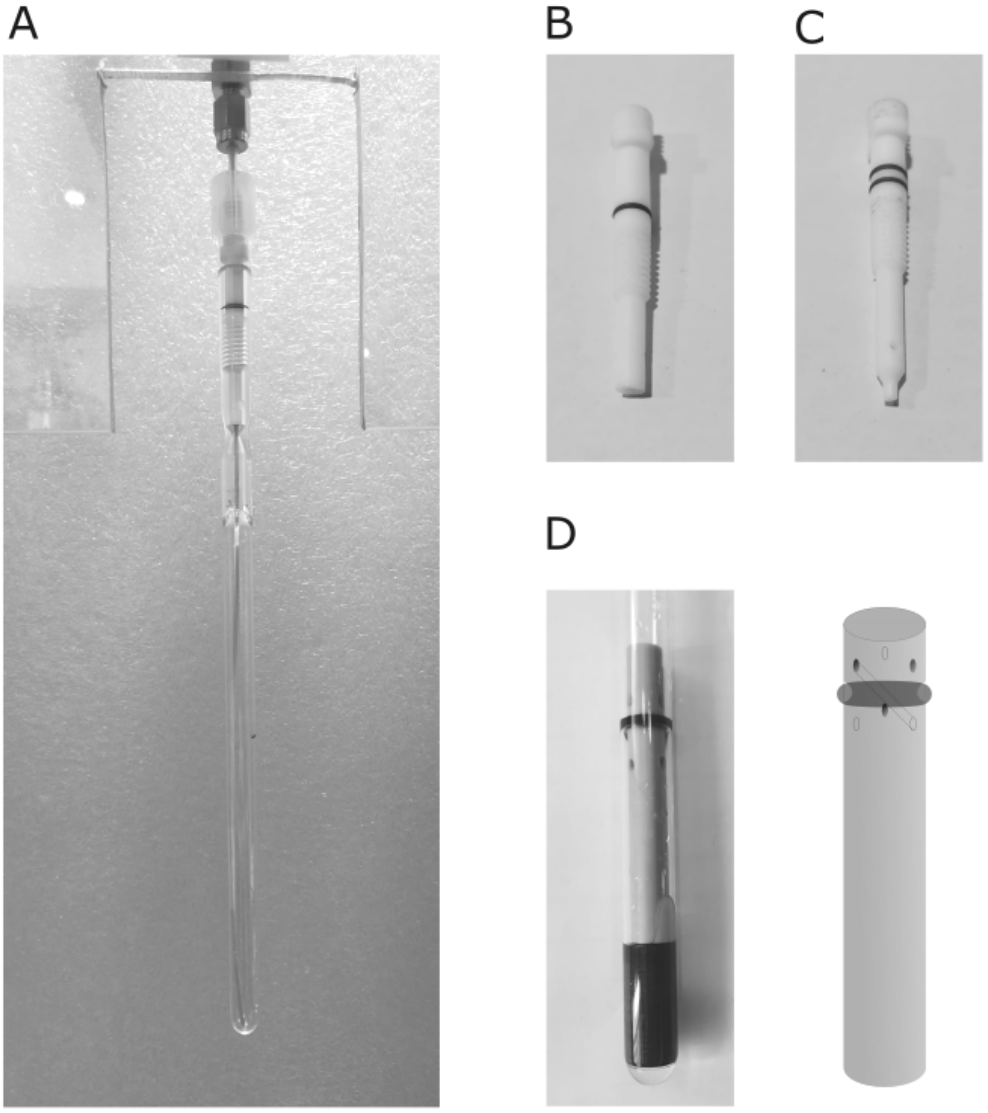

FIGURE 5.8: Images and schematic of the degassing system components and insert showing A) the degassing tube (tube A) fully set up, B) the cap used for tube A allowing the PEEK gas tube to be threading through it, C) the cap used for tube B showing a sealable tapered end with a hole for liquid movement prior to sealing, and D) the PEEK insert used to compact the GDL layers.

The rig was composed of lines for both vacuum and gas, or dual purpose lines, providing both a means of degassing the solution and transporting the liquid. Prior to use, the system was flushed with argon and vacuumed to remove any residual oxygen or contamination. A simplified explanation of the rig's operation is outlined below:

- The dry sample was fitted to the tube B inlet via a closed-end cap shown in Figure 5.8 C and purged by filling with argon, vacuuming, and repeating three times. The tube remained openly connected to the system and was left under vacuum,

- The solution, including the solute, was connected to the tube A inlet via an open-ended cap shown in Figure 5.8 B and bubbled through with argon for 10 minutes in tube A (Figure 5.8 A) to remove any residual oxygen,
- The vent was closed to introduce pressure in Tube A until the pressure exceeded 1 atm (to prevent any air entering the tube in the case of a faulty connection),
- The central 4-way valve was twisted to connect both tubes via the inside line,
- Upon opening the valve, the pressure difference drew the degassed liquid from tube A into tube B. Excess argon was sent into tube A via the outside line, pushing any liquid in the pipes into tube B,
- The white cap in tube B was screwed on completely to seal it. It could then be disconnected from the tube B inlet and put in the spectrometer.

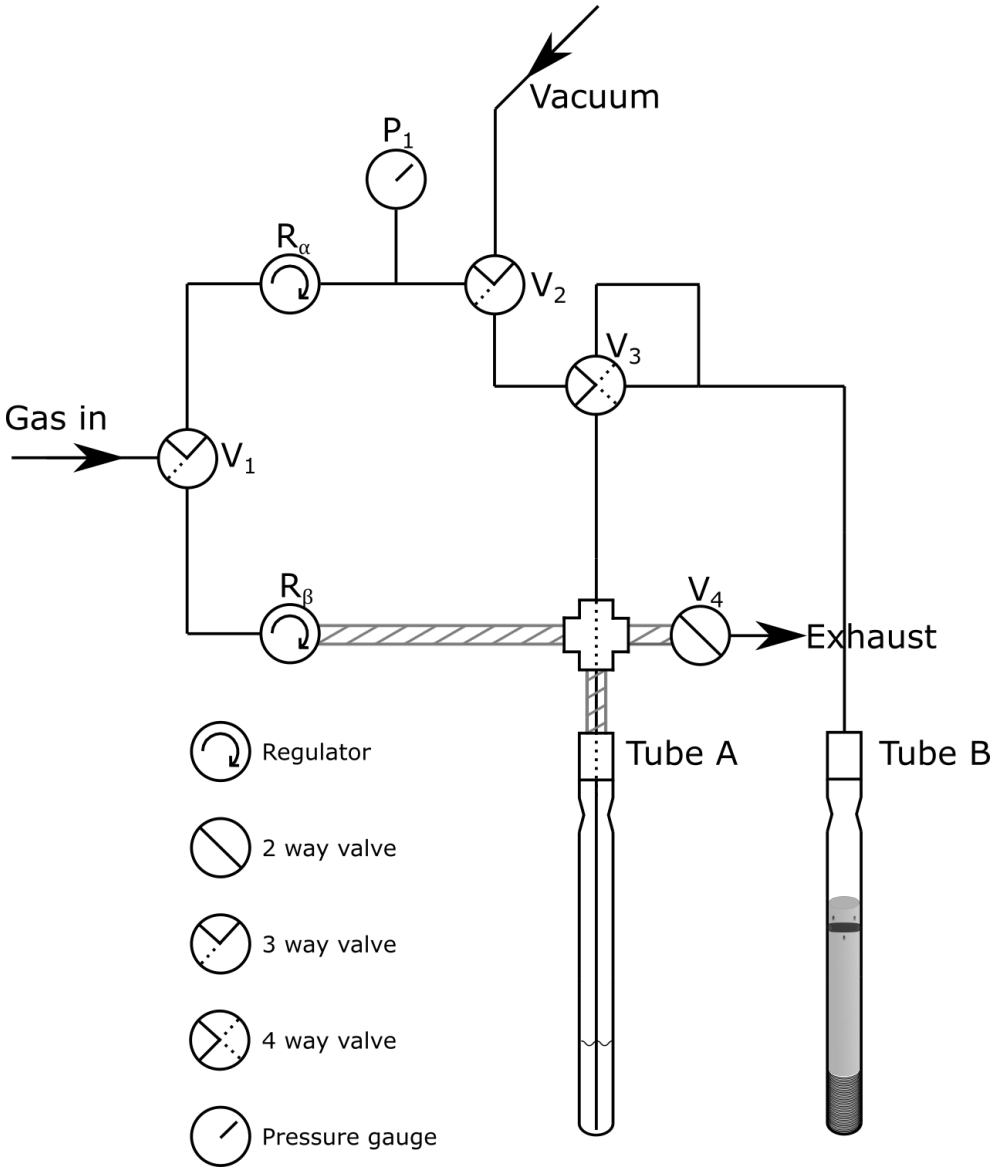

Figure 5.9: The degassing setup, showing the thin tubes for either liquid or gas transfer (solid black lines), where a dashed line is used to show the tube travelling through a joint or tube cap, and the outer gas bearing tube (grey dash filled line).

A "3 way valve" offers a right angle connection between any two adjacent tubes, where there are three initially connected. Thus, a "4 way valve" offers a right angle connection between any two adjacent tubes that would otherwise meet at a cross roads.

Prior to degassing, the solid insert was added to the tube by first detaching the valve from the main tube length via a glass cutter. The NMR tubes selected had built-in glass hemisphere inserts to maintain a flat bottom. The GDL was then packed onto this flat surface and compressed using the insert. The two sections of the tube were then fixed together such that the solid sample and insert sat below the pinch point of the valve. In this format, the tube was compatible with the degassing setup.

5.3.3 SEM imaging

The surface of the GDL disks was analysed using low vacuum SEM. The images were obtained using a Zeiss EVO LS 25 SEM equipped with a LaB6 filament. A 100 μm variable pressure aperture was used to prevent the need to sputter the samples with a conductive layer and a low-pressure methodology was adopted. The images were captured using SmartSEM software. The SEM operating conditions were 20 kV with a working distance of 10 mm for the vertical imaging and a beam current of 40.0 μA. A nominal I-probe current of 300 pA was used.

5.3.4 EDX imaging

In addition to SEM, EDX was also used to analyse the composition of the GDL surface as well as its architecture. This was achieved on an Oxford Instruments INCA 250 EDS, running INCA software and fitted within the SEM. Analysis was conducted on both the paper and cloth fibres, showing the composition of the disks. In addition to this, further analysis was conducted on any visible artefacts. Note that SEM did not require sputtering and so no heavy metal contamination were expected on the samples.

5.3.5 Data acquisition

For the acquisition of T_2 a version of CPMG pulse sequence, modified to work in a field-cycling mode, was used. A composite pulse is utilised to reduce inherent inhomoegeneity affects whilst at low field. As seen above, the central 180° pulse is cycled as with a standard CPMG pulse where the echo time is constant and the number of repetitions is cycled for each measurement. Since the low field pulses are cycled multiple times, a none compensated pulse would result in a build up of error. The echo time, τ, is kept deliberately short at 10 ms to limit the occurrence of DDIF. The number of

repetitions is taken from a user-defined variable list, optimised to produce a smooth curve. The normalised signal area is then plotted against:

$$S_{T_2}^{\mathrm{LF}}(n\tau) = Ae^{-n\tau/T_2^{LF}} \tag{5.3}$$

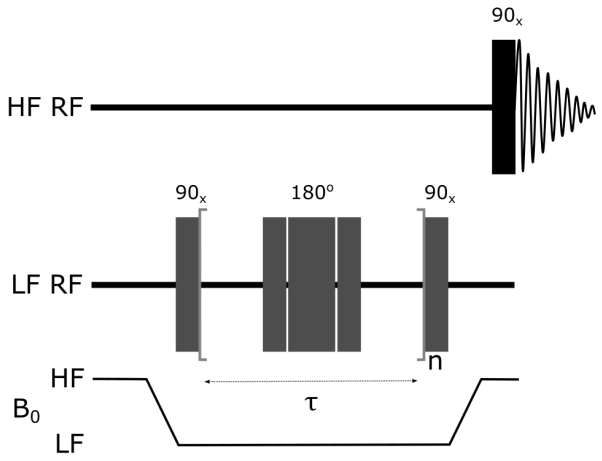

FIGURE 5.10: Pulse sequence used for the acquisition of transverse magnetisation in the dual-core set up. Where 180° represents a composite pulse formed of $90_x180_y90_x$.

To measure T_1, the field-cycling equivalent operates as an adaptation of the standard inversion recovery pulse sequence. In this case, the spins are flipped 180° and left to relax for a period, τ, after which a 90° pulse brings the magnetization to an observable plane. With this pulse sequence, one must wait an extended period of time (typically five times T_1) to ensure all residual magnetisation is abolished before repeating the experiment for the next delay period. This makes the overall experiment more time-consuming than the saturation recovery equivalent. However, given the novelty of the low field probe, and the possibility of temperature increase due to sample irradiation, it was determined that the more simplistic, slower inversion recovery pulse sequence was more suitable for the task at hand.

For the low field T_1 measurement, a composite pulse was not required as only one 180° pulse is performed and therefore the field inhomogeneities are negligible. The flip angle of the pulse, θ_x, is cycled between 0° and 180° while the receiver phase is also cycled the same way; this has the effect of cancelling out residual magnetisation that can potentially build up during transport between high and low field. The sample is transported to low field where the magnetisation is flipped by 180° and left to evolve for a variable time, τ. Within the evolution time, longitudinal magnetisation will begin to accumulate but is undetectable as it aligns with B_0. The final pulse, at high field, is the detection pulse to shift the remaining magnetisation to a detectable plane where it may be read. The normalised signal area is then fitted against:

$$S_{T_1}^{\mathrm{LF}} = A + Be^{-\tau/T_1^{LF}} \tag{5.4}$$

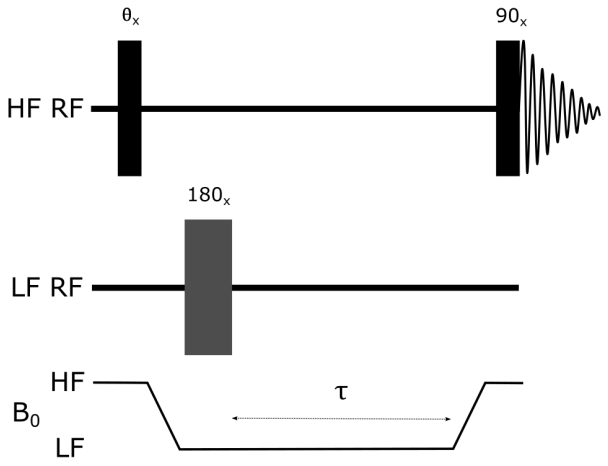

Figure 5.11: Pulse sequence used for the acquisition of longitudinal magnetisation in the dual-core set up.

5.4 Results and discussion

5.4.1 Low field probe

The work carried out in the preceding subsection was performed by T. Robertson (unless otherwise specified). Further details can be found in Robertson et al.[181]

Following rigorous testing to ensure correct shimming of the sample, and to calibrate the pulse length for a ^{13}C nucleus at 500 kHz, the field-cycling set-up was used to determine T_1 and T_2 within a blank sample.

Table 5.2: Relaxation rates of blank sample.

Relaxation rate	T_1^{HF} (s)	T_1^{LF} (s)	T_2^{HF} (s)	T_2^{LF} (s)
pyruvate-1-^{13}C in D_2O	64 ± 4	70 ± 2	9.5 ± 0.4	16.8 ± 0.6

From this, one can see the field dependence on both T_2 and T_1 with both increasing as the field decreases. The dependence of relaxation mechanisms on the external field has been discussed above and documented thoroughly in previous studies, showing that multiple relaxation mechanisms depend on B_0.[6] The low field methodology was also used to measure T_s but since singly labelled pyruvate is not a singlet hosting molecule, the experiments were run on another molecule and the results were not included here. However, this opens up the possibility of SAD-NMR, should the porous media of interest require the enhancements of both extended diffusion and low-field relaxation.

5.4.2 Carbon GDL preparations

The following work within this chapter was performed by myself as part of the thesis project.

In order to visually assess the GDL samples, SEM images were taken of both materials with the intent of assessing the size of the pores. Upon optical examination, the close-knit nature of the carbon cloth fibres implies an almost impenetrable surface with few diffusion pathways. However, upon closer inspection utilising SEM, it can be seen that pores of nearly 200 μm diameter exist within the structures. Unlike the scaffolds, these pores were not so clear and definitive, and still contained some intrusions in the form of stray fibres; however, there were clear pores through which molecules could diffuse.

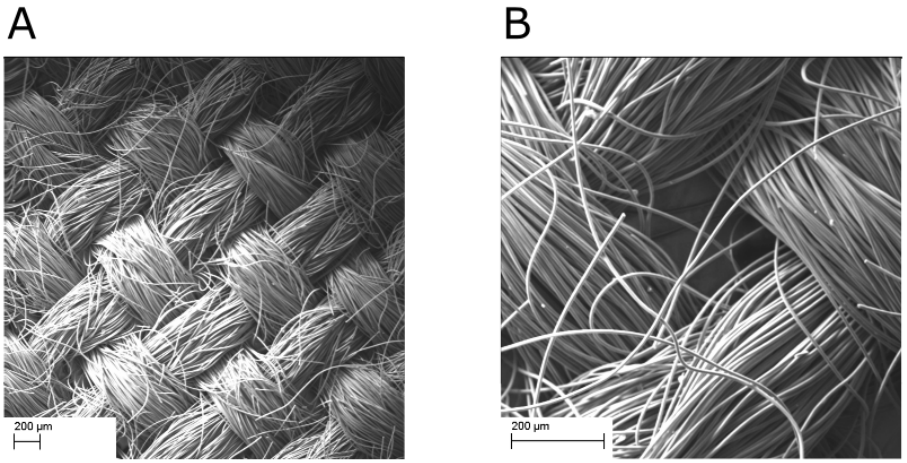

FIGURE 5.12: SEM images collected for a GDL cloth disk showing A) the surface structure and B) a typical pore.

On the contrary, the carbon paper had significantly smaller pores and demonstrated a far more compact architecture with PTFE webbing present between some of the fibres.

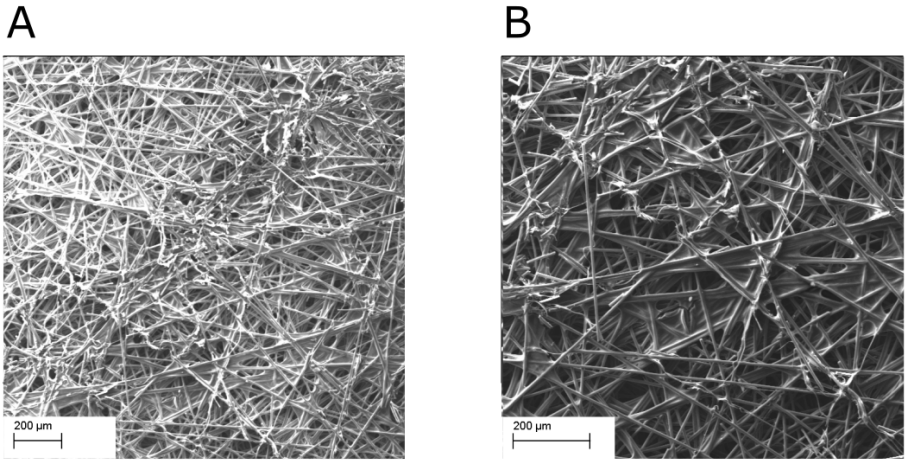

FIGURE 5.13: SEM images collected for a GDL paper disk showing A) the surface structure and B) a more zoomed display of the paper's pores.

EDX analysis was performed on the surface of both a carbon cloth and a paper disk in order to study the composition of the fibres.

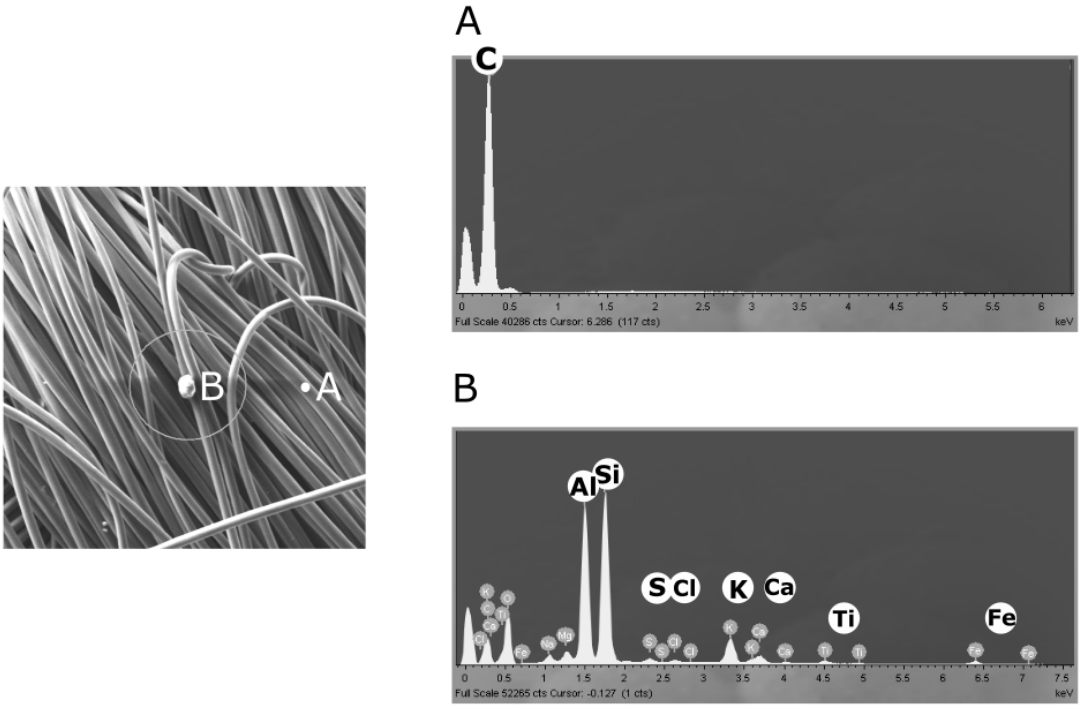

FIGURE 5.14: EDX analysis performed on the carbon cloth showing A) targeting on the carbon fibres themselves and B) targeting on the artefact present on one of the fibres. Also shown is a snippet of the cloth SEM image showing the approximate target location for both the fibre and artefact.

Upon initial SEM analysis, there was some evident contamination on the cloth in the form of bright spots on the surface of the fibres. These were further studied using EDX by targeting either the fibre or the contaminated spot. This was also done to compare the carbon paper fibres and the PTFE coating, webbed between some of the fibres.

EDX analysis on the carbon cloth showed the carbon fibre being predominately carbon, including a standard background noise peak present at zero keV. On the contrary, the contamination artefact held a wealth of atoms including a number of paramagnetic nuclei including iron and titanium. The unannotated peaks corresponded to many of the shown metals but also carbon, oxygen, sodium, and magnesium. The actual artefact and why it was present were not determined; however, upon inspection of the disk's surface, there were no other contaminations of this nature. Due to the presence of paramagnetic nuclei, it is expected that this form of contaminants would reduce the NMR signal through PRE. Should the diffusion simulation be performed on a digital reconstruction of the cloth disk it would not be subject to PRE effects.

Analysis of the paper and its coating showed the fibres also being composed of predominately carbon, with a slight amount of fluorine due to the coating. Alternatively, the

coating was mostly comprised of fluorine due to PTFE's monomer consisting of C_2F_4. However, the peak does not appear to have twice the fluorine compared to carbon due to the presence of the carbon fibres themselves. No contamination was seen.

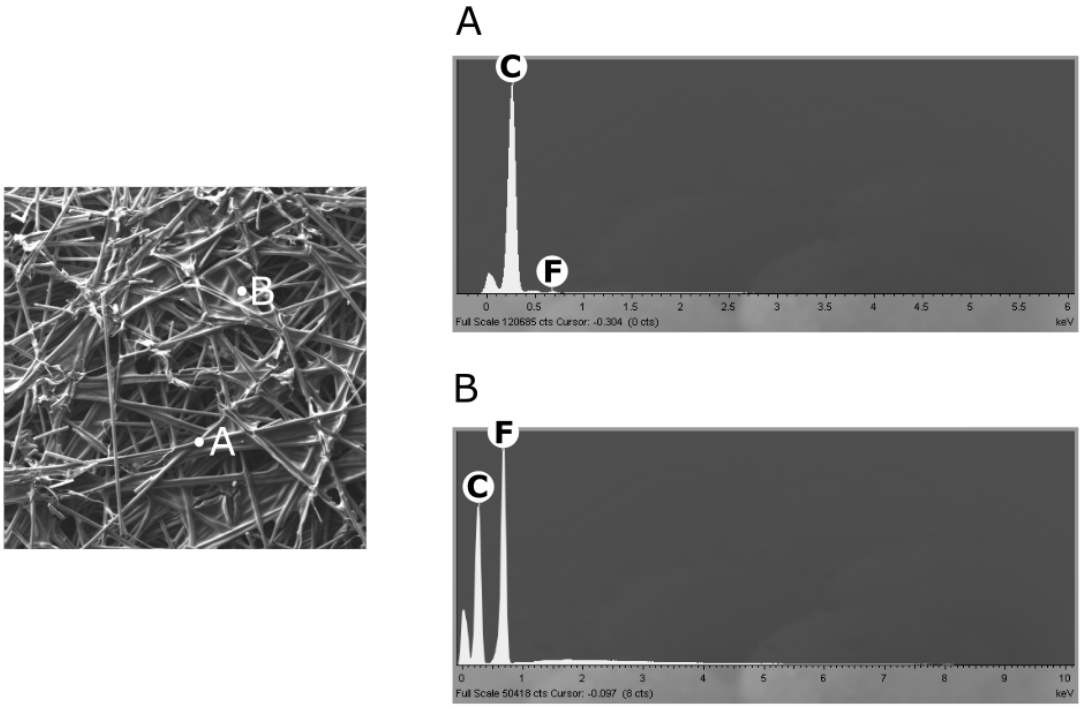

FIGURE 5.15: EDX analysis performed on the carbon paper showing A) targeting on the carbon fibres them selves and B) targeting on the PTFE coating present between a series of fibres. Also shown is a snippet of the paper SEM image showing the approximate target location for both the fibre and coating.

Following surface analysis the cut disks were packed into the specific LF NMR tubes, compacted using the insert, and the tube was resealed. Prior to filling the degassing set-up was tested to determine the desired quantity of liquid needed to fill the GDL containing tube. Initially, a replica tube, with a flat hemisphere base but open top, was filled with either 120 paper or 70 cloth disks and compressed with the insert. The tube was then filled with aliquotes of D_2O until the sample region was completely submerged and there were no evident air bubbles within the centre of the sample region. This was done for both the paper and the cloth and resulted in a minimum requirement of 1000 μL of solution for the cloth and 750 μL for the paper.

Following this, a study was conducted to determine the liquid lost during the transfer of the degassing process. For this, the sample was assembled within the degassing NMR tubes and the tubes were reattached to their valve-containing counterparts. Both tubes A and B were weighed when empty and tube A was weighed again following the addition of a known volume of D_2O. The degassing set-up was conducted as described above, after which the two tubes were weighed again. The transfer percentage and loss percentage were then calculated using the weights. This was repeated twice

more to determine the average transfer percentage. This, in addition to the minimum required volume, was used to determine the required amount of solution to make the final pyruvate-containing sample. An example of this is shown below:

Table 5.3: Liquid transfer percentage study of the degassing set-up.

	System	Value	Unit
Pre fill	Tube A empty	18.37	g
	Tube B empty	24.13	g
	Tube A full	19.25	g
	Tube A liquid	0.88	g
Post fill	Tube A full	18.39	g
	Tube A liquid	0.02	g
	Tube B full	24.68	g
	Tube B liquid	0.55	g
	Transfer rate	62.5	%

From the study, it was determined that an excess 40 % of liquid was required meaning solutions of 1.4 mL and 1.05 mL were required for the paper and the cloth respectively.

5.4.3 Carbon GDL experiments

Prior to testing the porous samples, the blank pyruvate sample was used to calibrate and shim the sample. After which, porous media samples were produced as outlined above. Upon initial experiments, it was evident that there was insufficient signal within the GDL samples for accurate diffusion measurements. Acquiring a simple 1D spectrum, after shimming on the blank sample, produced a small peak with poor resolution. This was a combination of the limited concentration of pyruvate in the solution and the lack of solution present within the sample due to porous media. Despite collecting the spectrum at a field of 9.4 T, and performing eight scans, there was still insufficient signal for any extensive data analysis. To perform diffusion tensor imaging, the diffusion experiment would need to be run for many scans, for a whole series of diffusion times, over at least six independent diffusion directions, as mentioned earlier. The total experimental time would be too great to warrant any reasonable data being collected on this sample without first considering altering its make up or composition.

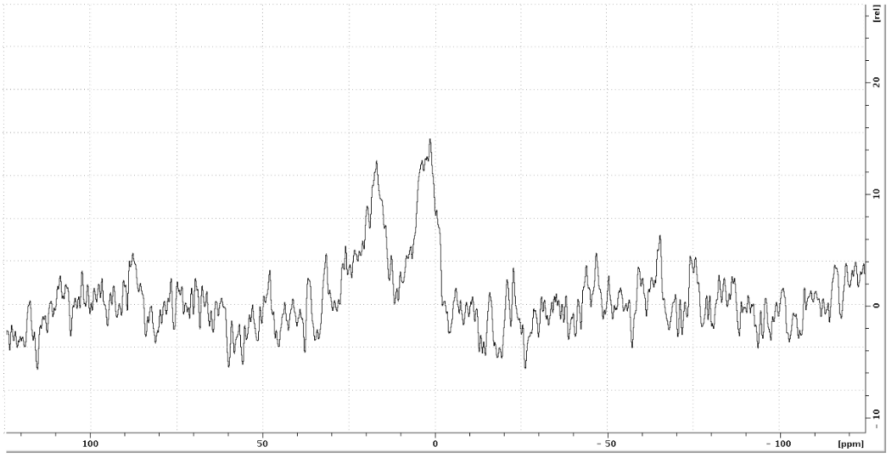

FIGURE 5.16: ^{13}C spectrum collected on a 0.4 M solution of sodium pyruvate-1-^{13}C in a degassed carbon paper sample.

Unfortunately, due to technical issues, both the low field probe and glass blowers were non-operational for an extended period of time, following these initial assessments, and there was insufficient time to change the sample to a more suitable material. Such a sample would have to have larger pores such that a greater volume of liquid could be used, meaning a larger number of nuclear spins are present to be observed. Alternatively, the solution could be changed to increase the concentration. A more drastic approach would be to use a molecule with a greater solubility meaning the solution could be further concentrated.

5.5 Conclusion

This chapter introduced a range of techniques and methodologies developed within both this project and this group as a whole. Firstly, the low field probe was presented including a schematic of the system as a whole and its integration in and around the current spectrometer. The operation of the dual-core set-up was also described, including the calibration of the systems shimming, and details of the low-field adapted pulse sequences. Further advancements of the low field probe, including the integration of singlet measurements, were also touched upon.

Additionally, this chapter contained a description of the hardware developed specifically for degassing solutions containing porous media. This involved details of how the glass tubes were designed and subsequently split and then joined together to insert the porous media below the tubes' bottleneck. The efficiency of the degassing set-up was tested to determine the percentage transfer rate of degassed liquid going into the porous media-containing tube.

The dual-core probe was used initially to shim and calibrate a blank sample prior to experimenting on the porous media. Unfortunately, due to complications arising in both the hardware and the sample tubes, a thorough exploration of the GDLs was not possible. However, possible alternatives and mitigations were discussed in preparation for future experiments.

Chapter 6

Applications of tortuosity in porous cellular scaffolds

This chapter is an extended version of T. A. A. Cartlidge, Y. Wu, T. Robertson, O. L. Katsamenis, and G. Pileio, 2024, *in press*.[226]

6.1 Synopsis

This chapter is an overview of the work carried out in order to fulfil objective four.

O$_4$ - Demonstrate the technique by applying both the simulation and the methodology to porous media that are of greater real-world significance and or importance.

The purpose of this chapter is to introduce future applications of the field cycling technique and progressions made towards solidifying these in porous media of significant importance. The following sections detail the selection of a material with real-world applications, namely 3D-printed scaffolds hosting cell cultures. This chapter also outlines multiple methodologies used to produce the samples and describes preparations used to enhance the samples for their current use. Lastly, this chapter explores the possibility of calculating diffusion within these samples via a computational approach.

6.2 Introduction

An ever-increasingly important aspect of the biomedical sciences is the introduction of lab-grown cell cultures for applications in tissue engineering.[227] The current remedy for bone fractures and defects is an invasive surgery involving metal implants and tools whereas tissue engineering offers an alternative in clinical therapy, with no removal surgery and potentially lowered costs.[228] The process of seeding bio-compatible scaffolds with stem cells is a fast-growing practice and often incorporates 3D structures for the cells to grow onto. These 3D scaffolds provide a micro-environment mimicking that which would be found *in vivo*.[98] Not only do the scaffolds provide structural support they also shape the tissue culture and ensure adequate diffusion pathways for both the delivery of nutrients and the removal of waste.[98] The latter is directly related to both the porosity and tortuosity within the cell culture, making these an imperative system for studying diffusion through porous media. Insufficient diffusion pathways can lead to the development of necrotic cores, which are directly impacted by the structure of the scaffold.[114] The scaffold design is also responsible for the adhesion and proliferation of cells, and scaffolds can vary in pore size, density, shape, and connectivity.[229] Due to the delicate nature of cell cultures and their requirements for such specific growth conditions, qualitative studies on scaffold design as a function of cell growth are difficult to perform. However, diffusion- NMR offers the opportunity to measure both diffusion and tortuosity in *in vitro* systems, offering a means to test scaffold design suitability.

The human body is composed of trillions of cells, each representing life in its simplest form and built up to form one large, complex, and intelligent being. Each cell is a perfectly balanced mixture of cytoplasm, proteins, and DNA yet each is so very specialised to its specific task. The roles played by cells, and their abilities and characteristics are used to divide them up into 215 different types of cells.[230] These types include; contractile cells which change their shape such as muscular cells; supporting cells such as astrocytes found in the central nervous system; and iron-transporting cells for balancing electrolyte concentrations, to name a few.[230] Not to mention a whole host of protein-secreting cells that can be subdivided further into immunity cells secreting cytokines and luminal protein-secreting cells that aid in digestion.[230] The most relevant and extraordinary cell type is stem cells: a class of regenerative cells that can differentiate into other cell types given the correct environment and growth stimuli.[231] A cell that differentiates into any other form of cell is called pluripotent whereas multipotent cells have the ability to differentiate into a particular lineage of cells.[232] An example of this is a human mesenchymal stem cell (HMSC) which can differentiate into muscle, bone, cartilage, connective tissue, marrow stroma, and other mesenchymal tissues.[232]

HMSC cells are a versatile cell line and have previously been used to treat bone fractures and defects as well as non-skeletal diseases.[233] The cells can be isolated due to

their adhesion to plastic surfaces and during culturing, can differentiate into a range of cells when exposed to the right environment or growth factors. The application of HMSCs is achieved through injections straight to the site of injury or grown on a scaffold and later inserted into the patient.[233] An example of this is a trachea replacement given to a rabbit by growing cells on a polycaprolactone (PCL), separated-ring structure.[234] The scaffold in this case had to be a very specific structure to ensure the tissue culture was of a suitable shape to replace the trachea, and of a material that was biocompatible. Owing to its biodegradability and bio-compatibility, PCL is a promising scaffold material for the ultimate aim of replacing tissue and organ transplants.[235,236]

The purpose of the scaffold is to situate the cells within an environment highly similar to that which would be found *in vivo*. This allows for the ideal conditions for differentiation into the desired phenotype.[237] The production of a suitable scaffold, seeded with stem cells, leads to the possibility of a bone graft: the implantation of bone material to repair fractures or sites previously damaged by disease.[238] Cells grown on the surface of the implanted scaffold can induce new bone formation at the site of insertion as they are responsible for biomineralisation and producing bone collagen.[239] Current methods include taking alternative bone material from within the patients but this can result in pain, scarring, blood loss, and other disadvantageous side effects.[238] Thus, bone grafting via scaffold cultures offers an alternative, less invasive surgical remedy.

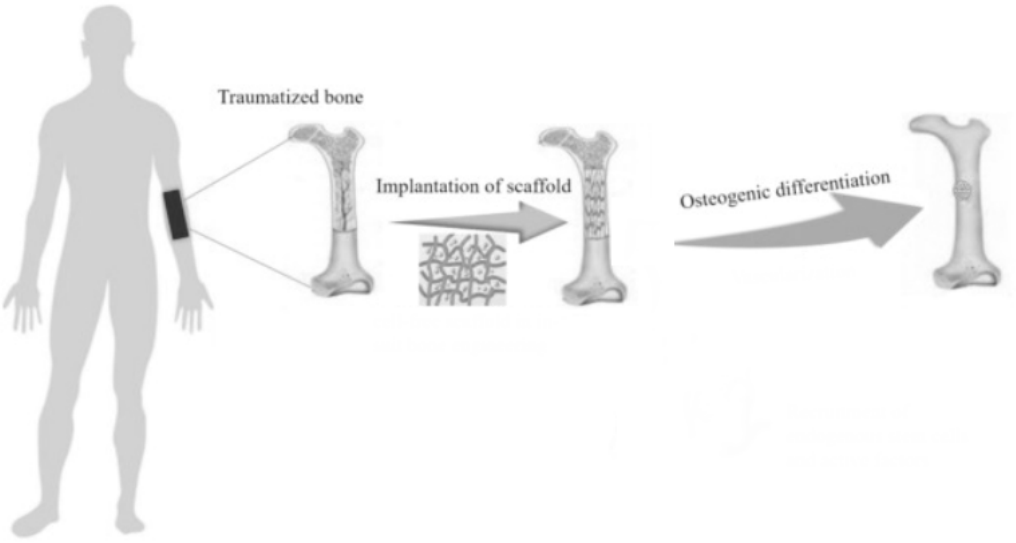

Figure 6.1: Example of a scaffold used for bone regeneration, adapted from.[240]

PCL is a versatile material, suitable for tissue engineering due to its biocompatibility and biodegradability, with the plastic being metabolised in three years.[241] There are multiple ways of producing PCL scaffolds which depend on the desired characteristics of the product. Possibly the most used technique is 3D printing; based on

forcing molten plastic through a nozzle to build a structure layer by layer, these include fused deposition modelling (FDM) and direct ink writing (DIW).[242] Alternatively, some methods use lasers to fuse plastic particles together, such methods include selective laser sintering (SLS) and particle binding (PB).[242] 3D printing offers a very selective and specific scaffold production method where the pore sizes and shapes can be carefully selected. An alternative method is electrospinning a fibrous polymer solution, with the intent of producing either nano or micro-width fibres. The solution is fired onto a collector plate by applying a high voltage to the capillary tube whilst pumping the solution into the tube. When the electrostatic forces of repulsion exceed the surface tension of the droplet, a thin liquid jet is propelled towards the plate.[241]

The application of 3D printed PCL scaffolds has advanced to incorporate silver nanoparticles within the pre-scaffold solution, producing a mesh with evenly distributed metal particles.[243] Since silver has previously exhibited antibacterial properties,[244] and with orthopaedic implants having a history of causing infection,[245] this offers a potential possibility of sterile scaffolds. However, porous scaffolds are not limited to tissue regeneration applications, they are also a principal aspect of cultured meat.[246] In this case, the scaffolds are often made of porous glutenin sponges with pore sizes ranging from 50 to 250 um. These scaffolds are suitable for use in food and do not require additional surface adhesion treatments, making them ideal candidates for food production. On top of the normal scaffold designs, these scaffolds must also meet the required palatable needs, adding an additional complication to their production. Furthermore, careful preparation of the scaffolds is required as incorrect pretreatment may lead to unstable configurations and the structures dissolving in water.[246]

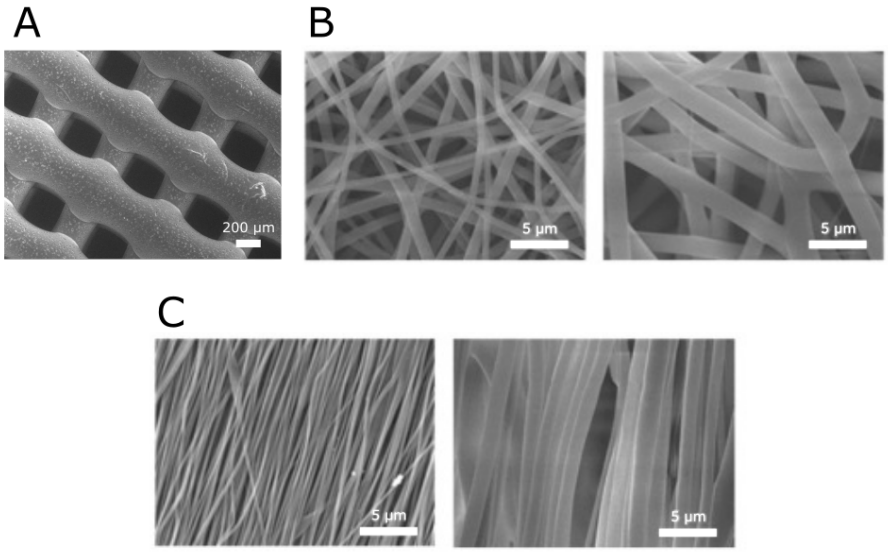

Figure 6.2: Examples of 3D PCL scaffold structures showing A) 3D printed scaffold, B) electrospun random fibres and C) electrospun aligned fibres, taken from.[247]

As we have seen, scaffolds can be a range of materials including solid plastic fibres, sponges, hydrogels, or even a combination: hydrogels with embedded polycaprolactone fibres.[236,246,248,249] The sponges exhibited pores which are, on average, 0 - 100 μm in diameter, with the majority below 50 μm.[246] However, the application of differentiating HMSCs into osteoblasts for bone tissue requires larger pores than this. Roosa et al saw more consistency in their bone in-growth where the scaffold had pores greater than 300 μm.[250] As for the hydrogels, they lack the mechanical properties present in an *in vivo* environment and additional work is required to push their mechanics to mirror those of cartilage or bone. Finally, PCL scaffolds offer the structural needs and pore specificity required to produce bone tissue. They are elastic and biodegradable and can be 3D printed into a range of shapes and structures, before seeding with HMSCs.[235,248]

HMSC have widespread applications and pose as an exciting potential substitution for tissue replacements and transplants; however, their culturing is naturally limited *in vitro*. The majority of stem cells are embryonic, which can differentiate into any cell lineage: a vital characteristic when developing a new life.[251] Due to ethical reasons, obtaining HMSCs from adults is a far more exercised method with the primary point of harvesting being the iliac crest, or hip bone.[252] This method of growing cell lines is, therefore, dependent on donors and potentially gives rise to samples with varying phenotypes and genotypes. Once harvested, these stem cells cannot be continuously propagated to produce stable samples as HMSCs loses potency when cultured for high numbers of passages.[251] And when they are cultured, their proliferation capacity is highly dependent on the donor's age.[253] As a result, though incredibly useful, stem cells may be difficult to obtain in sufficient numbers for some *in vitro* applications. This can be overcome to some degree via forced over-expression of certain genes to increase chromosomal stability;[254] however, the genetic mutation of stem cells is not a favourable attribute when aspiring to implant the cell culture within a patient.[253]

A promising substitute for evaluating 3D culturing techniques is the murine calvarial pre-osteoblast cell line (MC3T3-E1) which has proven its worth within the field of osteoblast biology.[255,256] Within this cell line, there have been 52 identified single-cell sub-clones, which can be grouped into categories based on their mineralising characteristics.[257] Particular sub-clones produce more alkaline phosphatase (ALP), a common marker for osteogenic differentiation.[258] The specific sub-clone can cause great discrepancies between the proliferation of MC3T3-E1 cultures.[255] This cell line has already been used in 3D culture studies, having been used to propagate both nanofibrous and solid-walled scaffolds.[259] Woo *et al.* grew MC3T3-E1 on both scaffold types and saw two orders of magnitude more bone sialoprotein (BSP) expression from the nanofibrous scaffold culture compared to the solid walled scaffold.[259] Indicating a greater expression of osteoblastic phenotypes,[260] and therefore mineralization, the final stage in the process of osteoblast differentiation.[261]

6.2.1 Cell growth limitations

With the goal of seeding scaffolds, one must first culture sufficient cells to populate the 3D structure. In order to do so, 2D cultures are cultivated and regularly counted requiring the cells to be detached from their culture flask to either be cultured in less dense flasks or transferred to the scaffolds. Detachment is done via trypsin, which breaks down the attachment proteins holding the cells to the surface. Unfortunately, prolonged exposure to trypsin can result in damage to the cell membranes.[262] It is therefore imperative to only expose cells to trypsin in small, monitored doses.

It has been noted that tissue engineering is currently affected by two substantial obstacles: even cell distribution during seeding, and sustaining tissues through adequate nutrient supply pathways.[3] In previous studies, it was noted that seeded cells mainly adhere to either the bottom of the well plate or only the bottom of the scaffold and do not distribute on the majority of the scaffold.[263] In order to prevent this, many studies have explored the possibility of coating the scaffolds with a layer of calcium phosphate apatite which the cells have a far greater affinity for.[264,265] SEM images showed homogeneous nucleation of the apatite to the surface of the scaffolds with the cells preferring to adhere to the coated scaffolds.[227] A recent study by Cámara-Torres *et al.*, focused on targeting the cell suspension by increasing the viscosity of the media, preventing the cells from sinking to the bottom before attaching to the scaffolds.[263] Their work involved adding sufficient density gradient media such that the solution was of equal density to that of the cells. With the cells no longer sinking during seeding, their results showed an even distribution of cells across the whole scaffold.

As for the scaffold, one study determined that a pore size of 300-400 μm was optimal for bone formation[266] but optimising the 3D architecture of the scaffold is far from perfect.[267] Where cells growing *in vivo* benefit from the constant supply of nutrients delivered by the cardiovascular system, *in vitro* grown tissue cultures are not afforded such luxury. Scaffold-based tissues must rely on molecular diffusion for both the supply of nutrients and removal of bio-waste else the centre most cells will deteriorate forming a necrotic core.[114] Such diffusion is a direct product of the pore network and tortuosity[2,268] formed by the scaffold and growing cells. Although the tortuosity of the scaffold may be readily determined, the cell pattern afforded by the scaffold forms a time-dependent structure which is less readily probed. It is therefore beneficial to have techniques capable of determining tortuosity to aid in future scaffold design.

6.2.2 Scaffold coating

Although PCL is a versatile and well-suited polymer for bioengineering, there are limitations to cell attachment when working with plastics. As a result of this, methods have been produced to enhance attachment and lead to better-distributed cells within

scaffolds. This can be done with both bio and inorganic techniques by coating the scaffold in a material that the cells have a high affinity for. As well as being beneficial for cell attachment, this coating must not interfere with the growth of the culture, or the ability of the cells to differentiate or perform mineralisation.

Like most plastics, PCL is a relatively inert material and must therefore be pre-treated to increase the reactivity of its surface. This can be done by introducing more reactive groups to the plastics' surface layer, via reactive ion etching (RIE). This is a plasma-based technique that involves bombarding the sample surface with reactive radicals. Initially, the sample chamber is vacuumed to create a low-pressure environment into which the selected gas can be released. The gaseous molecules are ionised and form a plasma as their electrons are stripped. The highly reactive molecules are then free to interact with the sample surface. In the case of PCL, the closed, inert polymer can be functionalised to expose polar groups on the plastic surface,[269] which can drastically change the properties of the material. This is achieved by replacing the inert species with more reactive carbonyl, carboxylic, or hydroxyl groups.[270] PCL can be transformed from a low bioreactive, hydrophobic material to one with a more reactive, hydrophilic surface.[269,271] Alterations in the micro and nanostructure of plasma-treated scaffolds can produce benefits such as cell proliferation and adhesion.[271]

Once the surface has been activated, the scaffolds can be treated with a solution of simulated body fluid (SBF) with the intention of coating them in a layer of calcium phosphate. SBF is a solution of inorganic salts with an ion concentration mimicking that of human blood plasma, that has been perfected through iterative testing to produce stable solutions.[265] Other groups have since enhanced the ion concentrations to produce a more rapid coating of scaffolds.[272] Upon exposing certain surfaces to the solution, a layer of calcium phosphate apatite will form, producing a medium through which living bone will attach *in vivo*.[273] This apatite has previously been shown to significantly enhance the attachment of bone tissue onto coated ceramics.[274]

Table 6.1: Typical human blood plasma ion concentrations

Ion	Concentration / mM
Na^+	142.0
K^+	5.0
Mg^{2+}	1.5
Ca^{2+}	2.5
Cl^-	103.0
HCO_3^-	27.0
HPO_4^{2-}	1.0
SO_4^{2-}	0.5

An alternative method is to coat the scaffolds in a biological material, such as bovine fibronectin protein (BFP), to mimic the *in vivo* environment. Prior to surface treatment, cell adhesion is mediated through the extracellular matrix (ECM) and its proteins, and is dependent on surface roughness, chemical composition, and micro-porosity.[275] In the case of fibronectin, the cells are exposed to a surface already coated in one of the major components in the ECM, making this an ideal surface for cell attachment.[276]

6.2.2.1 Bioreactors

An alternative propagation method to culturing scaffolds manually is to use a bioreactor. The purpose of these is to continuously refresh the media, preventing the need to expose the samples on a regular basis and risk contamination. Typically, the growth media would need to be refreshed every other day, involving removing the samples from the incubator, opening them within a fume hood, and replacing the media. However, the bioreactor possesses a large media reservoir, eliminating the need to continuously refresh the liquid and expose the cells to an unsterile environment

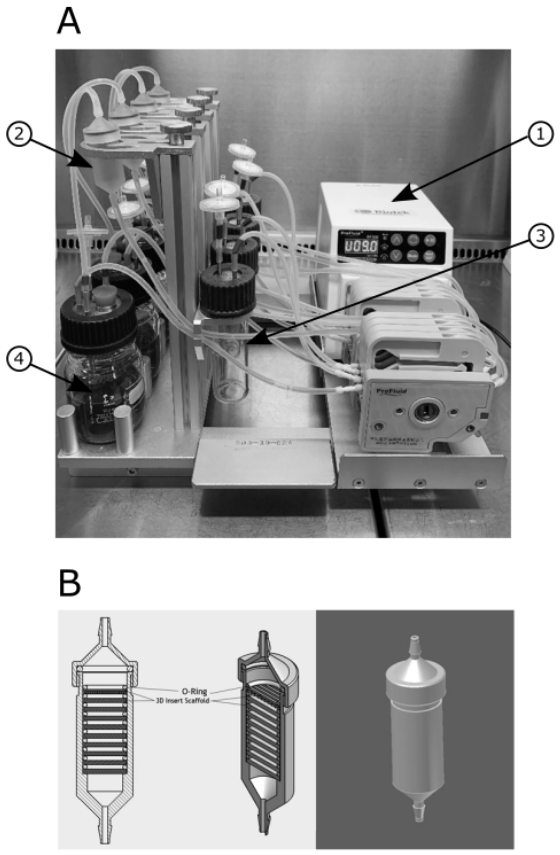

FIGURE 6.3: Bioreactor showing A) the full assembly with the pump (1), sample chamber (2), CO_2 humidifier (3), culture media reservoir (4), and B) the internal structure of the sample chamber showing the positioning of the scaffolds, taken from.[277]

Another advantage of bioreactors is the improved mass transport of nutrients: manually propagated scaffolds rely on slow diffusion mechanisms but bioreactors have active flow of culture media, continuously replenishing nutrients and removing waste.[278] Lastly, various biosensors can be integrated into the system for real time analysis of many variables such as pH, oxygen concentration, and glucose levels.[279]

6.2.3 Cell imaging

The process of culturing cells is a meticulous and precise operation, involving stringent, sterile techniques to maintain healthy and plentiful cell proliferation. Due to the requirements for enclosed, sterile conditions, they are often difficult to monitor or observe in a time-dependent fashion. There are a number of imaging techniques but those that offer probing, three-dimensional results do not allow for the continued growth of cultures following spectroscopic analysis. Alternatively, those that can be done in situ lack the ability to explore the sample in 3D. As such, analysis of tissue cultures may require innovative analytical methods, or the use of simulations to bridge the gap between visualising the empty scaffold and studying the final tissue culture.

One of the major requirements for tissue engineering is mimicking the ECM of bone, which is mostly comprised of collagen.[228] The matrix of proteins is formed of either parallel or bundled fibres ranging from 20 to 500 nm.[280] Unfortunately, due to their delicate nature, cell cultures are prone to breakage when exposed to vacuums, with the cell membrane of individual cells breaking,[281] leaving a microstructure scaffold of ECM with an empty cell component.[282] Alternatively, the microstructure of the ECM may be damaged by vacuums in weaker tissues.[281] This, combined with the possibility of cell shrinkage following fixation,[283] introduces errors in collected images as the cells do not exist in an identical format to *in vivo* cells.

Unfortunately, this is a relatively small issue given the other complications arising from imaging cells. Fluorescence microscopy is a valuable tool for the real-time imaging of tagged molecules within a cell culture.[284] For this technique, fluorescently labelled proteins are introduced to the culture and allow for the study of dynamic processes within tissue.[285] Alternatively, fluorescence can be obtained by the enzymatic conversion of non-fluorescent precursor molecules into fluorescent ones only in living cells, producing a means of measuring the viability of cells.[237] The main disadvantage of this 2D technique is the possibility of photobleaching which occurs when excited fluorophores release reactive oxygen species, capable of damaging neighbouring proteins and nucleic acids.[284] Some techniques have advanced to using a spatially dependant light source to limit photobleaching; however, it cannot be entirely avoided.[284]

A popular tissue imaging procedure, capable of 3D imaging, is second-harmonic generation imaging microscopy (SHG), a selective technique for the imaging for certain

biological structures. The requirement for SHG is a material that does not contain an inversion point and is therefore non-centrosymmetric, mainly collagen.[286] Besides its selectivity, SHG offers advantages over other imaging techniques as it does not require the use of molecular labelling, and can be used to produce 3D images.[287] By using higher, more penetrating energy sources, deeper tissue planes can be imaged and used to construct a 3D image.[288] Contrast is produced within images based on the type, alignment, and density of collagen fibrils.[288] Although SHG is a powerful tool for *in vivo* applications,[289] the selectivity of the technique does not lend itself to the study of scaffold design given the versatility available in scaffold composition.

A range of spectroscopic and microscopic techniques exist for the imagery of cell cultures, each with its own advantages and disadvantages. As well as imaging the cells and their proteins, some techniques exist for targeting specific cell characteristics. For example, transmission electron microscopy (TEM) can be used to study the presence of calcium phosphate and other mineral deposits within cells.[290] The Resolution of the technique allows for the analysis of elemental composition within mitochondrial granules.[290] However, this technique is utilised on thin sections, allowing only the analysis of one plane of cells, all be it in very high resolution, down to subnanometer.[291]

Two reoccurring methodologies used through these works are μ-CT and SEM, which have both been imperative for the studies at hand, but each limited in their own way. Although SEM can be used for high-quality surface analysis, it is destructive to the sample and as mentioned, the use of a vacuum is potentially damaging to the fixed culture. The same is true for μ-CT which can be used to produce high-resolution 3D reconstructions of samples yet requires destructive preparation techniques.

An alternative to physical imagery is simulated reconstruction; however, this often requires destructive methods for structural analysis. Previous computational studies have adopted one of two methods to recreate the digitized porous structure. As well as using X-rays or scanning laser microscopy, there is the possibility of reconstructing the media via statistical means.[68] Within a random and/or predictable material, a close-fitting micro-structure can be generated in a far more cost-effective and simple manner than physically scanning the porous media. As will be seen, the unpredictability of cell culture growth does not lend itself well to the statistical models and therefore this is not a fitting method to digitise the internal structure of the samples produced below.

6.3 Materials and methods

The work carried out in the preceding section is contained within the overall research project but was not within the scope of this PhD and was performed in parts with the assistance of Y. Wu (unless otherwise specified).

6.3.1 Cell preparation

Mouse osteoblastic cells (MOC) cells were obtained from the Institute for Developmental Science (IDS), Southampton General Hospital (Southampton, UK). They came frozen in a vial and were stored temporarily within dry ice until they were ready to be used. Prior to thawing, all necessary solutions and growth serums were prepared including the Basal media. This being a solution of 10% fetal bovine serum (FBS), 1% penicillin-streptomycin solution (PS), and 89 % GibcoTM Dulbecco's Modified Eagle Medium (DMEM) (the first of which was purchased from Sigma-Aldrich, the second two from Fisher Scientific). Where DMEM is a commonly used basal media for culturing mammalian cells. The solution provided the base environment within which the cells could grow. It contained sufficient growth nutrients, from the DMEM, and antibiotics to prevent infection and therefore death of the cultivation. Before use, the solution was warmed in a water bath at 37 °C. In addition to this, is was best practice to divide, into aliquotes, the remaining necessary solutions. This included portioning 2 ml vials of trypsin-EDTA solution, and 5 ml portions of phosphate buffered saline (PBS), both purchased from Sigma-Aldrich, and storing in the fridge until further use. It is to be mentioned here that in all solutions were pre-warmed to 37 °C, unless otherwise specified. Once complete, the cells were ready to be thawed.

The act of thawing the cells was carried out completely and quickly to ensure minimal stress to the cells themselves. The vial was therefore taken from dry ice storage and placed directly into a water bath of 37 °C with the previously prepared Basal media. Once fully thawed, the cells were transferred to a clean and sterile Eppendorf tube, taking care not to introduce bubbles during pipetting as this can affect cell adhering. The cell mixture must be rid of the cryopreservative media. This is done by adding 9 ml of Basal media, drop-wise to limit bubble forming. The solution was pipetted slowly up and down to evenly distribute the cells. The mixture was then centrifuged for 2 minutes at 300 xg. The supernatant was removed to leave a pellet of washed cells. The cells were re-suspended in a further 10 ml of Basal media. The suspension was mixed by pipetting up and down slowly, preventing bubble formation.

The cells were counted using Trypan blue solution, 0.4% sterile liquid, purchased from Thermo Fisher Scientific. Living cell tissues are impervious to the liquid but the dye can penetrate dead cell linings meaning only the non-blue, living cells contribute to the counting. To count the cells, 10 μL of cell suspension was added to a small-welled plate, followed by 10 μL of room temperature Trypan dye. The solutions were mixed by pipetting up and down then 10 μL was added to a hemocytometer. In each of the corner 1 mm^2 squares of the hemocytometer, the number of living cells was counted, counting those cells that intersect the top and right lines, and ignoring those on the bottom and left lines to account for the unit cell. The number of cells was then averaged across the four corner squares to give n_c. As each square represents one ten thousandths of a mL,

the concentration of cells in the solution was determined via the following equation:

$$\text{cells } (\text{ml}^{-1}) = n_c * 2 * 10{,}000 \ (\text{ml}^{-1}) \tag{6.1}$$

The two accounts for the half dilution of the cell solution by mixing equal quantities of the dye and the cell suspension. To determine the total number of cells, this value was scaled up by the number of ml in the original tube. In this case, this is 10 ml.

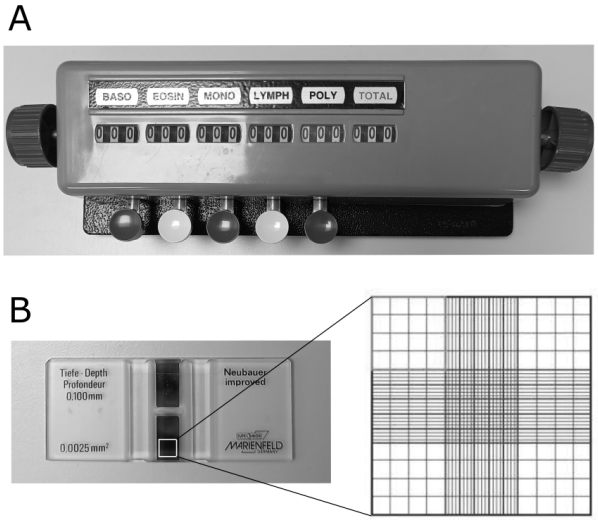

FIGURE 6.4: Cell counting apparatus showing A) the cell counter that can either be used for counting cell types or the number of cells in each quarter and B) the hemocytometer including an expanded view of the cross-hatched counting area.

6.3.1.1 Propagation

With a known number of cells in the original solution, the cells were divided into sufficient T75 (Nunc™ EasYFlask™) Cell Culture Flasks, obtained from Fischer Scientific, such that the seeding density was 5,000-6,000 cells cm^{-2}. The volume in the flasks was made up to 12 ml using Basal media. The flasks were placed in a Thermo Scientific BB 15 CO_2 incubator at 37 °C with 5% CO_2. As the cells grew, they became elongated in shape, as opposed to their round shape whilst suspended. The Basal media was changed one day post seeding then every other day following this. Once the cells had reached 80% confluence, they were reseeded in new flasks to prevent overpopulation via the method outlined below.

To remove the cells from the well, the Basal media was removed then the flasks were washed with 5 ml of PBS to remove any metabolic waste. The flasks were rinsed a further two times with PBS before the addition of 2 μL of trypsin. The solution was swirled around the plate before being transferred to the incubator for 5 minutes. Following this, the cells were viewed under the microscope to ensure they were spherical and free-moving when the well plate was shaken. Light tapping was applied to the

base of the flask but splashing of the solution onto the ceiling of the flask was avoided. Once the cells had become unstuck, 8 ml of Basal media was added to dilute the trypsin and prevent damage to the cells. Prolonged exposure to trypsin was avoided and any stubborn cells were left to prevent damage to the healthy cells. Following this, the solution was transferred to a 50 ml centrifuge tube and centrifuged for two minutes at 300xg. The supernatant was removed and the pellet was resuspended in a further 10 ml of Basal media. A 10 μL aliquote of cell suspension was removed and counted to determine the cell concentration. Using this concentration, new T75 flasks were seeded, again abiding by the seeding density of 5,000-6,000 cells cm^{-2}. When a sufficient number of cells have been grown, a portion could be frozen for future use. The majority were seeded onto PCL scaffolds as outlined in later sections.

6.3.1.2 Scaffold pre-treatment

As previously mentioned, the cells were prone to growth upon the untreated well plates resulting in large cultures on and around the base of the well, but little seeding upon the scaffolds themselves. To combat this, the scaffolds were treated to deposit a layer of apatite on the surface, increasing the affinity of the cells to the scaffolds. To produce this layer, the scaffolds were cleaned by soaking in 70 % ethanol for 10 minutes then treated using solutions of SBF derived from those produced by Kokubo and Takadama (the production of which is outlined in section 9.6.[265]

An additional solution was produced containing solute concentrations a factor of 10 times greater than those found in SBF. As such, this solution was deemed concentrated simulated body fluid (SBF_{10}) and was produced in a similar methodology to SBF. The reagent amounts and order of addition are given below:

Table 6.2: SBF_{10} reagents

Reagent	Formula	Quantity	Order
sodium chloride	NaCl	58.443 g	1
potassium chloride	KCl	0.7456 g	2
calcium chloride	$CaCl_2.2H_2O$	0.292 g	3
magnesium chloride	$MgCl_2.6H_2O$	1.0165 g g	4
mono-sodium phosphate	NaH_2HPO_4	1.1998 g	5
sodium hydrogen carbonate	$NaHCO_3$	0.355 g	6

Reagents 1 through 5 were added to 900 mL of deionized water, in a clean, dry, and plastic 1 L volumetric flask. The previous chemical was fully dissolved before the next one was added. After additions, the solution was made up to 1 L using deionized water, with a pH of ~4.37, and the solution was stored. Just prior to use, $NaHCO_3$ was added

to produce a 10 mM concentration of hydrocarbonate ions (HCO_3^-), this being 0.840 g. Ideally, this would raise the pH to ~6.5 at room temperature.

Following the production of SBF and SBF_{10}, the scaffolds were plasma treated using reactive ion etching (RIE). This was achieved with an Oxford Instruments Plasma Technology RIE80+ running PC2000 software. The RIE was operated using either oxygen or argon gas, with 30 W rf power, 300 mTorr pressure, 20 °C temperature, a gas inflow rate of 50 sccm, and a pressure of 5x10−5 Pa. The plasma chamber was cleaned initially by performing the plasma treatment in the absence of a sample, to remove any impurities. Immediately following plasma treatment the scaffolds were submerged in a SBF solution for a variable period of time. SEM images of the scaffolds were collected to assess the distribution of apatite on the surface.

An alternative coating method involved coating the scaffolds with BFP. The coating process was carried out as follows. A 100 μg ml^{-1} solution of BFP, purchased from Fischer Scientific, was made by dissolving the protein in PBS (pH 7.2) and stored in a water bath at 37 °C for 30 minutes. Each scaffold was then individually dipped in the solution 10 consecutive times, and left to dry in a class II sterile Laminar Flow Hood for 120 minutes. Once dry, the scaffolds were stored at 4 °C in a closed, sterile low-attachment surface 96-well plate, purchased from Fischer Scientific.

6.3.2 SEM imaging

To determine the success of apatite formation on the scaffolds, SEM images were obtained by viewing the birds-eye view using the sampling methodology as outlined in section 5.3.3 of chapter 5 but reiterated here. The images of the SBF coated scaffolds were obtained using a SEM collected on a Zeiss EVO LS 25 SEM equipped with a LaB6 filament. A 100 μm variable pressure aperture was used to prevent the need to sputter the samples with a conductive layer and a low-pressure methodology was adopted. The images were captured using SmartSEM software. The SEM operating conditions were 20 kV with a working distance of 10 mm for the vertical imaging and a beam current of 40.0 μA. A nominal I-probe current of 300 pA was used.

6.3.2.1 Scaffold seeding

Prior to seeding, the cells were counted to ensure there were sufficient numbers to populate the scaffolds. Following this, a cell suspension was made by detaching the cells via the Trypsin method and centrifuging for two minutes at 300 xg. The pellet was then redissolved in 10 μL of basal media to make a solution of known concentration. Sufficient liquid was extracted and transferred to a sterile Eppendorf tube and the concentration was made up to 4×10^{-6} cells mL^{-1} such that 20 μL contained 80k cells.

For manual seeding, the BFP scaffolds were placed individually in the wells of a low-attachment surface 96-well plate. To each scaffold, 20 μL of cell suspension was pipetted directly on top. After three hours, the cell solution was topped up to 200 ml using basal media. After seeding, the scaffolds were stored in the incubator and the media was refreshed every two days until the desired cultivation time had been achieved.

An alternative propagation method was also used and this involved an automatic bioreactor which continuously feed the cell cultures and removed waste. The 3D Perfusion PreFluid® BF200 Bioreactor was purchased from 3D Biotek and is purposely designed for the propagation of cell growth on 3D printed scaffolds. Prior to use the glassware, sample chambers, and pipes were autoclaved to sterilise them and then the whole apparatus was put in the class II sterile Laminar Flow Hood. 70% ethanol was used to wash the whole assembled system followed by a wash with cell culture media.

For the bioreactor, the scaffolds were seeded in an identical manner to those propagated in a manual fashion up until the media was topped up to 200 mL. The scaffolds were instead inserted into the bioreactor sample chambers and perfusion was set low at 1.2 rpm for the first 24 hours then 6 rpm until the desired cultivation time was reached.

6.3.3 Sample preparation

The methodologies outlined above were used to produce two series of scaffolds, one set manually propagated and one set cultivated in the bioreactor. There were six manually propagated scaffolds which were cultivated for 1, 4, 7, 11, 14, and 17 days. The same was done for the bioreactor scaffolds, omitting the first day.

The manually cultivated scaffold samples were produced first and were grown on a set of non-offset PCL scaffolds. This scaffold structure was undesirable as there were large pores through which the cell suspension could fall. It was later determined that the scaffolds were incorrectly produced and the fibres were to be offset from one another, removing these large z-direction channels. As a result, the bioreactor sample set was produced at a later date and using the corrected, offset scaffolds.

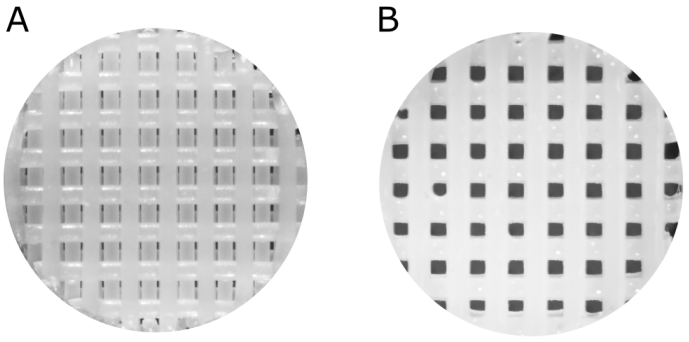

Figure 6.5: Comparison of the different scaffold types showing A) offset and B) non-offset scaffolds.

Following a scaffold's desired cultivation period, it was transferred to a clean, sterile 24-well plate and fixed using paraformaldehyde fixative solution (PFA), containing 3.7% (w/v) paraformaldehyde and 3% (w/v) sucrose in PBS, (pH 7.4), purchased from Alfa Aesar. This was achieved by submerging the scaffolds for 15 minutes before washing with 70% ethanol, twice. The fixed samples were then stored in 70% ethanol at room temperature for further analysis. The same process was used for both the manual and bioreactor sets, producing the following set of samples:

Table 6.3: Scaffold samples produced using 80k seeding density on PCL scaffolds

Propagation	Cultivation days					
Method	1	4	7	11	14	17
Manual [a]	Man-D1	Man-D4	Man-D7	Man-D11	Man-D14	Man-D17
Bioreactor [b]	N/A	Bio-D4	Bio-D7	Bio-D11	Bio-D14	Bio-D17

[a] Non-offset scaffolds.
[b] Offset scaffolds.

6.3.4 μ-CT

The samples were air-dried just prior to imaging, any residual moisture was removed by the μ-CT chamber vacuum. The 3D structures of the scaffolds were determined using a Nikon Med-X (alpha) scanner. The scans were conducted using an 80 kVp X-ray source, with 6.88 W power. The samples were exposed to the source for 708 ms. The resulting images had a resolution of 3.05 μm and were 2000x2000x~530 pixels.

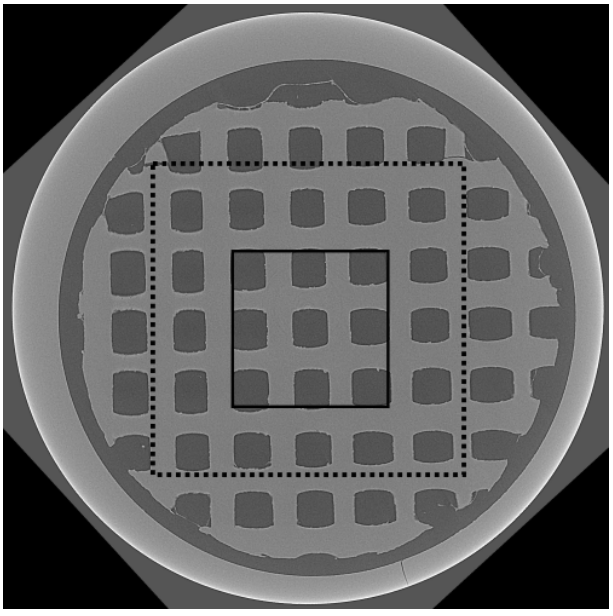

Figure 6.6: Comparison of the data included in 512x512 pixels in the original image (solid black line) and in the reduced image (dotted black line).

Due to the size of the images, 512 pixels in x and y were insufficient to grasp a statistically large enough area of the sample, and z contained blank space above and below the scaffolds. Unfortunately, the maximum file size was limited by the capability of the operating system used to perform the simulation. As such, the images were reduced by a factor of two, in all directions, such that the final resolution was 6 μm. Due to the reduction in pixel numbers, there were only ~265 pixels in z (sample dependant) meaning the images were stacked to ensure the sample was cubic.

To maintain consistency with the manual seeding approach, the images were all cut such that the x-y plane was centred within the scaffold. As the scaffolds were not perfectly consistent in structure the images ranged from 460 to 512 pixels in x and y in order to capture this grid. Due to the nature of the seeding, the cells tended to congregate on the lower surface of the scaffold and did not explore the entirety of its expanse. As such, there was only a small plane of fibres that contained cells growing on them. As a result, the μ-CT images were cut to contain all of the cells present across the z-axis including one full x-direction fibre and one full y-direction fibre. On the contrary to the 500 pixels present along x and y this left only 80 pixels in z. As such, the images were stacked to produce a cubic array simulating multiple scaffolds stacked upon one another. Since each cutting contained a fully repeating unit, that is, it began at the bottom of an x-direction fibre and ended at the top of the y-direction fibre, there was little discrepancy at the joining point of the stacked scaffolds.

As for the bioreactor scaffolds, the cell density was more consistent and so the μ-CT images were cut to contain 512x512 of the centremost pixels in x and y. As for z, the μ-CT data was cut to contain the smallest repeating unit, which was ~150 pixels. This incorporated two x-direction and two y-direction fibres such that the stacked images retained the offset pattern. Again, the stacking produced a cubic array of porous media.

6.4 Results and discussion

6.4.1 Scaffold treatment

The goal of coating the scaffolds to increase their affinity was explored using three solutions including SBF, SBF_{10}, and BFP. The former solution was derived from the studies of Kokubo but was deemed unsuccessful.[265] Initially, a 1 L solution of SBF was produced and the scaffolds were cleaned as mentioned above. Six scaffolds were cleaned and four were plasma-treated. Each plasma experiment was done with a vacuum power of 30 W, a pressure of 300 mTorr, and an inlet pressure of 50 sccm.

Following either cleaning or plasma treatment, the scaffolds were submerged in SBF for a week at room temperature. Unfortunately, none of the scaffolds showed any sign of apatite deposition, regardless of the plasma or treatment time. Following this, a

more concentrated solution was produced which contained ten times the ion concentrations found in SBF and was labelled SBF_{10}.

Table 6.4: Plasma treatment performed for various scaffold samples

Scaffold	Plasma	Time	Result
A1	O_2	60	None
A2	O_2	60	None
A3	Ar	60	None
A4	O_2	120	None
A5	N/A	N/A	None
A6	N/A	N/A	None

Even with the increased ion concentrations, the solution never crashed to form the expected precipitate. Upon initial investigation, it was determined that the pH could be held stable at 5.0 provided 9 mL of 1M HCL was added. Following this, a test was conducted to determine the optimal $NaHCO_3$ concentration to induce precipitation.

Table 6.5: Hydrogen carbonate ion concentration against precipitate time

Concentration / M	pH	Time / mins					
		1	3	5	7	12	20
0.012	0.633	clear	clear	clear	clear	clear	clear
0.014	0.643	clear	clear	clear	clear	clear	clear
0.016	0.667	clear	clear	slightly hazy	cloudy	distinctly cloudy	visibly crashing

It was determined that the 0.016 M solution was more suited to the scaffold coating as precipitate formation would occur under these conditions. Prior to plasma treatment 10 mL of solution (pre- SBF_{10}), without $NaHCO_3$, was put into clean and dry 50 mL conical tubes. The correct amount of hydrogen carbonate to form a 0.016 M solution in each tube was stored in ependorf tubes. All were taken within the clean rooms to the RIE. Using methods mentioned in 6.3.1.2, the scaffolds were cleaned and plasma treated for 5 minutes on each side, with a vacuum power of 30 W, a pressure of 300 mTorr, and an inlet present of 50 sccm for oxygen. $NaHCO_3$ was added to the pre-SBF_{10} whilst the RIE pressure was equalising and the tubes were shaken by hand to ensure the solute dissolved. The scaffolds were added straight away to the tubes, which were sealed and left to stand. After the following time periods (in hours), two scaffolds were removed, washed with deionized water, and left to air dry in a labelled 24-well plate: 1.5, 3, 4, 5, 7, and 24 hours. Every two hours the solution was refreshed until 7 hours had passed and then the samples were left overnight. The following day, SEM

images were taken of each scaffold to assess the degree of apatite formation. Images of scaffolds for each submersion time are given in Appendix 9.6.

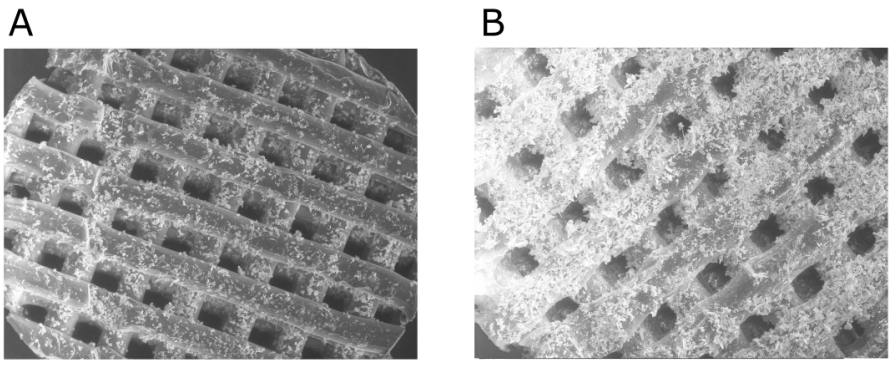

FIGURE 6.7: SEM images of a PCL scaffold plasma treated then submerged in SBF_{10} for A) 4 hours and B) 24 hours.

Considerable apatite had formed following four hours with many surfaces possessing crystalline calcium phosphate deposits, but only for one of the scaffolds. For the five-hour samples, both showed less deposition than the previous sample yet both hour-7 samples showed significant deposition, as well as the 24-hour samples which were heavily coated. The expected result was a homogeneous layer of fine crystal deposition whereas the results presented here show large and uneven crystals, forming an irregular surface for cells to attach onto. The irregularity of the deposition with time also hindered the possibility of producing an identical set of coated scaffolds and so the methodology shifted to BFP coating instead.

6.4.2 Scaffold samples

In order to capture the tortuous nature within the scaffolds, their μ-CT images were used within the tortuosity simulation described in chapter 4. The simulation parameters are given in Table 4.4 but are repeated below for reference:

TABLE 6.6: Simulation parameters

parameter	value
N_m	20,000
D_0 ($m^2 s^{-1}$)	2.2×10^{-10}
N_s	5,000
τ_s (for $\Delta = 60$ s)	12 ms
$\lvert < r_{j,k} - r_{j-1,k} > \rvert$ (for $\Delta = 60$ s)	4.0 μm
$\lvert < r_{N_s,k} - r_{1,k} > \rvert$ (for $\Delta = 60$ s)	281.4 μm
Starting cube (pixels)	130:330 [a] or 150:362 [b]

[a] For Man-D11
[b] For all other samples

As mentioned, the images were slightly different in size, accounting for the simulation being run from one of two central cubes. The simulation was run such that it calculated the diffusion matrix along the six independent axes, which could later be diagonalised to calculate tortuosity, as well as the eigenvalues and vectors.

6.4.2.1 Manual propagation

For the manually seeded scaffolds, the simulation was used to calculate the tortuosity as a function of diffusion time. For the tortuosity measurements, the diffusion times studies were 0.01, 1, 10, 30, 60, 90, 120, 150, 180, 210, and 240 seconds.

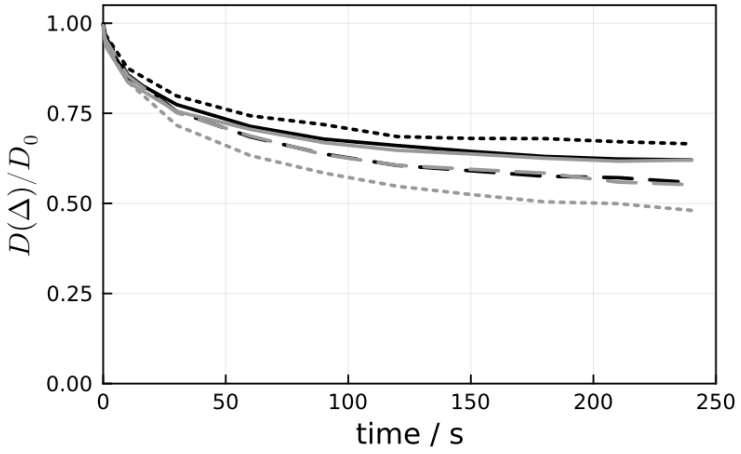

FIGURE 6.8: Tortuosity as a function of diffusion time for the scaffolds Man-D1 (solid black), Man-D4 (dash black), Man-D7 (dot black), Man-D11 (solid grey), Man-D14 (dash grey), and Man-D17 (dot grey).

From the plot above, there is evidence of a weak inverse relationship between the number of culture days and the tortuosity.

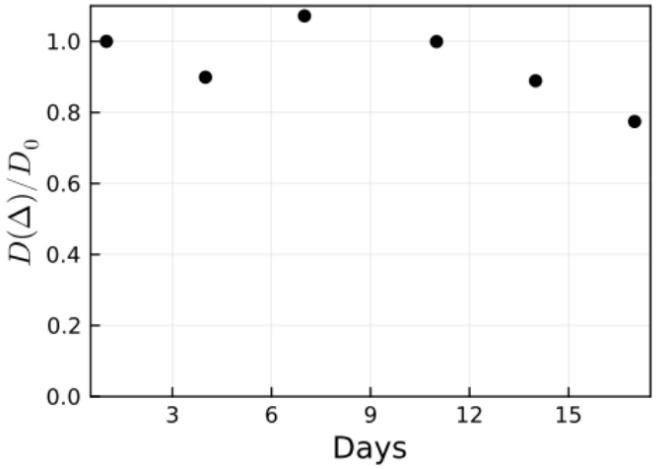

FIGURE 6.9: Tortuosity (at $\Delta = 240\ s$) as a function of cultivation days, normalised to the tortuosity of Man-D1.

The trend is more clearly shown by plotting the tortuosity as a function of cultivation days, given a delay of $\Delta = 240$ s. The weak inverse relationship may be attributed to the porous system becoming more tortuous as the cell culture grows. This is accredited to the cells partially, or in extreme cases, fully blocking the pores preventing diffusion of the solution in that direction. There are two notable outliers from the preceding two graphs, those being the tortuosity within the Man-D4 sample, and the Man-D7 sample. Firstly, the Man-D4 sample (dash black line in Figure 6.8) appears to show the same tortuosity as the Man-D14 sample despite the two μ-CT images showing a different pattern of cells. The similarity between the two can be explained by an unusually positive uptake of cells onto the Man-D4 scaffold. Since the scaffolds were treated with BFP, it could be that there was an unusually large deposit of protein on this scaffold, which aided in the cells' adherence to the scaffold. Methods of mitigation for this type of outlier are discussed below in the following section on advancements to this work.

As for Man-D7, it displays a tortuosity much less than Man-D1 which is contradictive to the assumption that Man-D1 can be treated as a completely empty scaffold. There is the possibility that the scaffolds themselves have differences in structure, which has a very clear effect on the tortuosity experiment. As mentioned above, it was determined following these experiments that the scaffolds had been incorrectly produced at source and so the degree to which they are offset cannot be ensured. It can therefore be assumed that each curve may also have some associated error, attributed to the scaffold itself. Given the close proximity of all curves, their significant difference cannot be guaranteed, regardless of the cell densities. Chapter 7 explores future applications and improvements and so these will not be discussed at length here. But one can imagine repeating the experiment with multiple scaffolds for each propagation day in order to produce averages and remove errors. However, to explore the current data further, one can also look into the individual components of the diffusion tensor. Namely the average diffusion coefficient, and the diffusion along each Cartesian axis.

From the individual plots, there is a weak inclination toward the preferred growth direction of the cells. Where the average diffusion coefficient slowly decreases (omitting the outlier that is Man-D4), the x, y, and z components do not necessarily follow suit. Most notably of all, D_{zz} remains constant in the first week and then lowers for the remainder of the cultivation days, indicating growth along the z-lab frame. There is a similar but less stark trend apparent in the D_{yy} plot showing the diffusion coefficient drops slightly between days 1 and 17. On the contrary, there is little to no trend for D_{xx} where the diffusion coefficient oscillates, albeit minimally, for all samples.

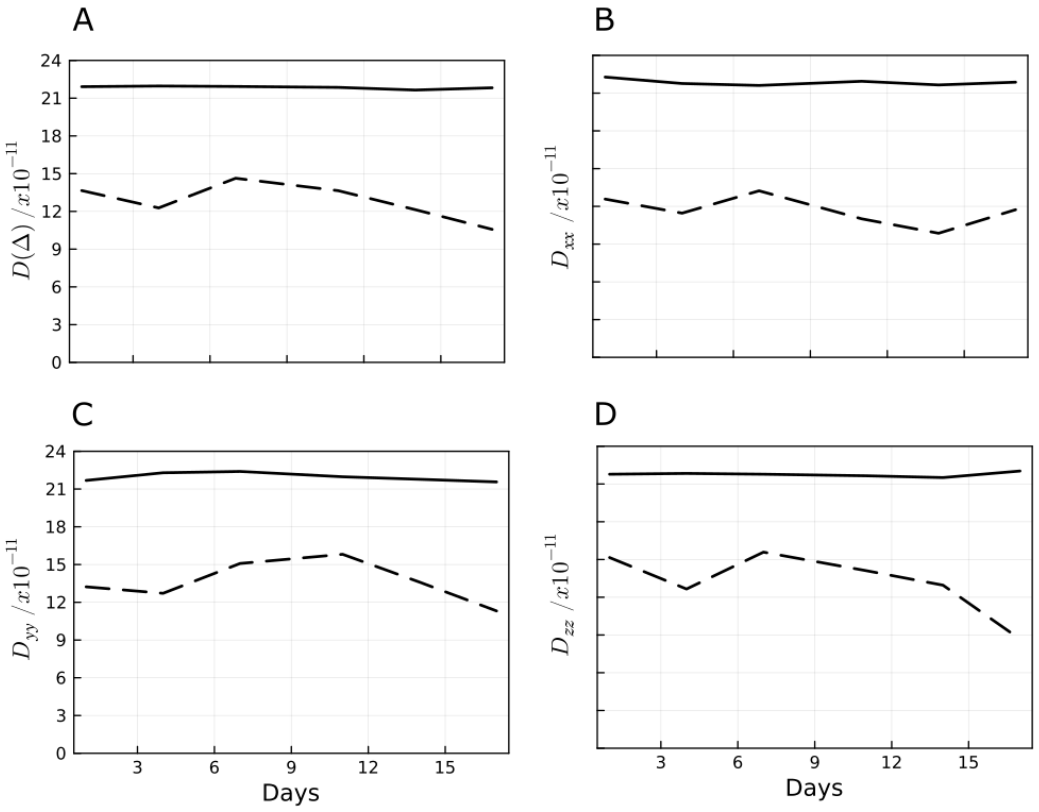

FIGURE 6.10: Restricted diffusion coefficient at in the manually grown scaffolds Δ=240 s showing A) the average coefficient, B) the diffusion along D_{xx}, C) the diffusion along D_{yy}, and D) the diffusion along D_{zz}, each as a dashed line and the unrestricted average diffusion coefficient at Δ=0.01 s (solid line).

The predominant drop in D_{zz} as opposed to the transverse axes indicates that there is more vertical growth than lateral growth as the cells spread out down the fibres, possibly aided by gravity. As for the average diffusion coefficient, and again, omitting Man-D4, we see the diffusion coefficient decreasing with time, but only minimally. Regardless of the preferred direction of growth, the simulation demonstrates its capability to capture the tortuous nature within the samples, highlighting the link between tortuosity and the number of cultivation days.

Lastly, through diagonalisation of the diffusion matrix, the fractional anisotropy (FA) can be calculated for each cell sample. In the case of the manually seeded samples (seen in Figure 6.11 B), the fractional anisotropy contains an interesting mix of minima and maxima. Following an initial drop, it increases with the cultivation days, with a maximum at 11 days, then begins to fall again. For the empty scaffold, Man-D1, the FA is already ~0.15 suggesting an innate anisotropy due to the fibre arrangement itself. As the cells were seeded on non-offset scaffolds, and given the slightly higher D_{zz} present in the Man-D1 sample, this may be due to the vertical channels within the scaffolds. The introduction of cells, Man-D7, actually reduces the FA hinting towards more spherical pores being present. Due to the greater possibility of the cells finding

a surface, it may be more probable that they attach at vertices, thus rounding out the internal pore shape. In the most anisotropic case, the pores have lost their spherical nature as cell growth differs along the three Cartesian axes. Yet the most densely populated sample shows similar FAs to the blank sample, indicating that sufficient cell growth has occurred to almost coat the inner scaffold surface in cells, returning the pore shape to its original state, just smaller.

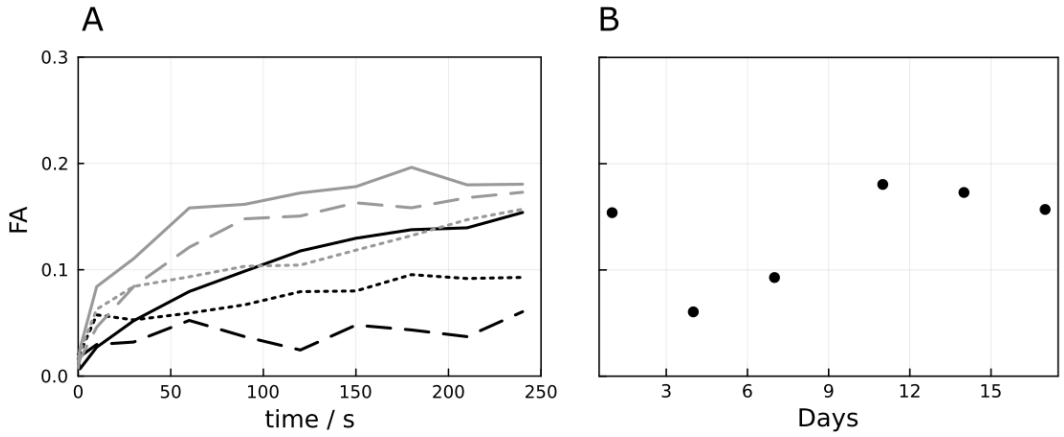

Figure 6.11: Fractional anisotropy in A) Man-D1 (solid black), Man-D4 (dash black), Man-D7 (dot black), Man-D11 (solid grey), Man-D14 (dash grey), and Man-D17 (dot grey) and B) as a function of the cultivation period, for each sample at Δ=240 s.

To take a look at the outliers, the FA of Man-D7 is indicative of the scaffold shape where further imaging (possibly through SEM or a visual microscope) would have to be carried out to determine the offset of the fibres. More interestingly is the FA of Man-D4, which appears not to follow its previously displayed trends. Before, it has always mimicked the results of Man-D14 in tortuosity and individual directional diffusion results yet it deviates in the FA. We see a consistently low level of anisotropy, counter-intuitive to its relatively anisotropic partner. One can attribute this to significant cell attachment at the vertices, producing more isotropic, spherical pores. This is opposed to sample Man-D14 where the deposited cells have had time to grow, thus spreading along the fibres and introducing anisotropy to the system.

6.4.2.2 Bioreactor propagation

As before, for the samples produced within the bioreactor, the tortuosities as a function of diffusion time can be summarised and plotted for comparison:

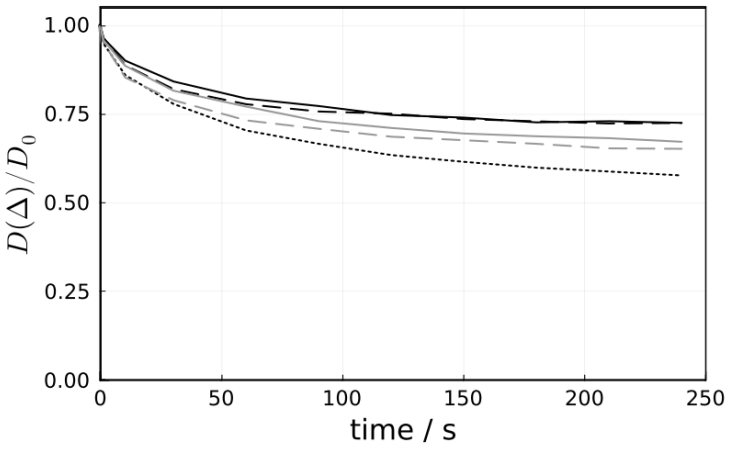

FIGURE 6.12: Tortuosity as a function of diffusion time for the scaffolds Bio-D4 (solid black), Bio-D7 (dash black), Bio-D11 (dot black), Bio-D14 (solid grey), and Bio-D17 (dash grey).

As before, it is evident from Figure 6.12 that there is a weak inverse relationship between the number of culture days and the tortuosity.

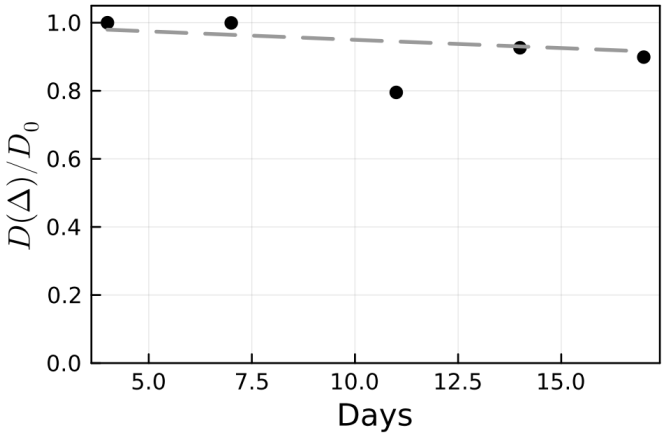

FIGURE 6.13: Tortuosity as a function of cultivation days showing the experimental points (black circles) and trend (dash grey) for $\Delta = 240$ s, normalised to Bio-D4.

The trend was calculated via a least squares linear fitting method producing a linear line with a gradient of -0.005, with an associated error of ±0.001. There is one notable outlier from Figure 6.13, this being the diffusion within the Bio-D11 sample, which appears to possess a far greater density of cells than all other samples. Due to the unpredictability of living cells, and the restricted sample size, there was no opportunity to assess the validity of this particular sample so it must be excluded as an outlier. The other results only show minimal relative differences between the first culture set, Bio-D4, and the last, Bio-D17. As before, the individual components of the diffusion tensor can be compared to study the growth pattern of the cells.

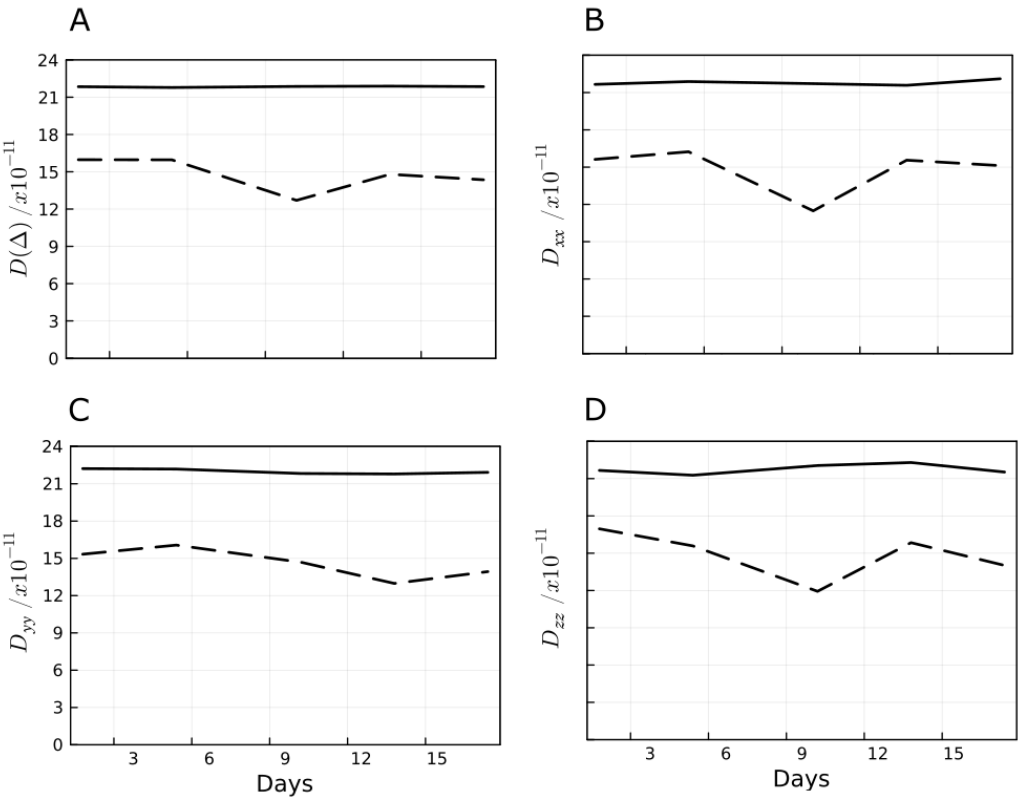

FIGURE 6.14: Restricted diffusion coefficient in the bioreactor grown scaffolds at Δ=240 s showing A) the average coefficient, B) the diffusion along D_{xx}, C) the diffusion along D_{yy}, and D) the diffusion along D_{zz}, each as a dashed line and the unrestricted average diffusion coefficient at Δ=0.01 s (solid line).

Excluding Bio-D11 from all comparisons, there is a slight decrease in diffusion coefficient when going from Bio-D4 to Bio-D17, indicating an added boundary for the diffusing molecules to be deflected from. As for the individual components, D_{xx} appears to change only minimally, which was also seen for the manually propagated samples. Diffusion along y follows suit and shows very little change between the different cultivation periods. The most differing sample is Bio-D14 which appears to have slight growth along D_{yy}. As for D_{zz}, there is a weak trend between restricted diffusion and the cultivation period, with the exception of Bio-D14. However, the increased growth in D_{yy} appears to counteract that in D_{zz} meaning it still follows the averaged trend. Since the trend seen in D_{zz} is the only one to follow the overall tortuosity trend, it can be presumed that this is the direction in which the majority of growth is occurring.

As for the fractional anisotropy, we see similar observations compared to the manually propagated samples, again, excluding Bio-D11. The FA appears to oscillate with the introduction of cells initially causing a more isotropic, spherical environment. This shifts to a larger anisotropy as the cell culture spreads across the scaffold only to lower again as the cells coat the inner walls.

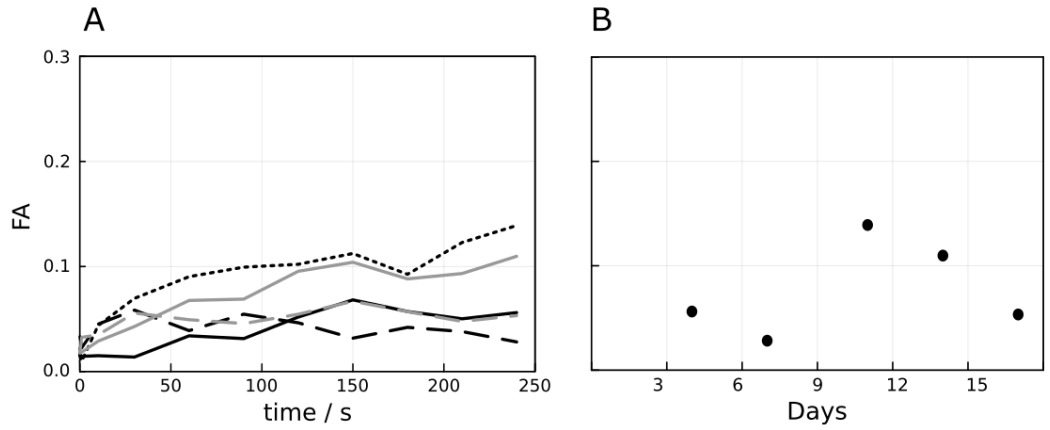

FIGURE 6.15: Fractional anisotropy in A) Bio-D4 (solid black), Bio-D7 (dash black), Bio-D11 (dot black), Bio-D14 (solid grey), and Bio-D17 (dash grey) and B) as a function of the cultivation period, for each sample at Δ=240 s.

6.4.3 Comparison

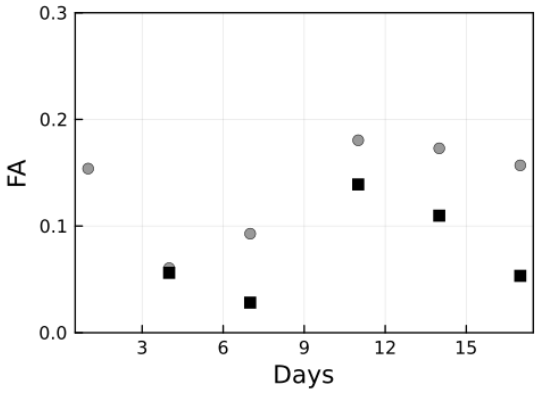

FIGURE 6.16: Fractional anisotropy in the manually grown scaffolds (grey circles) and the bioreactor grown scaffolds (black squares) as a function of the cultivation period, for each sample at Δ=240 s.

A comparison between the two seeding methods is difficult to study due to the relatively large percentage of samples being outliers in each case. An initial assessment of the two systems can be done, accepting the low statistical validity of the results. Contradictory to the manual seeding method, the outlier of the bioreactor sample set (with an unusually high cell density) has a large FA indicating anisotropic, dispersed cell growth whereas before we saw an unusually low FA. The reasoning may lay in the cultivation period: Man-D4 was a "younger" sample and the unusually high cell density had limited time to dispense. However, Bio-D11 may have had sufficient time for its greater quantity of cells to anisotropically infiltrate the scaffold. In practice, the cell growth pattern is incredibly sporadic with more cross-links being seen to span the

pores following longer cultivation periods. Additionally, since the cells preferred to grow on the bottom-most plane, growth patterns may be influenced by the container.

Lastly, there was insufficient time to conduct any physical diffusion experiments due to complications with the associated hardware. These would have been performed by producing degassed samples analogous to the GDL samples produced in the chapter above. The dual core probe would then be used to collect tortuosity measurements or perform DTI. However, it is expected that the results between computation and experimental would differ. The μ-CT images were captured on dried, fixed samples so it can be expected that the cells would have a smaller volume due to both shrinkage and potential loss of the ECM. A d-NMR experiment would therefore be probing a more torturous environment, due to the larger volume of space occupied by the cells. Furthermore, the presence of the ECM could affect diffusion due to absorption of the spy molecule or temporary intramolecular interactions between the spy and the ECM matrix slowing diffusion and skewing tortuosity measurements.

6.5 Conclusion

The aim of this chapter was to demonstrate the applicability of the previously developed techniques on a sample of real-world significance. It introduced the 3D scaffold samples and explained their importance for artificial tissue growth within the medicinal community as well as other disciplines. This chapter went on to discuss possible techniques used to improve the cell seeding methodology, which is a prevalent issue within the science of tissue cultures. Finally, this chapter detailed the analysis of diffusion, and measurement of tortuosity, through the scaffolds via computational means.

Sections of this chapter contained an extensive effort to increase cell adhesion via a range of methodologies centred around altering the chemical and physical properties of the scaffolds' surface. The success of these methods was minimal or in some cases, the surface was successfully altered but with a low reproducibility rate. As such, the use of unaltered scaffolds was most suitable and alternative methods, such as the bioreactor or using offset scaffolds, were used to improve cell infiltration.

The tortuosity simulation was successfully run within all samples showing not only the tortuosity but also the individual components of the diffusion tensor and the fractional anisotropy. Unfortunately, due to complications with cell growth and limited access to analytical apparatus, only one sample was produced for each seeding method and each cultivation day. Where the simulation has previously proven its suitability with diamagnetic porous materials, the erratic nature of the cells prevented any solid analysis from being drawn for a single scaffold of each sample type. For a more comprehensive and statistically significant study, one would require multiple scaffolds for each sample type, in order to prevent such a large percentage of samples dismissed as outliers.

Additionally, the introduction of an extensive number of variables made comparisons increasingly difficult. Not only were the cells altering the tortuosity but it was made clear in the manually propagated sample set that the scaffolds themselves varied, thus introducing errors into the control or "blank" scaffold. As such, no supported conclusion could be made on the growth tendencies of the cells and therefore, no assessment of the suitability of the scaffold design for tissue culturing.

Chapter 7

Future advancements

7.1 Synopsis

The purpose of this chapter is to explore possible advancements in the techniques, that were not achievable within the timescale of the project. This includes expanding the simulation further as well as advancing the practical methodologies. There are a number of possibilities that can be applied to improve the seeding process in order to produce a more dense and homogeneous array of cells.

7.2 Advancements

7.2.1 Simulation

In terms of computational studies, there are multiple routes that can be taken that would increase the accuracy of and improve the quality of the diffusion simulations. The random walk methodology is capable of capturing molecular movement through the system; however, there are multiple routes for improvement. Firstly, when the molecules encounter a boundary, they will continue selecting a random step until they have found a satisfactory position to move to. However, a more accurate methodology would include the molecules reflecting off of the boundary in a more realistic trajectory.

Building upon this, to incorporate a more realistic trajectory the molecules would have to interact with the surface via stringent boundary conditions. In the absence of a completely inert surface, any molecular-surface interaction would result in some form of attraction or repelling force which would alter the molecules' trajectory after a collision. This may in turn bring about surface relaxation which would be relevant for a total relaxation simulation. Although possible, this would require specific knowledge of the system's surface and a more advanced random walk methodology.

Finally, it was suspected that the glass beads used within chapter 4 contained some degree of paramagnetic material, accounting for the increased relaxation rate of the diffusing molecule. To account for this, the simulation could be adapted further to contain randomly distributed areas with some paramagnetic density which would form zones of increased susceptibility mismatch. Molecules diffusing within the vicinity of one of the paramagnetic zones would encounter far greater fluctuations in field strength and therefore relax quicker. However, this was not introduced into the simulation as the composition of the glass beads was not entirely known and so the density and magnitude of the paramagnetic zones could not be deduced. If the simulation were to be run in a sample with a completely understood composition, this extension would be applicable to produce a more realistic result.

7.2.2 Cell cultures

There are a number of different methods that could be used to improve the production of the scaffold samples. Unfortunately, there was insufficient time to explore these potential methods fully but a short list of possibilities is outlined below.

The first possibility applies more to the initial scaffolds with the non-offset configuration. Whilst seeding, it was common for the suspended cells to sink to the bottom of the well and therefore only attach to the bottom plane of fibres in the scaffolds. There were several attempts to prevent this including trying to coat the scaffolds with SBF to make the surface more amiable for the cells. However, as detailed above, the solution could not be perfected and therefore the method was replaced with the BFP coating process. In the future, this aspect could be improved by testing a variety of methods. One simplistic alternative is the addition of an insect pin, or other small insertable object, into the top of the scaffold. The purpose of which being to hold the seeding suspension above the scaffold, due to water adhesion, allowing the cells to adhere as the solution travels more slowly through the scaffold. The fundamentals of this method were tested but not applied to the scaffold samples used within this project due to time limitations. Note that, this methodology would not be suitable for the offset scaffolds within the bioreactor as the seeding method in this case does not lend itself well to the insertion of an external material into the scaffold. The offset fibres are a design element introduced to ensure slow percolation through the scaffold.

On a similar train of thought, previous methods have used the viscosity of the seeding solution to prevent the cells from sinking. To do so, the cell solution was combined with Ficoll-Paque^{TM} Plus solution (60 vol%) such that the density of the surrounding solution was similar to that of the cells. This methodology was developed by Cámara-Torres *et al.* and showed the cell density tripling with respect to normalised cell coverage area on one plane of fibres, with non-offset scaffolds.[263] The percentage of Ficoll-Paque solution was determined by producing a series of solutions between 20 and 80 vol%

(stained for ease of identification), producing a layered solution within a conical tube and centrifuging with cells. Their results are highlighted below in Figure 7.1.

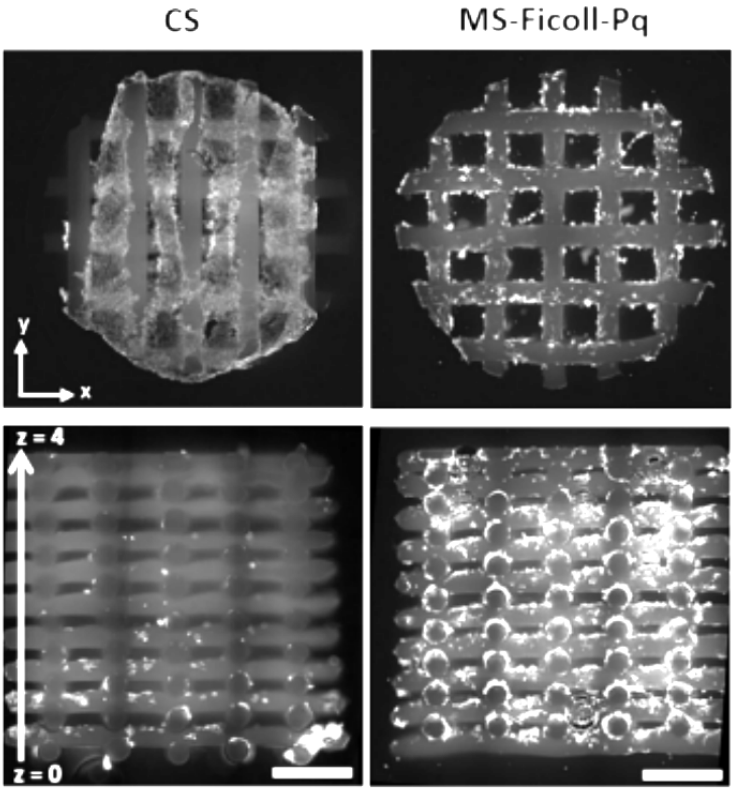

Figure 7.1: Fluorescent staining (F-actin, red) of cultured scaffolds either via the conventional seeding (no viscosity alteration) method (left) and with a solution of 60 vol% Ficoll-Paque solution. Adapted from.[263]

Although this was not tested with a cell suspension, with the support of the findings given in Figure 7.1, it is assumed that this method would be beneficial for producing a more homogeneous seeding in the offset scaffolds.

As explained above in section 6.4.2.1, simulations are negatively impacted by the limited number of scaffolds for each of the cultivation days, for each method. Due to the restricted sample pool, there is a lack of statistical evidence to recognise any clear trend. For this, one would rather have to culture at least three scaffolds for each cultivation period and collect μ-CT images for each. These could either be stacked on top of one another or run individually and averaged. However, there was insufficient time during this project to grow sufficient cells to produce this number of scaffolds.

Finally, to ensure the cell structure does not alter following the fixation, the scaffolds could be grown in order of longest growth to shortest cultivation period. As such, the Day17 sample would be seeded initially followed by two days of growth. On the third day the next sample would be seeded, Day14 in this case. As a result of this, all samples

would finish their designated growth period on the same day. All samples could then be fixed and taken to the μ-CT facility simultaneously.

7.2.3 Experimental

In terms of the physical experiments, assuming a now fully applicable set of multiple scaffold samples, one can look towards using NSSs to enhance the experimental procedures. The low field set-up has already shown its suitability for singlet-assisted diffusion in a field cycling environment, albeit in a model-packed beads system with a low viscosity solvent.[181] One can therefore picture the combination of the field cycling methodology, combined with the enhancements of singlet-assisted diffusion to probe the internal architecture of a growing tissue culture, as time progresses. This experiment would need to satisfy a number of particular requirements including; the degassing of the solution prior to addition to the porous media; and the production of a singlet-bearing molecule with sufficient solubility in a low viscous solvent that there is enough signal to overcome the reduced internal volume inherent to porous media.

Chapter 8

Conclusions

The purpose of this multidisciplinary project as a whole was to test the following: that magnetic susceptibility-induced relaxation is a principal culprit to the inability of NMR to operate within porous media but can be overcome through a combination of techniques such as long-lived states and field cycling methodologies. The individual contribution routed in this work is the theoretical derivation and the simulation framework production as well as experimental studies and their comparisons. Throughout these works, many aspects of both computational and experimental methodologies have been examined, focused on facilitating diffusion measurements in porous media.

In chapter 3, the theory of nuclear spins diffusing through porous media was outlined including an account of the derivations and assumptions used to produce the theory. This chapter set the scene for the current inhibitors of d-NMR in porous media, and the quantum mechanical reasoning as to why we see enhanced signal decay. The theory was incorporated into a simulation framework capable of taking 3D digitised reconstructions of diamagnetic porous media and accurately predicting decay due to diffusion in the internal field (DDIF). Thus demonstrating the validity of the simulation framework and the suitability of the selected diffusion modelling process.

Chapter 4 gave a detailed description of the computational advancements made within the framework, namely the introduction of tortuosity measurements. This was done by expanding off of the previous random walk-based method, with the introduction of hard boundaries and more efficient calculations. The simulation was capable of replicating a typical d-NMR experiment whereby diffusion is measured along six independent vectors in order to calculate diffusion within the principal frame. The result is an orientation-specific tensor describing the principal direction and relative rate of diffusion along x, y, and z. The simulation was tested in exemplar shapes before being used within bead samples, showing good agreement with experimental results.

The methodology portion, chapter 5, delved into the production and initial use of a custom-built dual-core spectrometer, capable of performing field cycling diffusion

NMR. The additional low-field probe was designed in collaboration with (and later built by) Bruker and sat within the stray field of the magnet. The system drew off the advantages of both high and low field namely the increased sensitivity and reduced DDIF, respectively. The apparatus was initially tested and calibrated with the intent to study gas diffusion layers; however, the actual experimental portion was not achievable within the time frame of the project. Regardless, the system showed promising initial results and has the potential to facilitate in-depth studies, given more time.

The penultimate chapter saw attempts made to study a sample of medicinal importance, using the theory, computations, and methodologies outlined in the preceding chapters. Chapter 6 detailed the use of 3D-printed scaffolds for tissue engineering, and the current challenges facing the medical community. These works included attempts made to improve the cell infiltration within these scaffolds which is a prevalent issue associated with 3D cultures. The techniques showed little success and the resulting samples showed little homogeneity in cell dispersion. Furthermore, issues around cell culture densities meant a very restricted sample selection was produced, demonstrating high variability in the adhesion and proliferation of cells. The large percentage of outliers and lack of replicable samples meant no solid conclusions could be drawn on the patterns of cell growth nor the suitability of scaffold architecture.

Finally, the potential future advancements within the project were discussed. These included slightly different methodologies and techniques that could be used should the experiments be repeated, as well as directions in which to continue work past the scope of this project. These involved heightening the sophistication of the simulation to contain surface interactions via a more molecular-dynamics-based simulation. Or, introducing paramagnetic elements into the simulation to account for samples that are not completely diamagnetic. As for experimental work, there are a number of techniques that could be utilised within the current methodology that could be executed during the production of the next sample set. As well as the introduction of nuclear singlet states which was already approached via the dual-core technique.

The results of this work are mixed, with great success in the theoretical and computational aspects which unfortunately were not reciprocated within the experimental portions. Despite the challenges, firm foundations have been laid for the accurate collection of d-NMR data within complex porous media. The degree of signal attenuation due to susceptibility-induced relaxation can successfully be calculated through the derived theory. However, the sample composition may decide whether this relaxation mechanism prevails over others, such as paramagnetic relaxation. As for data acquisition, the aforementioned methodologies are capable of extending the lifetime of d-NMR and should not be discounted as valuable techniques for long-lived state incorporating, field-cycling diffusion NMR for the purpose of studying porous media.

Chapter 9

Appendicies

9.1 Average Hamiltonian theory

In the instance of a time-dependent Hamiltonian, in order to obtain an approximate solution to the Liouville-von Neumann equation, average Hamiltonian theory (AHT) must be used. The Liouville-von Neumann equation being:

$$\frac{\partial}{\partial t}\hat{\rho}(t) = -i\,\hat{\hat{H}}_{(t)}\hat{\rho}(t) \tag{9.1.1}$$

The general solution to this is obtained through successive integrations:

$$\begin{aligned}\hat{\rho}(t) = \hat{\rho}(0) + (-i)\int_0^t \Big(\hat{\hat{H}}_{(t_1)}\hat{\rho} \\ +(-i)\int_0^{t_1} \hat{\hat{H}}_{(t_2)}\hat{\rho}(t)dt_2 \Big) dt_1 \cdots\end{aligned} \tag{9.1.2}$$

This infinite series should converge eventually but for now, it has been capped here at the second integral. The appearance of this equation can be simplified by defining the propagator, $\hat{\hat{U}}_n(0,t)$, which can be defined as:

$$\begin{aligned}\hat{\hat{U}}(0,t) = (-i)^n \int_0^t dt_1 \int_0^{t_1} dt_2 \cdots \int_0^{t_{n-1}} dt_n \\ \hat{\hat{D}}\,\hat{\hat{H}}_{(t_1)}\,\hat{\hat{H}}_{(t_2)}\cdots\hat{\hat{H}}_{(t_n)}\end{aligned} \tag{9.1.3}$$

Where $\hat{\hat{D}}$ is the Dyson operator which maintains the numerical order of the Hamiltonians as they may not all commute. The substitution of this into eq. (9.1.2) produces:

$$\hat{\rho}(t) = \sum_{n=0}^{\infty} \hat{\hat{U}}_n(0,t)\,\hat{\rho}(0) \tag{9.1.4}$$

Another way of writing the propagator is:

$$\hat{\hat{U}}_n(0,t) = \hat{\hat{D}}\,\frac{[-i\int_0^t \hat{\hat{H}}_{(t_1)}\,dt_1]^n}{n!} \tag{9.1.5}$$

Where the whole propagator is given as:

$$\hat{\hat{U}}(0,t) = \sum_{n=0}^{\infty} \hat{\hat{D}}\,\frac{[-i\int_0^t \hat{\hat{H}}_{(t_1)}\,dt_1]^n}{n!} \tag{9.1.6}$$

Upon closer inspection, it is evident that this represents a Taylor series whereby:

$$e^x = \sum_{n=0}^{\infty} \frac{x^n}{n!} \tag{9.1.7}$$

This can now be written as:

$$\hat{U}(0,t) = e^{-i \int_0^t \hat{H}_{(t_1)}\, dt_1} \tag{9.1.8}$$

Unfortunately, the propagator is infinite and not unitary meaning it is impractical to use it, to solve the Liouville-von Neumann equation. To overcome this, the Hamiltonian is split into small enough time increments, τ, that it can be assumed constant within each step:

$$t = \sum_k \tau_k \tag{9.1.9}$$

As such, each Hamiltonian is now time-independent and provided the Hamiltonian is Hermitian, the propagator is now unitary. As each Hamiltonian is assumed constant across τ_n, which can be removed from the integral, producing an infinite succession of rotations:

$$\hat{\hat{U}}(0,t) = e^{-i\,\hat{\hat{H}}_n\,\tau_n} \cdot \ldots \cdot e^{-i\,\hat{\hat{H}}_1\,\tau_1} \tag{9.1.10}$$

9.2 Accessing the rotating frame

The conversion of a Hamiltonian into another interaction frame begins with the definition of the Schrödinger's equation:

$$i\frac{\partial}{\partial t}\psi = \hat{H}_{(t)}\psi \tag{9.2.1}$$

The state, ψ can be shifted into another frame via a rotation:

$$\tilde{\psi} = \hat{R}\psi \tag{9.2.2}$$

Applying the complex conjugate:

$$\begin{gathered}\hat{R}^\dagger\tilde{\psi} = \hat{R}^\dagger\hat{R}\psi \\ \hat{R}^\dagger\hat{R} = 1\end{gathered} \tag{9.2.3}$$

Substituting this into the Schrödinger's equation:

$$i\frac{\partial\hat{R}^\dagger\tilde{\psi}}{\partial t} = \hat{H}_{(t)}\hat{R}^\dagger\tilde{\psi} \tag{9.2.4}$$

The derivative of a product is written as:

$$i\hat{R}^\dagger\frac{\partial}{\partial t}\tilde{\psi} + i\frac{\partial}{\partial t}\hat{R}^\dagger\tilde{\psi} = \hat{H}_{(t)}\hat{R}^\dagger\tilde{\psi} \tag{9.2.5}$$

This can be rearranged and factorised:

$$i\hat{R}^\dagger\frac{\partial}{\partial t}\tilde{\psi} = \left(\hat{H}_{(t)}\hat{R}^\dagger - i\frac{\partial}{\partial t}\hat{R}^\dagger\right)\tilde{\psi} \tag{9.2.6}$$

If the equation is multiplied through by the rotation operator:

$$i\hat{R}\hat{R}^\dagger\frac{\partial}{\partial t}\tilde{\psi} = \left(\hat{R}\hat{H}_{(t)}\hat{R}^\dagger - i\hat{R}\frac{\partial}{\partial t}\hat{R}^\dagger\right)\tilde{\psi} \tag{9.2.7}$$

The equation now resembles the Schrödinger's equation:

$$i\frac{\partial}{\partial t}\tilde{\psi} = \tilde{\hat{H}}\tilde{\psi} \tag{9.2.8}$$

Where:

$$\tilde{\hat{H}} = \hat{R}\hat{H}_{(t)}\hat{R}^\dagger - i\hat{R}\frac{\partial}{\partial t}\hat{R}^\dagger \tag{9.2.9}$$

By selecting $\hat{R}$ to be a clockwise rotation, many Hamiltonians, written in the correct interaction frame, can be greatly simplified.

Taking, for instance, the Hamiltonian in eq. (3.19), given again for reference:

$$\hat{H}(t) = -\gamma B_0\hat{I}_z - \gamma\boldsymbol{B}_d(t)\cdot\hat{\boldsymbol{I}} \tag{9.2.10}$$

Currently, $\left\|\hat{H}\right\|t \not\ll 1$ due to the Zeeman term, which can be removed via shifting to the Zeeman interaction frame. To do so, the rotation angle is set to the largest term of the Hamiltonian, such that:

$$\hat{R} = e^{i\omega_0\hat{I}_z t} \tag{9.2.11}$$

To insert this into the equation for the interactive frame Hamiltonian:

$$\begin{aligned}\tilde{\hat{H}}(t) = {} & e^{i\omega_0\hat{I}_z t}(\omega_0\hat{I}_z - \gamma\boldsymbol{B}_d(t)\cdot\hat{\boldsymbol{I}})e^{-i\omega_0\hat{I}_z t} \\ & -i\ e^{i\omega_0\hat{I}_z t}(-i\omega_0\hat{I}_z)e^{-i\omega_0\hat{I}_z t}\end{aligned} \tag{9.2.12}$$

since:

$$\frac{\partial}{\partial t}\hat{R}^\dagger = (-i\omega_0\hat{I}_z)e^{-i\omega_0\hat{I}_z t} \tag{9.2.13}$$

We can expand the brackets to find:

$$\begin{aligned}\tilde{\hat{H}}(t) = {} & e^{i\omega_0\hat{I}_z t}(\omega_0\hat{I}_z)e^{-i\omega_0\hat{I}_z t} \\ & +e^{i\omega_0\hat{I}_z t}(-\gamma\boldsymbol{B}_d(t)\cdot\hat{\boldsymbol{I}})e^{-i\omega_0\hat{I}_z t} \\ & -i\ e^{i\omega_0\hat{I}_z t}(-i\omega_0\hat{I}_z)e^{-i\omega_0\hat{I}_z t}\end{aligned} \tag{9.2.14}$$

As all z components commute with one another, we obtain:

$$\tilde{\hat{H}}(t) = \omega_0 \hat{I}_z - \omega_0 \hat{I}_z + e^{i\omega_0 \hat{I}_z t}(-\gamma \boldsymbol{B}_d(t) \cdot \hat{\boldsymbol{I}}) e^{-i\omega_0 \hat{I}_z t} \tag{9.2.15}$$

The result being:

$$\tilde{\hat{H}}(t) = e^{i\omega_0 \hat{I}_z t}(-\gamma \boldsymbol{B}_d(t) \cdot \hat{\boldsymbol{I}}) e^{-i\omega_0 \hat{I}_z t} \tag{9.2.16}$$

9.3 Dimensionless demagnetization field

The original equation for the magnetic field produced by a dipole, $boldsymbol{B}_d(\boldsymbol{m}$, relied on many parameters containing units, such as the distance, $\boldsymbol{r}$, and the dipole magnetic moment, $\boldsymbol{m}$:

$$\boldsymbol{B}_d(\boldsymbol{m},\boldsymbol{r}) = \frac{\mu_0}{4\pi}\frac{3(\boldsymbol{m}\cdot\check{r})\check{r}-\boldsymbol{m}}{r^3} \quad (9.3.1)$$

Where μ_0 is the vacuum permeability. The value of $\boldsymbol{m}$ can be calculated from known parameters, by rearranging using the following method:

$$\begin{aligned}\boldsymbol{m} &= \boldsymbol{M}\mathrm{v}\\ \boldsymbol{M} &= \chi\boldsymbol{H}\end{aligned} \quad (9.3.2)$$

Where $\boldsymbol{M}$ is the magnetisation, and v is the volume. Therefore:

$$\boldsymbol{m} = \chi\boldsymbol{H}\mathrm{v} \quad (9.3.3)$$

Where $\boldsymbol{H}$ is the magnetic field strength, and χ is the magnetic susceptibility of the material. Following on from this:

$$\begin{aligned}\boldsymbol{B}_0 &= \boldsymbol{H}\mu\\ \mu &= \mu_o(1+\chi)\end{aligned} \quad (9.3.4)$$

Where μ is the permeability of the material. Therefore:

$$\mathbf{m} = \frac{\chi\mathrm{v}\boldsymbol{B}_0}{\mu_o(1+\chi)} \quad (9.3.5)$$

The volume of the magnetisation area can be written in terms of the unit cell parameter of the CT data, l. Also, since $\chi \ll 1$, the value of $\frac{\chi}{1+\chi} \approx \chi$:

$$\mathbf{m} = \frac{\chi l^3\boldsymbol{B}_0}{\mu_o} \quad (9.3.6)$$

This can be substituted into the original equation for the demagnetizing field:

$$\boldsymbol{B}_d(\boldsymbol{m},\boldsymbol{r}) = \frac{\mu_0}{4\pi}\frac{3\left(\frac{\chi l^3}{\mu_o}\boldsymbol{B}_0\cdot\check{r}\right)\check{r}-\left(\frac{\chi l^3}{\mu_o}\boldsymbol{B}_0\right)}{r^3} \quad (9.3.7)$$

The scalar factors can be taken out of the fraction:

$$\boldsymbol{B}_d(\boldsymbol{m},\boldsymbol{r}) = \frac{l^3\chi}{4\pi}\frac{3(\boldsymbol{B}_0\cdot\check{r})\check{r}-\boldsymbol{B}_0}{r^3} \quad (9.3.8)$$

A new parameter, $\boldsymbol{b}_d$ can be defined as:

$$\boldsymbol{b}_d = \frac{\mathbf{B}_d}{\chi B_0} \quad (9.3.9)$$

The demagnetisation field can be divided through by χB_0:

$$\boldsymbol{b}_d(\boldsymbol{r}) = \frac{l^3}{4\pi}\frac{3(\check{\boldsymbol{B}}_0\cdot\check{r})\check{r}-\check{\boldsymbol{B}}_0}{r^3} \quad (9.3.10)$$

Another parameter, v, can be detailed as a dimensionless form of distance:

$$\begin{aligned}\boldsymbol{v} &= \frac{\boldsymbol{r}}{l}\\ \text{Where, } \check{v} &= \frac{\boldsymbol{r}\,l^{-1}}{r\,l^{-1}}\text{, and } v = \frac{r}{l}\end{aligned} \quad (9.3.11)$$

This can be substituted into $\boldsymbol{b}_d(\boldsymbol{r})$ to achieve:

$$\boldsymbol{b}_d = \frac{1}{4\pi}\frac{3(\check{\boldsymbol{B}}_0\cdot\check{v})\check{v}-\check{\boldsymbol{B}}_0}{v^3} \quad (9.3.12)$$

Here is a generalised case for the demagnetizing field, where all factors in the equation are dimensionless. The result of this equation can be scaled up by any factor, depending on the experimental parameters:

$$\boldsymbol{B}_d = \chi\,\boldsymbol{B}_0\,\boldsymbol{b}_d \quad (9.3.13)$$

9.4 Bead sample results

1D spectra collected within all samples. The TMS peak has been centred at 0 ppm, the peak at ~4.5 ppm corresponds to residual hydroxyl protons in the MeOD solution.

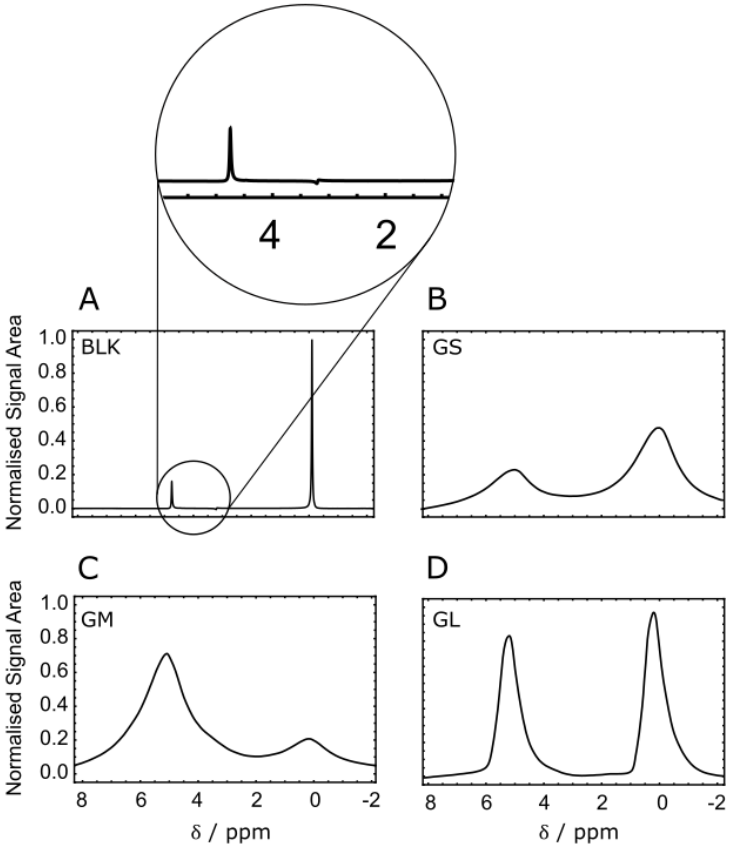

Figure 9.4.1: 1D NMR spectra of A) BLK, B) GS, C) GM, and D) GL taken at 16.4 T where spectra in B, C, and D have bee normalized to individual scales.

All spectra were normalised to individual scales since there was such a significantly greater signal within the blank sample due to the volume of spins present. Sources indicate the spectrum of deuterated methanol contains two peaks, accounting for residual hydroxyl and methyl protons. These occur at 4.78 and 3.31 ppm respectively.[292] For the blank sample, there is strong evidence of the hydroxyl protons with a persistent peak at ~4.7 ppm, present within all glass and plastic-containing samples. However, the methyl protons only gave rise to a small and badly phased peak at ~3.2 ppm. The difference in the relative amount of residual hydroxyl compared to residual methyl protons is unknown however it is theorised that, with the peak broadening in the bead samples, the methyl peaks are hidden within the other peaks.

The shape of the bead containing samples is never symmetric because of the inability difficulty arising from trying to shim in the porous media containing samples. As such,

the blank sample was shimmed and the same shim positions were used for all bead samples. This accounting for the poor shape.

Note: Due to the sample having to be remade, the 1D spectra of GM contains a different batch of MeOD-TMS solution which appears to have a greater concentration of MeOH than in most other samples. Additionally, the rise in residual solvent peaks in GM and GL could be attributed to water entering the system through contamination. Since water protons resonate at ~ 4.8 ppm, their presence may be masked within the methanol peaks and be indistinguishable due to line broadening.[292]

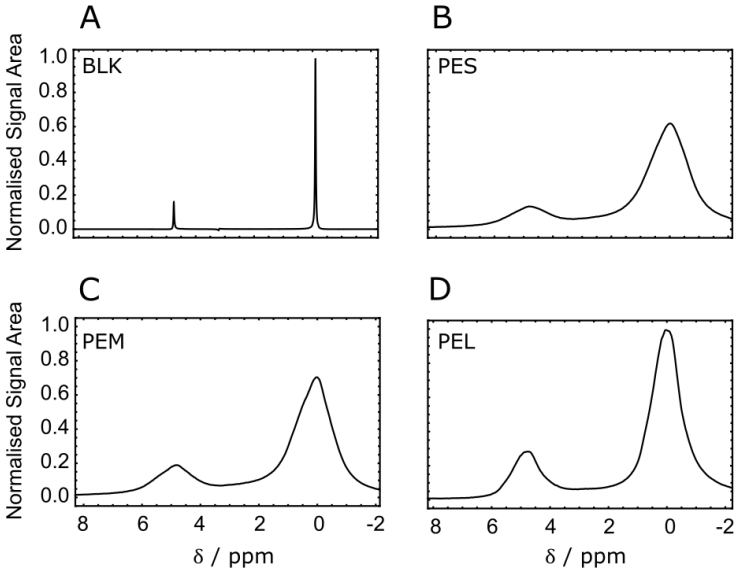

Figure 9.4.2: 1D NMR spectra of A) BLK, B) PES, C) PEM, and D) PEL taken at 16.4 T where spectra in B, C, and D have been normalized to individual scales.

Simulated propagator calculations (solid lines) and corresponding experimental data (symbols) for PES, PEM, and PEL at the three external field strengths.

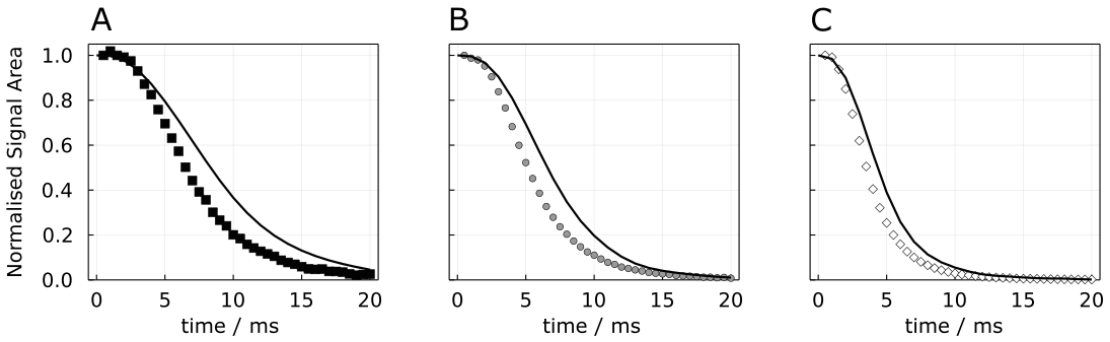

Figure 9.4.3: Simulated propagator calculation (solid line) and corresponding experimental data (symbols) for PES at A) 7.05 T, B) 9.4 T, and C) 16.4 T. Simulation parameters are collected in table Table 3.4.

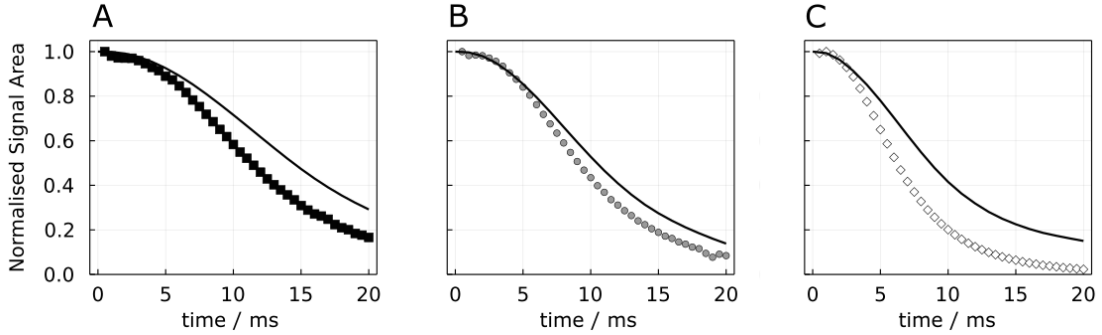

Figure 9.4.4: Simulated propagator calculation (solid line) and corresponding experimental data (symbols) for PEM at A) 7.05 T, B) 9.4 T, and C) 16.4 T. Simulation parameters are collected in table Table 3.4.

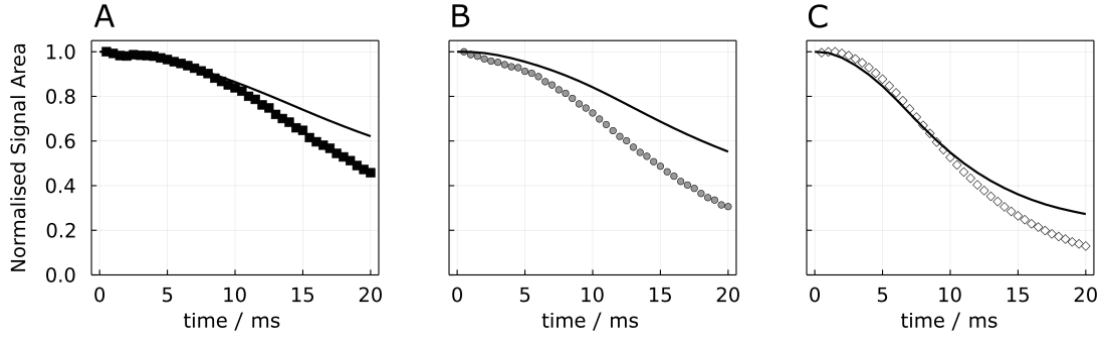

Figure 9.4.5: Simulated propagator calculation (solid line) and corresponding experimental data (symbols) for PEL at A) 7.05 T, B) 9.4 T, and C) 16.4 T. Simulation parameters are collected in table Table 3.4.

Simulated propagator calculations (solid lines) and corresponding experimental data (symbols) for GS, GM, and GL at the three external field strengths.

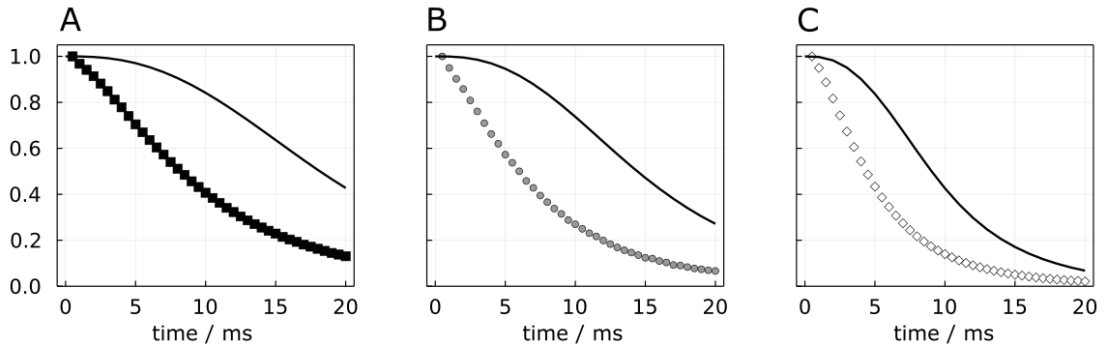

Figure 9.4.6: Simulated propagator calculation (solid line) and corresponding experimental data (symbols) for GS at A) 7.05 T, B) 9.4 T, and C) 16.4 T. Simulation parameters are collected in table Table 3.4.

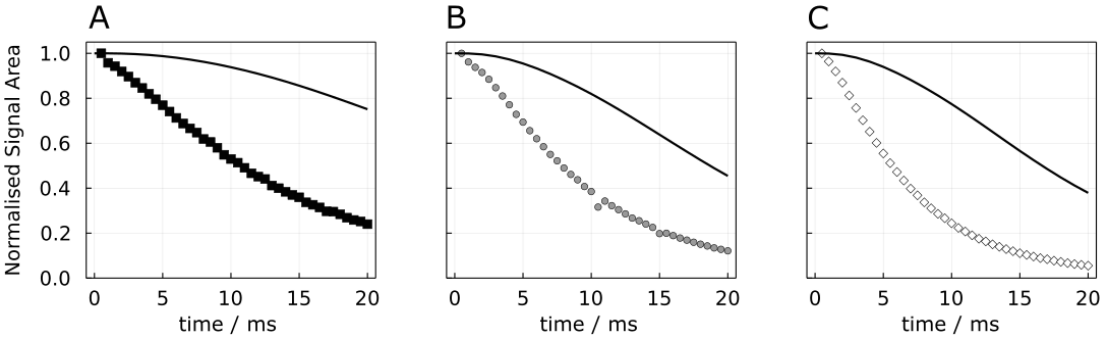

Figure 9.4.7: Simulated propagator calculation (solid line) and corresponding experimental data (symbols) for GM at A) 7.05 T, B) 9.4 T, and C) 16.4 T. Simulation parameters are collected in table Table 3.4.

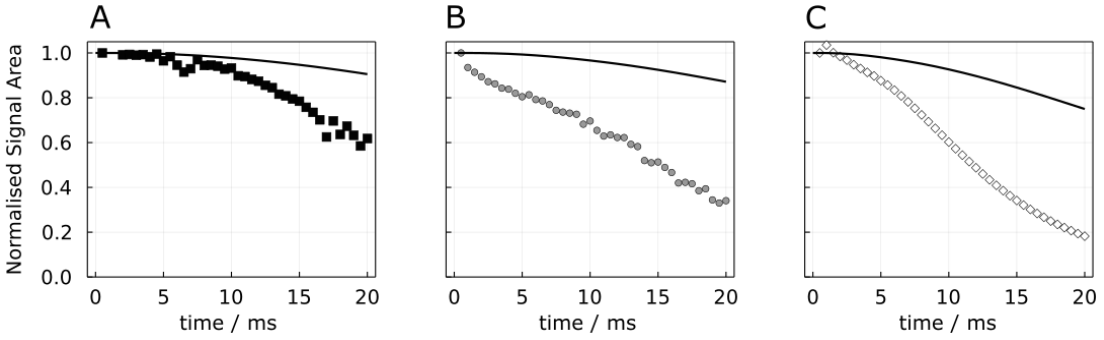

Figure 9.4.8: Simulated propagator calculation (solid line) and corresponding experimental data (symbols) for GL at A) 7.05 T, B) 9.4 T, and C) 16.4 T. Simulation parameters are collected in table Table 3.4.

9.5 PGSTE pulse sequence

The state of the system after the second 90_y pulse is as follows:

$$\begin{aligned}\hat{\rho}(4) = &- \hat{I}_y cos(\gamma g_z \delta z) \\ &- \hat{I}_x sin(\gamma g_z \delta z)\end{aligned} \tag{9.5.1}$$

Following the second gradient, the spins may have moved to a different z-coordinate and so the gradient is slightly different:

$$\begin{aligned}\hat{\rho}(5) = e^{-i\gamma g_z \delta z'} \Big[&-\hat{I}_y cos(\gamma g_z \delta z) \\ &- \hat{I}_x sin(\gamma g_z \delta z) \Big] \, e^{i\gamma g_z \delta z'}\end{aligned} \tag{9.5.2}$$

This will initially become:

$$\begin{aligned}\hat{\rho}(5) = &- \hat{I}_y cos(\gamma g_z \delta z) cos(\gamma g_z \delta z') \\ &+ \hat{I}_x cos(\gamma g_z \delta z) sin(\gamma g_z \delta z') \\ &- \hat{I}_x sin(\gamma g_z \delta z) cos(\gamma g_z \delta z') \\ &- \hat{I}_y sin(\gamma g_z \delta z) sin(\gamma g_z \delta z')\end{aligned} \tag{9.5.3}$$

One can utilise the following trig functions:

$$\begin{aligned}cos(x)cos(y) &= \frac{cos(x+y)+cos(x-y)}{2} \\ cos(x)sin(y) &= \frac{sin(x+y)-sin(x-y)}{2} \\ sin(x)sin(y) &= \frac{cos(x-y)-cos(x+y)}{2}\end{aligned} \tag{9.5.4}$$

This then results in:

$$\begin{aligned}\hat{\rho}(5) = &- \frac{\hat{I}_y}{2} cos(\gamma g_z \delta (z+z')) \\ &- \frac{\hat{I}_y}{2} cos(\gamma g_z \delta (z-z')) \\ &+ \frac{\hat{I}_x}{2} sin(\gamma g_z \delta (z+z')) \\ &- \frac{\hat{I}_x}{2} sin(\gamma g_z \delta (z-z'))\end{aligned} \tag{9.5.5}$$

$$\begin{aligned}&- \frac{\hat{I}_x}{2} sin(\gamma g_z \delta (z+z')) \\ &- \frac{\hat{I}_x}{2} sin(\gamma g_z \delta (z-z')) \\ &- \frac{\hat{I}_y}{2} cos(\gamma g_z \delta (z-z')) \\ &+ \frac{\hat{I}_y}{2} cos(\gamma g_z \delta (z+z'))\end{aligned}$$

Thus cancelling to:

$$\begin{aligned}\hat{\rho}(5) = &- \hat{I}_y cos(\gamma g_z \delta (z-z')) \\ &- \hat{I}_x sin(\gamma g_z \delta (z-z'))\end{aligned} \tag{9.5.6}$$

From here we can use the relations between $\hat{I}_y$ or $\hat{I}_x$, and the shift operators:

$$\begin{aligned}\hat{\rho}(5) = &\frac{i}{2} \hat{I}^+ cos(\gamma g_z \delta (z-z')) \\ &- \frac{1}{2} \hat{I}^+ sin(\gamma g_z \delta (z-z')) \\ &- \frac{i}{2} \hat{I}^- cos(\gamma g_z \delta (z-z')) \\ &- \frac{1}{2} \hat{I}^- sin(\gamma g_z \delta (z-z'))\end{aligned} \tag{9.5.7}$$

To further simplify:

$$\begin{aligned}\hat{\rho}(5) = &\frac{i}{2} \hat{I}^+ \left[cos(\gamma g_z \delta (z-z')) \right. \\ &\left. + i \, sin(\gamma g_z \delta (z-z')) \right] \\ &- \frac{i}{2} \hat{I}^- \left[cos(\gamma g_z \delta (z-z')) \right. \\ &\left. - i \, sin(\gamma g_z \delta (z-z')) \right]\end{aligned} \tag{9.5.8}$$

Exploiting Euler's formula neatens this equation to:

$$\begin{aligned}\hat{\rho}(5) = &\frac{i}{2} \hat{I}^+ e^{i\gamma g_z \delta (z-z')} \\ &- \frac{i}{2} \hat{I}^- e^{-i\gamma g_z \delta (z-z')}\end{aligned} \tag{9.5.9}$$

9.6 SBF production and imaging

The production of SBF follows the protocol described in Kokubo *et al.* but is reiterated here:[265]

The following chemicals were obtained from Sigma-Aldrich and were prepared in the following quantities:

Table 9.1: SBF reagents

Reagent	Formula	Quantity	Order
sodium chloride	NaCl	8.035 g	1
sodium hydrogen carbonate	$NaHCO_3$	0.355 g	2
potassium chloride	KCl	0.225 g	3
di-potassium hydrogen phosphate trihydrate	$K_2HPO_4.\ 3H_2O$	0.231 g	4
magnesium chloride hexahydrate	$MgCl_2.6H_2O$	0.311 g	5
calcium chloride	$CaCl_2$	0.292 g	7
sodium sulfate	Na_2SO_4	0.072 g	8
Tris-hydroxymethyl aminomethane	$(HOCH_2)3CNH_2$	6.118 g	9
1M hydrochloric acid	1M HCl	39 ml & 0-5 ml	6 & 10

700 ml of deionised water was added to a clean, dry, and plastic 1 L volumetric flask. The water was stirred within a water bath (1 L beaker) at 36.5 ± 1.5 °C. Reagents 1 through 8 were added in order and only once the previous reagent had fully dissolved. If the solution hadn't reached 900 mL it was topped up to this value. A pH meter was inserted and prior to Tris addition, the solution was ~2 pH. Tris was added in small aliquots, letting the pH settle between additions. Tris was added until the pH was just below 7.45. At this point, 1M HCl was added dropwise until the pH fell to 7.42. The previous two steps were repeated until all the Tris was dissolved. Finally, the pH was adjusted to be 7.4. The solution was made up to 1 L by allowing the solution to cool to 20 °C and then filling to the line with deionised water. The solution could then be stored.

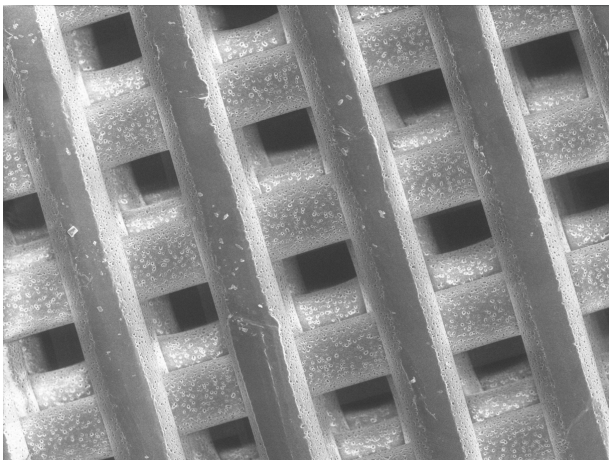

FIGURE 9.6.1: SEM images of a PCL scaffold plasma treated them submerged in SBF_{10} for 1.5 hours.

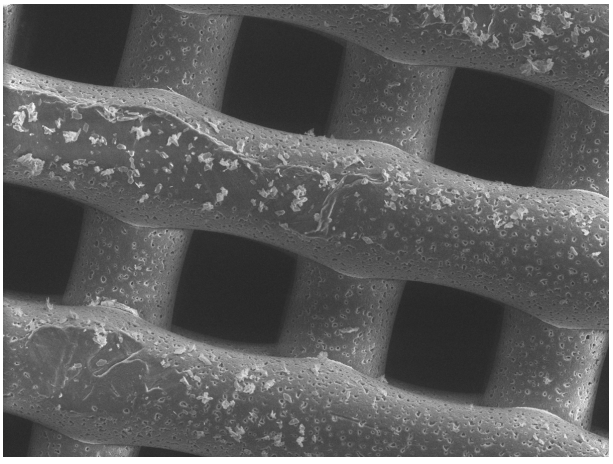

FIGURE 9.6.2: SEM images of a PCL scaffold plasma treated them submerged in SBF_{10} for 1.5 hours.

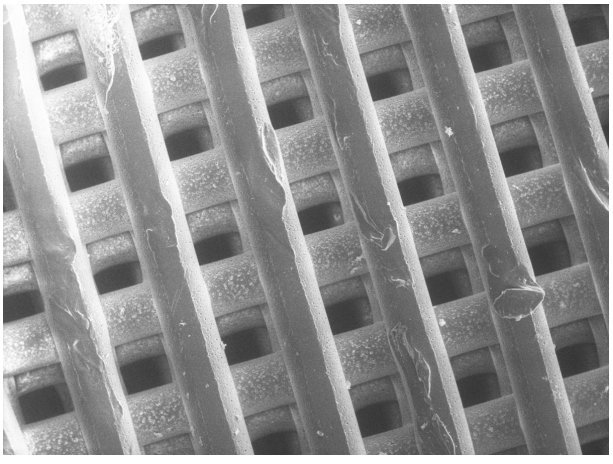

FIGURE 9.6.3: SEM images of a PCL scaffold plasma treated them submerged in SBF_{10} for 3 hours.

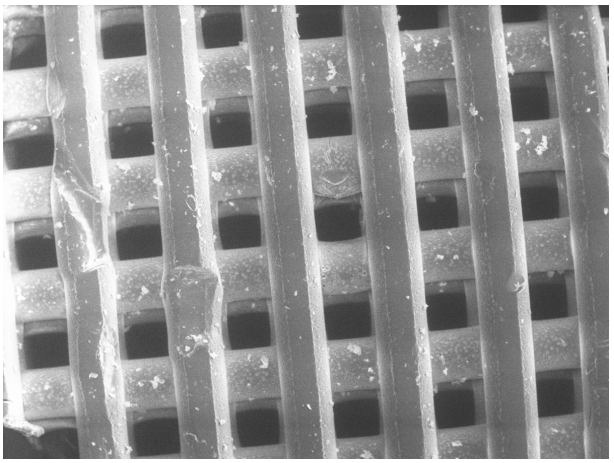

FIGURE 9.6.4: SEM images of a PCL scaffold plasma treated them submerged in SBF_{10} for 3 hours.

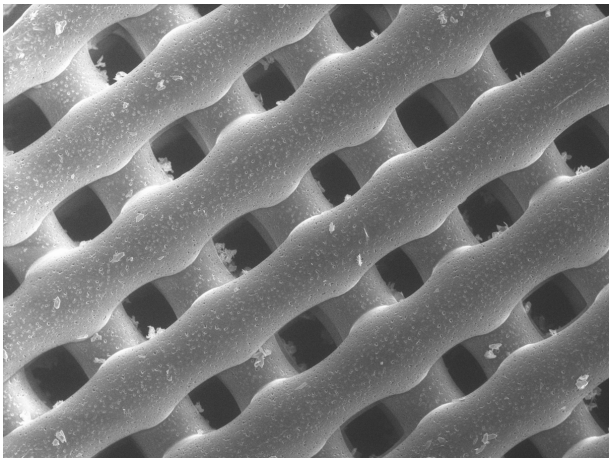

FIGURE 9.6.5: SEM images of a PCL scaffold plasma treated them submerged in SBF_{10} for 4 hours.

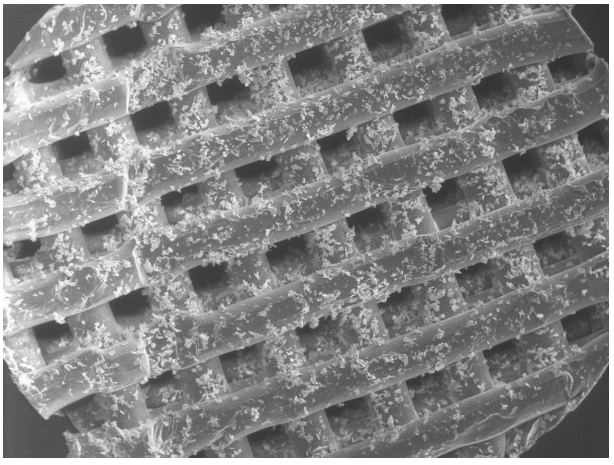

FIGURE 9.6.6: SEM images of a PCL scaffold plasma treated them submerged in SBF_{10} for 4 hours.

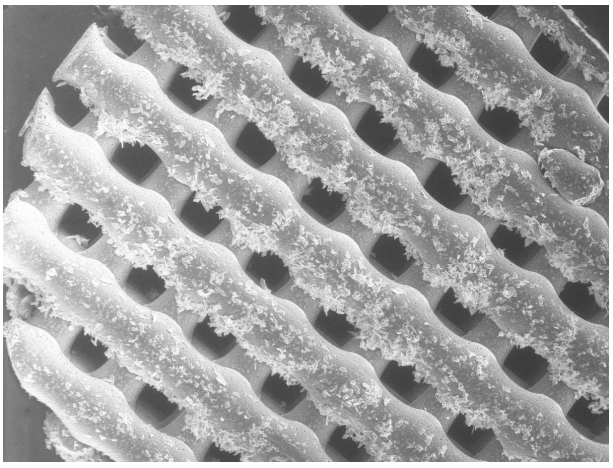

FIGURE 9.6.7: SEM images of a PCL scaffold plasma treated them submerged in SBF_{10} for 5 hours.

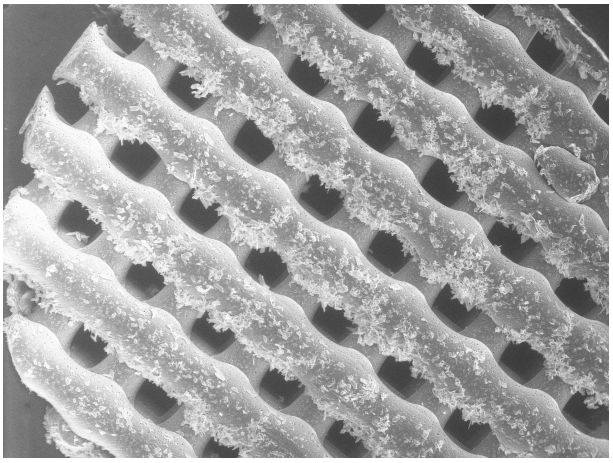

FIGURE 9.6.8: SEM images of a PCL scaffold plasma treated them submerged in SBF_{10} for 5 hours.

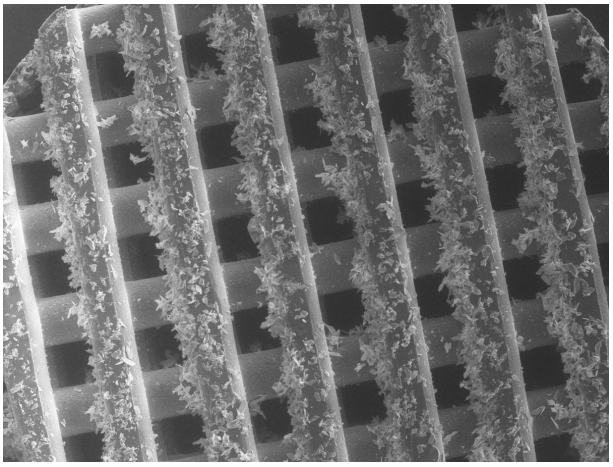

FIGURE 9.6.9: SEM images of a PCL scaffold plasma treated them submerged in SBF_{10} for 7 hours.

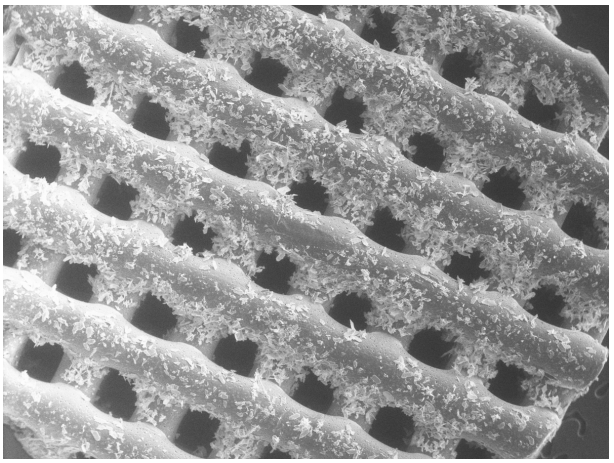

FIGURE 9.6.10: SEM images of a PCL scaffold plasma treated them submerged in SBF_{10} for 7 hours.

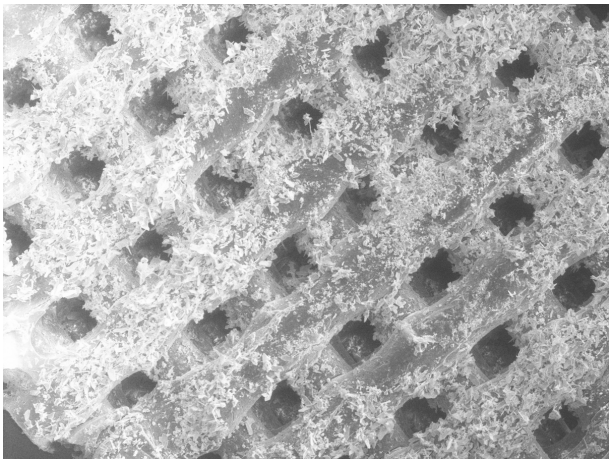

FIGURE 9.6.11: SEM images of a PCL scaffold plasma treated them submerged in SBF_{10} for 24 hours.

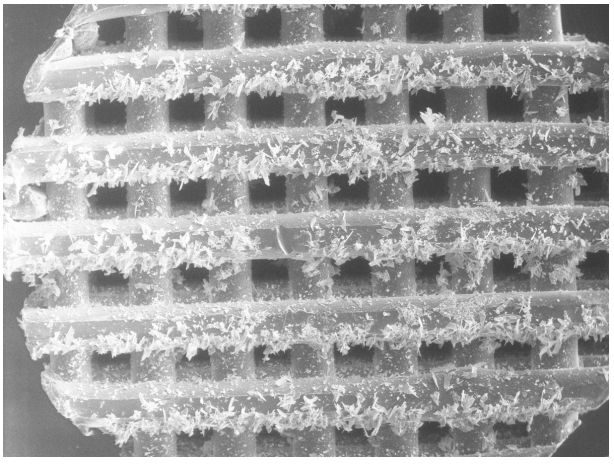

FIGURE 9.6.12: SEM images of a PCL scaffold plasma treated them submerged in SBF_{10} for 24 hours.

9.7 Tortuosity results

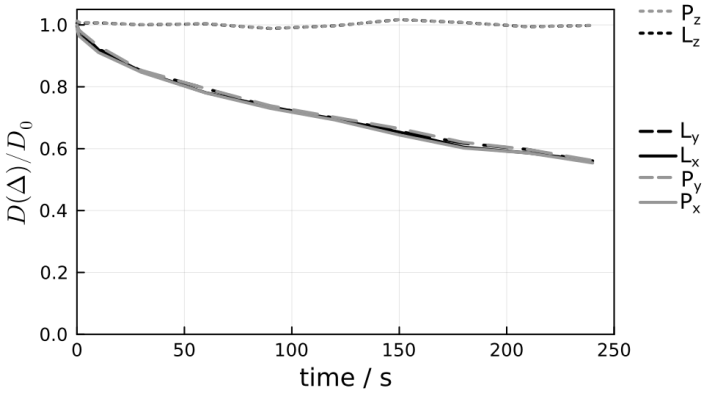

Figure 9.7.1: DTI in a 0° tilted cylinder with a radius of 0.5 mm showing the tortuosity for Lab-X (solid black), Lab-Y (dash black), Lab-Z (dot black), Principal-X (solid grey), Principal-Y (dash grey), and Principal-Z (dot grey).

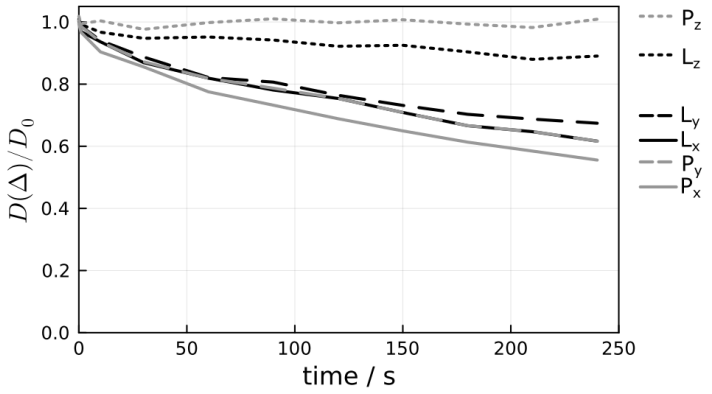

Figure 9.7.2: DTI in a 30° tilted cylinder with a radius of 0.5 mm showing the tortuosity for Lab-X (solid black), Lab-Y (dash black), Lab-Z (dot black), Principal-X (solid grey), Principal-Y (dash grey), and Principal-Z (dot grey).

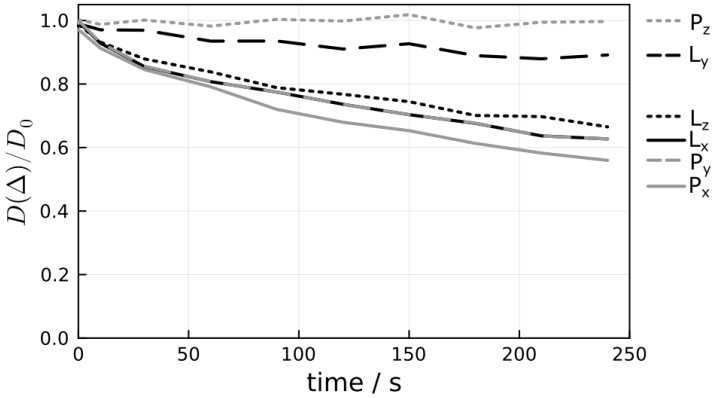

Figure 9.7.3: DTI in a 60° tilted cylinder with a radius of 0.5 mm showing the tortuosity for Lab-X (solid black), Lab-Y (dash black), Lab-Z (dot black), Principal-X (solid grey), Principal-Y (dash grey), and Principal-Z (dot grey).

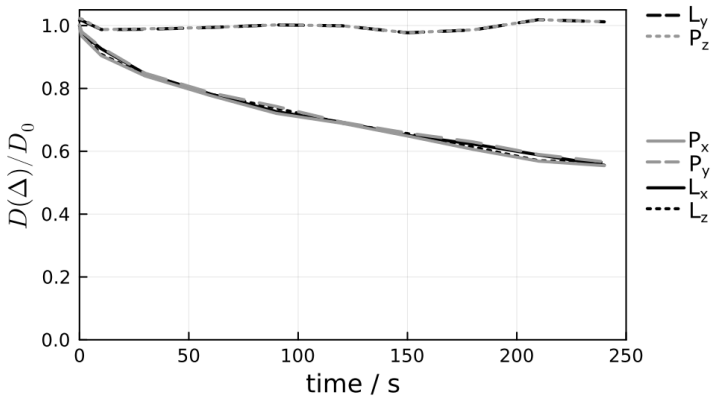

FIGURE 9.7.4: DTI in a 90° tilted cylinder with a radius of 0.5 mm showing the tortuosity for Lab-X (solid black), Lab-Y (dash black), Lab-Z (dot black), Principal-X (solid grey), Principal-Y (dash grey), and Principal-Z (dot grey).

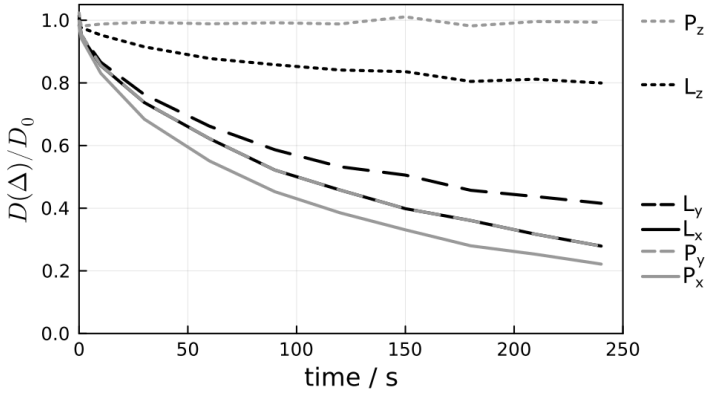

FIGURE 9.7.5: DTI in a 30° tilted cylinder with a radius of 0.25 mm showing the tortuosity for Lab-X (solid black), Lab-Y (dash black), Lab-Z (dot black), Principal-X (solid grey), Principal-Y (dash grey), and Principal-Z (dot grey).

References

[1] Q. Chen, A. E. Marble, B. G. Colpitts and B. J. Balcom, Journal of Magnetic Resonance, 2005, **175**, 300–308.

[2] I. V. Thorat, D. E. Stephenson, N. A. Zacharias, K. Zaghib, J. N. Harb and D. R. Wheeler, Journal of Power Sources, 2009, **188**, 592–600.

[3] F. P. Melchels, A. M. Barradas, C. A. van Blitterswijk, J. de Boer, J. Feijen and D. W. Grijpma, Acta Biomaterialia, 2010, **6**, 4208–4217.

[4] A. Bratland, T. Pavlin, K. Djurhuus and J. G. Seland, Journal of Magnetic Resonance, 2020, **310**, 106649.

[5] K.-J. Dunn, Journal of Magnetic Resonance, 2002, **156**, 171–180.

[6] A. M. R. Hall, T. A. A. Cartlidge and G. Pileio, Journal of Magnetic Resonance, 2020, **317**, 106778.

[7] A. Moysiadi, F. Giustiniano, A. M. R. Hall, T. A. A. Cartlidge, L. J. Brown and G. Pileio, Frontiers in Chemistry, 2021, **9**, 668044.

[8] S. A. Goudsmit and G. E. Uhlenbeck, Naturwissenschaften, 1925, **13**, 953.

[9] B. Bederson, Physical Review Letters, 2008, **101**, 010002.

[10] E. D. Commins, Annual Review of Nuclear and Particle Science, 2012, **62**, 133–157.

[11] P. Wolfgang, Zeit. f. Phys., 1927, **43**, 601–603.

[12] P. A. M. Dirac, Proceedings of the Royal Society of London. Series A, Containing Papers of a Mathematical and Physical Character, 1928, **117**, 610–624.

[13] D. M. Dennison, Proceedings of the Royal Society of London. Series A, Containing Papers of a Mathematical and Physical Character, 1927, **115**, 483–486.

[14] I. I. Rabi, Physical Review, 1937, **51**, 652.

[15] I. I. Rabi, J. R. Zacharias, S. Millman and P. Kusch, Physical review, 1938, **53**, 318.

[16] L. W. Alvarez and F. Bloch, Physical review, 1940, **57**, 111.

[17] N. Bloembergen, E. M. Purcell and R. V. Pound, Physical review, 1948, **73**, 679.

[18] J. T. Arnold, S. Dharmatti and M. Packard, The journal of chemical physics, 1951, **19**, 507.

[19] T. Polenova, R. Gupta and A. Goldbourt, 2015, **87**, 5458-5469.

[20] M. El Hariri El Nokab and K. O. Sebakhy, Nanomaterials, 2021, **11**, 1494.

[21] Q. Wang and U. G. Nielsen, Solid state nuclear magnetic resonance, 2020, **110**, 101698.

[22] C. He, S. Li, Y. Xiao, J. Xu and F. Deng, Solid State Nuclear Magnetic Resonance, 2022, **117**, 101772.

[23] W. Y. Chow, G. De Paëpe and S. Hediger, Chemical Reviews, 2022, **122**, 9795–9847.

[24] C. Hu, K. Guo, Y. Li, Z. Gu, J. Quan, S. Zhang and W. Zheng, Thin Solid Films, 2019, **688**, 137339.

[25] X. Liu, Y. Feng, K. Chen, B. Zhu, J. Zhao and T. Jiang, Optics express, 2014, **22**, 20107–20116.

[26] P. Yu, Y. Yao, J. Wu, X. Niu, A. L. Rogach and Z. Wang, Scientific reports, 2017, **7**, 7696.

[27] U. Holzgrabe, in Encyclopedia of Spectroscopy and Spectrometry (Third Edition), ed. J. C. Lindon, G. E. Tranter and D. W. Koppenaal, Academic Press, Oxford, Third Edition edn., 2017, pp. 393–395.

[28] J. Lee, S. H. Park, S. Cavagnero and J. H. Lee, Analytical chemistry, 2020, **92**, 5073–5081.

[29] B. Weber, K. Fliessbach and C. Elger, in Encyclopedia of Basic Epilepsy Research, ed. P. A. Schwartzkroin, Academic Press, Oxford, 2009, pp. 1549–1554.

[30] N. Panayiotis et al., Anal. Chem., 2014, **86**, 8206–8212.

[31] J. Eills, D. Budker, S. Cavagnero, E. Y. Chekmenev, S. J. Elliott, S. Jannin, A. Lesage, J. Matysik, T. Meersmann, T. Prisner et al., Chemical reviews, 2023, **123**, 1417–1551.

[32] B. Plainchont, P. Berruyer, J.-N. Dumez, S. Jannin and P. Giraudeau, Anal. Chem., 2018, **90**, 3639–3650.

[33] N. Salvi, in Annual reports on NMR spectroscopy, Elsevier, 2019, vol. 96, pp. 1–33.

[34] Q. Stern, J. Milani, B. Vuichoud, A. Bornet, A. D. Gossert, G. Bodenhausen and S. Jannin, The journal of physical chemistry letters, 2015, **6**, 1674–1678.

[35] P. R. Jensen, S. Meier, J. H. Ardenkjær-Larsen, J. Ø. Duus, M. Karlsson and M. H. Lerche, Chemical communications, 2009, 5168–5170.

[36] M. Carravetta, O. G. Johannessen and M. H. Levitt, Physical review letters, 2004, **92**, 153003.

[37] D. H. Lysak, F. V. Kock, S. Mamone, R. Soong, S. Glöggler and A. J. Simpson, Chemical Science, 2023, **14**, 1413–1418.

[38] J. Eills, E. Cavallari, R. Kircher, G. Di Matteo, C. Carrera, L. Dagys, M. H. Levitt, K. L. Ivanov, S. Aime, F. Reineri et al., Angewandte Chemie International Edition, 2021, **60**, 6791–6798.

[39] H. Kabasawa, Magnetic Resonance in Medical Sciences, 2022, **21**, 71–82.

[40] E. Lev and C. M. Boyce, Iscience, 2020, **23**, 101534.

[41] Y. Chen, Science and Technology of Engineering, Chemistry and Environmental Protection, 2024, **1**, 1–6.

[42] B. L. Edlow, A. Mareyam, A. Horn, J. R. Polimeni, T. Witzel, M. D. Tisdall, J. C. Augustinack, J. P. Stockmann, B. R. Diamond, A. Stevens et al., Scientific data, 2019, **6**, 244.

[43] A. J. Burghardt, R. Krug and S. Majumdar, in Vitamin D (Fourth Edition), ed. D. Feldman, Academic Press, Fourth Edition edn., 2018, pp. 1007–1041.

[44] Z. Zhang and A. Weller, Geophysics, 2021, **86**, JM11–JM22.

[45] M. C. Tourell, M. Kirkwood, M. J. Pearcy, K. I. Momot and J. P. Little, Journal of Magnetic Resonance Imaging, 2017, **45**, 1723–1735.

[46] M. C. Tourell, S. K. Powell and K. I. Momot, Journal of Physics D: Applied Physics, 2013, **46**, 455401.

[47] E. J. Fordham and J. Mitchell, Microporous and Mesoporous Materials, 2018, **269**, 35–38.

[48] S. Fichele, M. N. Paley, N. Woodhouse, P. D. Griffiths, E. J. Van Beek and J. M. Wild, Magnetic Resonance in Medicine: An Official Journal of the International Society for Magnetic Resonance in Medicine, 2004, **52**, 917–920.

[49] M. Müller-Petke, R. Dlugosch, J. Lehmann-Horn and M. Ronczka, Geophysics, 2015, **80**, D195–D206.

[50] H. J. Hogben, M. Krzystyniak, G. T. Charnock, P. J. Hore and I. Kuprov, Journal of Magnetic Resonance, 2011, **208**, 179–194.

[51] A. J. Allami, M. G. Concilio, P. Lally and I. Kuprov, Science Advances, 2019, **5**, eaaw8962.

[52] M. Hurlimann, K. G. Helmer, L. Latour and C. H. Sotak, Journal of Magnetic Resonance, Series A, 1994, **111**, 169–178.

[53] K. Keating and R. Knight, GEOPHYSICS, 2010, **75**, F71–F82.

[54] M. Kleinberg, R.;Horsfield, Journal of Magnetic Resonance, 1990, **88**, 9–19.

[55] H. Y. Carr and E. M. Purcell, Phys. Rev., 1954, **94**, 630–638.

[56] G. Q. Zhang, G. J. Hirasaki and W. V. House, Petrophysics-The SPWLA Journal of Formation Evaluation and Reservoir Description, 2003, **44**, 422–434.

[57] J. Korb, New Journal of Physics, 2011, **13**, 035016.

[58] G. Pileio and S. Ostrowska, Journal of Magnetic Resonance, 2017, **285**, 1–7.

[59] M. C. Tourell, I.-A. Pop, L. J. Brown, R. C. D. Brown and G. Pileio, Physical Chemistry Chemical Physics, 2018, **20**, 13705–13713.

[60] S. Blinder, in Introduction to Quantum Mechanics (Second Edition), ed. S. Blinder, Academic Press, San Diego, Second Edition edn., 2021, pp. 293–314.

[61] D. Graafen, S. Ebert, O. Neudert, L. Buljubasich, M. B. Franzoni, J. F. Dechent and K. Münnemann, in Annual Reports on NMR spectroscopy, ed. G. A. Webb, Academic Press, 2014, vol. 82 of Annual Reports on NMR Spectroscopy, pp. 167–215.

[62] S. Sinha, B. Tam and S. M. Wang, Membranes, 2022, **12**, 844.

[63] L. Yu, Y. Lei, Y. Ma, M. Liu, J. Zheng, D. Dan and P. Gao, Frontiers in physics, 2021, **9**, 644450.

[64] G. Palazzo and L. Paduano, in Colloidal Foundations of Nanoscience, Elsevier, 2022, pp. 257–287.

[65] L. Kisley, R. Brunetti, L. J. Tauzin, B. Shuang, X. Yi, A. W. Kirkeminde, D. A. Higgins, S. Weiss and C. F. Landes, ACS nano, 2015, **9**, 9158–9166.

[66] J. Sankaran and T. Wohland, Communications Biology, 2023, **6**, 699.

[67] O. C. Ibe, in Basic Concepts in Stochastic Processes, ed. R. Gouet, T. Olsen and J. Cochran, John Wiley & Sons, New Jersey, 2nd edn., 2013, ch. 2, pp. 29–48.

[68] L. Hao and P. Cheng, Journal of Power Sources, 2009, **186**, 104–114.

[69] F. Melzer, R. Breuer, R. Dahlmann and C. Hopmann, Journal of Cellular Plastics, 2022, **58**, 603–622.

[70] A. Valfouskaya, P. M. Adler, J.-F. Thovert and M. Fleury, Journal of Applied Physics, 2005, **97**, 083510.

[71] S. Didari, T. A. Harris, W. Huang, S. M. Tessier and Y. Wang, ECS Transactions, 2011, **41**, 499.

[72] M. H. Levitt, in Spin dynamics: basics of nuclear magnetic resonance, John Wiley & Sons, 2013, pp. 229–352.

[73] R. Ernst, G. Bodenhausen and A. Wokaun, Principles of nuclear magnetic resonance in one and two dimensions, Oxford university press, 1987.

[74] M. H. Levitt, Progress in Nuclear Magnetic Resonance Spectroscopy, 1986, **18**, 61–122.

[75] P. J. Hore, Nuclear magnetic resonance, Oxford University Press, USA, 1995.

[76] R. K. Ghosh, S. J. Kadlecek, N. N. Kuzma and R. R. Rizi, The Journal of Chemical Physics, 2012, **136**, 174508.

[77] R. McClung, eMagRes, 2007.

[78] H. S. Gutowsky, I. J. Lawrenson and K. Shimomura, Phys. Rev. Lett., 1961, **6**, 349–351.

[79] Z. J. Wang, M. A. Ohliger, P. E. Z. Larson, J. W. Gordon, R. A. Bok, J. Slater, J. E. Villanueva-Meyer, C. P. Hess, J. Kurhanewicz and D. B. Vigneron, Radiology, 2019, **291**, 273–284.

[80] K. Livo, M. Prasad and T. R. Graham, Scientific Reports, 2021, **11**, 290.

[81] B. E. Kinn, T. R. Myers and A. M. Allgeier, Current Opinion in Chemical Engineering, 2019, **24**, 115–121.

[82] A. T. Watson and C. P. Chang, Progress in Nuclear Magnetic Resonance Spectroscopy, 1997, **31**, 343–386.

[83] C. Honrao, N. Teissier, B. Zhang, R. Powers and E. M. O'Day, Molecules, 2021, **26**, 5115.

[84] S. Mizukami, R. Takikawa, F. Sugihara, Y. Hori, H. Tochio, M. Wälchli, M. Shirakawa and K. Kikuchi, Journal of the American Chemical Society, 2008, **130**, 794–795.

[85] K. T. O'Neill, D. Langford, E. O. Fridjonsson and M. L. Johns, Geophysical Journal International, 2023, **232**, 2017–2034.

[86] G. Pileio, in Lectures on Spin Dynamics: The Theoretical Minimum, Royal Society of Chemistry, 2022, pp. 143–162.

[87] H. Günther, in NMR spectroscopy: basic principles, concepts and applications in chemistry, John Wiley & Sons, Chichester, Second Edition edn., 1995, p. 581.

[88] V. Krishnan and M. Cosman, Journal of Biomolecular NMR, 1998, **12**, 177–182.

[89] C. P. Slichter and C. P. Slichter, Principles of Magnetic Resonance, 1990, 145–218.

[90] L. D'Silva, A. Pola, P. Dutta, G. V. Martinez, P. Sprenger, R. J. Gillies, P. W. Kuchel and S. Sendhil Velan, Magnetic Resonance in Chemistry, 2012, **50**, 443–448.

[91] M. H. Levitt, in Spin dynamics: basics of nuclear magnetic resonance, John Wiley & Sons, 2013, pp. 353–505.

[92] G. Pileio, M. Carravetta and M. H. Levitt, Proceedings of the National Academy of Sciences, 2010, **107**, 17135–17139.

[93] Z. M. Llarena, International Journal of Research in Pharmaceutical Sciences, 2017, **8**, 41–48.

[94] A. Atangana, in Fractional Operators with Constant and Variable Order with Application to Geo-Hydrology, ed. A. Atangana, Academic Press, 2018, pp. 15–47.

[95] B. Guo, in Well productivity handbook: vertical, fractured, horizontal, multilateral, multi-fractured, and radial-fractured wells, Gulf Professional Publishing, 2019, pp. 17–51.

[96] M. GINEBRA, in Bone Repair Biomaterials, ed. J. A. Planell, S. M. Best, D. Lacroix and A. Merolli, Woodhead Publishing, 2009, pp. 271–308.

[97] A. Ruys, in Alumina Ceramics, ed. A. Ruys, Woodhead Publishing, 2019, pp. 71–121.

[98] Q. L. Loh and C. Choong, Tissue engineering. Part B, Reviews, 2013, **19**, 485–502.

[99] J.-T. Guo, Y.-Q. Wei, S.-L. Chen, W. Sun, T.-T. Fan, M.-R. Xu and C.-C. Zhang, Petroleum Science, 2022, **19**, 1897–1904.

[100] J. E. Tanner, The Journal of Chemical Physics, 1970, **52**, 2523–2526.

[101] J. Kärger, D. M. Ruthven and D. N. Theodorou, Diffusion in nanoporous materials, Wiley Online Library, 2012, vol. 48.

[102] D. A. G. Bruggeman, Annalen der Physik, 1935, **416**, 636–664.

[103] A. Koponen, M. Kataja and J. Timonen, Physical Review E, 1997, **56**, 3319.

[104] M. B. Isichenko, Reviews of modern physics, 1992, **64**, 961.

[105] E. Fordham, S. Gibbs and L. Hall, Magnetic resonance imaging, 1994, **12**, 279–284.

[106] L. L. Latour, P. P. Mitra, R. L. Kleinberg and C. H. Sotak, Journal of Magnetic Resonance, Series A, 1993, **101**, 342–346.

[107] M. Urbanczyk, Y. Kharbanda, O. Mankinen and V.-V. Telkki, Analytical Chemistry, 2020, **92**, 9948–9955.

[108] P. N. Sen, L. M. Schwartz, P. P. Mitra and B. I. Halperin, Phys. Rev. B, 1994, **49**, 215–225.

[109] T. A. A. Cartlidge, T. B. R. Robertson, M. Utz and G. Pileio, The Journal of Physical Chemistry B, 2022, **126**, 6536–6546.

[110] M. Ko, X. Zhang, Z. Meng and K. A. Mirica, Journal of the American chemical society, 2017, **48**, 17229–17232.

[111] K. Ishikawa, Materials, 2010, **3**, 1138–1155.

[112] M. Marszałek, Z. Alexandrowicz and G. Rzepa, Environmental Science and Pollution Rsearch, 2014, **21**, 14023–14036.

[113] M. Klett, M. Giesecke, A. Nyman, F. Hallberg, R. W. Lindström, G. Lindbergh and I. Furó, Journal of American chemical society, 2012, **134**, 14654–14657.

[114] T. S. Karande, J. L. Ong and C. M. Agrawal, Annals of Biomedical Engineering, 2004, **32**, –.

[115] V. Anand and G. J. Hirasaki, Journal of magnetic resonance, 2008, **190**, 68–85.

[116] E. Grunewald and R. Knight, Near Surface Geophysics, 2011, **9**, 169–178.

[117] M. Ronczka and M. Müller-Petke, Geoscientific Instrumentation, Methods and Data Systems, 2012, **1**, 197–208.

[118] M. D. Hürlimann, Journal of Magnetic Resonance, 1998, **131**, 232–240.

[119] K. Yang, M. Li, N. N. Ling, E. F. May, P. R. Connolly, L. Esteban, M. B. Clennell, M. Mahmoud, A. El-Husseiny, A. R. Adebayo et al., Transport in Porous Media, 2019, **130**, 847–865.

[120] R. Bhattacharyya, B. Key, H. Chen, A. S. Best, A. F. Hollenkamp and C. P. Grey, Nature materials, 2010, **9**, 504–510.

[121] C. Multiphysics, Introduction to COMSOL multiphysics, 1998.

[122] T. Tranter, M. Kok, M. Lam and J. Gostick, SoftwareX, 2019, **10**, 100277.

[123] M. C. Wapler, J. Leupold, I. Dragonu, D. von Elverfeld, M. Zaitsev and U. Wallrabe, Journal of Magnetic Resonance, 2014, **242**, 233–242.

[124] E. Parzen, Stochastic processes, SIAM, 1999.

[125] J. Kärger, D. Ruthven and D. Theodorou, in Elementary Principles of Diffusion, John Wiley & Sons, Ltd, 2012, ch. 1, pp. 1–24.

[126] M. Ediger, Encyclopedia of Materials: Science and Technology, 2004, 1–5.

[127] M. E. von Neumann, John; Rose, Physics Today 1955-oct vol. 8 iss. 10, 1955, **8**, 21–21.

[128] P. W. Atkins, L. Muus et al., Electron spin relaxation in liquids, Plenum Press, 1972.

[129] P. Pechukas and J. C. Light, The Journal of Chemical Physics, 1966, **44**, 3897–3912.

[130] J. Jakowski and K. Morokuma, The Journal of Chemical Physics, 2009, **130**, 224106.

[131] J. C. Moodie and M. W. Long, Journal of Physics A: Mathematical and Theoretical, 2020, **54**, 015208.

[132] W. Magnus, Commun. Pure Appl. Math., 1954, **7**, 649–673.

[133] H. U. and W. J. S., Physical Review, 1968, **175**, 453–467.

[134] M. Edén, Concepts in Magnetic Resonance Part A, 2014, **43**, 109–126.

[135] L. A. Oberbroeckling, in Chapter 11 - Numerical Integration, ed. L. A. Oberbroeckling, Academic Press, 2021, pp. 183–191.

[136] G. D. SCOTT, Nature, 1960, **188**, 908–909.

[137] R. Hoffman, Journal of Magnetic Resonance, 2022, **335**, 107105.

[138] S. Meiboom and D. Gill, Review of Scientific Instruments, 1958, **29**, 688–691.

[139] S. B. W. Fukushima, Eiichi; Roeder, Experimental pulse NMR : a nuts and bolts approach, Perseus Books, Advanced Book Program, 1981.

[140] W. R. Inc., Mathematica, 2021.

[141] M. D. Abramoff, P. J. Magalhaes and S. J. Ram, Biophotomics International, 2004, **11**, 36–42.

[142] J. Bezanson, A. Edelman, S. Karpinski and V. B. Shah, SIAM review, 2017, **59**, 65–98.

[143] D. J. Griffiths, Introduction to electrodynamics, American Association of Physics Teachers, 2005.

[144] J. G. Proakis and D. G. Manolakis, Digital signal processing, Prentice Hall, 1996.

[145] M. L. Abell and J. P. Braselton, in Introduction to the Laplace Transform, ed. M. L. Abell and J. P. Braselton, Academic Press, Cambridge, 5th edn., 2018, ch. 8, pp. 399–460.

[146] G. E. Mueller, Powder Technology, 2010, **203**, 626–633.

[147] G. E. Mueller, Powder Technology, 2005, **159**, 105–110.

[148] R. Ek, T. Gren, U. Henriksson, H. Nyqvist, C. Nyström and L. ödberg, International Journal of Pharmaceutics, 1995, **124**, 9–18.

[149] A. Mahmood, H. Aboelkhair and A. Attia, Geoenergy Science and Engineering, 2023, **227**, 211855.

[150] J. He, Y. Ju, L. Lammers, K. Kulasinski and L. Zheng, Chemical Engineering Science, 2020, **215**, 115460.

[151] K. Lahti, R. Parkkola, P. Jääsaari, L. Haataja and V. Saunavaara, Pediatric Radiology, 2021, **51**, 1471–1480.

[152] A. Mehta, A. Sonabend and J. Bruce, Neurotherapeutics, 2017, **14**, 358–371.

[153] W. M. Pardridge, Journal of cerebral blood flow & metabolism, 2012, **32**, 1959–1972.

[154] U. Fagerholm, bioRxiv, 2022, 2022–09.

[155] M. Vidotto, D. Dini and E. De Momi, 2018 40th Annual International Conference of the IEEE Engineering in Medicine and Biology Society (EMBC), 2018, pp. 4901–4904.

[156] V. Langlois, V. Trinh and C. Perrot, Physical Review E, 2019, **100**, 013115.

[157] T.-T. Nguyen, A. Demortière, B. Fleutot, B. Delobel, C. Delacourt and S. J. Cooper, npj Computational Materials, 2020, **6**, 123.

[158] A. Johansen, in International Encyclopedia of Education (Third Edition), ed. P. Peterson, E. Baker and B. McGaw, Elsevier, Oxford, Third Edition edn., 2010, pp. 245–252.

[159] G. H. Gilmer, H. Huang, T. D. de la Rubia, J. Dalla Torre and F. Baumann, Thin Solid Films, 2000, **365**, 189–200.

[160] A. L. Brandao, J. B. Soares, J. C. Pinto and A. L. Alberton, Macromolecular Reaction Engineering, 2015, **9**, 141–185.

[161] R. Shimizu and D. Ze-Jun, Reports on Progress in Physics, 1992, **55**, 487.

[162] J. Hrabe, S. Hrabětová and K. Segeth, Biophysical journal, 2004, **87**, 1606–1617.

[163] J. R. Stiles, T. M. Bartol, M. M. Salpeter, E. E. Salpeter and T. J. Sejnowski, Synapses, 2001, **1**, 681–731.

[164] H.-H. Lee, A. Papaioannou, D. S. Novikov and E. Fieremans, Neuroimage, 2020, **222**, 117054.

[165] I. Alemany, J. N. Rose, J. Garnier-Brun, A. D. Scott and D. J. Doorly, Scientific Reports, 2022, **12**, 10759.

[166] J. D. Durrant and J. A. McCammon, BMC biology, 2011, **9**, 1–9.

[167] J. Chen, IOP Conference Series: Earth and Environmental Science, 2018, p. 012110.

[168] F. Mueller-Plathe, S. C. Rogers and W. F. Van Gunsteren, Macromolecules, 1992, **25**, 6722–6724.

[169] G. Pileio, Progress in Nuclear Magnetic Resonance Spectroscopy, 2017, **98-99**, 1–19.

[170] M. Carravetta and M. H. Levitt, The Journal of Chemical Physics, 2005, **122**, 214505.

[171] G. Pileio, Long-lived Nuclear Spin Order: Theory and Applications, Royal Society of Chemistry, 2020, vol. 22.

[172] M. Carravetta and M. H. Levitt, Journal of the American Chemical Society, 2004, **126**, 6228–6229.

[173] S. Elliott, C. Bengs, L. Brown, J. Hill-Cousins, D. O'Leary, G. Pileio and M. Levitt, The Journal of chemical physics, 2019, **150**, 064315.

[174] B. Kharkov, X. Duan, E. S. Tovar, J. W. Canary and A. Jerschow, Phys. Chem. Chem. Phys., 2019, **21**, 2595–2600.

[175] G. Pileio, M. Carravetta, E. Hughes and M. H. Levitt, Journal of the American Chemical Society, 2008, **130**, 12582–12583.

[176] C. Bengs, M. Sabba, A. Jerschow and M. H. Levitt, Physical Chemistry Chemical Physics, 2020, **22**, 9703–9712.

[177] A. S. Kiryutin, B. A. Rodin, N. N. Lukzen, A. V. Yurkovskaya, H.-M. Vieth and K. L. Ivanov, 2020.

[178] G. Pileio, in Encyclopedia of Spectroscopy and Spectrometry (Third Edition), ed. J. C. Lindon, G. E. Tranter and D. W. Koppenaal, Academic Press, Oxford, Third Edition edn., 2017, pp. 456–462.

[179] M. C. D. Tayler and M. H. Levitt, Phys. Chem. Chem. Phys., 2011, **13**, 9128–9130.

[180] Y. Feng, T. Theis, X. Liang, Q. Wang, P. Zhou and W. S. Warren, Journal of the American Chemical Society, 2013, **135**, 9632–9635.

[181] T. Robertson, R. C. Bannister, T. A. A. Cartlidge, T. Hugger, S. Breham, K. Zick, F. Engelke, S. Thompson and G. Pileio, Frontiers in Chemistry, 2023, **11**, 1229586.

[182] Bruker installs world's first 1.2 GHz NMR, https://cen.acs.org/business/instrumentation/Bruker-installs-12-GHz-NMR/98/i19.

[183] B. C. Percival, M. Grootveld, M. Gibson, Y. Osman, M. Molinari, F. Jafari, T. Sahota, M. Martin, F. Casanova, M. L. Mather et al., High-throughput, 2018, **8**, 2.

[184] L. Liu, Z. He, X. Cai and S. Fu, Applied Magnetic Resonance, 2021, **52**, 15–31.

[185] B. Blümich, Journal of Magnetic Resonance, 2019, **306**, 27–35.

[186] T. Parker, E. Limer, A. Watson, M. Defernez, D. Williamson and E. K. Kemsley, TrAC Trends in Analytical Chemistry, 2014, **57**, 147–158.

[187] L. Zhu, Q. Ma, J. Chen and G. Zhao, Food Chemistry, 2022, **396**, 133706.

[188] A. Adams, TrAC Trends in Analytical Chemistry, 2016, **83**, 107–119.

[189] E. Steimers, Y. Matviychuk, D. J. Holland, H. Hasse and E. von Harbou, Magnetic Resonance in Chemistry, 2022, **60**, 1113–1130.

[190] S. Baroni, R. Consonni, G. Ferrante and S. Aime, Journal of agricultural and food chemistry, 2009, **57**, 3028–3032.

[191] P. Conte, L. Cinquanta, P. L. Meo, F. Mazza, A. Micalizzi and O. Corona, Food Research International, 2021, **139**, 109845.

[192] P. Conte, A. Maccotta, C. De Pasquale, G. Alonzo et al., Fresenius Environ. Bull, 2010, **19**, 2077–2082.

[193] P. Lo Meo, F. Mundo, S. Terranova, P. Conte and D. Chillura Martino, The Journal of Physical Chemistry B, 2020, **124**, 1847–1857.

[194] P. Conte and P. Lo Meo, Agronomy, 2020, **10**, 1040.

[195] S. Godefroy, J.-P. Korb, L. K. Creamer, P. J. Watkinson and P. T. Callaghan, Journal of colloid and interface science, 2003, **267**, 337–342.

[196] R. M. Steele, J.-P. Korb, G. Ferrante and S. Bubici, Magnetic Resonance in Chemistry, 2016, **54**, 502–509.

[197] T. Zavada, S. Stapf, U. Beginn and R. Kimmich, Magnetic resonance imaging, 1998, **16**, 711–713.

[198] M. Pasina, G. Ferrantea and D. Krukb, Stelar, 2017, **1**, 1–4.

[199] A. Rachocki and J. Tritt-Goc, Food chemistry, 2014, **152**, 94–99.

[200] E. G. Ates, V. Domenici, M. Florek-Wojciechowska, A. Gradišek, D. Kruk, N. Maltar-Strmečki, M. Oztop, E. B. Ozvural and A.-L. Rollet, Trends in food science & technology, 2021, **110**, 513–524.

[201] C. Bengs, in Long-lived Nuclear Spin Order: Theory and Applications, The Royal Society of Chemistry, 2020.

[202] I. V. Zhukov, A. S. Kiryutin, A. V. Yurkovskaya, Y. A. Grishin, H.-M. Vieth and K. L. Ivanov, Physical Chemistry Chemical Physics, 2018, **20**, 12396–12405.

[203] A. Navarro, M. Gómez, L. Daza and J. López-Cascales, Scientific Reports, 2022, **12**, 4219.

[204] Y. Chen-Yang, T. Hung, J. Huang and F. Yang, Journal of Power Sources, 2007, **173**, 183–188.

[205] W.-k. Lee, C.-H. Ho, J. Van Zee and M. Murthy, Journal of power sources, 1999, **84**, 45–51.

[206] H. Liu, T. Zhou and P. Cheng, Journal of Heat Transfer, 2005, **127**, 1363–1379.

[207] J. Hussain, D.-K. Kim, S. Park, M. W. Khalid, S.-S. Hussain, A. Ali, B. Lee, M. Song and T.-S. Kim, Materials, 2023, **16**, 4554.

[208] M. Ceniceros-Reyes, F. Rodríguez, Y. Perera-Mercado, E. Saucedo-Salazar and E. D. Barriga-Castro, Acta Microscopica, 2014, **23**, 78–84.

[209] B. J. Griffin, Electron microscopy: methods and protocols, 2007, 467–495.

[210] A. Burnstock and C. Jones, in Radiation in Art and Archeometry, ed. D. Creagh and D. Bradley, Elsevier Science B.V., Amsterdam, 2000, pp. 202–231.

[211] F.-Q. Zhou, Frontiers in Medicine, 2022, **9**, 905978.

[212] B. Alberts, A. Johnson, J. Lewis, M. Raff, K. Roberts and P. Walter, in Molecular Biology of the Cell. 4th edition, Garland Science, 2002.

[213] L. R. Gray, S. C. Tompkins and E. B. Taylor, Cellular and molecular life sciences, 2014, **71**, 2577–2604.

[214] V. Ceperuelo-Mallafré, L. Reverté, A. Madeira, A. Gutierrez-Valencia, E. Ruiz-Mateos, M. J. Buzón, T. Auguet, F. Vidal, A. Rull and S. Fernández-Veledo, Frontiers in immunology, 2022, **13**, 912579.

[215] I. Elia, J. H. Rowe, S. Johnson, S. Joshi, G. Notarangelo, K. Kurmi, S. Weiss, G. J. Freeman, A. H. Sharpe and M. C. Haigis, Cell metabolism, 2022, **34**, 1137–1150.

[216] J. M. Park, S. Josan, R. E. Hurd, J. Graham, P. J. Havel, D. Bendahan, D. Mayer, Y. Chung, D. M. Spielman and T. Jue, Pflügers Archiv-European Journal of Physiology, 2021, **473**, 1761–1773.

[217] E. Bliemsrieder, G. Kaissis, M. Grashei, G. Topping, J. Altomonte, C. Hundshammer, F. Lohöfer, I. Heid, D. Keim, S. Gebrekidan et al., Scientific reports, 2021, **11**, 1191.

[218] D. Lesnicki, V. Wank, J. D. Cyran, E. H. Backus and M. Sulpizi, Physical Chemistry Chemical Physics, 2022, **24**, 13510–13513.

[219] J. Damitio, G. Smith, J. Meany and Y. Pocker, Journal of the American Chemical Society, 1992, **114**, 3081–3087.

[220] R. J. Perkins, R. K. Shoemaker, B. K. Carpenter and V. Vaida, The Journal of Physical Chemistry A, 2016, **120**, 10096–10107.

[221] Y. Pocker, J. E. Meany, B. J. Nist and C. Zadorojny, The Journal of Physical Chemistry, 1969, **73**, 2879–2882.

[222] K. Golman, R. in 't Zandt and M. Thaning, Proceedings of the National Academy of Sciences, 2006, **103**, 11270–11275.

[223] S. Margolis and B. Coxon, Analytical Chemistry, 1986, **58**, 2504–2510.

[224] R. J. Rapf, R. J. Perkins, B. K. Carpenter and V. Vaida, The Journal of Physical Chemistry A, 2017, **121**, 4272–4282.

[225] I. Marco-Rius, M. C. Tayler, M. I. Kettunen, T. J. Larkin, K. N. Timm, E. M. Serrao, T. B. Rodrigues, G. Pileio, J. H. Ardenkjaer-Larsen, M. H. Levitt et al., NMR in Biomedicine, 2013, **26**, 1696–1704.

[226] T. A. A. Cartlidge, Y. Wu, T. B. R. Robertson, O. L. Katsamenis and G. Pileio, In press.

[227] I. G. Beşkardeş and M. Gümüşderelioğlu, Journal of Bioactive and Compatible Polymers, 2009, **24**, 507–524.

[228] J. M. Holzwarth and P. X. Ma, Biomaterials, 2011, **32**, 9622–9629.

[229] S. J. Hollister, Nature materials, 2005, **4**, 518–524.

[230] H. K. Mostafa, Journal of Microscopy and Ultrastructure, 2022, **10**, 40–46.

[231] A. Romito, G. Cobellis et al., Stem cells international, 2016, **2016**, 9451492.

[232] D. Bhartiya et al., Stem Cells International, 2013, **2013**, 547501.

[233] A. Aldahmash, W. Zaher, M. Al-Nbaheen and M. Kassem, Annals of Saudi medicine, 2012, **32**, 68–77.

[234] Y. She, Z. Fan, L. Wang, Y. Li, W. Sun, H. Tang, L. Zhang, L. Wu, H. Zheng and C. Chen, Frontiers in cell and developmental biology, 2021, **9**, 629796.

[235] C. L. Salgado, E. M. Sanchez, C. A. Zavaglia and P. L. Granja, Journal of Biomedical Materials Research Part A, 2012, **100**, 243–251.

[236] F. Zia, M. Salman, M. Ali, R. Iqbal, A. Rasul, M. Najam-ul Haq, M. Asgher and K. M. Zia, in Bionanocomposites, Elsevier, 2020, pp. 173–205.

[237] S. J. Gutiérrez-Prieto, S. J. Perdomo-Lara, J. M. Diaz-Peraza, L. G. Sequeda-Castañeda et al., Advances in Pharmacological and Pharmaceutical Sciences, 2019, **2019**, 5420752.

[238] L. Polo-Corrales, M. Latorre-Esteves and J. E. Ramirez-Vick, Journal of nanoscience and nanotechnology, 2014, **14**, 15–56.

[239] N. Mulchandani, A. Prasad and V. Katiyar, in Materials for biomedical engineering, Elsevier, 2019, pp. 87–125.

[240] S. Cao, Y. Zhao, Y. Hu, L. Zou and J. Chen, Composites Part B: Engineering, 2020, **202**, 108445.

[241] P. Ginestra, E. Ceretti and A. Fiorentino, Procedia CIRP, 2016, **49**, 8–13.

[242] M. Guvendiren, J. Molde, R. M. Soares and J. Kohn, ACS biomaterials science & engineering, 2016, **2**, 1679–1693.

[243] S. Radhakrishnan, S. Nagarajan, H. Belaid, C. Farha, I. Iatsunskyi, E. Coy, L. Soussan, V. Huon, J. Bares, K. Belkacemi et al., Materials Science and Engineering: C, 2021, **118**, 111525.

[244] R. O. Darouiche, New England Journal of Medicine, 2004, **350**, 1422–1429.

[245] J. R. Morones-Ramirez, J. A. Winkler, C. S. Spina and J. J. Collins, Science translational medicine, 2013, **5**, 190ra81–190ra81.

[246] N. Xiang, J. S. Yuen Jr, A. J. Stout, N. R. Rubio, Y. Chen and D. L. Kaplan, Biomaterials, 2022, **285**, 121543.

[247] I. Jun, H.-S. Han, J. R. Edwards and H. Jeon, International journal of molecular sciences, 2018, **19**, 745.

[248] M. DiCerbo, M. M. Benmassaoud and S. L. Vega, Frontiers in Medical Technology, 2022, **4**, 884314.

[249] J. Visser, F. P. Melchels, J. E. Jeon, E. M. Van Bussel, L. S. Kimpton, H. M. Byrne, W. J. Dhert, P. D. Dalton, D. W. Hutmacher and J. Malda, Nature communications, 2015, **6**, 1–10.

[250] S. M. M. Roosa, J. M. Kemppainen, E. N. Moffitt, P. H. Krebsbach and S. J. Hollister, Journal of Biomedical Materials Research Part A: An Official Journal of The Society for Biomaterials, The Japanese Society for Biomaterials, and The Australian Society for Biomaterials and the Korean Society for Biomaterials, 2010, **92**, 359–368.

[251] I. Ullah, R. B. Subbarao and G. J. Rho, Bioscience reports, 2015, **35**, e00191.

[252] J. Narbona-Carceles, J. Vaquero, S. Suárez-Sancho, F. Forriol and M. E. Fernández-Santos, Injury, 2014, **45**, S42–S47.

[253] A. Aldahmash, W. Zaher, M. Al-Nbaheen and M. Kassem, Annals of Saudi medicine, 2012, **32**, 68–77.

[254] J. L. Simonsen, C. Rosada, N. Serakinci, J. Justesen, K. Stenderup, S. I. Rattan, T. G. Jensen and M. Kassem, Nature biotechnology, 2002, **20**, 592–596.

[255] P. W. Hwang and J. A. Horton, Scientific reports, 2019, **9**, 8299.

[256] M. Izumiya, M. Haniu, K. Ueda, H. Ishida, C. Ma, H. Ideta, A. Sobajima, K. Ueshiba, T. Uemura, N. Saito et al., International journal of molecular sciences, 2021, **22**, 7752.

[257] D. Wang, K. Christensen, K. Chawla, G. Xiao, P. H. Krebsbach and R. T. Dr. Franceschi, Journal of Bone and Mineral Research, 1999, **14**, 893–903.

[258] A. Hermenean, A. Codreanu, H. Herman, C. Balta, M. Rosu, C. V. Mihali, A. Ivan, S. Dinescu, M. Ionita and M. Costache, Scientific reports, 2017, **7**, 16641.

[259] K. M. Woo, J.-H. Jun, V. J. Chen, J. Seo, J.-H. Baek, H.-M. Ryoo, G.-S. Kim, M. J. Somerman and P. X. Ma, Biomaterials, 2007, **28**, 335–343.

[260] H. Y. Zhou, H. Takita, R. Fujisawa, M. Mizuno and Y. Kuboki, Calcified tissue international, 1995, **56**, 403–407.

[261] J. B. Lian and G. S. Stein, The Iowa orthopaedic journal, 1995, **15**, 118.

[262] Y. Kurashina, C. Imashiro, M. Hirano, T. Kuribara, K. Totani, K. Ohnuma, J. Friend and K. Takemura, Communications biology, 2019, **2**, 393.

[263] M. Cámara-Torres, R. Sinha, C. Mota and L. Moroni, Acta Biomaterialia, 2020, **101**, 183–195.

[264] F. Yang, J. Wolke and J. Jansen, Chemical Engineering Journal, 2008, **137**, 154–161.

[265] T. Kokubo and H. Takadama, Biomaterials, 2006, **27**, 2907–2915.

[266] E. Tsuruga, H. Takita, H. Itoh, Y. Wakisaka and Y. Kuboki, Journal of biochemistry, 1997, **121 2**, 317–24.

[267] J. Knychala, N. Bouropoulos, C. J. Catt, O. L. Katsamenis, C. P. Please and B. G. Sengers, Annals of Biomedical Engineering, 2013, **41**, 919–930.

[268] J. Fu, H. R. Thomas and C. Li, Earth-Science Reviews, 2021, **212**, 103439.

[269] D. Sankar, K. Shalumon, K. Chennazhi, D. Menon and R. Jayakumar, Tissue Engineering Part A, 2014, **20**, 1689–1702.

[270] A. Oyane, M. Uchida, Y. Yokoyama, C. Choong, J. Triffitt and A. Ito, Journal of Biomedical Materials Research Part A, 2005, **75A**, 138–145.

[271] H. Jeon, H. Lee and G. Kim, Tissue Engineering Part C: Methods, 2014, **20**, 951–963.

[272] A. C. Tas and S. B. Bhaduri, Journal of materials research, 2004, **19**, 2742–2749.

[273] C. Ohtsuki, S. Kotani, T. Kitsugi, T. Yamamuro and T. Kokubo, Bioceramics, 1993, **2**, 105–112.

[274] P. Ducheyne and Q. Qiu, Biomaterials, 1999, **20**, 2287–2303.

[275] S. Samavedi, A. R. Whittington and A. S. Goldstein, Acta biomaterialia, 2013, **9**, 8037–8045.

[276] E. Salamanca, C. S. Choy, L. M. Aung, T.-C. Tsao, P.-H. Wang, W.-A. Lin, Y.-F. Wu and W.-J. Chang, Polymers, 2023, **15**, 2619.

[277] Products - 3D Bioreactor, https://3dbiotek.com/prod_3dbioreactor.aspx.

[278] C. Selden and B. Fuller, Bioengineering, 2018, **5**, 32.

[279] J. Lee, H. Kim, H.-R. Lim, Y. S. Kim, T. T. T. Hoang, J. Choi, G.-J. Jeong, H. Kim, R. Herbert, I. Soltis et al., Science Advances, 2024, **10**, eadk6714.

[280] K. E. Kadler, D. F. Holmes, J. A. Trotter and J. A. Chapman, Biochemical Journal, 1996, **316**, 1–11.

[281] A. D. McInnes, M. A. Moser and X. Chen, Journal of functional biomaterials, 2022, **13**, 240.

[282] D. A. Taylor, P.-F. Lee, Y. Barac, C. Hochman-Mendez and L. C. Sampaio, in Emerging technologies for heart diseases, Elsevier, 2020, pp. 291–310.

[283] O. Nadiarnykh, R. B. LaComb, M. A. Brewer and P. J. Campagnola, BMC cancer, 2010, **10**, 1–14.

[284] R. Hoebe, C. Van Oven, T. Gadella Jr, P. Dhonukshe, C. Van Noorden and E. Manders, Nature biotechnology, 2007, **25**, 249–253.

[285] A. Ettinger and T. Wittmann, Methods in cell biology, 2014, **123**, 77–94.

[286] A. Aghigh, S. Bancelin, M. Rivard, M. Pinsard, H. Ibrahim and F. Légaré, Biophysical Reviews, 2023, **15**, 43–70.

[287] O. Nadiarnykh, R. B. LaComb, M. A. Brewer and P. J. Campagnola, BMC cancer, 2010, **10**, 1–14.

[288] N. H. Green, R. M. Delaine-Smith, H. J. Askew, R. Byers, G. C. Reilly and S. J. Matcher, Scientific reports, 2017, **7**, 13331.

[289] A. Zoumi, A. Yeh and B. J. Tromberg, Proceedings of the National Academy of Sciences, 2002, **99**, 11014–11019.

[290] S. Boonrungsiman, E. Gentleman, R. Carzaniga, N. D. Evans, D. W. McComb, A. E. Porter and M. M. Stevens, Proceedings of the National Academy of Sciences, 2012, **109**, 14170–14175.

[291] M. Winey, J. B. Meehl, E. T. O'Toole and T. H. Giddings Jr, Molecular biology of the cell, 2014, **25**, 319–323.

[292] NMR solvent data chart, https://chem.washington.edu/sites/chem/files/documents/facilities/nmrsolventschart_001.pdf.